University of Trento

Synthesis and characterization of nanocatalysts for applications in water purification and hydrogen production

PhD Candidate: Yaksh Jyotindra Popat

Supervisor: Prof. Antonio Miotello

Co-supervisor: Dr. Nainesh Patel

Department of Physics

Doctoral Program in Physics

32nd cycle

Synthesis and characterization of nanocatalysts for applications in water purification and hydrogen production

by

Yaksh Jyotindra Popat

B.Sc, Mithibai College, University of Mumbai (2014)

M.Sc in Physics, University of Mumbai (2016)

Thesis submitted to the Doctoral Program in Physics in partial fulfilment of the requirements for the degree of *Doctor of Philosophy in Physics*

Committee members:

1) **Prof. Giovanni Mattei**, University of Padova, Italy.
2) **Prof. Karl Whittle**, University of Liverpool, UK.
3) **Prof. Giacomo Baldi**, University of Trento, Italy.

To my parents and family…

Abstract

The research fields of water purification and renewable energy sources have gained a lot of interest in the past few decades owing to the growing distress caused by rapid industrialization and population outburst. This thesis is aimed at developing materials as catalysts for applications in water purification and electrochemical H_2 production, which can take us a step closer to living in a clean and sustainable environment. The thesis is mainly divided in three sections, the first one gives an overview of the current water scarcity and pollution issues while addressing the need for treating the industrial wastewater in a clean and efficient manner through photocatalysis. It also sheds light on the existing energy crisis due to strong dependence on fossil fuels and their impact on the climate while acknowledging hydrogen as a potential renewable energy carrier for sufficing the future energy needs of the planet.

Section 2 contains different approaches taken into consideration for addressing the problem of water pollution caused by the emission of industrial organic pollutants, mainly dyes and phenols, into natural water streams/reservoirs. The first approach consists of synthesizing photocatalyst coatings forming heterojunction to tackle the problems of agglomeration of catalyst and charge recombination. Pulsed Laser Deposition (PLD) was realised as an effective technique for fabrication of photocatalyst coatings with desired morphologies. $CoFe_2O_4$/CoO hierarchical-type nanostructured coatings were deposited by PLD for evaluating the photocatalytic activity towards degradation of MB dye. The role of morphology, optical properties and heterojunction between $CoFe_2O_4$ and CoO were studied through an in-depth characterization and analysis. In our next work, the strategies of doping and composite formation were combined as an effective approach in reducing the bulk and surface recombination of photoexcited charges. Tungsten doped TiO_2/reduced graphene oxide (rGO) nanocomposite photocatalysts were synthesized and tested for para-Nitrophenol (p-NP) degradation. The synthesized photocatalyst exhibited good photocatalytic activity in degradation of organic pollutant p-NP with superior activity compared to rGO/TiO_2, TiO_2 and W-TiO_2 respectively. Similar studies were performed on reduced graphene oxide (rGO)-TiO_2 composites by varying the GO to TiO_2 concentration. The synthesized composite rGOT-3 (rGO/TiO_2 weight ratio of 3) displayed the highest photocatalytic activity for degradation of p-NP compared to TiO_2, GO and other composites. Experimental measurements were conducted in order to study and analyse the synthesized composites. In the final approach, the photocatalytic activity of metal oxide films exhibiting high surface area were tested under

concentrated natural sunlight. The PLD synthesized monoclinic nanostructured “flower-shape like” tungsten oxide (WO_3) coatings demonstrated good photocatalytic degradation of MB dye in solar PDC (parabolic dish concentrator) setup under photo-Fenton conditions. The coatings also show stable performance in acidic media thereby broadening the industrial applications.

Section 3 deals with electrochemical water splitting, a promising technique for clean and renewable H_2 and O_2 production. This section comprises of developing Water Oxidation Catalysts (WOC’s) made up of cheap, scalable and efficient materials exhibiting low overpotentials for Oxygen Evolution Reactions (OER). IrOx and RuOx are considered as a benchmark for WOC performance in acidic media, however, in recent years, transition metal oxides based on iron, cobalt and nickel have gained a lot of attention because of their stability and promising performances as WOC in alkaline media. NiOx films with different morphologies were synthesized by PLD to functionalize solar light absorbing photoanodes. The synthesized porous films demonstrated low overpotentials for OER thereby opening ways for the application of NiOx as OER co-catalysts in photoanodes for photoelectrochemical (PEC) technology. In our final work, mixed metal oxide coatings were fabricated by PLD for alkaline water oxidation studies. Boron was introduced to study its influence on the electrochemical activity of the films. The role of Co, Fe and B were individually studied through detailed characterization and electrochemical studies.

Table of Contents:

Chapter 1: Environment and Energy

1.1 Environment

a) Water as a resource

Water is the most important resource humans have on planet earth. Though it is a renewable source of energy, it is not unlimited. Hence it is a resource which has to be conserved so as to suffice the needs of the present and the future generations of all the species. The uses of water are well known and ranges from the domestic level to the industrial scale. With the current population approaching 8 billion, more and more food is required which means more water will be consumed. Agriculture is the primary consumer of water and with the increase in growth of water thirsty meat and vegetables, a significant load has been put on the water resources.

Water resources are the primary sources of water on planet earth. Out of the total water present, about 97% is present in oceans in the form of saltwater (**Fig. 1**). The remaining 3% has majority of it frozen in glaciers and polar ice caps, leaving less than 1% freshwater available on our planet in the form of ground water and other freshwater resources on land. Hence it is very important to understand how limited freshwater resources are and efforts have to be made to preserve their purity thereby maintaining the quality of water.

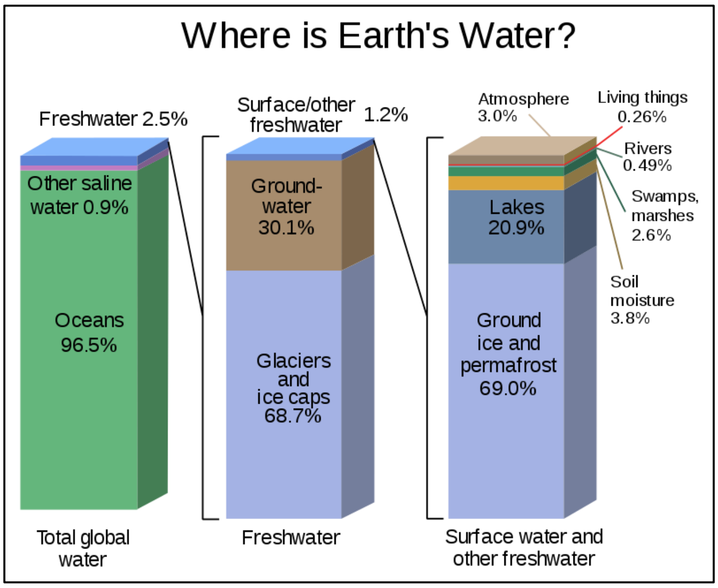

Figure 1: *graphical representation of earth's water distribution [1].*

b) Current issues

Water demand has increased widely in the past few decades and exceeds the supply in many parts of the world. A lot of developing and under developed countries are already facing water crisis and this imbalance is expanding to other developed countries too. This imbalance arises firstly due to the fact that the existing freshwater resources in the world are not evenly distributed. Hence, there are some parts of the world which are in deficit and some in surplus. More than a billion people lack access to safe drinking water, almost 3 billion have little or no sanitation and millions of people die annually from diseases transmitted through unsafe water [2]. The adversities of water shortage and uneven distribution are felt all over the world. According to UN reports, about 700 million people worldwide could be displaced by intense water scarcity by 2030 [3]. A third of the world’s biggest groundwater systems are already in distress [4]. Nearly half the global population are already living in potential water scarce areas at least one month per year and this could increase to about 4.8–5.7 billion in 2050. About 73% of the affected people live in Asia (69% by 2050) [5].

Another important factor adding to the changing water levels is the climate change. Sudden change in the climate patterns have significant impacts on water resources in the world because of the close dependance of hydrologic cycle on climate. There have been many reports on melting of ice in the glaciers and snowy regions leading to an increase in the sea level along with significant damage to the existing ecosystem. About 10% of land area on Earth is covered with glacial ice. Almost 90% of that is in Antarctica, while the remaining 10% is in the Greenland ice cap. Rapid glacial melt in Antarctica and Greenland influences the ocean currents, as massive amounts of cold glacial-melt water enter the warmer ocean waters and slow down the ocean currents. **Fig. 2** displays the amount of ice loss in Greenland and Antartica along with the increase in sea levels in recent years.

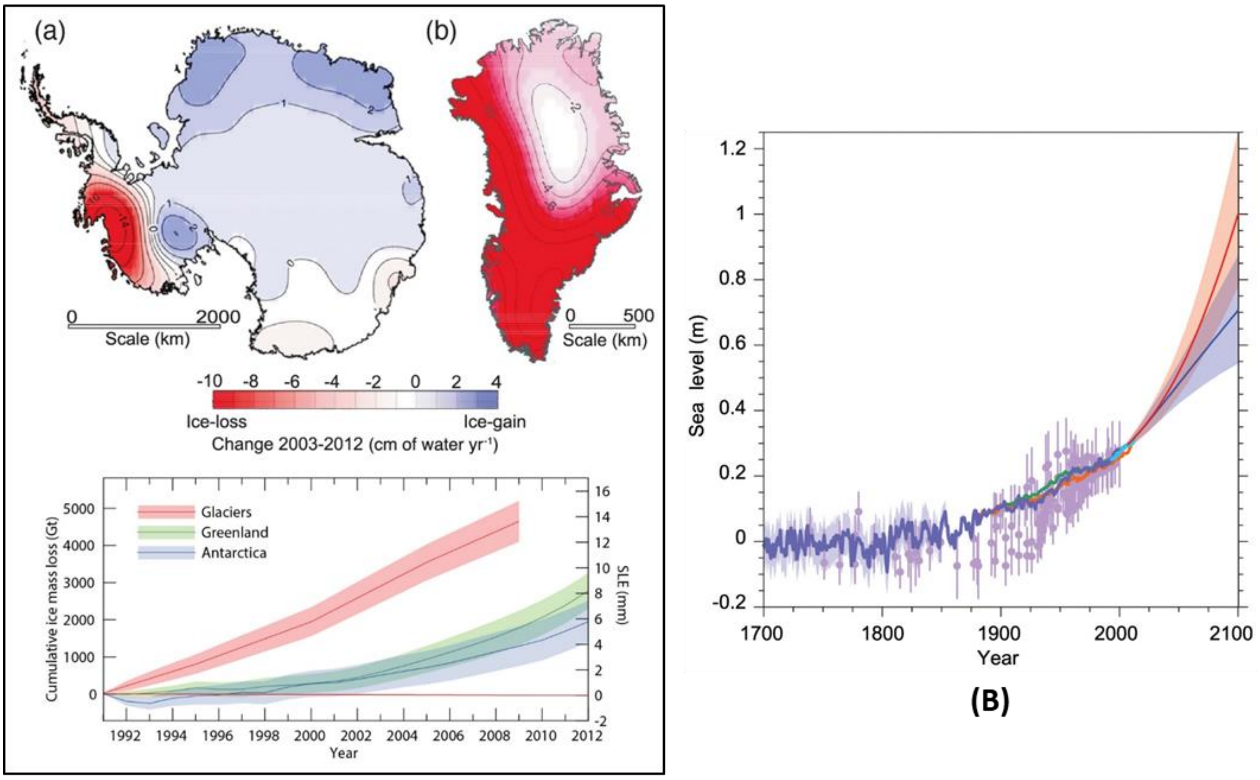

(A)

(B)

Figure 2: *(A) Graphical representation of ice loss in Greenland and Antartica in the past decades and (B)graph showing the increase in sea level in recent times [6]*

c) Wastewater treatment

Wastewater treatment is another aspect which needs to be addressed in order to suffice the water needs of the planet. In both developing as well as developed countries, an increasing number of contaminants are entering water supplies from human activity: from traditional compounds such as heavy metals to emerging micro-pollutants such as endocrine disrupters and nitrosoamines [7,8]. Globally, it is likely that over 80% of wastewater is released to the environment without adequate treatment. The opportunities from exploiting wastewater as a resource are enormous. Safely managed wastewater is an affordable and sustainable source of water, energy, nutrients and other recoverable materials. Several water-related diseases, including cholera and schistosomiasis, remain widespread across many developing countries, where only a very small fraction (in some cases less than 5%) of domestic and urban wastewater is treated prior to its release into the environment [9]. Water availability is also affected by pollution. Most problems related to water quality are caused by intensive agriculture, industrial production, mining and untreated urban runoff and wastewater [10]. By 2050, close to 68% of the world’s population will live in cities, compared to 55% in 2018. Currently, most cities do not have inadequate infrastructure and resources to address wastewater management in an efficient and sustainable way [11]. More than a billion people use a source of drinking water contaminated with faeces, putting them at risk of contracting cholera, dysentery, typhoid and polio. The greatest increases in exposure to pollutants are expected to occur in low- and lower-middle income countries, primarily because of higher population and economic growth in these countries, especially those in Africa and the lack of wastewater management systems [9].

Water treatment is one possible solution to tackle the current issues and help avoid the future water crisis. Conventional methods of water disinfection and decontamination can be used to address many of these problems. Currently available water treatment technologies such as adsorption by activated carbon or coagulation merely concentrate the pollutants present by transferring them to other phases, they still remain in the active form and are not being completely “eliminated” or “destroyed” [12,13]. Other conventional water treatment methods such as sedimentation, filtration, chemical and membrane technologies involve high operating costs and could generate toxic secondary pollutants into the ecosystem [13]. These concentrated toxic contaminants are highly dangerous and concerns regarding their safe degradation bring up a secondary problem. For example filters, when full of waste, must be disposed of, usually by incineration. This procedure emits into the atmosphere substances which are harmful to health and environment. A typical and widely used chemical disinfection process is Chlorination. The disinfection by-products generated from chlorination are mutagenic and carcinogenic to human health [14,15]. These drawbacks from the current water treatment methods which are focused on large systems, precludes their use in much of the world.

d) Industrial pollution and photocatalysis

In view to address these problems, development of advanced low-cost and highly efficient water treatment technologies to treat the wastewater are desirable. The possible reuse of onsite rural wastewater or the treated municipal wastewater from treatment plants for agricultural and industrial activities can be a good step towards wastewater management. Since these wastewaters constitute one of the largest possible water resources, its reuse will help fight water shortage as well as water pollution effectively. More than 100,000 dyes are available commercially and over 1 million tons of organic dyes are produced per year, of which 50% are textile dyes. In India alone, the dye industry produces around 60,000 metric tons of dyes, which is approximately 6.6% of total colorants used worldwide. The largest consumer of organic dyes are the textile industries accounting for two third of the total production of dyes [16].

Most of the dyes cause water colourization at very low concentrations (even at 1 mg/L) and hence their uncontrolled discharge in the natural water resources creates serious ecological problems [17]. In addition, the dyes can affect the development of aqueous ecosystems as well as disturb the photosynthesis activity of the marine flora. Their high chemical and photo resistance creates potential risk for human health through their accumulation in the food chain transport. Citing these reasons, the treatment of wastewaters containing dyes prior their disposal in the water resources is obligatory, but at the same time a complicated process.

A promising method is the Advanced Oxidation Process (AOP) which can be used to purify wastewater containing organic pollutants, such as organic dyes and pathogens, by the production of hydroxyl radicals ($OH^{\bullet}$) which are highly reactive chemical species. The organic pollutants are completely mineralized by AOP leading to the end products of CO_2 and inorganic ions. Among AOPs, heterogeneous photocatalysis has proved to be of real interest as efficient tool for degrading organic contaminants. Photocatalysis is initiated by the photocatalyst (e.g. semiconductor TiO_2, **Fig. 3**) upon irradiation with photons (from an artificial light source or solar light). These photons excite the electrons (e^-) in the photocatalyst to the conduction band (CB) if the energy of the photons is greater than the band gap, leaving behind a positive hole in the valence band (h_{VB}^+) [18]. Eq 1 represents the initiation reaction with TiO_2 as the photocatalyst.

$$TiO_2 + h\nu \rightarrow h_{VB}^+ + e_{CB}^- \qquad (1)$$

The excited electrons that are now in the conduction band (e_{CB}^-) will react with oxygen (O_2) from the atmosphere producing superoxide radicals (O_2^-), see Eq. (2) [19]. While this reaction is occurring, the oxidation of water takes place at the positive hole (h_{VB}^+) in the valance band generating hydroxyl radicals ($OH^{\bullet}$) and hydrogen ions (H^+), see Eq. (3). These reactive species (radicals) in turn oxidize the organic pollutant [19]. Even though degradation begins with a partial degradation, the term ‘photocatalytic degradation’ usually refers to complete photocatalytic oxidation by mineralizing the organic pollutant to essentially CO_2, H_2O and halide ions.

$$e_{CB}^- + O_2 \rightarrow O_2^- \qquad (2)$$

$$h_{VB}^+ + H_2O \rightarrow OH^{\bullet} + H^+ \qquad (3)$$

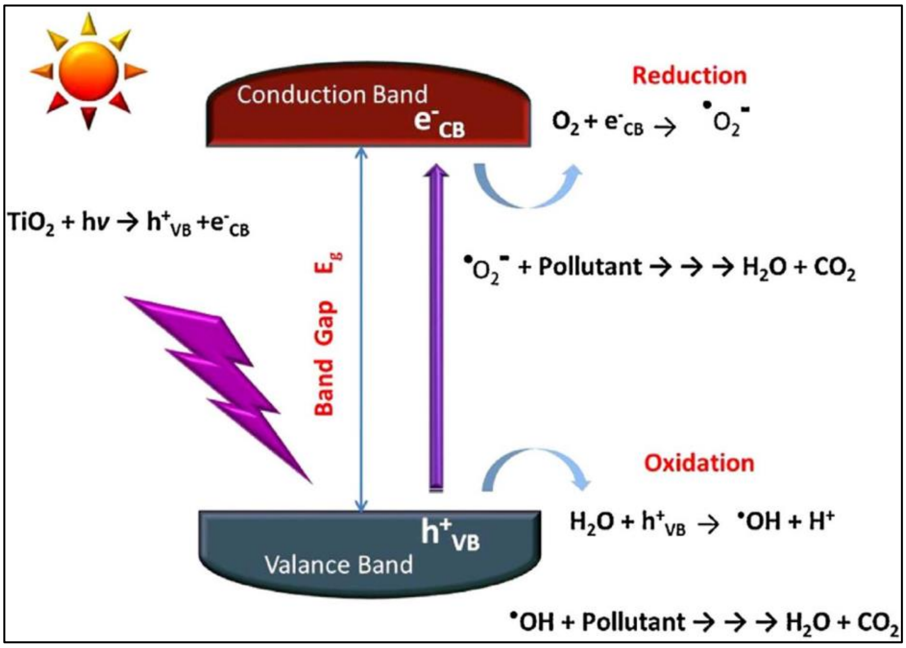

Figure 3: *A demonstration of photocatalysis reaction with TiO_2 as the photocatalyst [20].*

e) Direct photolysis of H_2O_2

Direct photolysis of H_2O_2 is another way of degrading organic pollutants where H_2O_2 is commonly used as a sacrificial oxidizing agent. After its discovery in 1818, it was first used to reduce odor in wastewater treatment plants and soon became widely employed in wastewater treatment [21]. It is one of the first oxidants tested in photocatalytic applications and it has been tested with a large number of organic compounds in recent years [2]. However, since hydrogen peroxide itself is not an excellent oxidant for many organic pollutants, it must be combined with UV light, salts of particular metals or ozone to produce the desired degradation results [22]. When exposed to UV light, the H_2O_2 molecule undergoes a direct photolysis and $OH^{\bullet}$ radicals are produced:

$$H_2O_2 + h\nu \rightarrow 2\,OH^{\bullet} \qquad \text{(a)}$$

Reaction (a) takes place only with photons of wavelength $\lambda < 280$ nm [23]. The hydroxyl radicals produced can directly participate in the oxidation of the organic pollutants present in wastewater. However, this technique requires large quantity of H_2O_2 and intense UV light for long durations, making it expensive for industrial applications.

f) Fenton and photo-Fenton reactions

AOP's such as photo-Fenton reaction are cost effective and efficient process to remove organic pollutants in presence of H_2O_2 and metal cations [24,25]. Importantly, photo-Fenton reaction may proceed by absorption of visible light which is a big advantage over direct photolysis of H_2O_2 and photoexcitation of TiO_2 which require high intensity UV light [2].

The Fenton reaction (a mixture of H_2O_2 and Fe^{2+} in acidic medium having powerful oxidizing properties) is a process in which Fe^{2+} ions are oxidized to Fe^{3+} and H_2O_2 is reduced to hydroxide ion (OH^-) and hydroxyl radical ($OH^\bullet$) in absence of light.

$$Fe^{2+} + H_2O_2 \rightarrow Fe^{3+} + OH^\bullet + OH^- \qquad \text{(b)}$$

The ferric ion produced in Equation (b) can in principle be reduced back to ferrous ion by a second molecule of hydrogen peroxide:

$$Fe^{3+} + H_2O_2 \rightarrow Fe^{2+} + H^+ + HO_2^\bullet \qquad \text{(c)}$$

The problem is that equation (c) is much slower than the initial step (Equation b) and hence addition of relatively large amounts of Fe (II) may be required in order to degrade the pollutant of interest [26]. Another important limitation of the Fenton reaction is the formation of recalcitrant intermediates that can inhibit complete mineralization of the organic pollutant [27]. Despite these potential limitations, the conventional Fenton reaction has been widely used for the treatment of effluents [28,29].

The irradiation of Fenton reaction systems with UV/Vis light (250-400 nm) strongly accelerates the rate of degradation. This behavior is due principally to the photochemical reduction of Fe (III) back to Fe (II), for which the overall process can be written as:

$$Fe^{3+} + H_2O + h\nu \rightarrow Fe^{2+} + OH^\bullet + H^+ \qquad \text{(d)}$$

This reaction combined with the Fenton reaction (equation b) is called as photo-Fenton reaction. Looking at reaction (d), it is possible to notice two benefits from it: the generation of Fe^{2+} ions that are essential for the Fenton process and the production of another hydroxyl radical that contributes to the mineralization process of the pollutant. This way it is possible to have a regeneration of the catalyst carried out by light and so, with less amount of Fe^{2+}, with respect to the Fenton process, a complete degradation of organic molecules can be achieved. As a consequence of these two effects, the photo-Fenton process is faster than the conventional Fenton process [27,30].

1.2 Energy

a) Global energy sources and trends

A clean and sustainable source of energy is one of the most important challenges facing humanity in the 21st century. Energy is needed for a variety of activities which can be residential, commercial, transportation and industrial. Humans are heavily depended on energy consuming utilities like heating, cooling, lighting, driving etc. Compared to the previous ages, the human population has experienced a high growth rate, especially as a consequence of the industrial revolutions. The big innovations in the technical tools allowed a progressive improvement of the life expectancy and quality. The increasingly energy intensive human activities multiplied by the growing world population produced in the last three centuries have created a lot of stress on the existing energy resources. The current use of the primary energy sources available on our planet are clearly unsustainable. **Fig. 4** gives an idea about the Total Primary Energy Supply (TPES) by fuel in units of Mtoe (Million tonnes of oil equivalent) which shows more than two-fold increase in TPES in 40years. This clearly shows the increasing need of energy in the global economy resulting in increased consumption which in turn increases the energy demand.

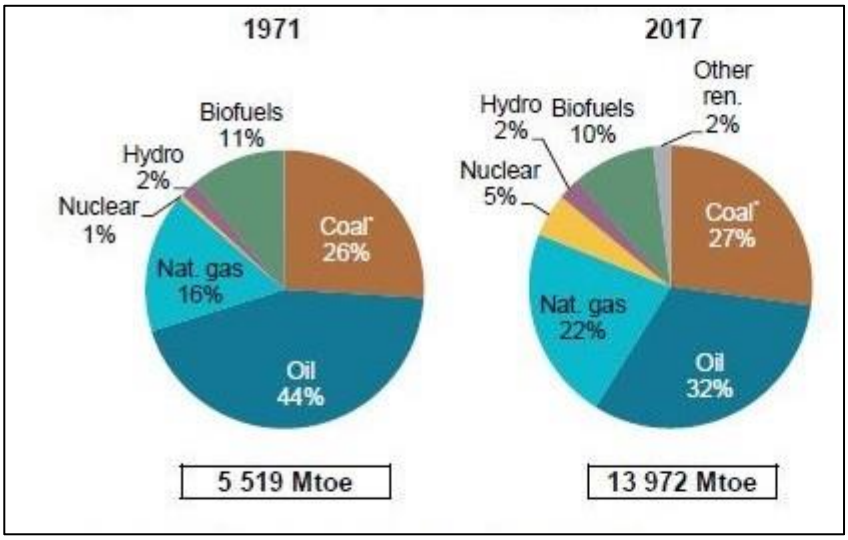

Figure 4: *World total primary energy supply by fuel* [31].

The major sources for the energy in the world are fossil fuels (Oil, Coal and Natural Gas) which are consumed without regard for the consequences. The depletion of these resources have already altered the natural habitat, climatic conditions and ecosystems on the planet resulting in irreversible damages like melting of ice caps, glaciers and increase in air and water pollution. In 2016, the rate of global energy consumption was in the range of 18.5 TW [32]. Owing to rapid growth in industrialization in underdeveloped and developing countries, this global value will continue to rise at a faster rate due to the exponential increment in world population. With the estimated projections based on current growth, the global annual energy consumption rate will reach 27 TW by 2050 and almost 50 TW by the end of the century [33]. More than three quarters of the total global energy consumed at present comes from burning fossil fuels which are limited energy resources of the planet thereby facing an immediate threat of depletion. **Fig. 5** demonstrates the world energy consumption by energy source indicating the high dependence on coal, natural gas and liquid fuels for energy. The energy consumption is given in terms of quadrillion BTU (British Thermal Units) [1quad BTU = $1.055 * 10^{18}$ J].

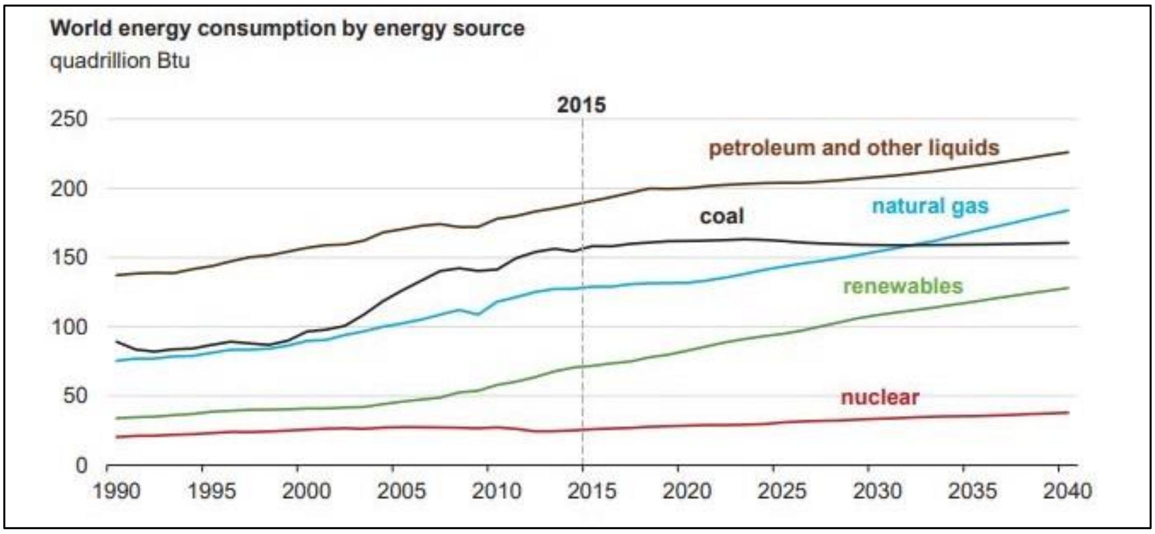

Figure 5: *World energy consumption by all the sources [34].*

The global energy consumption in 2018 increased at nearly twice the average rate of growth since 2010, which is mainly due to a robust global economy and climate changes accounting for increased heating and cooling. Natural gas contributed to 45% of the rise in energy consumption during this period with maximum requirement in the United States and China. Almost a fifth of the increase in global energy demand came from higher demand for heating and cooling as average winter and summer temperatures in some regions approached or exceeded historical records. These findings are part of the International Energy Agency’s latest assessment of global energy consumption and energy-related CO2 emissions for 2018.

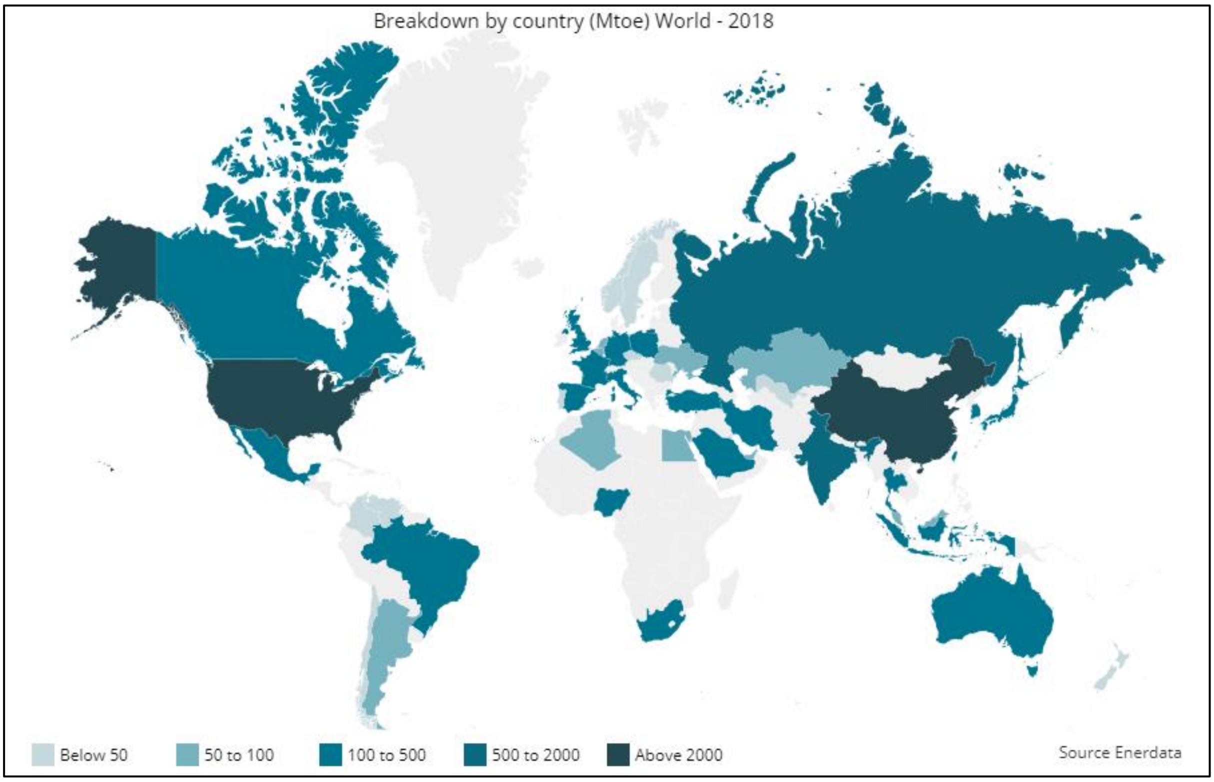

Figure 6: *World consumption statistics by country (in Mtoe) as per 2018* [35].

Fig. 6 shows the world energy consumption statistics (in Mtoe) in 2018 on the world map with measured energy consumption by each country. China and USA lead the world in terms of energy consumers with more than 2000 Mtoe of energy consumed in 2018. With more and more developing countries exhibiting rapid industrial growth, the energy consumption is bound to increase at an alarming rate. **Fig. 7** gives the Total Primary Energy Demand (TPED) of the world and indicates the projections of the ever increasing energy demand in terms of energy source. Coal, oil and natural gas are the major sources of energy and are rapidly depleting. In the next 40-50 years we will run out of both oil and natural gas respectively, while coal will last only for the next 129 years. Thus it is of great concern that we look towards renewable sources of energy so as to avoid the disruption of services in the near future.

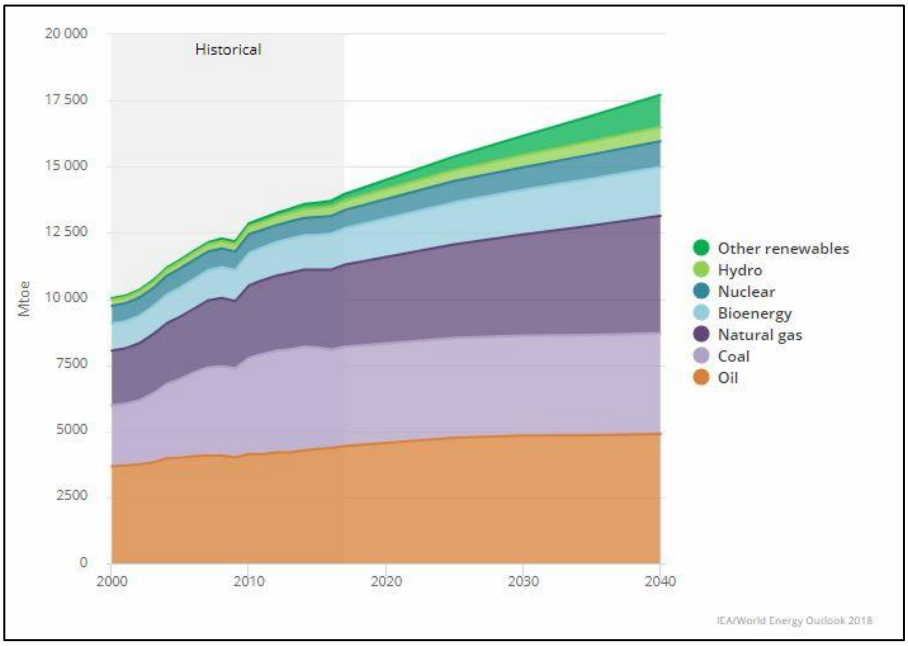

Figure 7: *Total Primary Energy Demand (TPED) of the world* [36].

b) Effects on climate

Fossil fuel depletion is not the only immediate concern at present. The exponential rise in population coupled with industrialization have brought another severe issue to the podium, i.e., climate change. Since more than three quarters of the energy is delivered by burning the fossil fuels (coal, oil and gas), this adds to the increase in CO_2 levels in the atmosphere along with other harmful greenhouse gases like methane and nitrous oxide. About 50% of the anthropogenic emissions of CO_2 from the beginning of Industrial Age (1750) have occurred between 1970 and 2010 signifying the catastrophic impact on the ecosystem. In the same period the emissions of CO_2 from fossil fuels combustion and industrial processes contributed to ~78% of the total greenhouse gases emissions increase [37]. About 40% of the emissions have remained in the atmosphere while the rest was removed from the atmosphere and stored on land (in plants and soils) and in the ocean. The ocean has absorbed about 30% of the emitted anthropogenic CO2, causing ocean acidification [37]. The global atmospheric concentration of CH_4 has increased from a pre-industrial value of about 715 ppb to 1732 ppb in the early 1990s, and was 1774 ppb in 2005 while the global atmospheric N_2O concentration increased from a pre-industrial value of about 270 ppb to 319ppb in 2005. Many halocarbons (including hydrofluorocarbons) have increased from a near-zero pre-industrial background concentration, primarily due to human activities [38]. These Greenhouse Gases (GHGs) concentrations in the atmosphere are unprecedented in atleast the last 800 thousand years and without interventions will increase more and more. **Fig. 8** demonstrates greenhouse gases emissions by various economic sectors in 2010, out of the total GHGs emissions 35% of GHG emissions were released in the energy supply sector 24% in AFOLU, 21% in industry, 14% in transport and 6.4% in buildings. When emissions from electricity and heat production are attributed to the sectors that use the final energy (i.e. indirect emissions), the shares of the industry and buildings sectors in global GHG emissions are increased to 32% and 19%, respectively.

The fifth assessment report on climate change, 2014 says that the continued emission of greenhouse gases will cause long-lasting changes in all components of the climate system, increasing the likelihood of severe, pervasive and irreversible impacts for people and ecosystems. Limiting climate change would require substantial and sustained reductions in greenhouse gas emissions which, together with adaptation, can limit climate change risks. Increase in land and ocean surface temperatures along with an increase in the sea level are major issues faced due to global warming. Each of the last three decades has been successively warmer at the Earth’s surface than any preceding decade since 1850. The period from 1983 to 2012 was likely the warmest 30-year period of the last 1400 years in the Northern Hemisphere. The globally averaged combined land and ocean surface temperature data as calculated by a linear trend show a warming of 0.85°C in the period from 1880 to 2012 [37].

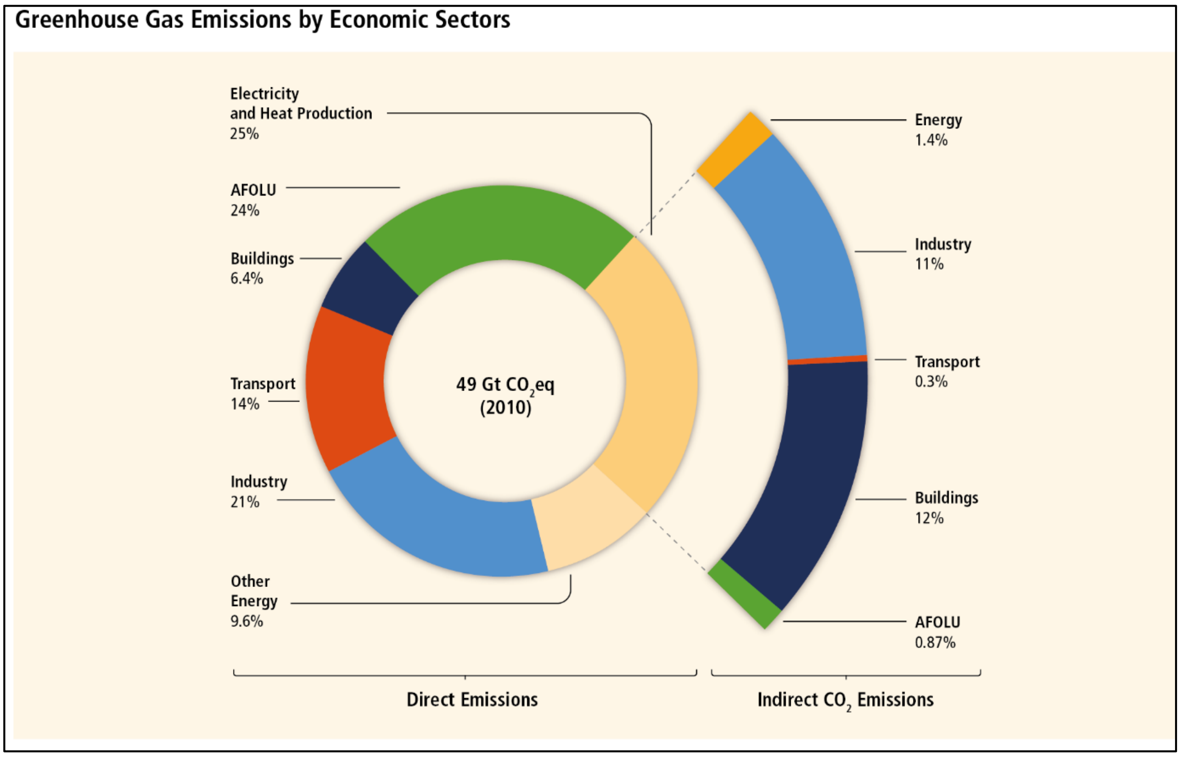

Figure 8: *Greenhouse gas emissions by different economic sectors as per 2010* [39].

Over the period 1992 to 2011, the Greenland and Antarctic ice sheets have been losing mass and glaciers have continued to shrink almost worldwide. There is high certainty that permafrost temperatures have increased in most regions since the early 1980s in response to increased surface temperature and changing snow cover. The annual mean Arctic sea-ice extent decreased over the period 1979 to 2012, with a rate that was very likely in the range 3.5 to 4.1% per decade. Arctic sea-ice extent has decreased in every season and in every successive decade since 1979. Owing to the melting of snow cover and increase in permafrost temperatures, the global mean sea level rose by 0.19 m over the period 1901 to 2010. The rate of sea level rise since the mid-19th century has been larger than the mean rate during the previous two millennia [37]. **Fig. 9** shows the global trends regarding issues discussed above and it is high time humans understand these direct consequences of global warming. Acidification of the ocean is another adversity which needs immediate attention in order to safeguard the aquatic ecosystems. Since the beginning of the industrial era, oceanic uptake of CO_2 has resulted in acidification of the ocean. The pH of ocean surface water has decreased by 0.1, corresponding to a 26% increase in acidity, measured as hydrogen ion concentration. Thus, it is of primary importance to tackle the issue of global warming at the earliest and move towards a sustainable carbon neutral ecosystem.

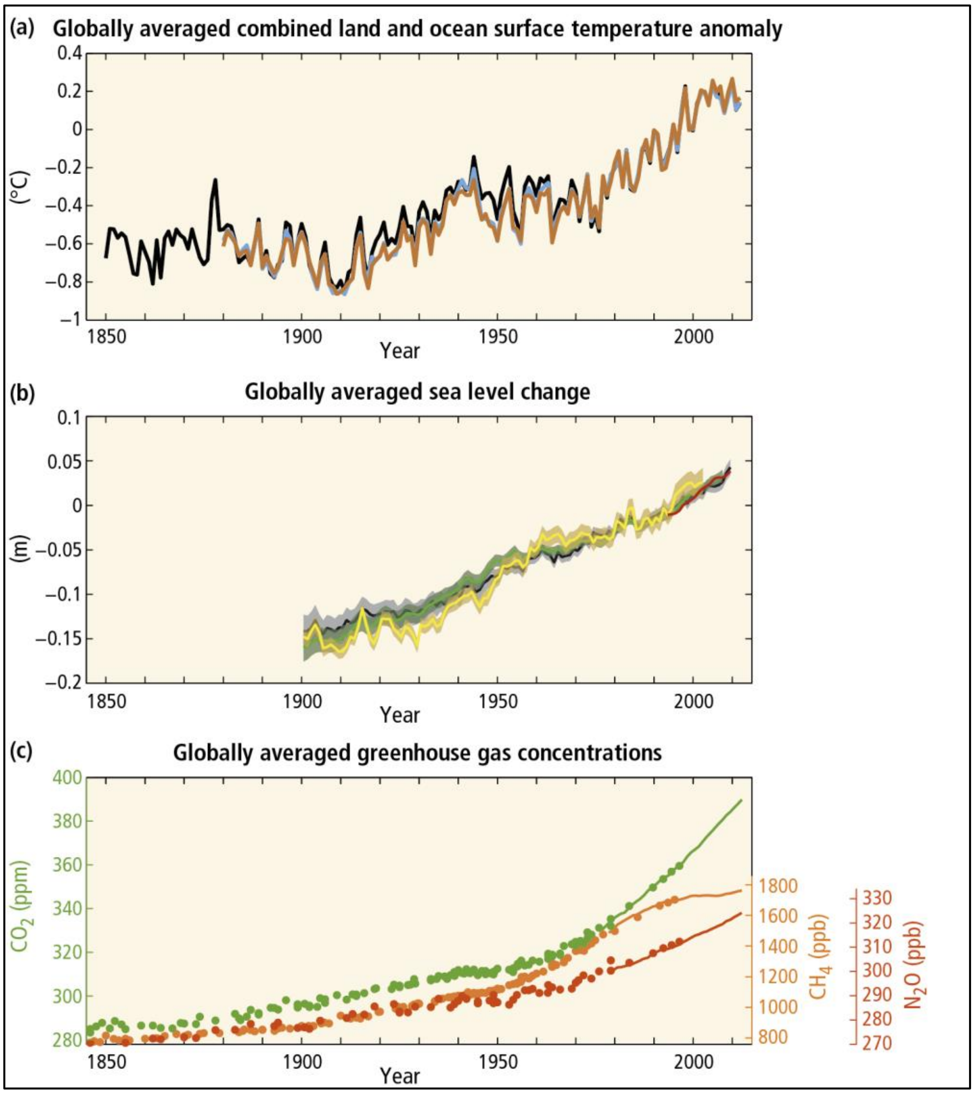

Figure 9: *global trends displaying the a) average temperature rise on land and ocean surface, b) average sea level rise and c) average GHG concentration increment* [37].

c) Need for a sustainable renewable source

A clean renewable source of energy can help get rid of the fossil fuel depletion and the carbon emission problems, however it is extremely unlikely that one particular type of renewable energy will solve the world's energy problems. To meet the terawatt challenge all renewables need to be exploited. Solar energy, being the most intense and prominent renewable energy source can be utilized and the developed technology can be optimized to meet the growing energy demands of the world. Solar energy has a potential of generating upto 23000 TW/yr which is much higher than the current energy needs of the planet (18TW/yr). If a fraction of this quantity can be used to somehow convert the CO2 in the atmosphere into fuel then it could be an effective strategy to tackle both the problems of energy and global warming.

A promising route comes from the conversion of CO_2 and water into fuel by a clean technology called artificial photocatalysis. As the name suggests, this process mimics the natural photosynthesis done by plants in presence of light, CO_2 and H_2O. There has been a growing research interest in the photochemical and photoelectrochemical reduction of CO_2 in the past few decades. The possibility of producing fuels like methane, methanol and carbon monoxide along with chemicals like formic acid in solar photoelectrochemical cells using carbon dioxide and water has fascinated scientists all over the world [40,41]. Moreover, there is an active research field which use these CO_2-derived substances in the development of fuel cells to generate electricity efficiently [42]. There are however many obstacles towards achieving the reality of CO_2 reduction with good efficiency which include thermodynamic limits and kinetic challenges, fabricating a suitable catalyst and designing of a proper fuel cell. Currently, the multiple electron and proton transfers necessary to produce fuels such as methane or methanol have not been demonstrated with high efficiency. Carbon dioxide is shown to be reduced directly on metal surfaces [43], but the development of stable, efficient and cheap catalysts for CO_2 reduction is still a less explored domain.

For success in CO_2 reduction it is imperative that the technology developed is clean and doesn't contribute to carbon emissions. Fuel cells with suitable semiconducting photocathodes in photoelectrochemical setup are one of the best solutions that are realised. Working on optimizing the catalysts for obtaining good efficiency in CO_2 reduction with low overpotentials by electrochemical and photoelectrochemical methods is therefore a booming field. Upon attaining success, this research field has a great potential, since it could display the use of liquid fuels as energy carriers, overcoming the energy storage issue [44]. CO_2 capture and storage are another possible strategies to fight global warming and move towards a cleaner environment.

d) Hydrogen as a fuel and its production

Hydrogen, with its high gravimetric energy density, is another promising route for shifting the global energy industry towards renewable energy. Being the lightest element on earth, hydrogen, is industrially employed in many sectors like the production of chemicals, semiconductor manufacturing, generator cooling and fertilizer production. It can be stored for relatively long periods of time and is considered thermally more efficient than gasoline primarily because it burns better in air and permits the use of higher compression ratio. Moreover, hydrogen gas is a clean and non-toxic renewable fuel. When it burns, it releases only water vapour as the by-product to the environment. Given its high abundance in nature, less than 1% of the total hydrogen content is present as molecular gas. Most of the hydrogen can be found concentrated in strongly bonded chemical compounds and so its production and extraction becomes difficult [45]. Currently, H_2 is mainly produced by the steam reforming of natural gas, a process which emits massive amounts of greenhouse gases (CO2 and CO). Other H_2 production methods like plasma reforming, coal/petroleum gasification and reforming of industrial off gases/oil refinery also proceed through emission of GHGs. Thus, it is important to implement cleaner routes for H_2 production using least amount of energy to make the hydrogen energy cycle environmentally green.

In recent years, efforts have been made in developing new methods to generate H_2 using sunlight thereby making the whole process renewable and sustainable. There are several ways for solar hydrogen production namely, electrochemical/photoelectrochemical water splitting, biomass reforming and water electrolysis using solar cell [46]. Amongst these, photoelectrochemical water splitting using semiconductor catalysts is one of the promising techniques for producing renewable H_2 given the simple nature of the process along with no harmful gas emission and high conversion efficiency. H_2 produced by this method is highly pure and can be stored for later use or transformed directly into electricity using fuel cells.

In this thesis, electrochemical water splitting is discussed which is a process where energy required for water splitting is supplied externally through electricity (in the case of photoelectrochemical water splitting, energy is supplied by sunlight). An electrochemical cell consists of two electrodes namely, anode and cathode, immersed in an electrolyte and connected by an external circuit. At least one of the two electrodes is a semiconductor catalyst and the other electrode is typically a metal. The redox reactions resulting in the production of H_2 and O_2 take place at the electrode-electrolyte interface. **Fig. 10** displays a schematic representation of a simple electrochemical cell for production of O_2 and H_2 through water splitting.

The two half reactions occurring in the electrochemical cell at both the electrodes are summarized as follows:

At Anode: $2\mathrm{H_2O} \rightarrow 4H^+ + O_2 + 4e^-$

At Cathode: $4H^+ + 4e^- \rightarrow 2H_2$

For the electrochemical cell to function effectively and drive these two half reactions, it is essential to develop efficient, stable, and economically viable hydrogen and oxygen evolution catalysts [47,48].

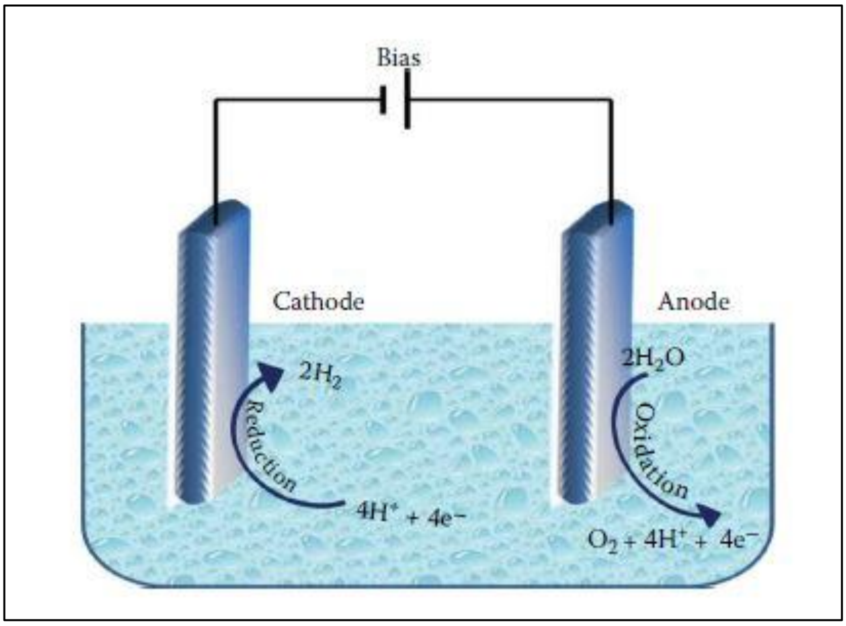

Figure 10: *A simple electrochemical cell for water splitting* [49].

Thus, the research field dedicated to optimizing and searching new materials as hydrogen and oxygen evolution electrocatalysts has gained tremendous interest. The electrocatalysts developed can be used to functionalize solar absorbers for use in a photoelectrochemical cell thus making the whole process renewable. The produced H_2 being clean and pure is a very good source of producing electricity through fuel cells.

e) Fuel cells

A fuel cell is an electrochemical cell which basically combines hydrogen and oxygen to produce electricity giving out water and heat as its by-product. Since the emissions are eco-friendly, fuel cells are considered a promising technology for a sustainable economy. A typical combustion-based fossil fuel power plant operates at about 35% efficiency, while a fuel cell operates at about 40 to 60% efficiency to produce electricity which can be increased to 85% if waste heat is captured [50]. The noiseless operation with virtually no moving part make it even more appealing as a device for the future. Hydrogen fuel cells are likely to replace the internal combustion engine completely due to the green nature of the process along with its reliability. Lithium ion batteries that power laptops, cell phones and other electronic devices, deteriorate with time and use; whereas a fuel cell will continue to generate electricity as long as the fuel is supplied thereby having an infinite lifetime. The power generation process in a fuel cell is analogous to that of a battery, i.e. converting chemical energy to electrical energy. A typical fuel cell produces relatively small electrical potentials of about 0.7 V, hence, to produce a significant amount of voltage, single fuel cells are stacked together to form a fuel cell-stack. A typical fuel cell consists of three sections namely; anode, cathode and electrolyte. There are various types of fuel cells available depending on the electrolyte used; each with its own advantages, limitations and potential applications. **Fig 11** shows the schematic representation of a fuel cell. The basic principle remains the same for all the types, the fuel (H2 gas) is injected through the inlet which dissociates into ions and electrons at the anode. The electrons travel through the external circuit generating electricity whereas the ions pass through the electrolyte. Both the ions and electrons recombine at the cathode along with O2 giving out H2O as the by-product. The applications of fuel cells are vast ranging from electronics, small scale industrial activities to transportation thereby making this technology widely accepted worldwide.

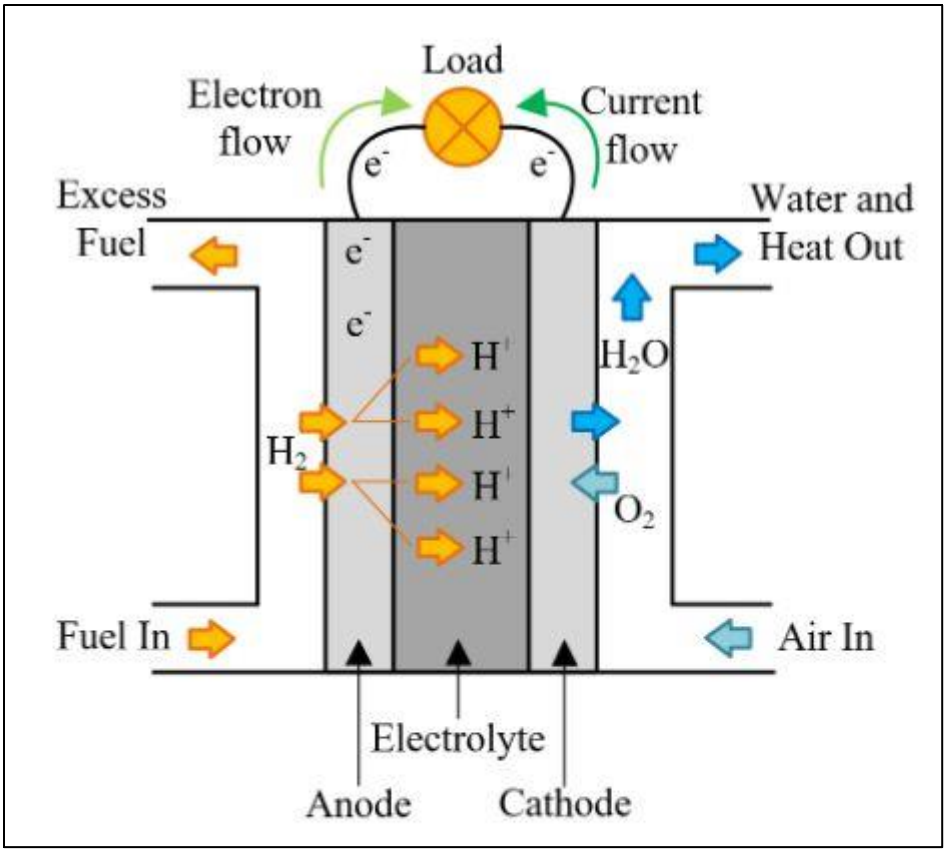

Figure 11: *A typical fuel cell schematic* [51].

Chapter 2: Experimental techniques and Characterizations

Catalysts are substances that increase or decrease the rate of a chemical reaction without taking part in the reaction. In general, chemical reactions occur faster in presence of a catalyst because of the lower activation energy needed for the catalytic reactions to proceed. Catalysts are generally of two types; homogeneous (reactants and catalyst are in the same phase, usually liquid) or heterogeneous (where the reactants and catalysts are in separate phases). Heterogeneous catalysts are usually solids that act on substrates in a liquid or gaseous reaction mixture. Today's needs for clean energy and better environment call for new advanced nanomaterials to catalyze the primary issues of energy and environment. Nanostructured catalyst coatings for electrochemical water splitting into hydrogen and oxygen are studied extensively. Powder and thin film catalysts fabrication with particular morphologies have gained a lot of interest for photocatalytic applications in degradation of organic pollutants in wastewater. This chapter explains the experimental methodology implemented to achieve sustainable catalysts in various forms (powders and thin film coatings). It discusses specifically the Pulsed Laser Deposition (PLD) technique and sol-gel method which were adopted for synthesis of catalyst coatings and powder catalysts in this thesis. The various characterization techniques used for understanding the material properties, morphologies and composition are also discussed in this section.

2.1 Experimental techniques

a) Sol-gel method

Sol-gel process has been extensively studied for fabrication of metal oxide nanostructures in the field of engineering and technological applications, especially metal oxides of silicon (Si) and titanium (Ti) due to the controlled shape and size exhibited by the obtained products. Several forms of materials such as thin films, nanoparticles, glass and ceramics can be achieved using sol-gel method in a cost-effective way [52]. Low temperature chemistry, high surface to volume ratio and reproducibility of obtained products are other advantages of using sol-gel method. Sol-gel process have opened up new avenues in bioengineering fields including drug delivery, organ implantation, pharmaceuticals and biomaterial synthesis due to the purity and quality of the yields from this process. These advantages have attracted researchers and industrialists to utilize this method widely for past few decades [53]. Sol-gel synthesis of metal oxides can be done at relatively low temperature compared to the solid-state reactions. In general, sol-gel process involves formation of sol from homogeneously mixed solution, converting them into gel by polycondensation process and finally heat treating the product according to the material required [54]. The formation of crystalline materials such as nanoparticles or thin films and non-crystalline materials like ceramics, xerosol, aerosol and glasses depends upon the final heat treatment steps [55].

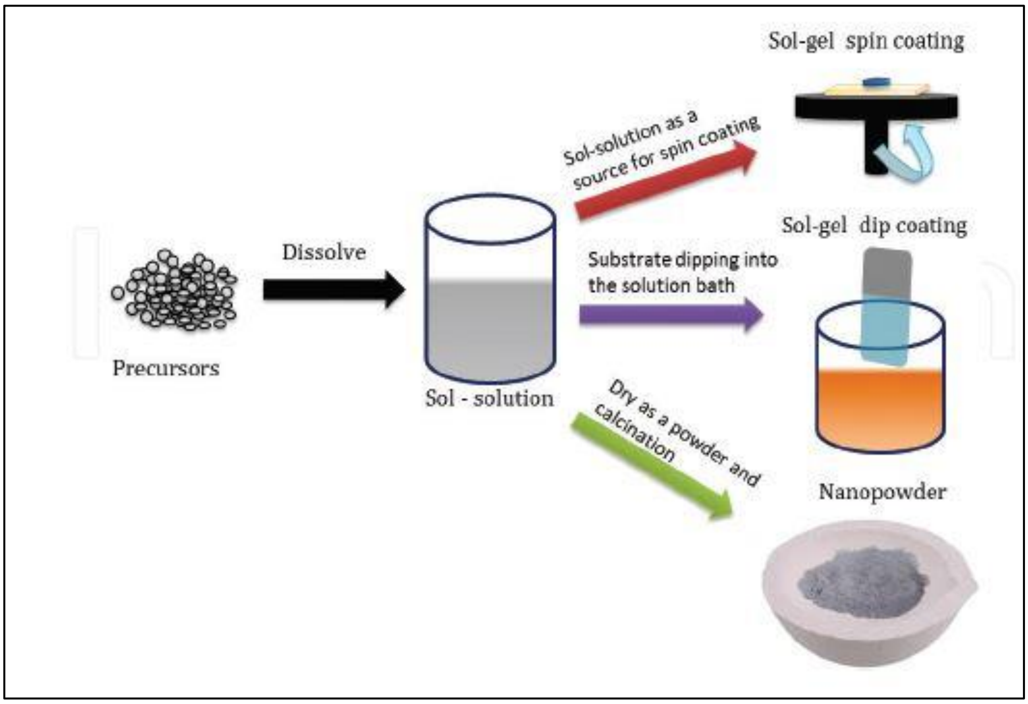

Figure 12: *Schematic diagram of sol-gel technique* [56]

The experimental set up consists of obtaining sol by either hydrolysis or polymerization reactions by adding suitable reagents in the precursor solution. The sol can be deposited onto preferred substrates as thin films using two techniques, namely spin coating and dip coating (**Fig. 12**). The gelation process done through condensation of the sol or addition of polymers converts this sol to gel. This gel can be used to form materials of different types such as nanoparticles, xerogel, glass or ceramics depending upon the further processing steps involved. Nanoparticles and xerogels can be obtained by simple evaporation of solvent. The obtained xerogel can be formed as ceramics by heat treatment and glassy nature can be induced by melting techniques [56]. Thus, sol-gel method can be used to obtain different forms of materials, controlled phase and shape and size of the derived materials [54]. The outcome of sol-gel method can be controlled by varying the parameters such as (1) concentration of precursor used, (2) nature of solvent used, (3) pH of the solution, (4) type of additives added and their concentration, (5) pre and post heat treatment of the materials, (6) aging of the solution and (7) nature of polymer used for condensation [57]. The particles formed in gel matrix possess uniform shape and size that enhances the optical, electrical, magnetic and other intrinsic nature of the materials. Low cost, low temperature chemistry, simple experimental set up and highly controllable synthesis are the major advantages of this method over other synthesis procedure. The large surface to volume ratio of sol-gel-derived material makes it suitable for catalytic applications. Apart from this, low temperature chemistry ensures less defects to be induced in the materials formed. The purity and high quality yield with good physical properties makes researchers in biomedical and biotechnical field to adapt this method mostly for biomedical applications [58].

b) Pulsed Laser Deposition technique (PLD)

Pulsed Laser Deposition (PLD) is a widely used physical vapour deposition technique to fabricate multi-component stoichiometric films, based on the interaction between a high power laser beam and a target made up of the material to be deposited. The laser bean is directed towards the target with the help of appropriate optics and hits the target surface at an angle of 45º. There are three types of thermodynamic processes that happen upon the laser-matter interaction namely; evaporation, normal boiling and phase explosion. The presence and the relevance of each one depend mainly on the heating rate and on the temperature of the target. The heating rate is strongly influenced by the laser energy density and by the pulse duration [59]. Evaporation describes the emission of target atoms due to the transition from the liquid or solid phase to the vapor phase whereas normal boiling happens when the boiling temperature is reached, creating bubbles with the heterogeneous nucleation (due to impurities and defects in the material) process which then escape from the liquid surface. Normal boiling is characterized by slow kinetics [59]. On the other hand, Phase explosion occurs when short pulses (ns/fs duration) and high energy density heat up the target material at a rate of $\sim10^{11}$-10^{12} K/s and a temperature of about ~0.9Tc (critical temperature) is reached. Strong homogeneous nucleation occurs in a super-heated metastable liquid and just below the target surface. At about 0.9Tc vapor and liquid nanodroplets are ejected from the surface forming a plume of vapor and liquid droplets and eventually get deposited on the substrate as nanoparticles [59]. Phase explosion is thus extremely relevant for nanoparticles deposition and for achieving highly nanostructured thin films.

The ablated material forming the plasma plume moves in the forward direction normal to the target surface. The plasma plume by definition is composed of charged particles (electrons and ions) and also neutral atoms. The collisions among these particles induce an anisotropic expansion that determines the plume shape and is influenced by the pressure present in the chamber. The vaporized material, containing neutrals, ions, electrons etc. in the plasma plume expand rapidly away from the target surface (velocities typically ~10^6cms^{-1} in vacuum). It is possible to use a so called reactive gas like O_2, N_2 which can react with the plume species in order to obtain the desired film stoichiometry, or to use an inert gas like argon to constrain the expansion of the plume and influence the deposition rate, spatial distribution, topology and microstructure of the thin film. The film growth occurs depending on the overall effect of all the deposition parameters including the laser fluence, deposition temperature, background gas and pressure etc. In this way NPs assembled coatings are obtained, which are very interesting for a variety of applications of which catalysis is a prominent one. This technique can be used to deposit compact as well as porous films, thin or thick.

The PLD technique provides some important advantages:
- High deposition rate
- Large variety of materials can be ablated and deposited.
- Good control of the stoichiometry by varying the deposition parameters.
- Highly directed and confined plume, which minimizes the loss of the material (very important for expensive targets).
- The deposition process can occur in an ambient/controlled atmosphere.
- The process is very clean and hence suitable for applications which require high purity.

Of course there are also some disadvantages:
- PLD is a complex and expensive technique.
- The profile of the plume is inhomogeneous and hence there is a lack of homogeneity in the deposited film.
- The deposited films exhibit high roughness due to droplets and cluster deposition. This characteristic however can be an advantage in the catalytic applications.

Experimental setup:

The apparatus for PLD was designed and realised by IdEA laboratory at University of Trento, Italy (**Fig 13**). Complete description of the PLD apparatus can be found in [60].

An LPX220i Lambda Physik KrF excimer laser with a wavelength of 248 nm was used as the energy source, with a maximum pulse energy of 450 mJ, a repetition rate that can be varied from 1 Hz to 200 Hz with a maximum average power of 80W and nominal pulse duration of

20ns. The energy per pulse can be tuned by changing the pumping high voltage. During the operation, the system is water cooled in order to dissipate the intense heat produced.

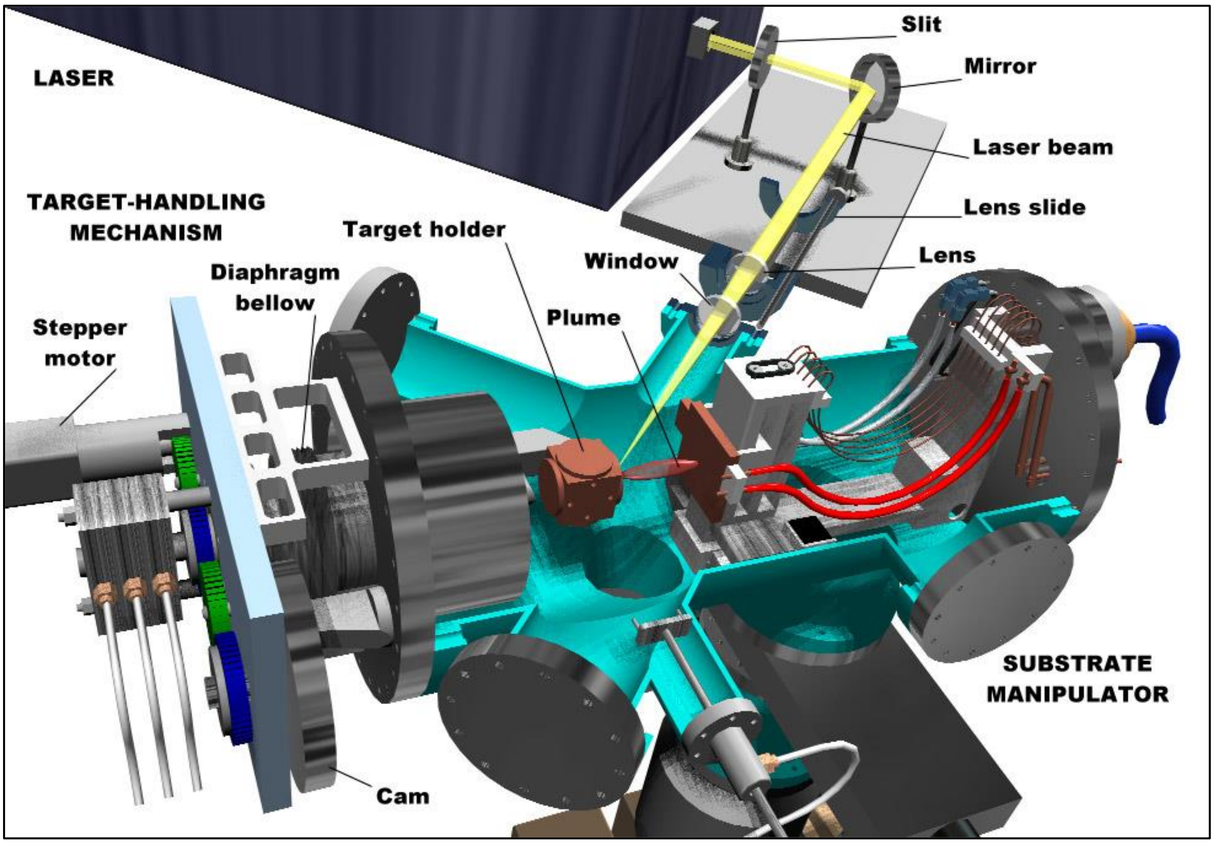

Figure 13: *A schematic 3D view of the laser deposition apparatus* [60].

The laser beam is directed and focused towards the target via an optical system consisting of a slit, mirror and lens. In front of the laser exit window a slit removes all the haloes of the beam and then deflects the beam by 90º with the help of a dielectric mirror. A 400 mm focal length lens focuses the beam on the target at an angle of 45º. This lens is mounted on a slide which permits to vary the position (of about ±15 cm) and consequently the laser fluence can also be varied.

Different films require different atmospheres and pressures for the deposition. Therefore it is necessary to use a vacuum system that permits a precise regulation of the atmosphere composition in the deposition chamber. The vacuum system of the used apparatus is composed of a coupled system of a rotary pump used and a turbomolecular pump. Before the depositions, the deposition chamber is kept at high vacuum, i.e. about 10^{-6} mbar, which prevents presence of impurities inside the chamber and on the substrate during the deposition. For obtaining high vacuum, the chamber is first brought in low vacuum state with the help of the rotary pump.

The chamber is then connected to the turbomolecular pump through a bypass valve till it reaches a pressure of 10^{-2} mbar. This is done to preserve the turbomolecular pump from high flux of air entering through the chamber and damaging the pump. The deposition chamber is then connected directly to the turbomolecular pump by opening the gate valve to maintain a pressure of 10^{-6} mbar in the chamber before deposition. Depending on the deposition conditions, the required gas is introduced into the chamber through a mass-flow meter which receives a feedback pressure signal from a capacitance-pressure transducer. The target is set in rotating during the deposition to avoid non-uniform ablation of the target material.

2.2 Characterization techniques

Different characterization techniques were used for understanding the material composition, elemental analysis, crystallinity and film/particle morphology. This section discusses some of the techniques that were used during this thesis to characterize the produced materials namely: Scanning Electron Microscopy, micro-Raman analysis, X-Ray Diffraction and UV-Vis-NIR Spectroscopy.

a) Scanning Electron Microscopy (SEM)

The scanning electron microscope is a powerful instrument that allows to investigate the microstructural characteristics of solid specimens like morphology, surface topography and composition in the micrometer or submicrometer range. It can reach a resolution of about 5-10 Å under optimal conditions, much higher than that achievable with an optical microscope, which is limited by the wavelength of visible light at 0.1-0.2 mm.

This technique is based on the emission of an electron beam which passes through a focusing lens arrangement and impinges on the sample. The interaction between the constituent atoms and incident electrons produces a large variety of signals which in turn give information about the material composition and morphology. The electrons can be emitted in two ways: by thermionic effect (Tungsten cathode and Lanthanum Hexaboride cathode are the most common sources) or by field emission.

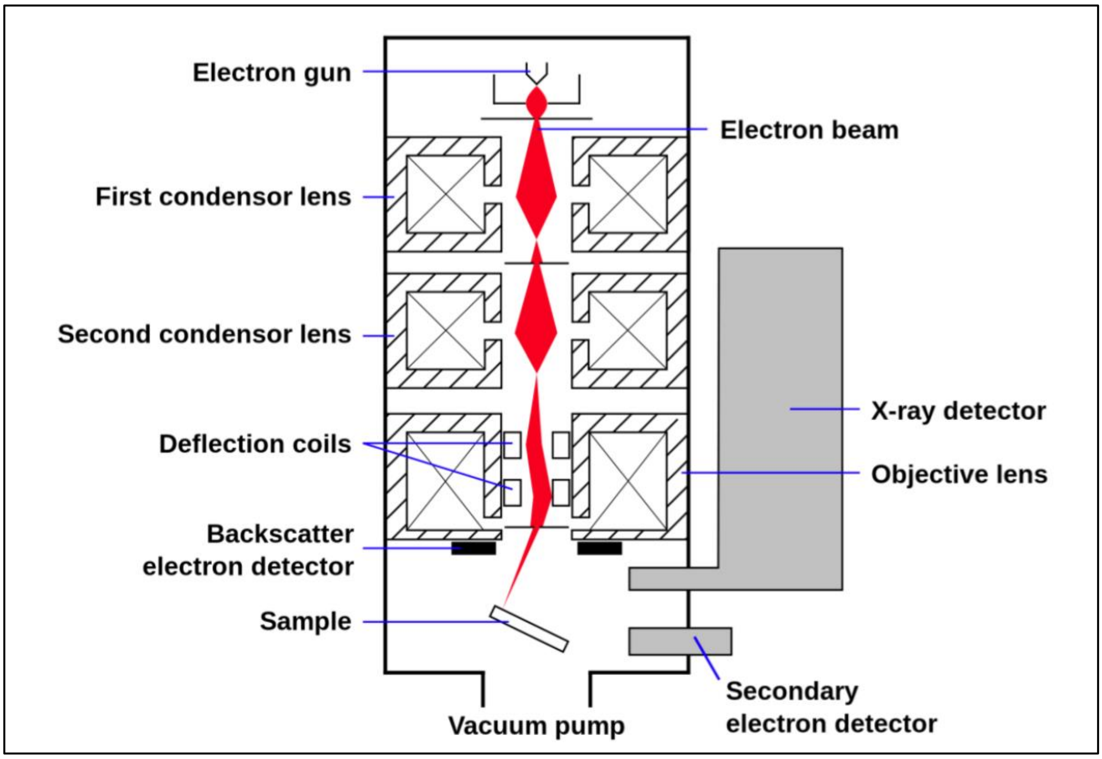

Figure 14: *Schematic diagram of SEM [61].*

The generated electron beam is accelerated and focused on the specimen by a series of electromagnetic lenses and apertures, as shown in **Fig. 14**. This way the diameter of the beam spot is decreased and the electron beam is focused on a fine spot as small as 1 nm in diameter on the specimen surface. The deflection coils are the final lenses which deviate the beam in the x and y axes to scan in a raster fashion over a rectangular area of the sample surface. When the electron beam hits the sample, different signals are generated coming from different kinds of interactions. The three prominent signals studied are the emission of secondary electrons, the backscattered electrons and the characteristic X-ray (only if an X-ray detector is present). These three signals come from different depths of the sample, as shown in **Fig. 15** carrying different information about the object under study. The secondary electrons (SE) are valence electrons emitted when an inelastic collision between the electrons of the beam and the electrons of the sample's atoms takes place. They have low energies (5-10 eV) and so only the electrons produced near the surface can escape from the sample. For this reason SE bring information about the surface of the sample, in particular the material topography. The tilt angle between the incident beam and the sample surface influences the number of emitted secondary electrons. If the specimen inclination with respect to the electron beam increases, the interaction volume increases and consequently the SE signal increases as well. In SEI (Secondary Electrons Imaging) this results in higher contrast for the surface topography.

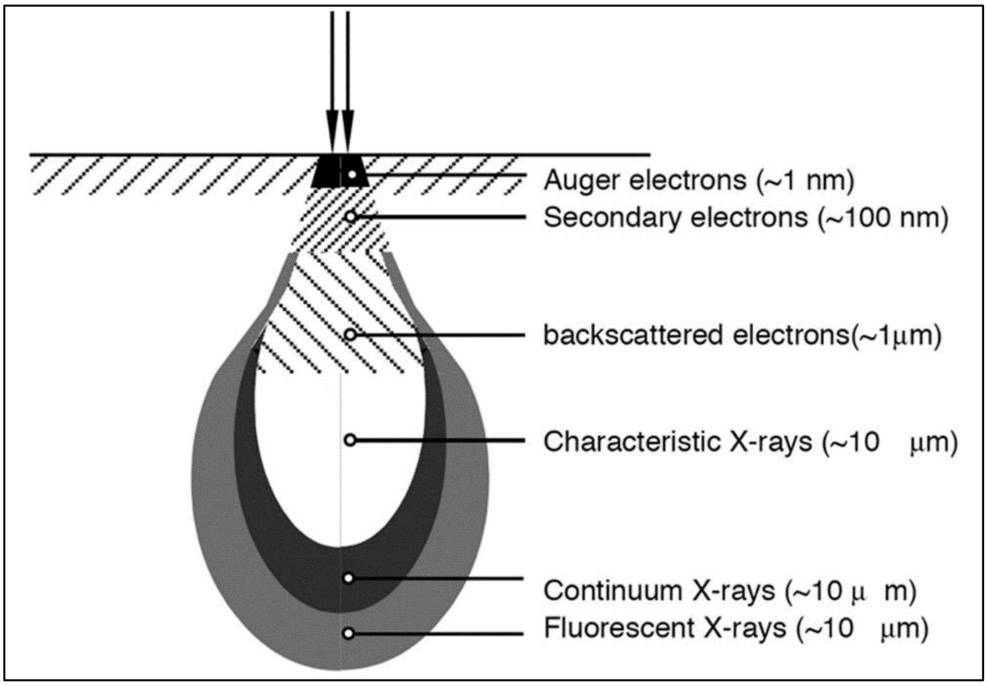

Figure 15: *Interaction volumes for signals generated by SEM [62].*

Backscattered electrons (BSEs) are elastically scattered electrons by the nuclei of the atoms in the specimen. Being scattered elastically, BSE have high energies with respect to SE and come from a deeper region of the specimen. The larger interaction volume results in BSE mode having a lower resolution than SE mode. The number of BSEs increase with the atomic number Z of the atoms, so a material with a higher Z will appear brighter on the image than a material having a lower Z.

X-Rays are another type of signal arising from inelastic collisions and can be formed by two distinctly different mechanisms: Bremsstrahlung and fluorescence. In the first case, the electron beam experiences deceleration in the Coulombic field of the specimen atoms as a result of which there is a loss of energy by emission of x-rays. The resultant x-rays exhibit a continuum spectrum which are not useful for material’s analysis. In the second case, the beam electron interacts with a tightly bound inner-shell electron, ejecting the electron and leaving a vacancy which is fulfilled by an outer shell electron. The energy difference of the transition is a characteristic value and this excess energy can be released from the atom in one of two ways: 1) Auger process, the difference in shell energies can be transmitted to another outershell electron, ejecting it from the atom as an electron with specific kinetic energy;

2) Characteristic x-ray process, the difference in energy is given out as electromagnetic radiation of characteristic value, in contrast to the bremsstrahlung process, which produces photons spanning an energy continuum.

Energy Dispersive Spectrometer (EDS) is used for measuring the energy of the characteristic x-rays and it provides information about the elemental composition of the sample and concentration of each element.

b) Micro-Raman Spectroscopy

The Raman analysis is a spectroscopic technique based on the interaction between light and matter. The light (usually a laser) interacts with vibrational energy states of the atoms/molecules under study. For investigation of small areas of the specimen, the laser beam is usually passed through an optical microscope which reduces the area to be measured. This technique is generally referred to as micro-Raman. In a micro-Raman spectrometer, the light is reflected by an optical filter towards the microscope and the focused beam impinges on the specimen under study.

Raman spectroscopy deals with the interaction of light with the atoms/molecules of the specimen which can be either an elastic or an inelastic interaction. The former indicates that an incident photon is absorbed and emitted without any loss of kinetics energy. This is the predominant process and is known as Rayleigh scattering. The latter means that the absorbed/incident photon and the one emitted by the atom/molecule after the transition have different frequency. This is due to the fact that the atom/molecule does not return in the same stable state after the emission as before. If the final vibrational state of the molecule is more energetic than the initial state, the inelastically scattered photon will possess a lower frequency for the total energy of the system to remain balanced. This shift in frequency is designated as a Stokes shift (**Fig. 16**). On the contrary, if the final vibrational state is less energetic than the initial state, then the inelastically scattered photon will possess a higher frequency, which is designated as an anti-Stokes shift.

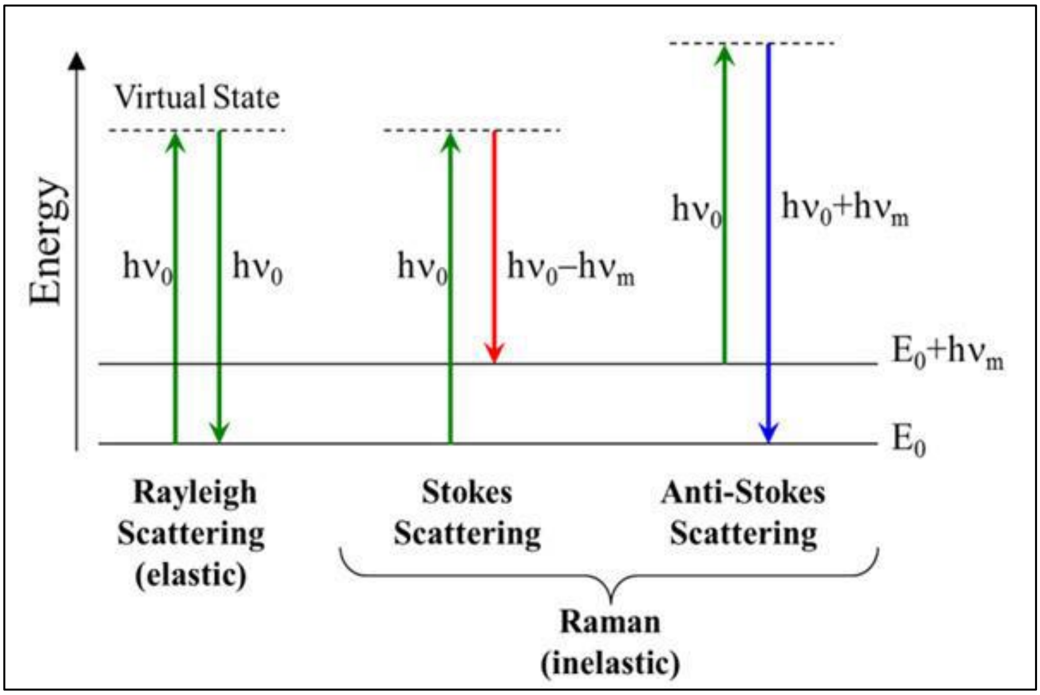

Figure 16: *A schematic diagram explaining the Rayleigh and Raman scattering [62].*

This technique is used to identify the chemical bonding of different materials and provides information about the vibrational structures of the specimen, the crystallographic orientation of a sample along with many other applications in solid state physics.

A typical Raman spectroscopy technique consists of a monochromatic light (laser), illumination system, focusing lenses, an optical filter, detectors and computer control software. The laser beam is irradiated on the specimen and the scattered photons are filtered by a notch filter which block the elastically scattered photons and transmit the low intensity Raman scattered photons (around 0.001% of total intensity). The Raman scattered photons are dispersed by the grating followed by amplification and then detected by a CCD detector. To acquire a large spectrum of the scattered light the grating alignment is varied. The output signal is processed using a specific software to display the Raman spectra for the given specimen. **Fig. 17** shows a schematic representation of Raman spectroscopy apparatus.

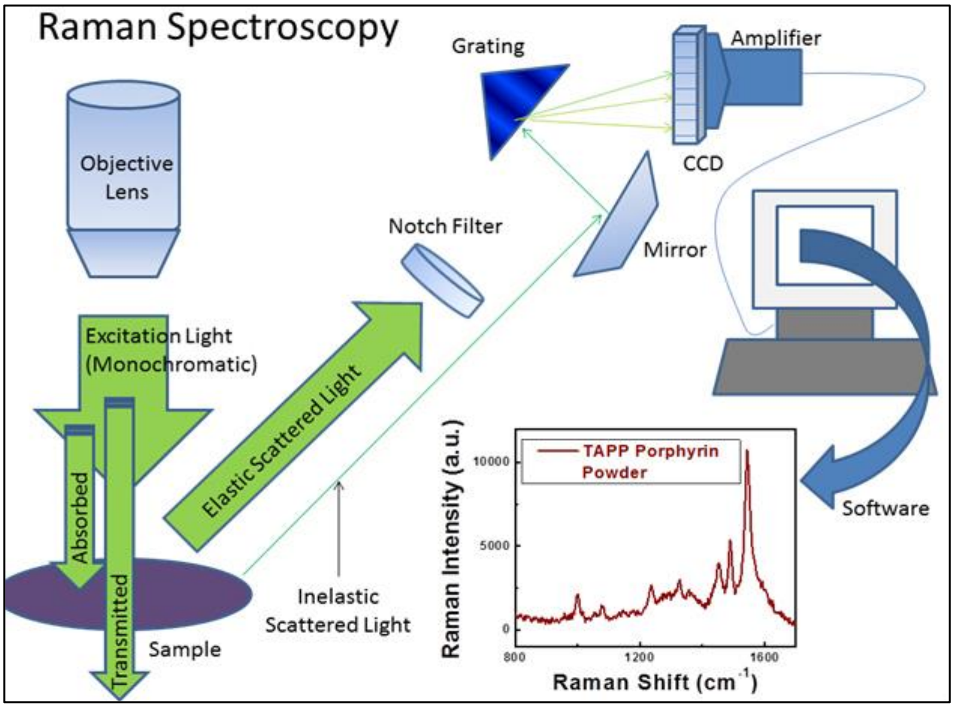

Figure 17: *Raman spectroscopy apparatus schematic [63].*

c) X-ray Diffraction (XRD)

The X-ray diffraction is a bulk characterization technique used to measure the average spacing between different crystalline planes, determine the orientation of a single crystal or grain, study the crystal structure of an unknown material and measure the size, shape and internal stress of small crystalline regions .Since the wavelength of x-rays is in the range of the distance between the atoms in a crystal lattice, a special interference phenomenon of diffraction can give information about the distance between the atoms. In fact X-ray wavelengths vary from about 10 nm to 0.001 nm. When an X-ray beam hits an atom, the electrons absorb the energy of the x-rays and oscillate around their mean positions. Since the energy is not sufficient enough for the electrons to be ejected from the atom, the electrons emit the energy in the form of x-rays. This process is called as elastic scattering. A generic crystal is composed by several ordered planes of atoms, so a lot of x-rays are emitted because of the interaction of each atom with the incoming x-ray beam. An interference pattern can be produced by the superposition of the emitted waves. This pattern depends on the wavelength and on the incident angle of the incoming beam. A positive or constructive interference occurs when the path difference between the two incident rays is equal to an integer multiple of the wavelength. This relation is called Bragg's law and is represented as:

$$n\lambda = 2d\sin\theta$$

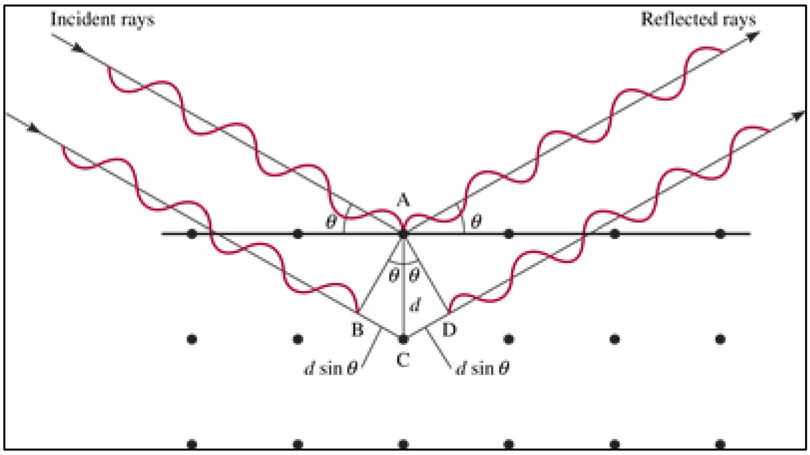

Figure 18: *schematic explaining x-ray diffraction [64].*

Fig. 18 displays a schematic of X-ray diffraction through a crystal. A typical XRD pattern is obtained by varying the angle of incidence of the x-ray beam and measuring the intensity of the emitted radiation. A number of peaks are observed in the pattern corresponding to diffraction from different atomic planes of the material. By identifying the peaks in the diffraction pattern and comparing with the standard peaks for different crystalline materials it is possible to identify the phase of the material under study.

A typical X-ray diffractometer has three basic components: x-ray source, a sample stage and an x-ray detector (**Fig. 19**). The angle between the plane of the specimen and the incident x-ray beam is identified as θ and called as Bragg angle. On the other hand, the angle between the detector and the projection of the source beam is identified as 2θ. The diffractometer geometry is therefore called as θ–2θ, or Bragg-Brentano geometry. The x-ray source is usually fixed and the specimen is moved by θ°/min while the detector measures the output radiation at 2θ°/min with respect to the source path.

The most common x-ray radiation source is the Cu Kα with a known wavelength of λ = 1:5414 Å.

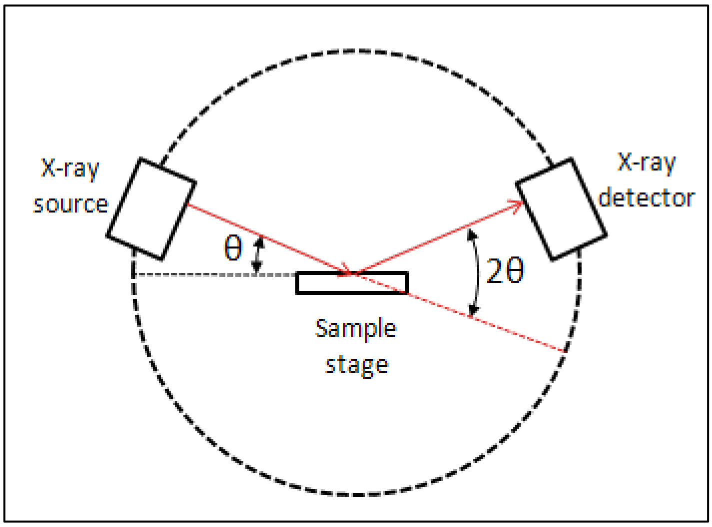

Figure 19: *Block diagram of a typical x-ray diffractometer [65].*

d) UV-VIS-NIR spectroscopy

The optical properties of materials can be studied through the Ultraviolet-Visible-Near Infrared spectroscopy, a non-destructive, economic and versatile technique based on the electronic transitions induced by the absorption of incident photons [66].

The absorption spectroscopy is studied in UV (10-200 nm), near UV (200-380 nm), visible light (380-780 nm) and rarely near the IR spectrum (780-3300 nm). For our work, we study the absorption spectra in the range of 200-800nm, which is the wavelength range where electronic transitions due to absorption occur. For light beam incident on a target material along with absorption mechanisms, transmission and reflection also occur.

The absorption is possible only if the photons have the required energy for electrons to have transition from a lower energy level to a higher energy level. The absorption bands are very narrow and characteristic for each molecule. However, a real absorption spectrum shows broadened peaks, because of the superposition of vibrational and rotational energy levels of the molecule on the electronic energy levels [66].

In case of molecules, the total energy is given by the sum of three contributions:

$$E_{total} = E_{electronic} + E_{vibrational} + E_{rotational}$$

The transition between electronic states is caused by the absorption of visible-UV light (10-700nm). The transition between the vibrational states is due to the absorption of infrared radiation (700nm-1mm) and the rotational states are typically promoted by microwave radiation (1mm-1m).

When light passes through a sample, the amount of light absorbed is the difference between the incident radiation (Io) and the transmitted radiation (I). The amount of light absorbed is expressed as either transmittance or absorbance. Transmittance usually is given in terms of a fraction of 1 or as percentage and is defined as follows:

$$T = I/I_0$$

Or

$$\%T = I/I_0 * 100$$

Absorbance is defined as the negative of log T and is written as,

$$A = - \log T$$

Or

$$A = \log[I_0/I] \qquad (1)$$

The Beer-Lambert law states that the amount of light absorbed by the solution is directly proportional to the molar concentration of the absorbing species in the solution and the optical length of the solution:

$$I = I_0\, e^{-\varepsilon l C} \qquad (2)$$

where ε is the molar absorption coefficient, l the optical length of the sample and C the concentration. Substituting eqn (2) in the definition of the absorbance (eqn 1), the Beer-Lambert law becomes,

$$A = \varepsilon l C$$

Knowing the thickness and the molar absorption coefficient of the sample under study, it is possible to obtain the concentration of the solute in the solution.

A typical UV-VIS-NIR spectrophotometer consists of a light source, a monochromator, a beam splitter, two holders (one for the sample and one for the reference), and two photodiode detectors (**Fig. 20**). Light from a source is focused onto a monochromator which separates the light emitted by the source into its component wavelengths. To achieve a constant light intensity over a wide spectrum, two sources are used: a deuterium arc lamp (for the UV region) and a tungsten-halogen lamp (for the visible range). The obtained monochromatic beam is then split into two beams by a beam splitter: this way the light from the source reaches both the sample and the reference. The light at the end of the two paths is collected by the two photodiode detectors and the ratio of the two beams is displayed.

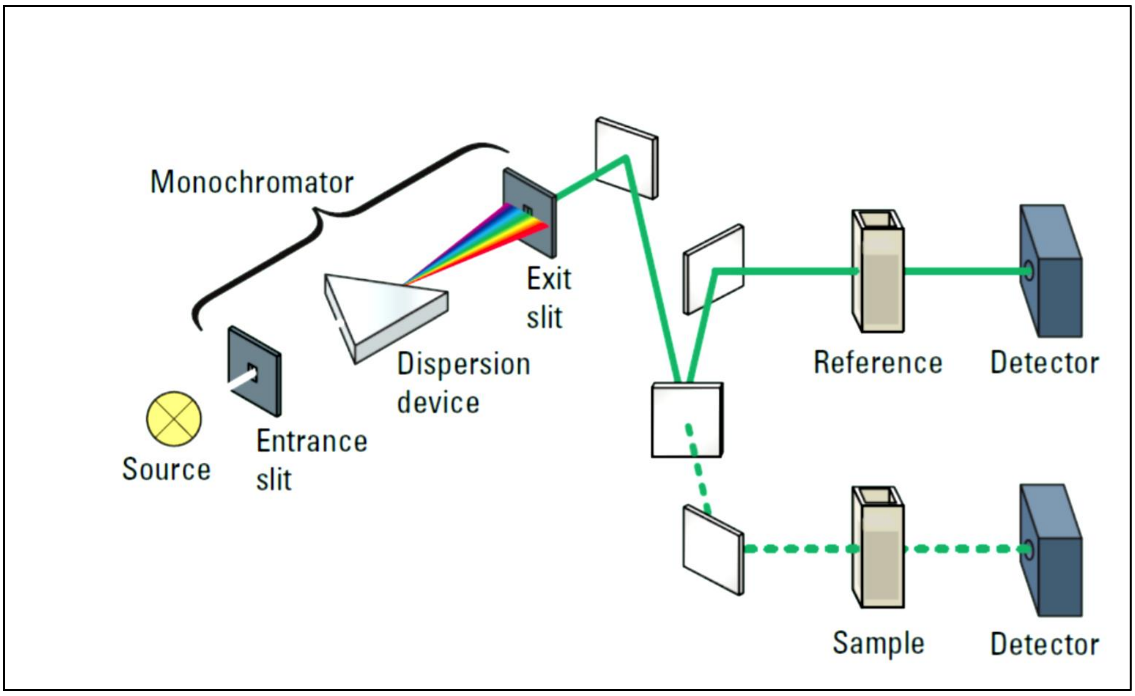

Figure 20: *schematic representation of a UV-VIS-NIR spectrophotometer [66].*

Chapter 3: Pulsed laser deposition of $CoFe_2O_4$/CoO hierarchical-type nanostructured heterojuction forming a Z-scheme for efficient spatial separation of photoinduced electron-hole pairs and highly active surface area

Preview: Single oxide hierarchical/urchin structures of Fe and Co demonstrated excellent photocatalytic activity towards degradation of the organic pollutant Methylene Blue. In view of the enhanced activity, mixed metal oxide hierarchical coatings of $CoFe_2O_4$/CoO were synthesized by Pulsed Laser Deposition for application in dye degradation. The synthesized coatings degraded MB dye completely and exhibited superior photocatalytic activity compared to Fe_2O_3 and Co_3O_4 coatings. The role of morphology, optical properties and heterojunction between $CoFe_2O_4$ and CoO were studied through an in-depth characterization of the catalyst and photocatalytic measurements.

My contribution to this work includes the synthesis of $CoFe_2O_4$/CoO coatings, performing photocatalytic measurements along with other characterizations, interpreting the data/results obtained and preparation of the manuscript for publication.

The content of this chapter is adopted from;

Y. Popat, M. Orlandi, N. Patel, R. Edla, N. Bazzanella, S. Gupta, M. Yadav, S. Pillai, M.K. Patel and A. Miotello, Applied Surface Science 489 (2019), 584-594.
https://doi.org/10.1016/j.apsusc.2019.05.314

3.1 Introduction

Recently, a tremendous amount of attention is gained by 3D-hierarchical nanostructures formed by 1D nanowires and/or 2D nanosheets due to the combination of unique properties of each nanostructure obtained in a single material. A wide range of applications in various fields including nanoelectronics, catalysis, bio-medical, separations and sensors have been demonstrated by such hierarchical structures owing to their peculiar properties [67–69]. Specifically in photocatalysis these nanostructures not only provide high surface area but are also efficient in light trapping in the gap, formed between nanostructures, having dimension similar to the wavelength of light. Hierarchical structures of several semiconductor-based photocatalysts like TiO_2 [70], ZnO [71], Fe_2O_3 [72] and WO_3 [73] were realized in the past with improved photocatalytic activity towards water splitting, degradation of water pollutants, self-cleaning, and air purification. However, the major problem related to the intrinsic property of semiconductors, the recombination of photogenerated charge carriers, still need to be addressed in such nanostructures. Thus, focus has been diverted from single-component materials towards multicomponent based nanostructures. These multicomponent systems combine various semiconductors, metals, carbon and polymer to form heterojunction in the nanostructured morphology [74]. The heterojunction formed using multicomponent provides unique properties and multiple functionalities, which are not observed in single-component structures and can be used for a wide range of applications. p-n junctions formed between two different semiconductors in 1D heterojunction nanowires (NWs) are very useful for effective charge separation in photocatalytic reactions [75]. Metal-semiconductor heterojunctions are also well suited for such reactions. Multicomponent heterojunctions have been successfully used in other fields like biosensors [76], nanoscale photodetectors [77], separation [78], gene delivery [79], and catalysis [80].

Multicomponent based 3D-hierarchial nanostructures formed by low band gap metal oxides are an optimal solution for three major problems of photocatalysis reactions i.e. low absorption of visible light, electron-hole recombination processes, and low surface area [81,82]. A variety of nanostructured heterojunctions including core-shell, 0D-quantum dots over nanoparticles or nanowires or nanosheets, segment NWs, composite of 2D nanosheets etc. have been synthesized, to date, largely by chemical synthesis techniques. Though giving advantage of facile method, these routes are able to produce primarily powder-based systems having recycling and recovering issues for photocatalytic reaction along with instability of nanostructures which deteriorate with time. Therefore, physical deposition techniques, such as Pulsed Laser Deposition (PLD), are very versatile techniques to manufacture nanostructure-based heterojunctions in form of coating stabilized on any substrate which will solve the issue for reusing.

In terms of photocatalytic materials, single metal oxides of Cobalt or Fe, like Fe_2O_3, Co_3O_4

and CoO have gained a lot of interest due to their natural abundance, non-toxic properties and enhanced visible light absorption compared to many other metal oxides along with good photocatalytic activity [83–92]. In our recent work, hierarchical 3D porous/urchin nanostructured Co_3O_4 and α-Fe_2O_3 coating with high photocatalytic activity towards degradation of Methlyene Blue (MB) dye was synthesized by pulsed laser deposition (PLD) [87]. Even though Co_3O_4 is the most stable oxide, CoO catalyst formed through non-equilibrium process such as PLD and mechanical ball milling displays outstanding catalytic property [88]. Also, these coatings exhibit very good chemical and mechanical stability, which allowed them to be tested in a continuous-flow photoreactor coupled to a solar concentrator, for the treatment of real industrial wastewaters [93,94]. Lately more attention is given to ternary mixed metal oxides based on transition metals (Co, Ni, and Fe) such as cobalt ferrite ($CoFe_2O_4$) and nickel ferrite ($NiFe_2O_4$) with spinel structure for photocatalysis applications [95–97]. These oxides have lower bandgaps (1.2-1.4 eV) than single metal oxides and have the capacity to absorb light in the entire solar spectrum. Their magnetic nature also allows for easy recovery of photocatalyst [98]. However, neither Co nor Ni ferrite displayed the remarkable photocatalytic activity owing to the very rapid recombination of the photogenerated electron-hole pair during the reaction. This problem can be mitigated by formation of heterojunctions by coupling two (or more) different materials leading to an increase in the charge separation and extends the range of visible light absorption due to involvement of two semiconductors of different band gap, thereby improving the photocatalytic response. Thus, the research works are now focused in forming interfaces between $CoFe_2O_4$ and single metal oxides or conductors, primarily due to the enhancement in visible light absorption and an improvement in photogenerated charge separation [99–104]. $MoS_2/CoFe_2O_4$ nanocomposites fabricated by a simple hydrothermal method demonstrated good photocatalytic activity in degradation of RhB and congo red dyes [99]. Improved photoinduced charge separation, due to Z-scheme mechanism, and reduction in aggregation because of thin MoS_2 sheets providing large active surface area, were the primary reasons for the enhanced photocatalytic activity. Nanocomposite of $CoFe_2O_4$ nanoparticles incorporated in urchin-like TiO_2 microspheres synthesized as a smart material for recyclable photocatalysis reactions [100] showed superior photocatalytic activity in degradation of MB dye because of the reduction in recombination of photogenerated charge carriers. A $CoFe_2O_4$/g-C_3N_4 magnetically active nanocomposite synthesized by simple calcination method exhibited good photocatalytic activity towards degradation of MB dye [101]. Synergistic effect between $CoFe_2O_4$ and g-C_3N_4 led to the activation of H_2O_2 thereby enhancing the photocatalytic activity. Core-shell structured $CoFe_2O_4$ incorporated Ag_3PO_4

nanocomposites prepared by a precipitation approach demonstrated higher degradation efficiency towards MB and RhB dyes [102]. The heterojunction structure of Ag_3PO_4-$CoFe_2O_4$ nanocomposite inhibited the recombination of electrons and holes, along with a reduction in the band gap. Amongst the solutions offered by current literature to improve photocatalysis performance, heterojunction-based Z-scheme designs are promising ones, along with 3D hierarchical nanostructuring. Even after these recent advances on $CoFe_2O_4$ and its nanocomposites, implementing these approaches on an industrial scale is still a challenge given the powder form of the catalyst and the need for separation of the catalyst from the system after use, although the latter has been mitigated by a separation method exploiting the magnetic nature of $CoFe_2O_4$ [101,103]. Immobilization of the photocatalyst as a coating supported on a substrate would be an ideal solution to avoid this problem. PLD is a very convenient technique in synthesizing such photocatalysts with fine control over the morphology and providing good adhesion with the substrate.

Given these premises, we report here on the fabrication of $CoFe_2O_4$/CoO coatings by PLD and forming a Z-scheme heterojunction design in 3D-hierarchical urchin-like nanostructures. The coatings prove to be highly efficient both in direct photocatalysis and in photo-Fenton reaction, with yields higher than similarly structured single-metal oxide counterparts (Co_3O_4 and Fe_2O_3). This finding is discussed on the basis of the structural properties of the material and the role of the Z-scheme design and nanostructuring.

3.2 Experimental

3.2.1 Synthesis

Fe metallic (Alfa Aesar, 325 mesh), Co metallic (Alfa Aesar, 98.5%) and Boric acid (H_3BO_3, Sigma-Aldrich, >99.5%) powders were mixed in molar ratio of 1:1:1 and the prepared mixture was compressed in the form of a disc to be used as a target for the deposition of mixed oxide coatings by PLD. A KrF excimer laser (Lambda Physik) with an operating wavelength of 248 nm, pulse duration of 25 ns, and repetition rate of 20 Hz was used for deposition. The fluence of the laser was always maintained at 3 J/cm^2 for ablation. The PLD apparatus details and the mechanisms involved in the laser matter interactions are presented in our past reports [84,105]. The PLD chamber was evacuated up to a base pressure of 10^{-6} mbar prior to all the depositions. Deposition of the coating was carried out in an Ar atmosphere at a pressure of 1.5×10^{-2} mbar. The target to substrate distance was fixed at 4.5cm with the substrate positioned parallel to the target. The coatings were deposited on Si and quartz (for characterization) and glass substrates (for photocatalytic activity) maintained at room temperature. Thermal annealing of all the deposited coatings were carried out in air at 500 ºC, 600 ºC (all substrates) and 700ºC (quartz only) for 5 h with a heating rate of 5 ºC/min in order to obtain the hierarchical urchin-like structures of mixed metal oxides.

3.2.2 Characterization

A Scanning Electron Microscope (SEM-FEG, JSM 7001F, JEOL) with 20keV electron beam energy equipped with energy dispersive spectroscopy analysis (EDS, INCA PentaFET-x3) was used for examining the surface morphologies of all the samples prepared by PLD. Transmission Electron Microscopy (TEM) and High resolution TEM (HR-TEM) analyses were performed with a JEOL 2100F Cs-corrected analytical FEG TEM with an accelerating voltage of 200 kV equipped with an energy-dispersive X-ray spectrometer (EDS). Images were analyzed using Digital Micrograph software from Gatan. Copper grids (300 mesh) with Holy-carbon film were used as substrate to prepare samples for TEM analysis. Structural characterization was performed using X-Ray Diffractometer (XRD) with Cu K_α radiation (λ = 1.5414 Å) in grazing angle mode with the incident angle of 1.5°. Micro-Raman spectroscopy was performed using a Labram Aramis Jobin-Yvon Horiba μ-Raman system equipped with a He-Ne laser source (632nm). Absorption spectra were obtained with UV-VIS-NIR absorption spectrophotometer (Varian Cary 5000 UV-VIS-NIR absorption spectrophotometer). Surface composition and chemical states of each element present in the sample were analyzed with X-ray Photoelectron Spectroscopy (XPS) using a PHI 5000 Versa II instrument equipped with a monochromatic Al K_α (1486.6 eV) X-ray source and a hemispherical analyzer. Appropriate electrical charge compensation was required to perform the XPS analysis. XANES measurements of the coatings at Co and Fe $L_{2,3}$ edges were performed at the APE-HE beam line, in Elettra-Synchrotron, Trieste, Italy [106]. A total electron yield (TEY) detection system was used to collect spectra of the samples and a base pressure of 10^{-10} mbar was maintained during acquisition of spectra from the samples.

3.2.3 Photocatalytic activity

The photocatalytic activity of the synthesized samples was evaluated by studying the degradation of model MB dye solutions in presence of H_2O_2 and light. 30ml of MB dye (10 ppm) mixed with 1ml of H_2O_2 (1M), as an oxidizing agent, in an aqueous solution was used for degradation by photo-Fenton reaction. The catalyst coatings (prepared on glass slide of area

2.5 cm × 7.5 cm) were dipped in the above prepared MB dye solution and kept in the dark for 30 mins at constant stirring to establish adsorption equilibrium between the solution and the catalyst surface. After dark reading, a tungsten lamp (225W) emitting mostly visible light was used as the light source. 1ml of MB dye solution was collected after fixed intervals of time during the reaction to study the amount of degradation by measuring the UV-Vis absorption spectra and analyzing the characteristic peak of MB at 664 nm. All the photocatalysis experiments were performed at room temperature. CO_2 evolution was followed in selected experiments by an IR sensor (COZIR Wide range 100 or COZIR Wide range 5) placed in proximity of the solution surface. Note that since the reactor is open, the measurement is not quantitative, but can only show a variation in the atmospheric level of CO_2.

3.3 Results and Discussion

The as-deposited (AD) coating as well as the coatings annealed at different temperatures in air were studied by SEM to get insights on the surface morphologies and the changes that occur upon annealing. The AD coating (**Fig. 21a & 21b**) deposited in Ar atmosphere displays particle-like morphology following a broad particle size distribution from tens of nanometer to few micrometer with a film thickness in the range of tens of micrometers. This film thickness is optimal and doesn’t affect the catalytic performance significantly as long as the whole substrate is covered by the material. Such morphology is expected owing to the phase explosion process taking place below the target surface which comes close to the thermodynamic critical temperature upon irradiating with high laser fluence and is independent of the film thickness. The particles constituting the coating surface are in core-shell structure where different contrast between core and shell suggests that the core is composed of heavier elements (Fe and Co) while the covering shell contains lighter elements (mainly B). Irrespective of particle size, the thickness of the shell is in the range of 200-300 nm. The topography of the particles completely changes upon annealing in air at 500 ^{o}C (**Fig. 21c & 21d**), 600 ^{o}C (**Fig. 21e-21g**) and 700 ^{o}C (**Fig. 21h**). At 500˚C, the shell starts to disintegrate leading to the formation of small nanowires (NWs) on the surface of the particles. This indicates initial development of the hierarchical nano-structure which on further annealing at 600˚C leads to complete transformation from spherical particulates to an urchin-like structure with vertically grown NWs from surface of the particulates (**Fig. 21e & 21f**). The length and diameter of the NWs varies from 0.5 to 1 μm and 10-30 nm respectively. Another very important feature established from the image is that the surface coverage density of the NWs in urchin-like particle is very high. In addition to urchin-like particle, some particulates also transform into flower-like structure with nanosheets of thickness 20-25 nm and widths of 800-900 nm (**Fig. 21g)**. Although there are only about 10% of such flower-like particulates, their contribution towards the catalytic activity cannot be neglected. On annealing at even higher temperature (700 °C) both the urchin density as well as the length of NW's on the urchins increases (tens of micrometres) (**Fig. 21h)**. The obtained morphology is in well agreement with our previous reports [87,107] on the PLD deposited hierarchical urchin-like Fe oxide as well as for Co oxides coatings where the growth mechanism is thoroughly discussed.

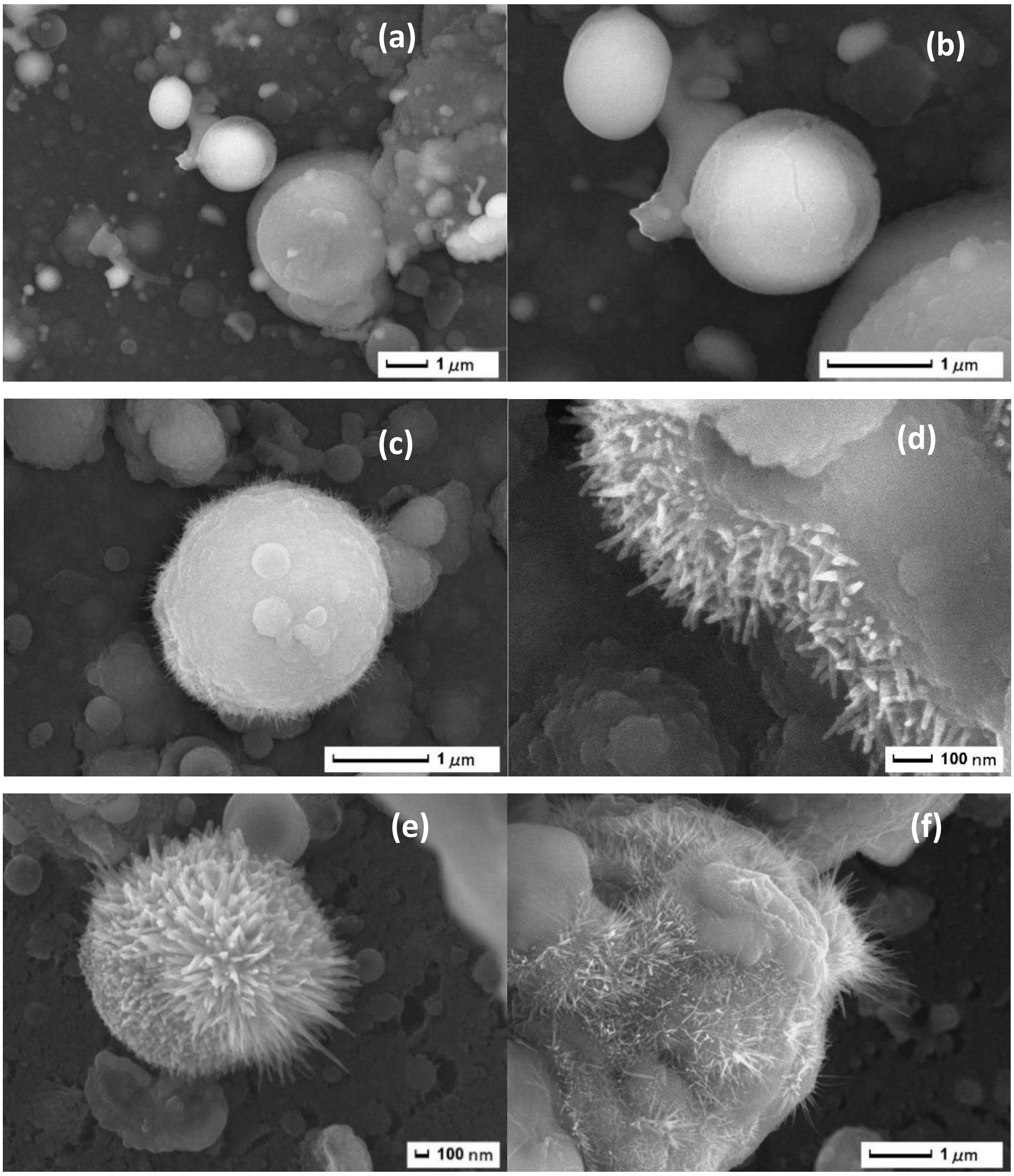

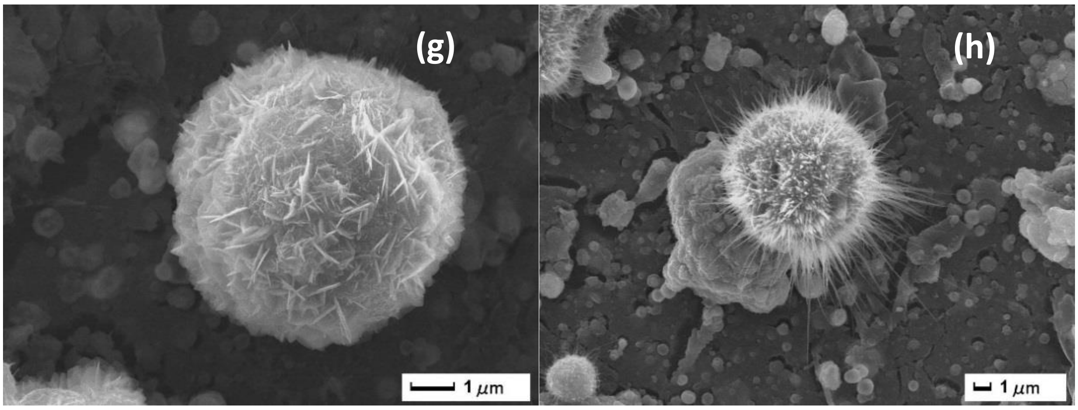

Figure 21: *SEM images of as deposited coating (a & b) and that annealed at 500^{o}C (c & d), 600°C (e,f &g) and 700°C (h) in air for 5 h.*

The EDS measurement on the overall coating displays Fe/Co ratio of ~1.77 which is higher than that in the target used for deposition, with ratio of 1. This suggests the preferential ablation of Fe as compared to Co during the PLD deposition. Nevertheless, this ratio is quite different for particulates with urchin-like and flower-like nanostructuring that are formed after annealing at 600 ˚C in air for 5h. The magnified EDS mapping on urchin-like particles showed Fe/Co ratio of 0.33 while that for flower-like particles is about 50 (**Fig. 22 and Table 1**). This indicates that latter is composed of only Fe while former contains mixture of both metals with Co in dominating amount.

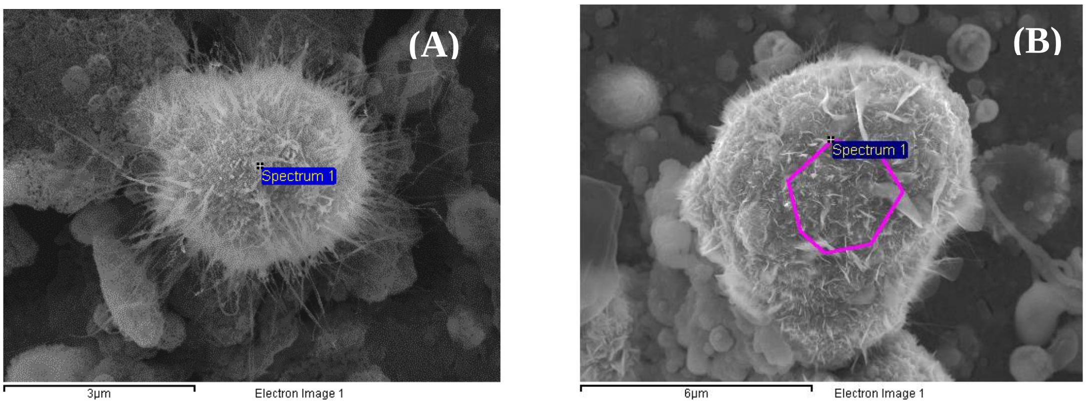

Figure 22: *SEM image of (A) urchin-like particle and (B) hierarchical particle with 2D nanosheet structure, observed on the surface of PLD deposited coating annealed at 600˚C in air for 5 h.*

As majority of coating surface is covered (90%) with urchin-like particles, further investigations were mainly concentrated on the NWs using TEM. NWs emerging from the particulate having length from 100 to 700 nm with average thickness of 20-35 nm are clearly visible in TEM images (**Fig. 23**).

Source	Fe/Co Atomic ratio
SEM Image of Overall Film	1.77 ± 0.20
SEM Image 22A (Urchin-like)	50.1 ± 0.50
SEM Image 22B (Hierarchical)	0.33 ± 0.04
TEM image of NWs (Fig. 24)	0.31 ± 0.03
XPS spectra (Fig. 26)	1.06 ± 0.10

Table 1: *Fe/Co atomic ratio measured through SEM-EDS, TEM-EDS and XPS.*

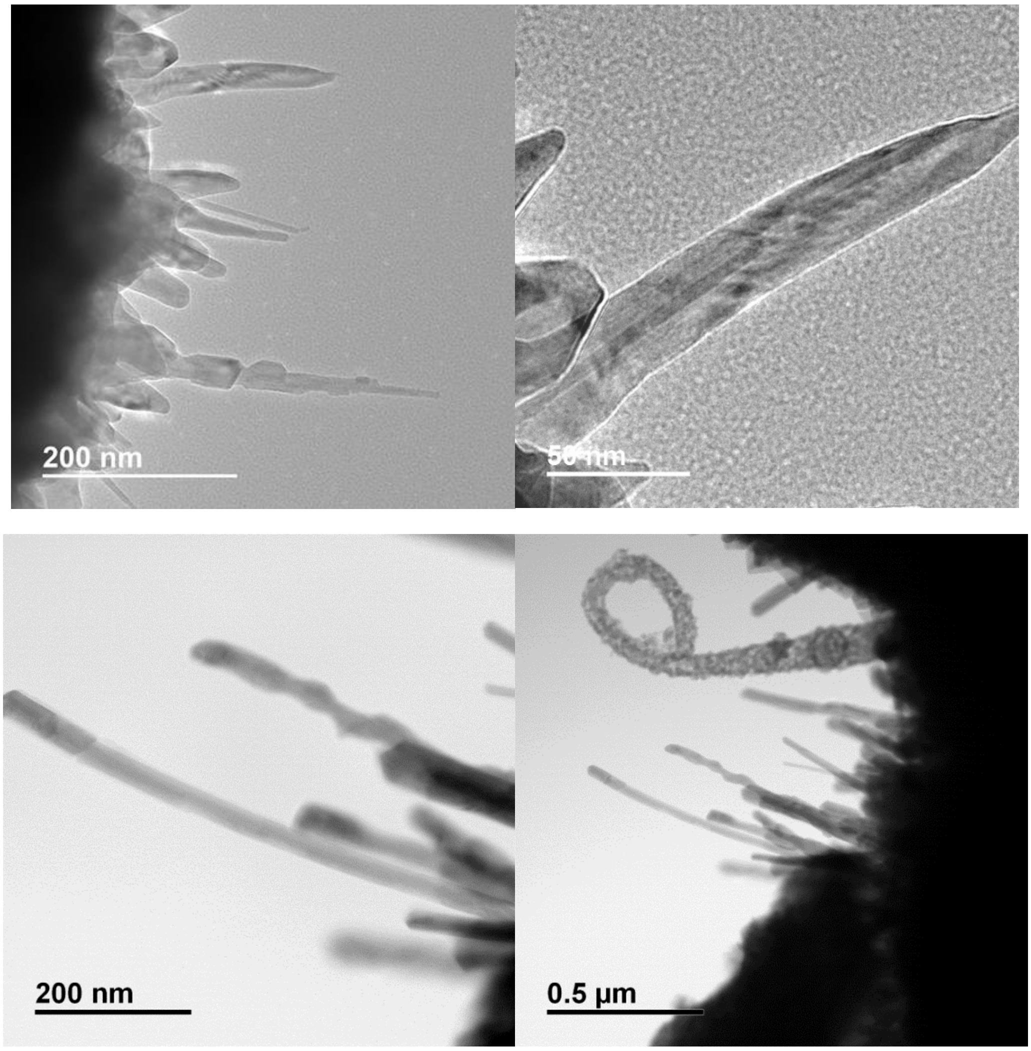

Figure 23: *TEM images of nanowires extruded from core in urchin structure.*

Several sets of lattice planes are observed on magnifying the single NW in HRTEM image (**Fig 24a, 24b, 24d & 24e**). A set of three d-spacing of 0.14, 0.21 and 0.29 nm are measured in **Fig 24b** where 0.14 nm and 0.29 nm are ascribed to (044) and (022) planes of $CoFe_2O_4$ phase (JCPDS file: 22-1086) whereas d-spacing of 0.21nm is common to that of (002) planes of CoO phase (JCPDS file: 75-0533) as well as (004) plane of $CoFe_2O_4$ phase. Fast-Fourier Transform (FFT) (**Fig. 24c**) of this NW can be perfectly indexed to $CoFe_2O_4$ and CoO phases. Similarly, in another NW shown in **Fig. 24d and 24e**, the lattice plane spacings are measured as 0.24 nm and 0.48 nm. A d-spacing of 0.48 nm can be attributed to (111) planes of $CoFe_2O_4$ phase but the value of 0.24 nm is again common to (111) planes of CoO phase as well as (222) planes of $CoFe_2O_4$ phase. FFT of this particular NW also confirms these phases (**Fig. 24f**). EDAX maps of individual NW were recorded to observe the distribution of various elements (**lower panel of Fig. 24**). Both Co and O are uniformly distributed throughout the wire, however, the distribution of Fe varies along the length. The Fe/Co ratio of about 0.31 measured on single NW is in good agreement with the composition of urchin-like particle obtained through EDS in SEM image. This implies that the concentration of Co is more in the NWs coming from a secondary Co phase i.e. CoO. Thus, it can be speculated that the phase of NWs is a mixture of $CoFe_2O_4$ and CoO phase.

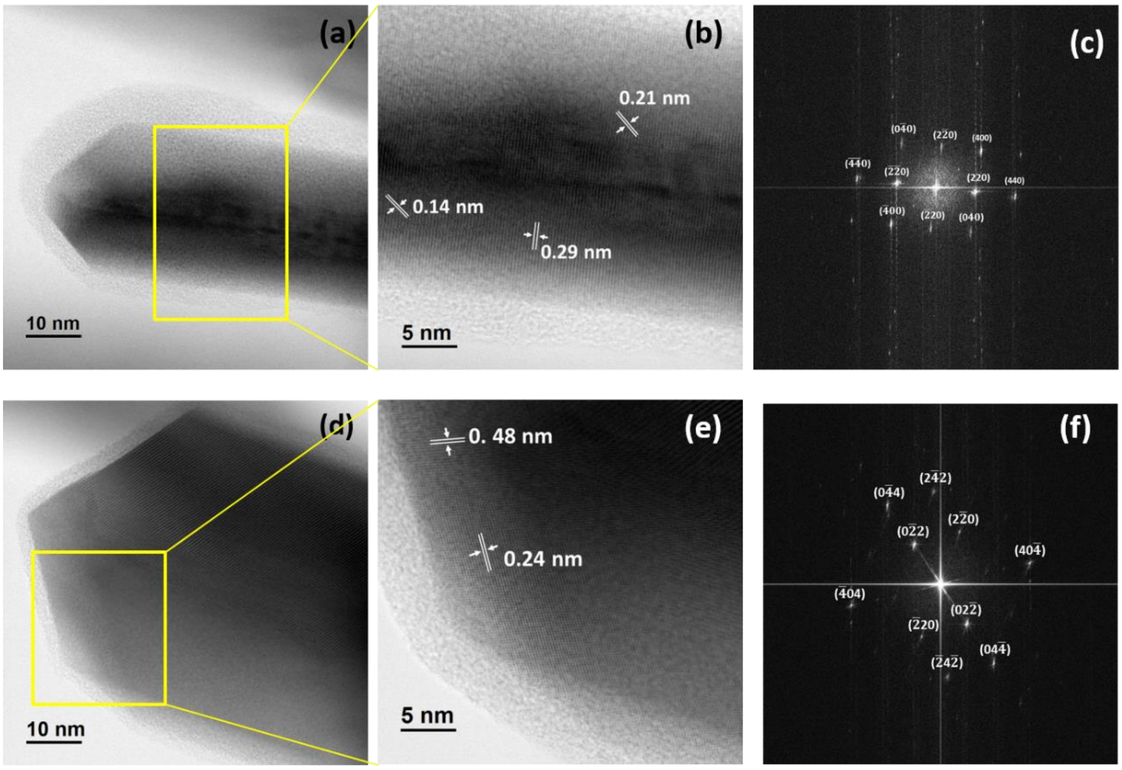

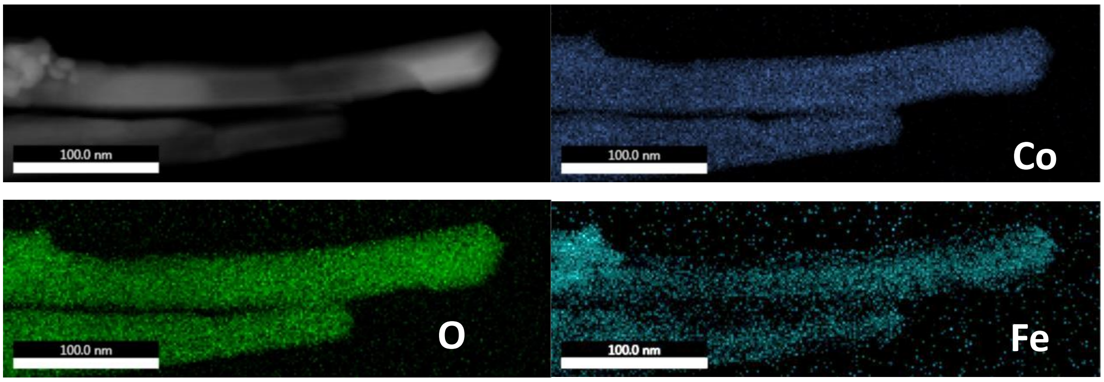

Figure 24: *TEM (a & d) and HRTEM (b & e) images of single nanowire of urchin stucture formed after annealing the coating at 600 °C for 5 h. The FFT converted electron diffraction patterns (c & f) could be indexed to* $CoFe_2O_4$ *and CoO phases present in this nanowire. Lower panel shows the elemental mapping for nanowires.*

In order to further confirm the phases in the coatings with urchin-like particle, XRD was performed and reported in **Fig. 25a**. The XRD pattern was acquired with a glancing angle of 1.5° to mainly investigate the crystallinity of the particulates on the coating surface. For AD coating, the peaks centered at 44.7° and 56.1° are assigned to Fe-B and Co-B phases respectively. On annealing at 500 °C, the peak at 56.1° completely disappears, while the intensity of peak at 44.7° decreases. In addition to these peaks, a small peak at 35.6° due to $CoFe_2O_4$ phase (JCPDF-22-1086) starts to appear. This $CoFe_2O_4$ phase grows prominently at 600 °C with distinct signals at 35.6° and 34.6°. A peak due to α-Fe_2O_3 is also visible at 33.1° at this temperature. All three peaks are also visible in coating annealed at 700˚C with higher intensity. The signal due to α-Fe_2O_3 is anticipated to be generated from the flower-like hierarchical structure which contain only Fe as confirmed by EDS. Similar kind of α-Fe_2O_3 based hierarchical structures are obtained upon deposition of Fe+H_3BO_3 coating by PLD and annealing at 600˚C in air as reported in our previous work [107]. On the other hand, the signal coming from $CoFe_2O_4$ is expected to appear from the urchin-like particles containing both Co and Fe elements which is also confirmed from HRTEM analysis. Although the crystalline phase of CoO is not detected in XRD pattern, its existence cannot be neglected considering the Fe/Co atomic ratio in the NWs. Thus to confirm the phases on the surface of the nanostructured particulates, Raman spectroscopy was performed.

The Raman spectra of AD coating and that annealed at 600˚C in air are reported in **Fig. 25b** in the range of 150 to 800 cm^{-1} where signature vibrations due to metal oxides are located.

The broad nature of the peaks in AD coating indicate that metal oxides are mostly in an amorphous state. Upon annealing at 600˚C, the Raman vibration modes are intensified which is further deconvoluted into six peaks centered at 184, 290, 470, 534, 615 and 682 cm^{-1}. The main peaks at 470 and 682 cm^{-1} are assigned to T_{1g} and A_{1g} mode of spinel $CoFe_2O_4$ phase as well as to E_g and A_{1g} mode of CoO phase respectively [108,109]. Another intense peak at 615 cm^{-1} is attributed to A_{1g} mode of vibration of only spinel $CoFe_2O_4$ phase while the peaks at 184 and 534 cm^{-1} are pertinent to F_{2g} mode of CoO phase only. This confirms that the coating after annealing at 600˚C in air forms a composite of spinel type $CoFe_2O_4$ and CoO phase in an urchin-like structure. Nevertheless, the existence of small amount of α-Fe_2O_3 in flower-like structure is also observed with a low intensity peak at 290 cm^{-1} assigned to E_g mode of α-Fe_2O_3 [110]. Confirmation of the oxides phase can also be carried out by identifying the oxidation state of Fe and Co and its location in the oxide structure using XPS and XANES.

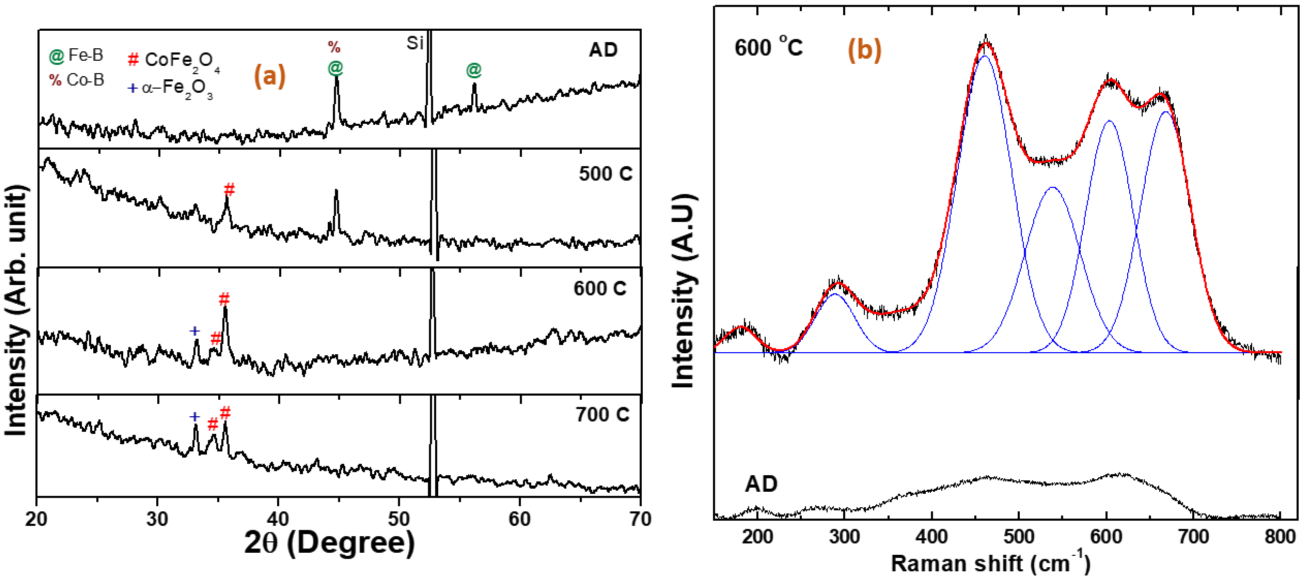

Figure 25: *(a) XRD patterns of as deposited coating and, that annealed at 500˚C, 600˚C, and 700˚C in air for 5 h. (b) Raman Spectra of as deposited coating and that annealed at 600˚C in air for 5 h.*

Elements such as Co, Fe, B and O along with residual carbon are detected in the elemental survey scan of XPS. Focus scan of XPS spectra for Fe_{2p}, Co_{2p}, B_{1s} and O_{1s} level are shown in **Fig. 26**. In Fe_{2p} level, two peaks attributed to $2p_{3/2}$ and $2p_{1/2}$ level are clearly visible in the spectra for all coatings. The deconvolution of $2p_{3/2}$ levels for AD coating displays two peaks at 711.3 and 713.4 eV assigned to Fe^{3+} state in FeOOH and $FeBO_3$ phase [111] respectively, with corresponding satellite peak at higher BE of 718 eV. Both these peaks are also visible for coating annealed at 500˚C but with relatively lower intensity for Fe^{3+} of FeOOH phase. After annealing at 600˚C and 700˚C, the $2p_{3/2}$ level is again deconvoluted into two peaks but with different BE values centered at 710.6 and 712.8 eV due to contribution from Fe^{3+} ions located in octahedral sites and tetrahedral sites respectively, in spinel $CoFe_2O_4$ phase [112]. The shake peak at 718 eV for Fe^{3+} ions is distinctly evident in the annealed samples. The peak at 710.6 eV is also characteristic of Fe^{3+} in α-Fe_2O_3 phase. No signal due to Fe^{2+} is detected in XPS spectra. Similar signals for Fe^{3+} at 725.5 eV and corresponding satellite peak at 730.4 eV are visible in $2p_{1/2}$ state. In Co 2p XPS spectra, the broad peak in $2p_{3/2}$ level is deconvoluted into two peaks, for AD and 500˚C annealed coatings, centred at 781.8 eV and 87.0 eV assigned to Co^{2+} state in $Co(OH)_2$ and its corresponding satellite peak, respectively [86]. Upon annealing at 600 ˚C and 700 ˚C, three peaks are required to deconvolute the main peak, having BE of 780.1, 781.4 eV and 786.2 eV. The first two peaks are ascribed to Co^{2+} ions in octahedral site and tetrahedral site of spinel $CoFe_2O_4$ [112]. The broad peak at 786.2 eV is the characteristic shake up peak of Co^{2+} cations in octahedral site. The peak at 780.1 eV also corresponds to Co^{2+} in CoO phase. Similar to the case of Fe^{2+}, no sign of Co^{3+} is observed in the spectra. The core-level spectrum of B 1s of AD coating is deconvoluted into three peaks cantered at 191.3 eV (40%), 192.6 eV (15%) and 193.8 eV (45%) which are attributed to B_2O_3, $FeBO_3$ and H_3BO_3, respectively. After annealing at 500˚C, the peak of H_3BO_3 completely disappears leading to transformation into mostly $FeBO_3$ having peak at 192.6 eV which is in majority (66%) as compared to B_2O_3 (34%) at 191.3 eV. Nevertheless, this ratio is exactly reversed upon annealing at 600 ˚C. The peak at 191.3 eV (64%) due to B_2O_3 results enhanced in comparison to $FeBO_3$ peak (36%). The content of B_2O_3 (70%) on the surface further increases by small amount at annealing temperature of 700 ˚C. The spectra of O_{1s} level is composed of two peaks at 530.7 eV and 532.1 eV assigned to FeOOH/$Co(OH)_2$ and B_2O_3/H_2BO_3 species, respectively, for AD coating. Upon annealing at 500 ˚C, the peak position due to B_2O_3 remains as it is but the peak at lower BE shifts to 531.1 eV due to the contribution from $FeBO_3$. The spectra of O1s level required three peaks for deconvolution of broad peak recorded for coatings annealed at 600 ^{o}C and 700 ^{o}C. The peaks such as 530.1 eV, 531.2 eV and 532.5 eV correspond to the O in metal oxides ($CoFe_2O_4$, CoO and α-Fe_2O_3), $FeBO_3$ and B_2O_3 respectively. The content of B_2O_3 increases at highest annealed temperature of 700 ^{o}C as confirmed in B 1s spectra. The above XPS results evidently confirm that in AD coating, both the metals are in form of hydroxide (FeOOH and $Co(OH)_2$) while boron is oxidized (B_2O_3) and small amount is bonded with Fe to form $FeBO_3$. On the contrary, the hierarchical nanostructure formed after annealing at 600 ^{o}C mostly contains $CoFe_2O_4$, CoO and α- Fe_2O_3 along with B_2O_3. Most importantly, no sign of either Fe^{2+} or Co^{3+} is identified through XPS, thus discarding the possibility of presence of other oxide phases, such as Fe_3O_4 and Co_3O_4, which is in line with XRD, HRTEM and Raman results.

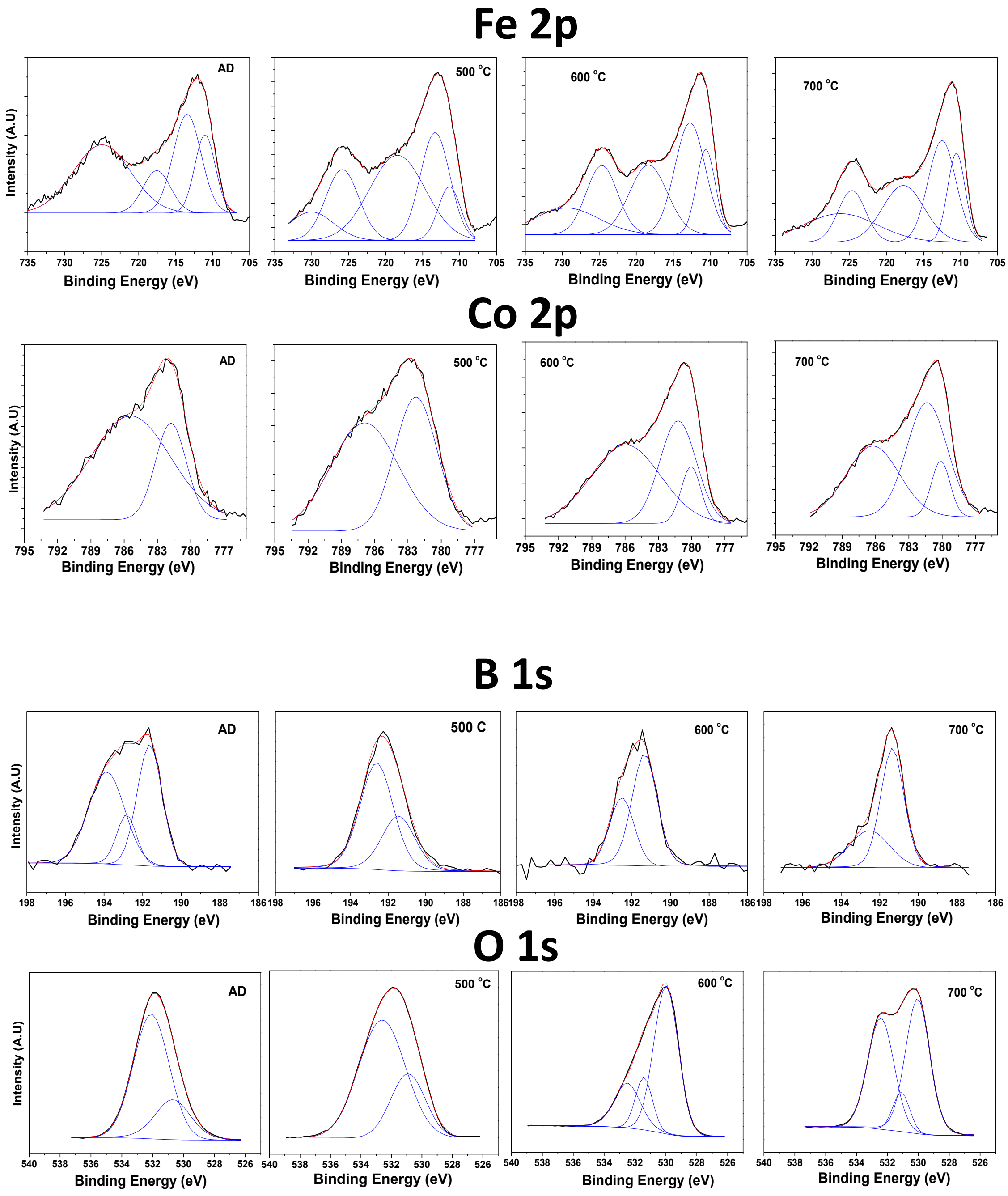

Figure 26: *XPS Spectra of Co 2p, Fe 2p, B 1s, and O 1s level of as deposited coating and that annealed at 500˚C, 600˚C, and 700˚C in air for 5 h.*

To gain more insights on the oxidation states and local geometry of Co and Fe, XANES analysis was carried on the AD coating and annealed coating at 600 °C in air (**Fig.27**). Fe $L_{2,3}$

edge of AD coating displayed two peaks at 709.4 and 711.2 eV in L_3 region with nearly equal intensity. The former peak arises due to the presence of Fe^{3+} cation located at tetrahedral site specifically as reported for the FeOOH species [113] while latter peak arises due to Fe^{3+} positioned in octahedral site. On annealing at 600 °C, the peak at 709.4 reduces but it is still present in the form of a distinct shoulder of the peak 711.2 eV whose intensity remains unchanged. The spectra matches perfectly with that reported for spinel cobalt ferrite where Fe^{3+} cations are present at both octahedral and tetrahedral sites [114]. Similarly for Co $L_{2,3}$ edge, the L_3 region contains a main peak composed of two peaks at 780.3 eV and 781.4 eV pertinent to Co^{2+} cations located at tetrahedral and octahedral site for AD coating [114]. The intensity of both these peaks are maintained for the coating annealed at 600 °C. A very small shoulder at 778.6 eV arising from Co^{3+} state is detected for both the coatings. The formation of Co^{3+} is supposed to be due to long exposure of samples in air before the measurement which might convert small amount of Co^{2+} to Co^{3+}. The XANES results likewise confirms that Fe and Co are present mostly in Fe^{3+} and Co^{2+} state after annealing at 600 °C leading to the formation of $CoFe_2O_4$ phase in majority, along with CoO and α-Fe_2O_3 phases which again match well with the XPS, Raman, XRD and HRTEM results.

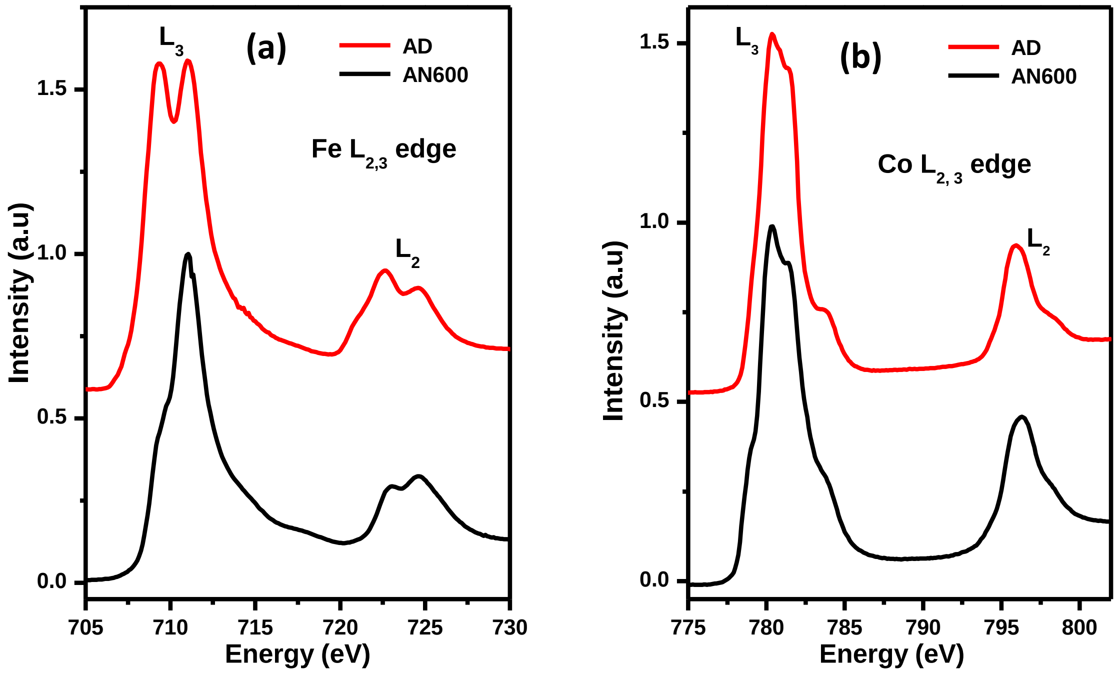

Figure 27: *XANES Spectra at (a) Fe $L_{2,3}$ edge (b) Co $L_{2,3}$ edge, of as deposited coating and that annealed at 600˚C in air for 5 h.*

The mechanism involved in the formation of urchin-like and flower-like hierarchical particles comprising Co and Fe oxide, respectively, is explained in detail in our previous work on single metal oxide [87,107]. Here, in mixed oxide, the composition and crystal phases involved during the formation of these hierarchical structures is briefly clarified on the basis of the characterization results obtained above. During PLD, the high laser fluence is mainly responsible for phase explosion process occurring just below the target surface which leads to the deposition of particulates of wide range of sizes in the AD coating. These particulates are in the form of core-shell structure, as observed in SEM images, with heavy elements such as Fe and Co forming the core which is covered by light elements such as B and O bonded with Fe and Co. XPS and XANES show the presence of only B_2O_3, $FeBO_3$, FeOOH and $Co(OH)_2$ on the surface of AD coating. During annealing, mechanical stress is generated between the core and shell due to the large difference between thermal expansion coefficient of metals and metal oxides, borides and hydroxides. In order to release this stress, the shell starts to disintegrate leading to the emerging of core metal in form of NWs on the surface of particulates at 500 ˚C. On further annealing to 600 ˚C and 700 ˚C, these NWs grow in length to further release the stress. The NWs are composed of mixed phases of $CoFe_2O_4$ and CoO, formed by metal reacting with O_2 in air, as confirmed by the results of XPS, XANES, Raman, XRD, HRTEM and EDS. As there is a preferential ablation of Fe, some core-shell particulates contain only Fe core with Fe-B-O shell. Indeed these specific particulates release stress to form flower-like hierarchal structure having α-Fe_2O_3. Such nano-structure formation is consistent with that obtained for the coating prepared by PLD using Fe and H_3BO_3 as target and annealed in air for 600 ˚C [107]. However, majority of hierarchal particulates are composed of urchin-like structure having NWs of mixed oxides of $CoFe_2O_4$ and CoO.

As the present synthesized mixed oxide urchin-like coatings will be applied for photocatalysis application, it is mandatory to investigate their optical properties. UV-vis spectra acquired in transmission mode is presented in **Fig. 28a** for coating annealed at 600 ˚C where urchin structure is well developed. The catalyst coating seems to be active in absorbing visible light in the range from 300 to 800 nm. However, $CoFe_2O_4$ and CoO are the major phases present in the urchin structure as confirmed by above results, where the former is an indirect band gap semiconductor with value of ~1.2 eV [115,116] and the latter has a direct band gap of ~2.4 eV [117]. Thus, the Tauc representation was plotted for analysis of both indirect as well as direct transitions in **Fig. 28b**. The energy gap value of 1.35 eV and 2.37 eV was measured for indirect and direct transition, respectively. These values are very close to that reported for the band gap of $CoFe_2O_4$ and CoO, respectively, thus again confirming the presence of both these phases in the urchin-like nanostructure. Most decisively, this mixed oxide urchin-like coating seems to be very efficient in absorbing visible light.

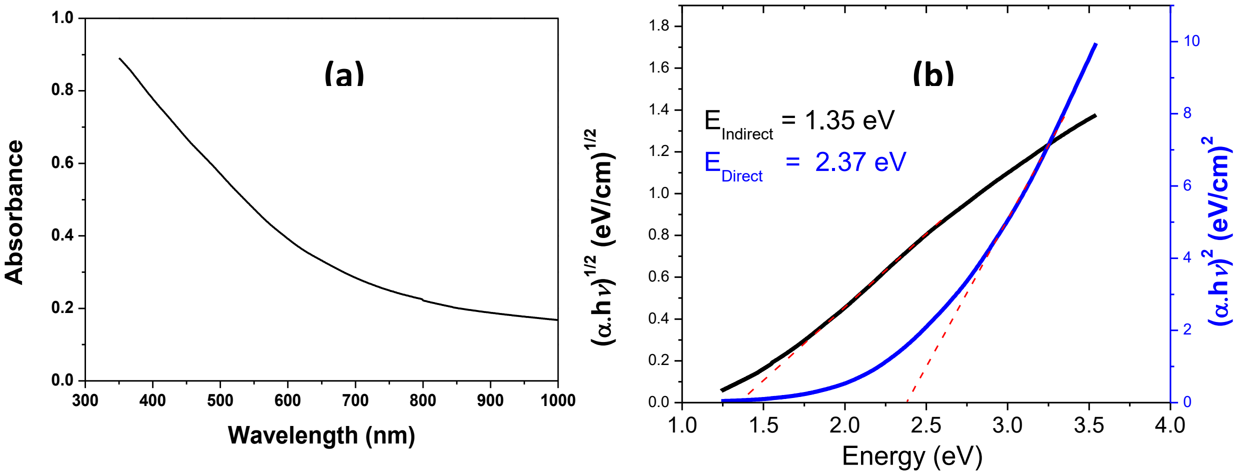

Figure 28: *(a) UV-Vis absorbance spectra of the PLD deposited coating annealed at 600˚C in air for 5 h, and corresponding (b) Tauc plot to determine direct and indirect band-gap.*

The effectiveness of the synthesized mixed metal oxide urchin-like hierarchical nanostructure by PLD as a photocatalyst was studied by using it for degradation of model MB dye through a photo-Fenton reaction involving H_2O_2. The variation in the MB dye concentration as a function of irradiation time was measured by monitoring the variation in the characteristic absorption peak at 664 nm. Adsorption is the major prerequisite condition for any heterogeneous catalytic reaction, thus all the catalyst coatings were kept stirring in the dye solution under dark for 30 min. The role of light, H_2O_2 and catalyst, in catalytic degradation was first verified by performing the separate degradation of MB dye, (1) in presence of light only, (2) with added H_2O_2 and light, (3) with coating annealed at 600˚C and light, and (4) combination of all three (H_2O_2, light and catalyst). The degradation results are presented in **Fig. 29a.** In 60 mins, the degradation of MB dye in light is only 19% which increases to 28% after inclusion of H_2O_2. Finally adding urchin-like mixed oxide coatings along with H_2O_2 and light the degradation reaction is almost completed in 60 mins. This indicates that the catalyst coating follows photo-Fenton reaction by generation of $OH^{\bullet}$ radicals by dissociation of H_2O_2. Most importantly, the catalyst coating is also able to degrade 47% of MB dye in absence of H_2O_2. This suggests that the mixed oxide catalyst coating also works as a pure photocatalyst which might be able to generate hydroxide radicals from adsorbed H_2O on the surface.

Although the involvement of H_2O_2 is very useful, the catalyst coating can however also be utilized without H_2O_2.

It is of paramount importance to understand the impact of mixed oxides phases ($CoFe_2O_4$ and CoO) in urchin structure on the photocatalytic activity. Thus the performance of photocatalytic degradation of MB dye with single oxide of Co_3O_4 urchin-like and α-Fe_2O_3 flower-like hierarchical nanostructure prepared by same technique is compared with that of mixed oxides urchin-like coating prepared in the present case (**Fig. 29b**). The complete analysis on morphology, structure, composition, phases and chemical states of single oxide coatings prepared with PLD having mainly identical hierarchical structure is reported and discussed in our previous work [87,107]. In all experiments the weight of the catalyst was constant and the irradiated geometric area was maintained around 2.5 cm × 7.5 cm respectively. As observed from **Fig. 29b**, $CoFe_2O_4$ /CoO mixed oxide urchin-like coating was able to achieve almost complete degradation (97%) of MB dye in just 60 mins which is half of the time required by α-Fe_2O_3 (120 mins) and less than half time required by Co_3O_4 (150mins) urchin-like coatings. This evidently proves a significant improvement in photocatalytic activity for the mixed metal oxide coatings achieved by synergic effect created by the heterojunction between CoO and $CoFe_2O_4$, lower bandgap of $CoFe_2O_4$ and high surface area obtained in urchin-like structure. The smaller bandgap will improve visible light absorption leading to generation of large number of electron-hole pairs which will be separated at the heterojunction formed at the interface of CoO and $CoFe_2O_4$ to reduce the recombination problem. On the other hand, the number of exposed active sites will be enhanced by the high surface area in the urchin-like particle. Although the combination of these three features seems to be very effective in enhancing the photocatalytic activity, it is very essential to evaluate the contribution of each one of these features towards efficient degradation reaction.

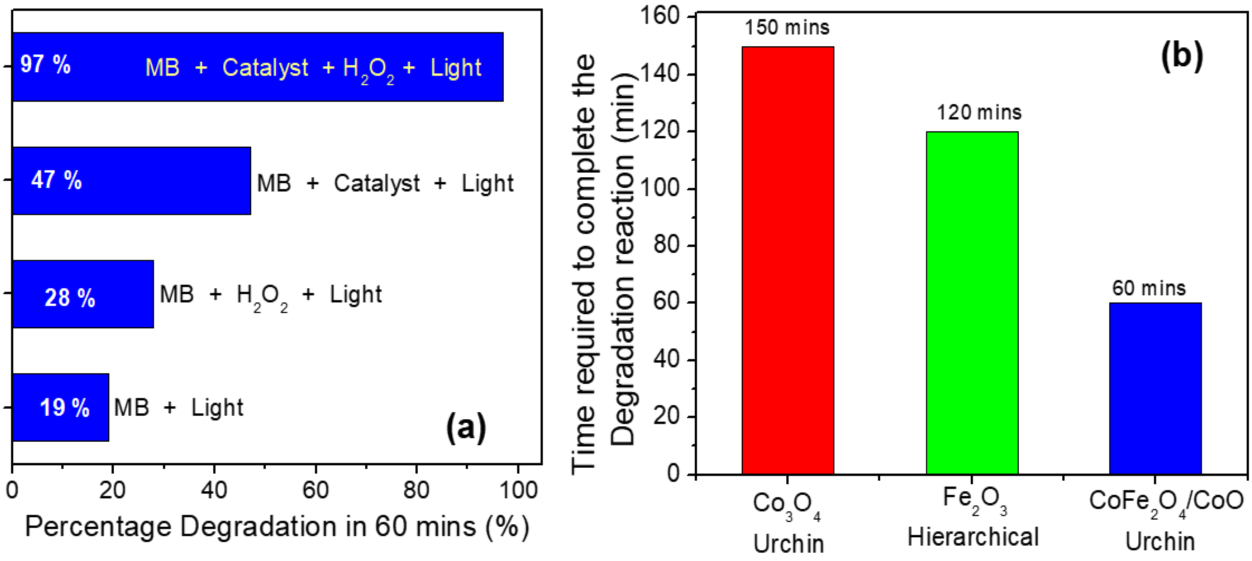

Figure 29: *(a) Percentage degradation of MB dye after 60 mins in presence of PLD despoited coating annealed at 600 °C,* H_2O_2 *and visible light. (b) Comparison of performance for* Co_3O_4 *urchin-like, α-*Fe_2O_3 *hierarchical-like, and* $CoFe_2O_4$*/CoO urchin-like coatings deposited by PLD and annealed in air at 600 °C, for degradation of MB dye in presence of* H_2O_2 *and visible light.*

To investigate the effect of urchin-like structure, the photocatalytic degradation of MB in presence of H_2O_2 was investigated for the mixed-oxide AD coating and for that annealed at different temperatures of 400˚C, 500˚C, 600˚C and 700˚C in air for 5 h (**Fig. 30a**). Except for coating annealed at 600˚C, all the other coatings showed comparable activity with the catalyst annealed at 700˚C displaying the worst activity. AD coating was able to degrade only 53% in 150 mins mainly due to lack of any urchin-like particle and the required phase on the surface. With annealing at 400 and 500˚C, the coating shows slight improvement in photocatalytic activity (60% and 64% degraded in 150 min respectively) which is attributed to the start of formation of urchin-like particle having NWs of very short length as confirmed by SEM image (**Fig. 21d**). Only when the urchin with well-developed NWs are formed at 600˚C, it illustrates high photocatalytic degradation of about 97% in just 60 mins. This definitely highlights the role of urchin-like nanostructure providing the large number of active sites obtained through high surface area. The coatings annealed at 700˚C showed very poor adhesion to the substrate, when immersed into the dye solution that indeed caused the peeling of coating in the solution. It is suspected that at this temperature the length of NWs are large thus causing the lifting of urchin-like particulates from the coating surface. These loosely bond particulates are expected to be removed during the catalytic reaction, hence delaying the reaction time. However, the degradation rate attained with 600˚C annealed coating confirms the important role of urchin-like hierarchical structure in enhancing the MB dye degradation.

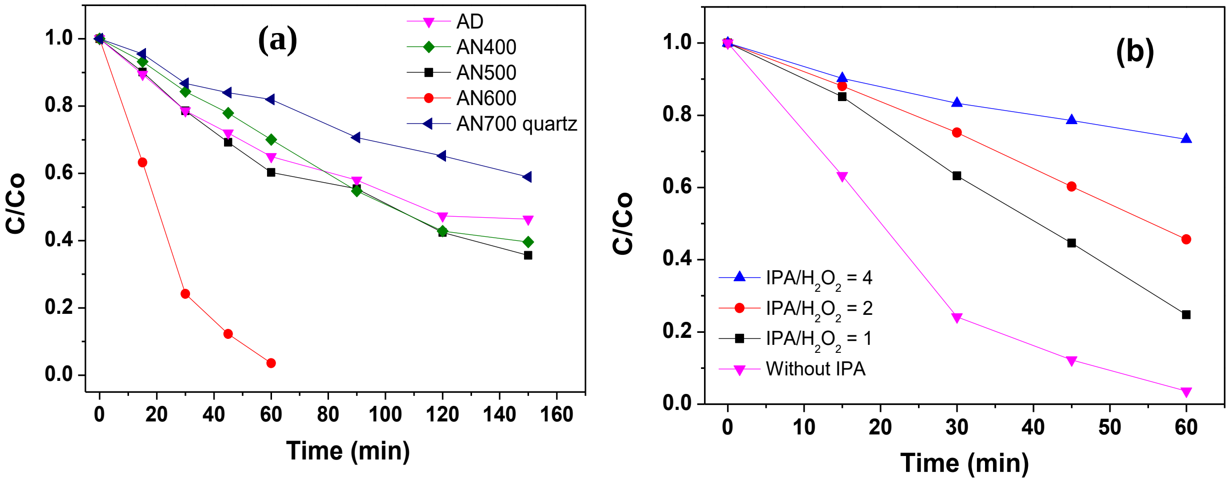

Figure 30: *Time dependent degradation ratio of MB dye solution in presence H_2O_2, and visible light (a) using mixed-oxide coatings, as deposited by PLD and that annealed at various temperatures 400 °C, 500 °C, 600 °C and 700 °C in air for 5 h and (b) using catalyst coating annealed at 600 °C in presence of isopropanol (IPA) of different molar ratio.*

To explore the formation of heterojunction and its effect on photocatalytic activity, it is necessary to investigate the band edge of both $CoFe_2O_4$ and CoO. The band edge of conduction band (CB) and valence band (VB) reported for $CoFe_2O_4$ in past literature [118] is located at +0.16 eV and +1.44 eV respectively, having band gap of 1.2 eV. For CoO with band gap of 2.4 eV, the CB and VB are located at +0.9 eV and +3.3 eV respectively [88]. The schematic diagram in **Fig. 31** shows the band edge position of $CoFe_2O_4$ and CoO along with the redox potential for $O_2^{\bullet}$ radical ($O_2/O_2^{\bullet}$) and $OH^{\bullet}$ radical ($OH^-/OH^{\bullet}$) formation at -0.13 eV and +2.4 eV, respectively. Considering the band position of both the semiconductors and the fact that both are p-type semiconductors it will not form p-n type II junction. Rather it will form a z-scheme junction which is only formed in p-p or n-n type semiconductor because the combination of p and n-type semiconductor will create space charge region to inhibit the charge carrier Z-scheme migration [119]. Thus, during light irradiation, the band gap of $CoFe_2O_4$ and CoO permits both the semiconductors to absorb visible light to produce electron-hole pairs. The excited electrons from CoO will combine with holes of $CoFe_2O_4$ to spatially separate the electrons in $CoFe_2O_4$ and holes in CoO which further take part in photocatalysis reaction. As the redox potential of $O_2/O_2^{\bullet}$ (-0.13 eV) is more negative than the CB edge of $CoFe_2O_4$, all the electrons formed during excitation of $CoFe_2O_4$ will be utilized to activate H_2O_2, which is a well-known electron acceptor, to form $OH^•$ radical. Alternatively, the VB edge of CoO is more positive than the redox potentials of $OH^-/OH^•$ formation (2.4 eV), thus the hole accumulated on CoO will participate in formation of $OH^•$ radical from the absorbed OH^- ion. According to proposed mechanism, $OH^•$ radical is the only active radical that will be formed to oxidize the MB dye. To confirm this, the scavenger of $OH^•$ radical in form of isopropanol (IPA) was introduced during the reaction with different IPA/H_2O_2 molar ratios (1, 2 and 4) (**Fig. 30b**). For 60 mins, the amount of MB degradation reduces to 75%, 52% and 25% for IPA/H_2O_2 molar ratio of 1, 2 and 4 respectively. At highest concentration of IPA, the catalytic activity drastically decreases and the obtained amount of degradation is similar to that achieved with MB + light after 60 mins. For each H_2O_2 molecule two $OH^•$ radicals are generated, thus at IPA/H_2O_2 ratio of 2, it is expected to be enough to completely stop the reaction because all $OH^•$ produced from H_2O_2 will be scavenged by IPA. Yet this is not the case and the degradation amount (52 %) is decreased by half in 60 mins. This value is consistent with that achieved with using only catalyst and light without H_2O_2 (47 %) (**Fig. 29a**). The observation through this $OH^•$ scavenging experiment clarifies two phenomena: 1) $OH^•$ is the only active radical formed and is responsible for the degradation of MB and 2) $OH^•$ radicals are not only formed by H_2O_2 activation but also by oxidation of OH^- ions coming from water molecules adsorbed on the catalyst surface. This proves our hypothesis that $CoFe_2O_4$ and CoO forms a Z-scheme type heterojunction to reduce the recombination of electron-hole pair to produce $OH^•$ radicals not only in presence of H_2O_2 by photo-Fenton reaction but also by the oxidation of OH^- ions to induce direct photocatalysis in the absence of H_2O_2. The attained direct photocatalysis due to formation of Z-scheme heterojunction between $CoFe_2O_4$ and CoO was also confirmed by comparing with the results of single oxide Co_3O_4 urchin-like and α-Fe_2O_3 flower-like coatings tested without H_2O_2. The degradation of only 15-20% was achieved after 60 mins, thus suggesting that single oxide Co_3O_4 and α-Fe_2O_3 are active only in presence of H_2O_2 where the photo-Fenton type reaction takes place [87,107]. This verifies that formation of Z-scheme heterojunction is mostly accountable for higher photocatalytic activity in mixed oxide in comparison to single oxide urchin-like coating. In addition to the improved photogenerated charge separation at the heterojunction, the higher amount of visible light absorption owing to lower bandgap of $CoFe_2O_4$ will also contribute in enhancing the photocatalytic activity of mixed oxide urchin-like coatings, though contribution due to this is difficult to quantify.

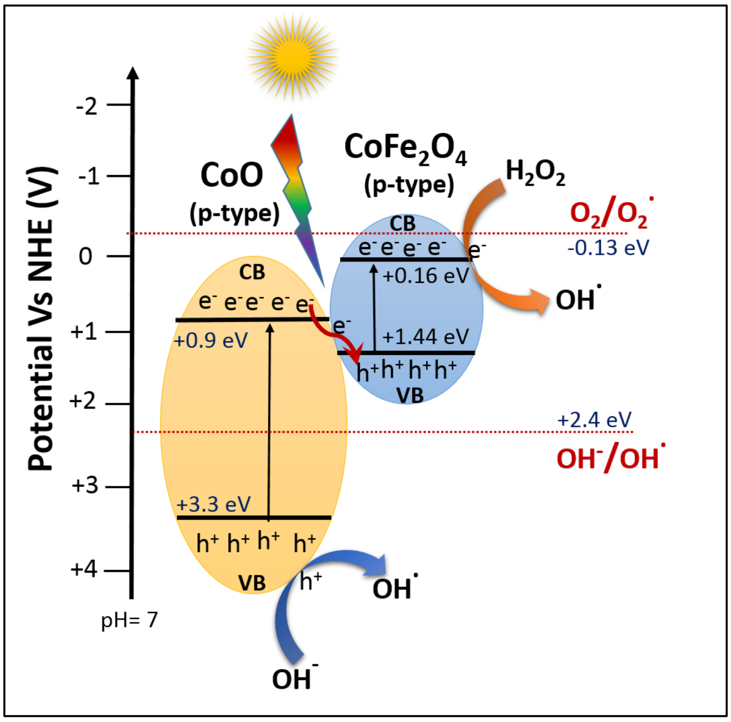

Figure 31: *Schematic diagram of z-scheme junction between CoO and CoFe*$_2$*O*$_4$ *p-type semiconductors.*

To investigate the mineralization of MB dye to H_2O and CO_2, the photocatalytic activity of the 600°C annealed coating was also done with the CO_2 sensor mounted on top of the reaction vessel. The sensor was able to measure the CO_2 generated from the photocatalytic reaction revealing an increase in the CO_2 level (measured in ppm) as soon as light is irradiated on the catalyst surface (**Fig. 32**) thereby giving the direct proof of MB degradation with CO_2 as the by-product.

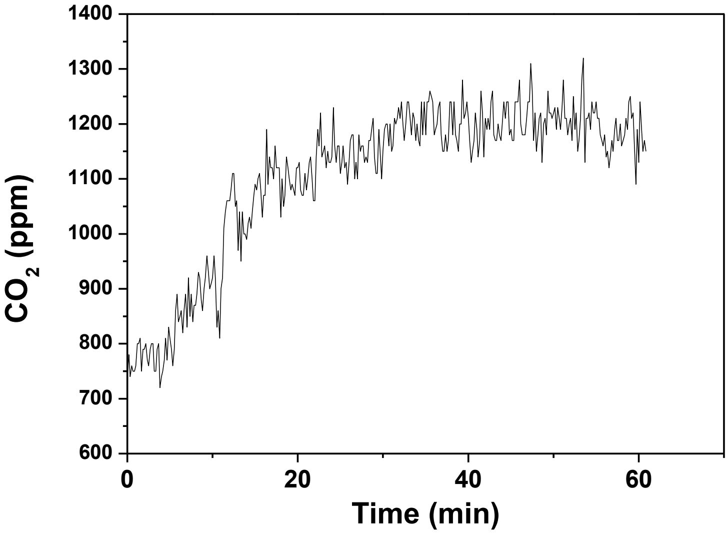

***Figure 32:** CO_2 evolution during MB degradation by $CoFe_2O_4$/CoO urchin-like coatings deposited by PLD and annealed in air at 600 °C, in presence of H_2O_2 and visible light.*

3.4 Conclusion

Hierarchical urchin-like structures of mixed-metal oxides were successfully obtained as coatings by PLD. An in-depth structural characterization revealed $CoFe_2O_4$ and CoO as the main components, leading to the formation of heterojunctions. $CoFe_2O_4$/CoO shows remarkable photoactivity towards degradation of the organic pollutant, accompanied by CO_2 evolution indicating (qualitatively) conversion to inorganic carbon. Almost total degradation (97%) is obtained by $CoFe_2O_4$/CoO in half the time with respect to comparable single-metal oxides (60 min. compared with 120 min. for α-Fe_2O_3 and 150 min. for Co_3O_4). The enhanced photocatalysis performance is attributed to both the urchin-like structure, resulting in a large surface-area increase, and the formation of a Z-scheme heterojunction between $CoFe_2O_4$ and CoO. The latter not only improves charge-separation by spatial separation of photogenerated electron-hole couples, but also activates a direct photocatalysis route for the degradation reaction. Indeed, while the single-metal oxides show only photo-Fenton activity, $CoFe_2O_4$/CoO is considerably active (47% degradation in 60 min.) also in absence of H_2O_2. These findings prove that hierarchical nanostructuring and especially Z-scheme designs are very powerful tools to enhance the photocatalysis performance of materials. Their application here on immobilized photocatalysts, which can be easily recovered and used again, is particularly important from an industrial perspective. Additionally, both materials (Fe, Co and B) and fabrication method (PLD) employed are easily scalable, bringing the photocatalysis technology a step-further towards industrial application. In principle, this technique can be also extended to synthesis of all the ferrites possible in existence as long as the precursors in the form of metallic powders are available.

Chapter 4: Tungsten-doped TiO_2/reduced Graphene Oxide nano-composite photocatalyst for degradation of phenol: A system to reduce surface and bulk electron-hole recombination

Preview: One of the major issues TiO_2 faces as a photocatalyst is the high bulk and surface recombination of photo-excited charges. To tackle this problem, a combined strategy was adopted by doping TiO_2 with tungsten and forming a nanocomposite with reduced graphene oxide (rGO). Tungsten doped TiO_2/reduced graphene oxide (rGO) nanocomposite photocatalysts were synthesized and tested for para-Nitrophenol (p-NP) degradation. The synthesized photocatalyst exhibited good photocatalytic activity in degradation of organic pollutant p-NP with superior activity compared to rGO/TiO_2, TiO_2 and W-TiO_2 respectively. The effect of doping and composite formation on the activity of the photocatalyst was investigated in detail.

My contribution to this work includes the synthesis of GO, TiO_2 and rGO/TiO_2 composites along with the study of their optical properties with UV-Vis-NIR spectroscopy. I also performed the photocatalytic measurements for GO, TiO_2 and rGO/TiO_2 samples along with data plotting and interpretation.

The content of this chapter is adopted from;
Manisha Yadav, Asha Yadav, Rohan Fernandes, Yaksh Popat, Michele Orlandi, Alpa Dashora, D.C. Kothari, Antonio Miotello, B.L. Ahuja and Nainesh Patel, Journal of Environmental Management 203 (2017), 364-374.
https://doi.org/10.1016/j.jenvman.2017.08.010

4.1 Introduction

TiO_2 has been widely used by many researchers for photocatalysis based applications due to its well-known properties such as non-toxicity, chemical stability, high oxidative power, abundance and low cost [120,121]. However, TiO_2 is a wide bandgap material absorbing only UV light of the solar spectrum. Further, the instantaneous recombination of photogenerated electrons with holes in TiO_2 affects its catalytic activity. These are the two major drawbacks of TiO2 photocatalysts. Therefore, much research has been focused on band-gap engineering to extend TiO2 absorption in the visible region. However, it is necessary that a photocatalyst material should not only be able to generate the electron-hole pair under visible light, but at the same time the photogenerated electrons should reach the surface active sites before recombination with the hole in the valence band. In this regards, many strategies have been proposed and implemented, such as doping with metals/non-metals [122–125], loading of noble metal nanoparticles (NPs) [126], sensitizing with dye molecules and combining with other semiconductors [127]. Recently, W-doped TiO_2 is gaining interest because of its high catalytic activity and surface acidity [128–137][138]. Doping TiO_2 with high valence cations like tungsten (W^{6+}) modifies the electronic structure of TiO_2, introducing energy levels just below the conduction band [139]. Thus it can act as an electron trap and can help in increasing the lifetime of charge carriers in the excited state.

However, W doping is only able to reduce the recombination in the bulk of TiO_2; whereas, the defects which are present on the surface of TiO_2 act as recombination centers. Thus, surface recombination should also be taken into consideration to enhance the photocatalytic activity by utilizing the maximum number of charge carriers in separated form. Different strategies were employed in order to enhance the transport of charge carriers such as coupling them with a noble metal [140], another semiconductor [141] or carbonaceous materials [142]. Among these, carbonaceous materials such as activated carbon, CNTs, fullerene and graphene are the most promising because of their high charge carrier mobility and large surface area. Studies have shown that there are several drawbacks with TiO_2- CNT and TiO_2-fullerene composites such as reduced light intensity reaching the surface of the catalyst, insolubility of CNT in common solvent and polydispersity in CNT length and diameter [143]. On the other hand, graphene and its derivatives, Graphene Oxide (GO) and reduced Graphene Oxide (rGO), serve as excellent support materials having large surface area, improved mobility of charge carriers, high thermal conductivity and good chemical stability [144]. rGO as compared to graphene is hydrophilic due to the existence of oxygen atoms bound to the carbon scaffold that makes it easily dispersible in water [145]. In addition, rGO contains both aromatic (sp^2) and aliphatic (sp^3) domains which further expand the types of interaction that can occur with the surface [145]. It is reported that coupling TiO_2 with rGO enhances the catalytic activity by transferring the electrons from TiO_2 to rGO which suppresses the recombination of photo-generated electrons and holes [146–148]. Most importantly, electron transfer from TiO_2 to rGO is faster than electron-hole recombination on the surface defect. Therefore, we employ combined strategy to modify TiO_2 to reduce the comprehensive recombination of charge carriers (on the surface as well as in the bulk) to enhance its photocatalytic activity.

Herein, we synthesize rGO/W-doped TiO_2 composite for the first time, to the best of our knowledge. W-doped TiO_2 was synthesized by sol-gel method and reduction of GO was carried out with the help of TiO_2 in UV light. TiO_2 with different concentration of W was synthesized to optimize W content. The ratio of GO with respect to TiO_2 was also varied to determine the optimized concentration of GO with TiO_2 to enhance its activity. The efficiency of the composite was evaluated by degrading an organic pollutant (p-nitrophenol) in the presence of light. The role of rGO in separating the charge carriers was studied with the help of time resolved photoluminescence.

4.2 Experimental methods

4.2.1 Synthesis of TiO_2 and W-doped TiO_2

Titanium (IV) n-butoxide ($Ti(OC_4H_9)_4$) and Sodium tungstate dihydrate ($Na_2WO_4.2H_2O$) were used as precursors for TiO2 synthesis and W doping, respectively. A sol-gel method was used to prepare TiO_2 and W-doped TiO_2 photocatalyst. Briefly, undoped TiO_2 was prepared by mixing $Ti(OC_4H_9)_4$ with ethanol and stirred for 1 h. A solution of H_2O, ethanol and HNO_3 (catalyst) was stirred for 1 h separately for homogeneous mixing and it was gradually added to the Ti precursor solution. The resultant solution was further stirred for 2 h to obtain a homogeneous solution. The molar ratio of $Ti(OC_4H_9)_4/H_2O$/ethanol/HNO_3 was kept constant at 1/30/20/0.1. To synthesize W-doped TiO_2, sodium tungstate was mixed with the acidic solution before addition of the Ti precursor solution. The resulting solution was kept for gelation overnight at room temperature. After 24 h the final solution was washed with water and ethanol several times and kept for drying at 120 ºC for 3 h to remove excess solvent. The powder was then calcined in air at 400 ºC for 2 h. Five different concentrations of W (0.1, 0.25, 0.5, 1 and 3 at. %) were used to synthesize W-doped TiO_2 in order to investigate the role of W dopant.

4.2.2 Preparation of GO, TiO_2/GO and W-TiO_2/GO composites

Graphene oxide was synthesized by a modified Hummer's method as reported by Kalambate et al. [149]. In a typical synthesis, the commercially available graphite powder was exfoliated using H_2SO_4 and oxidized to graphite oxide by reaction with strong oxidants such as $KMnO_4$ and $NaNO_3$. The reaction was then terminated with H_2O_2. The resultant suspension of graphite oxide was filtered and washed with HCl and distilled water several times and finally with ethanol. The obtained product was dried in vacuum. Graphite oxide was then converted into graphene oxide by dispersing in distilled water and sonicating for 1 h.

To prepare rGO/TiO_2 composites, separate aqueous solutions of GO and TiO_2 powder were sonicated for 1 h. The suspension of GO was added to the TiO2 suspension and again stirred for 1 h for homogeneous mixing. The resulting solution was kept under UV irradiation with constant stirring for 24 h. Under UV light irradiation electron-hole pairs are produced in conduction band and valence band of TiO_2 respectively. These electrons are able to reduce the hydroxyl group, epoxy group and carboxylic functional group on the surface of GO sheet. As a result, GO is converted to rGO sheets, which is also confirmed from the color change from brown to black. rGO/W-TiO_2 composite was also prepared as described above except that W TiO_2 was used instead of TiO_2. Composites of different weight ratio of GO and TiO_2 were synthesized in order to obtain the optimized concentration for component interaction.

4.2.3 Characterization techniques

The structural characterization of all samples was carried out by X-ray Diffraction (XRD) (Rigaku ultima IV) using Cu Kα radiation (λ = 1.5414 Å). The optical band gap of all the photocatalysts was determined by using a UV-Vis-NIR spectrophotometer (Cary) in diffuse reflectance mode in the range of 200-800 nm. The surface morphology of the samples was determined by using scanning electron microscope (SEM-FEG, JSM 7001F, JEOL). Bright field, high resolution transmission electron microscope (HR-TEM) images and selected area electron diffraction (SAED) pattern were recorded using a FEG-TEM 300 kV system (Tecnai G2, F30). The radiative recombination of the photo generated charges was studied by collecting photoluminescence (PL) emission spectra using a Fluorescence spectrophotometer (Varian, Cary Eclipse). The photocatalyst was excited at a wavelength of 385 nm (bandgap of TiO2). The Time-Resolved photoluminescence spectroscopy (TRPL) was carried out to determine the lifetime of the charge carriers using an ISS Chronos BH fluorometer. For excitation, a pulsed diode laser (Hamamatsu) of wavelength 405 nm with pulse width of 70 ps operating with a peak power of 100 mW was used. Both PL and TRPL spectra were acquired by dispersing 2 mg of photocatalyst powder in a fixed amount of aqueous medium and transferred into 1 cm * 1 cm cuvette for the measurement. Glycogen dispersed in water was used to measure the instrument's response function while the multi exponential curve fitting was done using Vinci Analysis software. The chemical state and surface composition present in the sample were studied by X-ray Photoelectron Spectroscopy (XPS) using PHI 5000 Versa-Probe II instrument with a monochromatic Al Kα (1486.6 eV) X-ray source and a hemispherical analyzer. Appropriate electrical charge compensation was employed to perform the analysis and the binding energy was referenced to the C 1s peak at 284.8 eV. Raman measurements were performed on a Horiba LabAramis setup equipped with a He-Ne 633 nm laser as source and a confocal microscope (100x objective) coupled to a 460 mm focal length CCD based spectrograph equipped with a four interchangeable gratings turret. The signal was collected on an air-cooled multichannel CCD, with a wavenumber accuracy of ±1 cm^{-1} in the range of 200-1500 nm. The laser power of 15 mW, was used with the maximum spot size is 5 μm. FT-IR measurements were carried out in transmission mode at normal incidence in the spectral range between 4000 and 400 cm^{-1} using a JASCO FT-IR-660 plus spectrometer operated at room temperature. The BET surface area of all the samples was measured by adsorption of nitrogen at 77 K and desorption at room temperature.

4.2.4 Photocatalytic activity measurement

The photocatalytic activity of all the samples was evaluated by photo-degradation of p-nitro phenol (p-NP) under 150 W xenon lamp having spectrum similar to the solar spectrum. 10 mg of photocatalyst were dispersed in 50 ml of aqueous p-NP (10 ppm). Prior to light irradiation, the solutionwas stirred for 30 min in dark so that the catalyst achieves adsorption desorption equilibrium with p-NP. The distance between the light source and the reactor was kept constant at 47 cm. After fixed intervals of time, 1 ml of aqueous solution was filtered out in a 1 cm * 1 cm cuvette. The absorbance of p-NP was measured using a UV-Vis spectrophotometer. In order to evaluate the photocatalytic activity, the normalized intensity of the absorption band of p-NP at 320 nm was measured and plotted as a function of irradiation time. All the photocatalytic experiments were done at room temperature and at neutral pH.

4.3 Results and discussion

TiO_2 was doped with W in different concentrations of 0.1, 0.25, 0.5, 1 and 3 at.%. **Fig. 33a** shows the XRD patterns of all the W-doped TiO_2 samples. The peaks observed at of 25.3°, 37.7°, 48.1°, 53.8°, 55.1°, 62.7°, 68.8°, 70.3°, and 75.1° in pure TiO2 sample correspond to the (101), (004), (200), (105), (211), (204), (116), (220), and (215) planes of the anatase phase respectively. It is clear from the diffraction pattern that all the W-doped TiO_2 samples show pure anatase phase similar to the undoped TiO_2, indicating that the phase is maintained even after doping. A shift in the peak position is not expected and is not observed here after W-doping, as the ionic size of Ti^{4+}(0.0605 nm) is similar to the W^{6+} (0.0600 nm) [139]. No peak due to WO_3 was detected in the XRD spectra. As calculated by Scherrer's formula, the average crystallite size of all the samples was estimated to be in the range 6-9 nm, thus confirming the formation of TiO_2 nanoparticles which was later confirmed by TEM analysis.

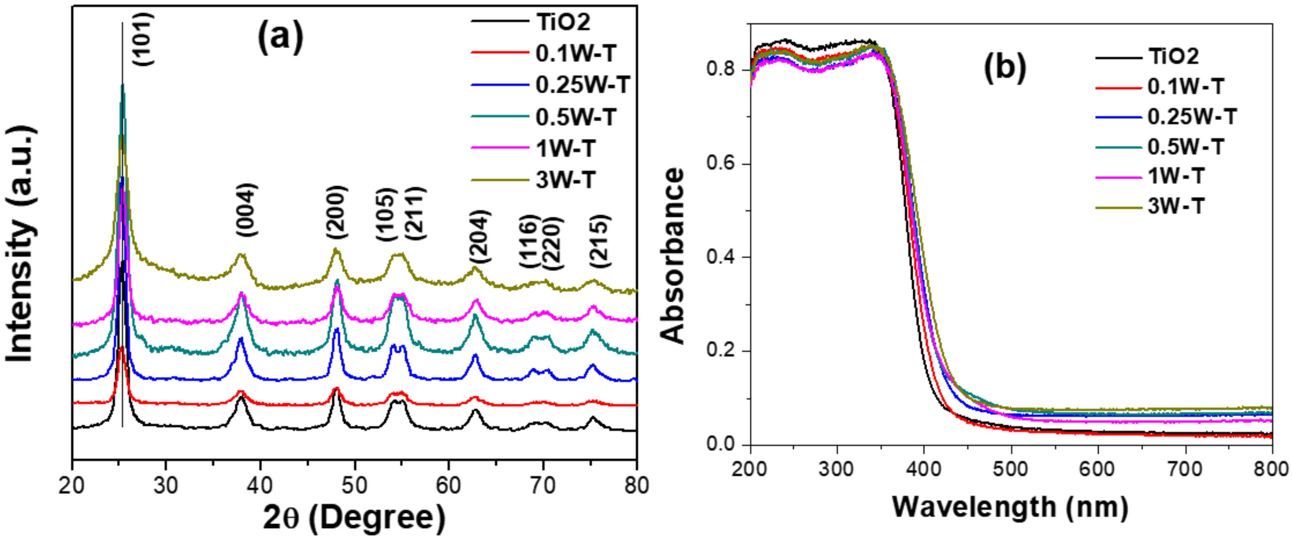

Figure 33: *(a) XRD patterns and (b) UV-Vis absorption spectra (taken in diffuse reflectance mode) of pure TiO_2 and W-doped TiO_2 with different doping concentration of W.*

The optical properties of TiO_2 and W-doped TiO_2 were measured by UV-vis spectroscopy in diffuse reflectance mode. The absorption spectra were taken in the range of 200-800 nm as shown in **Fig. 33b**. There is no major shift in the absorption edges of W-doped TiO_2 as compared to pure TiO_2, indicating that W does not contribute in reducing the bandgap of TiO_2 in the visible region. The reason for this is that W forms impurity energy levels just below the conduction band, shifting the band gap by a very small amount for W-doped TiO_2. In fact, the band gap of W-doped TiO_2 (3.09 eV) shifts marginally as compared to pure TiO_2 (3.21 eV).

The recombination of photogenerated charge carriers is studied by acquiring the PL spectra of TiO_2 and W-doped TiO_2 (**Fig. 34a**), as it measures the radiative recombination of electron-hole pairs. The excitation, lying in the region of steep absorption doesn't affect the PL intensities because the absorption of all the W-doped samples are similar and no significant difference is noted in their absorbance. Thus, the differences in their PL intensities are due to doping and not due to different excitation efficiencies. Four distinct peaks are observed at 420, 438, 485 and 526 nm. The first two peaks (420 and 438 nm) are due to the relaxation of self-trapped excitons generated through the transition along the band edges while the other two peaks at 485 and 526 nm are due to the intraband transition within the trap levels or surface defects due to the oxygen vacancies [150]. The emission intensity of all the W-doped TiO_2 samples is reduced as compared to that of pure TiO_2. Among all the concentrations, 1W- TiO_2 (where 1W indicates 1 at.% W) displayed the minimum emission intensity indicating maximum reduction in the radiative recombination of e^--h^+ pairs. Thus, W-doping induces better charge separation of photogenerated charge carriers as compared to pure TiO_2. To determine the lifetime of the charge carriers, TRPL spectra were acquired (**Fig. 34b**) for all the W-doped TiO_2 samples. In the TRPL experiment, the PL is measured at an integrated value. The decay curve is fitted by a double exponential, yielding an average lifetime of 2.67 ns for pure TiO_2. There is a difference in measured lifetimes of defect-related PL and exciton related PL, hence the average carrier lifetime is displayed for comparison. As per the decay value, it is demonstrated from 20.5ns in order to understand the time evolution from where the decay initiates. The relaxation time gets increased after W doping in TiO_2 and a maximum lifetime of 3.52 ns is obtained for 1W- TiO_2. The lifetime of charge carriers decreases again with further increase in the concentration of W. Several factors can reduce radiative recombination, but the main reason, as discussed in previous reports [130,135], is that W dopant in the form of W^{6+} forms a shallow energy level near the conduction band minima (CBM) which acts as the trapping site for electrons to improve lifetime and reduce recombination. However, the same trapping sites act as recombination centers at higher metal ions doping according to the mechanism described in [151,152].

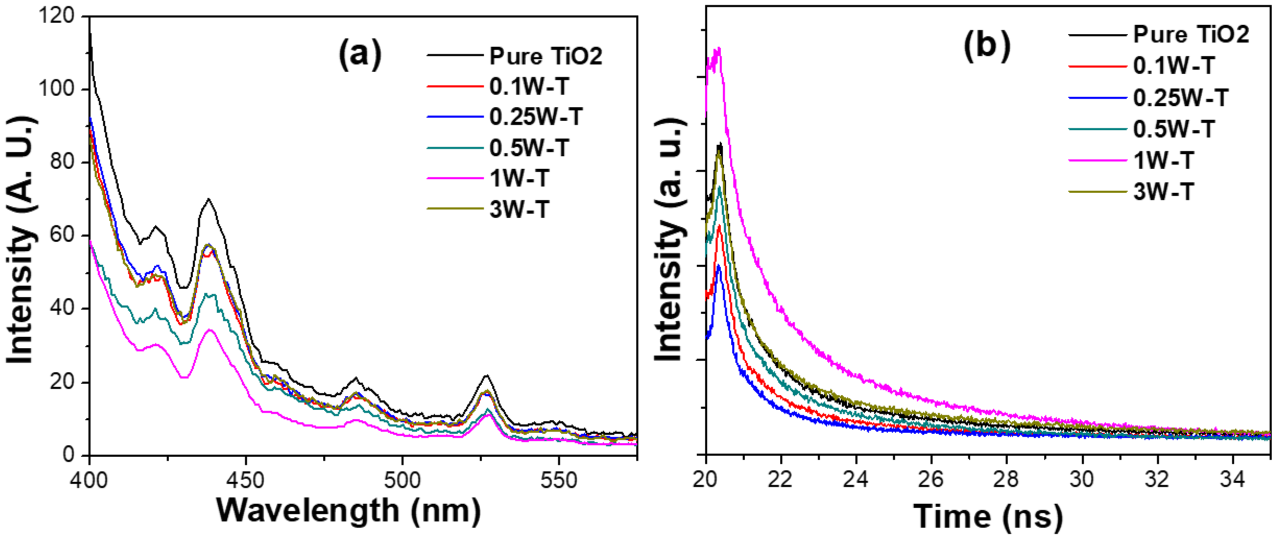

Figure 34: *(a) Photoluminescence emission spectra and (b) Time-resolved photoluminescence decay curve of pure* TiO_2 *and W-doped* TiO_2 *with different doping concentration of W.*

The photocatalytic activity of all W-doped TiO_2 photocatalyst was evaluated by conducting degradation tests of p-NP and monitoring the corresponding absorption peak as a function of time. Results are presented in **Fig. 35**. The degradation rate of W-TiO_2 for all atomic concentrations of W is noticeably increased as compared to undoped TiO_2. Among W-doped TiO2 samples, 1W-TiO_2 showed the highest photocatalytic activity by degrading 62% of p-NP as compared to 30% for pure TiO2 in 180 min. Activity increases with the increase in W concentration and reaches a maximum at 1%, while decreasing at the highest concentration of 3%. This result is in agreement with the PL and TRPL results discussed above, in which 1W-TiO_2 shows the highest lifetime of charge carriers in excited states corresponding to the lower recombination of e^- and h^+ pairs, which is mainly responsible for the increase in the photocatalytic activity in W-doped TiO_2. This is achieved by replacing Ti^{4+} ions with W^{6+} ions in the lattice to contribute holes which act as trapping sites for electrons. Therefore, photogenerated holes on TiO_2 have more time to travel to the surface to form $OH^\bullet$ radicals for degradation of organic pollutants such as p-NP. The photocatalytic degradation of p-NP was also conducted in UV light (**Fig. 36**). The activity is doubled for 1W-TiO_2 as compared to pure TiO_2 even under UV light thus showing the effectiveness of W^{6+} ions in charge separation irrespective of wavelength of light. At the same time it also demonstrates that the W-doping does not assist in absorption of visible light unlike other metal dopants.

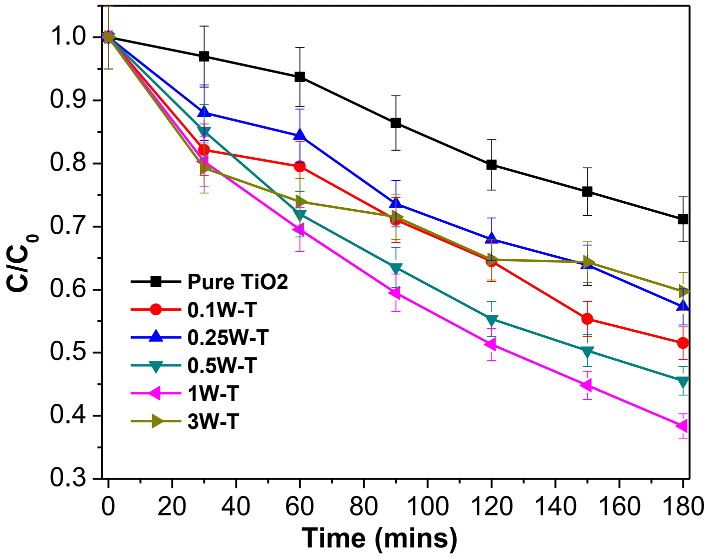

Figure 35: *Comparison of photocatalytic degradation of p-nitrophenol under light irradiation in presence of pure TiO_2 and W-doped TiO_2 powders with different dopant concentrations. Plot are in terms of the normalized intensity of the absorption band of p-NP at 320 nm in UV-vis spectra vs irradiation time (lines are drawn to guide the eye).*

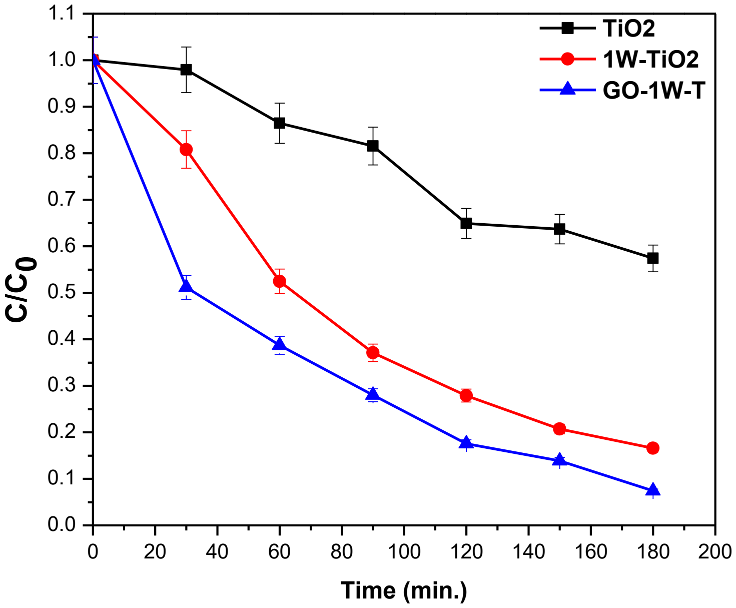

Figure 36: *Comparison of photocatalytic degradation of p-nitrophenol under UV light irradiation in presence of pure* TiO_2*, W-doped* TiO_2 *and rGO/1W-*TiO_2 *composite powders. Plot are in terms of the normalized intensity of the absorption band of p-NP at 320 nm in UV-vis spectra vs irradiation time (lines are drawn to guide the eye).*

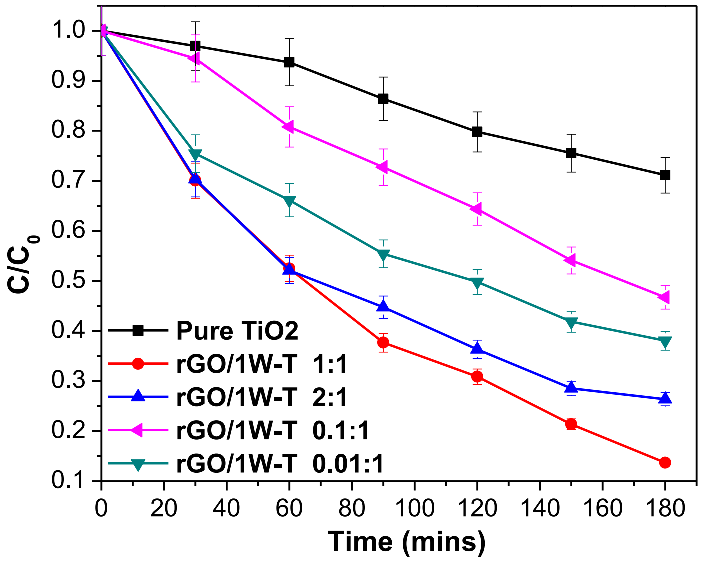

Figure 37: *Comparison of photocatalytic degradation of p-nitrophenol under light irradiation in presence of pure* TiO_2 *and rGO/1W-* TiO_2 *composite powders with different rGO and 1W-* TiO_2 *weight ratio.*

Though in W-doped TiO_2, the recombination process is slowed down by e^- trapping, the most convenient route to completely avoid the recombination of charges is by separating them spatially. Thus electrons, confined in the trapping sites, have to be transported from TiO_2. This can be realized by coupling W-TiO_2 with rGO. Hydrophilic rGO is conducting and acts as an effective electron acceptor.

The composite of rGO/TiO_2 can be fabricated in three different ways: a) by decorating TiO_2 particles with small amounts of rGO (i.e 1 wt %) on the surface. b) by taking equal amount (1:1) of TiO2 and rGO and c) by decorating rGO 2D sheets with well dispersed TiO_2 nanoparticles (1-5%). The first system is the most studied and reported in the literature, while the other two are rarely investigated. The first two composite materials can be easily experimentally reproduced, while synthesis of the last is technically very difficult because the amount of TiO_2 is not sufficient to convert all GO into rGO during the synthesis of the composite. Thus, for the present study only the first two systems were adopted with weight ratios rGO/1W-TiO_2 of 0.1 & 0.01 and 1 & 2 respectively.

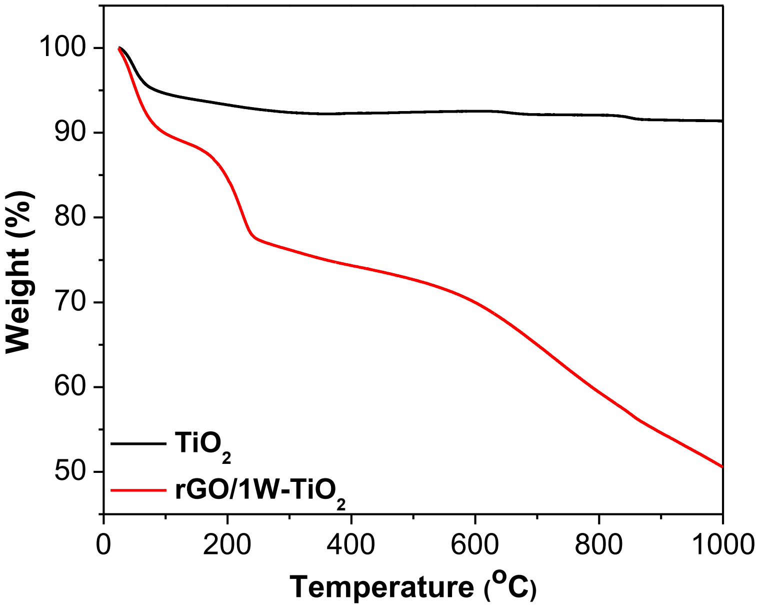

Figure 38: *TGA measurement of pure TiO_2 and rGO/1W-TiO_2 photocatalyst.*

The photocatalytic activity of all different weight ratios of rGO/1W- TiO_2 was evaluated for the degradation of p-NP and presented in **Fig. 37**. All the composites showed better activity as compared to pure TiO_2. Nevertheless, the lower weight ratios (0.1 and 0.01) showed lower activity as compared to higher weight ratios (1 and 2) in the composite. These results indicate that using an equal amount of 1W-TiO_2 and rGO, produces an ideal condition for effective interaction between rGO and TiO_2, leading to better charge transfer. On the other hand, for lower weight ratios, rGO is not enough to be effective as an electron sink, thus showing inferior degradation rate in comparison to rGO/1W-TiO_2 with higher weight ratio. Considering the above results, further analysis was focused only on rGO/ 1W-TiO_2 with weight ratio of 1:1. A composite of rGO with pure TiO2 with the same weight ratio was also synthesized to understand the roles of rGO and W in the composite. TGA measurement was performed in order to confirm the 1:1 wt ratio of rGO/1W-TiO_2 and results are reported in **Fig. 38**. In pure TiO2, there is only 5% of weight loss mainly due to evaporation of water molecule and hydroxide groups. On the other hand, for rGO/1W-TiO_2 1:1 ratio the weight loss take place in three different temperature ranges; 1) at low temperature (25-110 ºC), the water and OH group from the surface is removed, 2) In range of 150-250 ºC, the weight loss is attributed to decomposition of epoxy, hydroxyl and oxygen containing functional groups attached to graphene oxide layers, and 3) from 250 to 1000 ºC the weight loss is assigned to burning and decomposition of Carbon skeleton. The total weight loss in rGO/ 1W-TiO_2 is around 50% which confirms the 1:1 wt ratio.

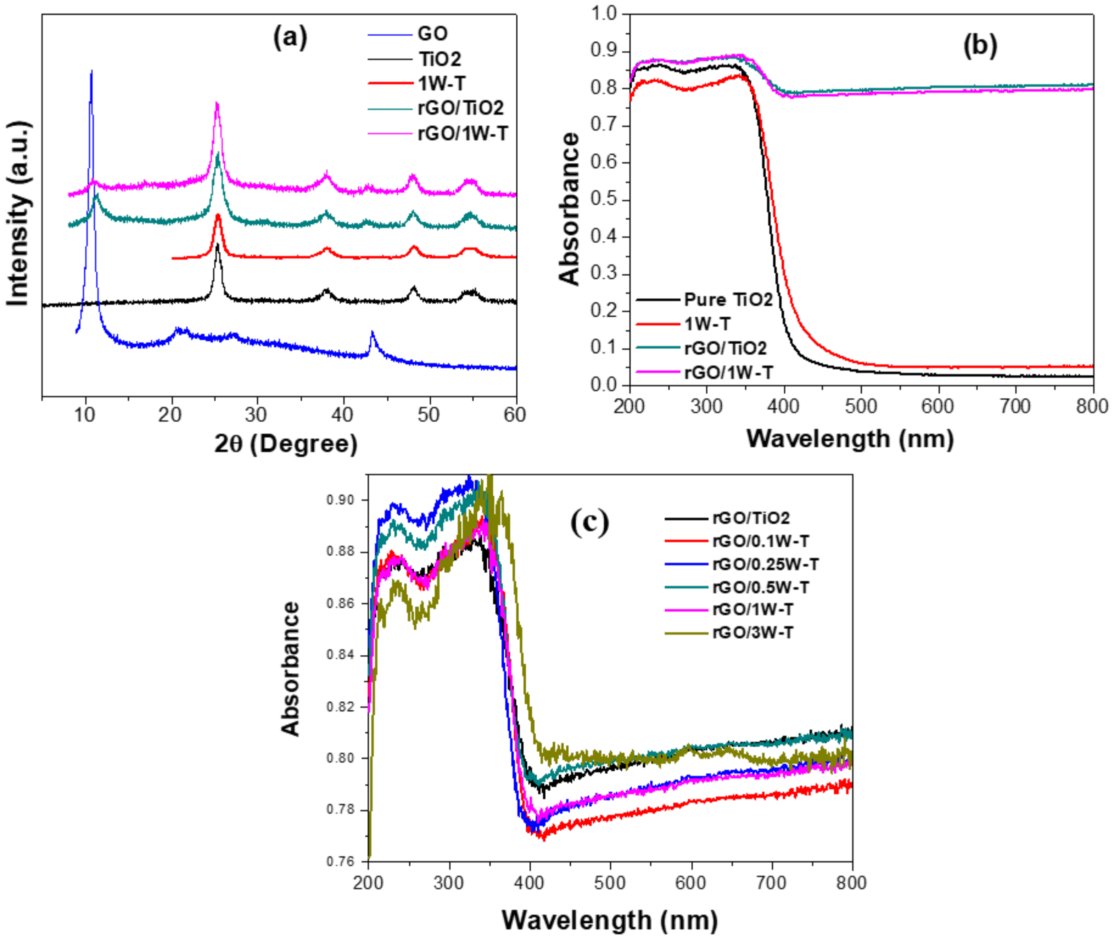

Figure 39: *(a) XRD patterns, (b) UV-vis absorption spectra (taken in diffuse reflectance mode) of pure TiO_2, GO, W-doped TiO_2, rGO/TiO_2 and rGO/1W-TiO_2 composite powders and (c) UV-vis absorption spectra of rGO/TiO_2 along with different concentrations of W doped TiO_2/rGO composites.*

Fig. 39a shows the XRD patterns of TiO_2, 1W-TiO_2, GO, rGO/TiO_2 and rGO/1W-TiO_2. Characteristic peaks of anatase TiO2 at 25.3º, 37.7º, 48.1º, 53.8º and 55.1º corresponding to (101), (004), (200), (105) and (211) planes are observed for all the TiO_2 based samples. The as-prepared GO shows a diffraction peak at 10º confirming the formation of the graphene oxide. The intensity of this main peak of GO becomes very weak after the reduction of GO with 1W-TiO_2 under UV irradiation. This implies that significant amount of GO (above 95%) is reduced to rGO during the composite synthesis. No peak due to rGO is observed in XRD patterns due to the prominent peak of anatase TiO_2 which lies in the same region of 2θ angle. The optical absorption of rGO/TiO_2 composites was studied and compared with TiO_2 (**Fig. 39b**). It is observed that the absorption edge of TiO_2 is at 400 nm, whereas, the absorption edge for rGO/TiO_2 and rGO/1W-TiO_2 is evidently shifted in the visible region. Thus, the composite is able to harvest light in the visible region. **Fig. 39c** shows the absorption spectra for rGO/W-TiO_2 composites with different W concentrations. All the composites show nearly the same absorption profile with the maximum absorption edge in the case of rGO/3W-TiO_2 composite.

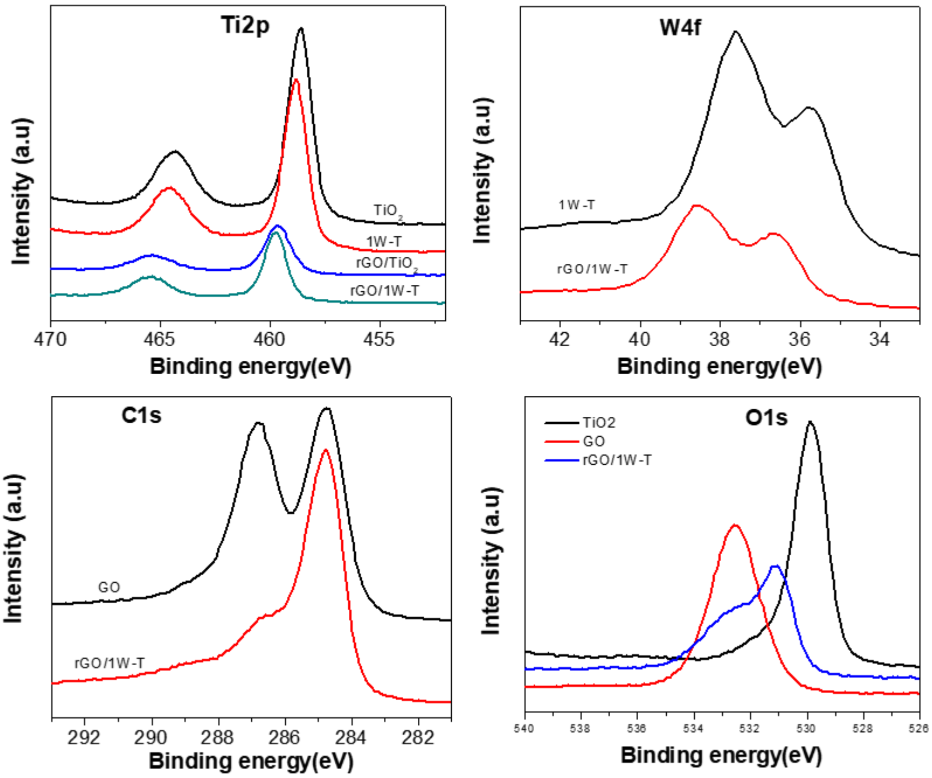

Figure 40: *XPS spectra of Ti2p, O1s, C1s and W4f levels of pure TiO_2, GO, W-doped TiO_2, rGO/TiO_2 and rGO/1W-TiO_2 composite powders.*

In order to study the interaction between GO and TiO2, the surface states were analyzed by XPS for all five powder samples (**Fig. 40**). In Ti2p core level, two peaks at 458.8 eV and 464.5 eV assigned to Ti2p3/2 and Ti2p1/2 of Ti^{4+} states are clearly visible for pure TiO_2 and 1W-TiO_2. However, introducing GO with both these TiO_2 leads to a positive shift in Binding Energy (B.E.) by 0.9 eV to 459.7 eV in 2p3/2 state. This prominent shift to higher B.E. clearly suggests that a large number of electrons transfer from TiO_2 to rGO causes a strong interaction between them by forming bonds. The decrease in the intensity of Ti2p core level is due to the coverage of rGO over TiO_2 on the surface. The C1s level of GO is deconvoluted into three peaks with two major peaks at 284.8 eV and 286.8 eV corresponding to C-C bond in sp2 carbon and C-O-C bond in hydroxyl or epoxy groups. The small peak at 288.2 eV is due to the C=O bond in GO. In composites with TiO_2, the significant decrease in the two peaks of C-O and C=O indicates the removal of oxygen containing group from GO to form rGO, which is strongly bonded to TiO_2. In pure TiO_2 and 1W- TiO_2, a broad peak in O1s level is deconvoluted into two peaks at 530.1 eV (80%) and 531.0 eV (20%) attributed to oxygen connected to Ti^{4+} in TiO_2 and hydroxyl group attached to the surface. Oxygen is present only in the form of hydroxyl and epoxy groups on the surface of GO with a peak at 532.5 eV. This peak at 532.5 eV reduces to large extent for the composite samples (rGO/TiO2 and rGO/1W-TiO2), thus confirming the decrease of oxygen containing group in the composite due to the formation of rGO. Importantly, the peak related to O in TiO_2 at 531.0 eV shows a positive shift of 1 eV similar to Ti2p level of composite. This again confirms the existence of a strong interaction between TiO_2 and rGO occurring due to the bonding created by the electron transfer. W in the case of 1W- TiO_2, is in oxidized state (W^{6+}) having peaks at 35.7 eV and 37.6 eV for $W4f_{7/2}$ and $W4f_{5/2}$, respectively. However, both these peaks shift to higher B.E. at 36.6 and 38.5 eV for the composite which is attributed to the change in chemical environment on the surface of TiO2 caused by a large number of electrons transferred from TiO_2 to rGO. The amount of W was measured around 0.9 ± 0.1 at.% on the surface which is consistent with the doping concentration (1 at.%) used during synthesis. The presence of rGO is determined by Raman spectroscopy by investigating sp2 and sp3 hybridized carbon atoms. The Raman spectra of all the four samples are displayed in **Fig. 41a**. Pure TiO_2 showed vibrational peaks at 145, 396, 515 and 640 cm_1 corresponding to E_g, B_{1g}, A_{1g} and B_{2g} modes of vibration of anatase TiO_2 respectively. However, these peaks are shifted to lower wavenumber by around 5-10 cm^{-1}. This red shift is mainly due to the phonon confinement effect caused by the change in the crystal size. In GO/TiO_2 composites, surface strain is developed due to the strong interaction between TiO_2 and GO which affects the crystal size of TiO_2 to create the red shift [153]. This is in line with the XPS result indicating firm bonding between TiO2 and GO. In as-synthesized GO, two main peaks are visible at 1365 and 1594 cm^{-1} attributed to D and G bands related to amorphous disordered structure of sp2 carbon and to the in plane stretching motion of symmetric sp2 C-C bonds (inset of **Fig. 41a**). These D and G bands are centered at 1345 and 1583 cm^{-1} for GO/TiO_2, respectively, with the red shift suggesting the reduction of GO and rGO in the presence of TiO2 (inset of **Fig. 41a**) [154]. The intensity ratio of I_D/I_G also provides information about the GO to rGO conversion. The intensity ratio decreases in the case of rGO/ 1W-TiO_2 as compared to pure GO thus confirming the formation of composites with strong bonding between Ti and C via Ti-O-C bonds on the surface. Other groups [154–156] also displayed similar low values of I_D/I_G for TiO_2/rGO composites and attributed them to the strong interaction between TiO_2 and GO. In order to confirm the decrease in I_D/I_G ratio, reduced graphene oxide was synthesized (inset of **Fig. 41a**). The intensity ratio matches very well with that for rGO/TiO_2 composite thus confirming the GO to rGO conversion.

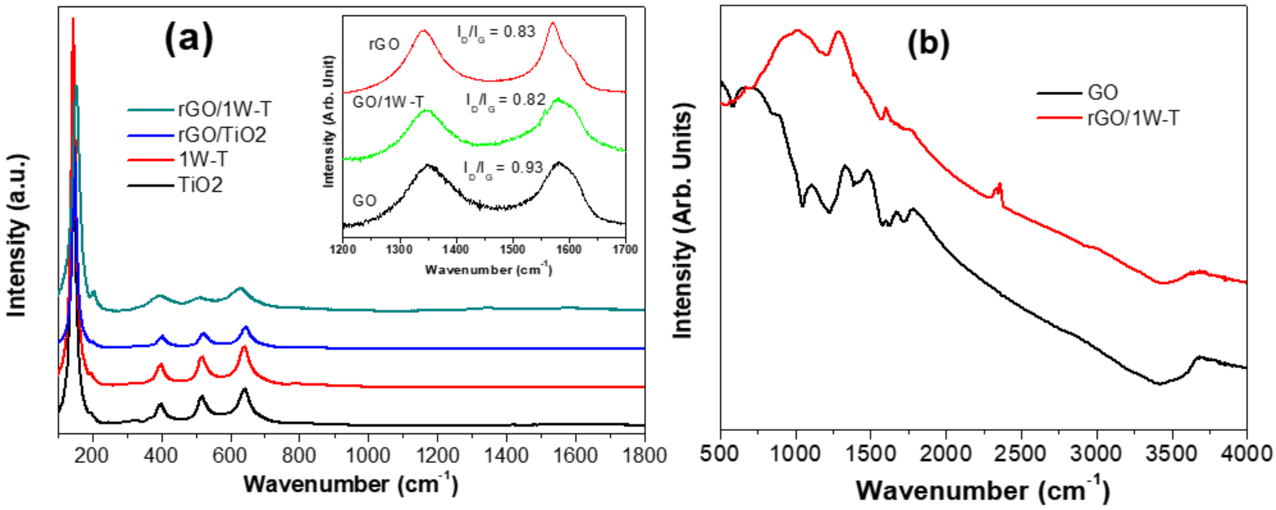

Figure 41: *(a) Raman spectra of pure TiO_2, W-doped TiO_2, rGO/TiO_2 and rGO/1W-TiO_2 composite powders. (b) FTIR spectra of GO and rGO/1W-TiO_2 composite powders. Inset of (a) shows the D and G band of GO, rGO, and rGO/1W-TiO_2 composite powders.*

The FTIR spectra of GO and rGO/1W-TiO_2 is shown in **Fig. 41b**. A broad peak at 3000-3500 cm^{-1} corresponds to the stretching of eOH and/or physically adsorbed H2O. A decrease in the intensity in the case of rGO/1W-TiO_2 was observed and implying a reduction in the water content. The bands at 1714 cm^{-1}, 1625 cm^{-1}, 1220 cm^{-1} and 1040 cm^{-1} are attributed to C=O stretching of COOH groups, C-C, C-O-C and C-O stretching modes respectively [135]. The peak at 1579 cm^{-1} is caused by the skeletal vibration of GO [153]. For GO/1W-TiO_2, these peaks due to oxygen containing functional groups either disappeared completely or the intensity is significantly decreased implying the reduction of GO to rGO.

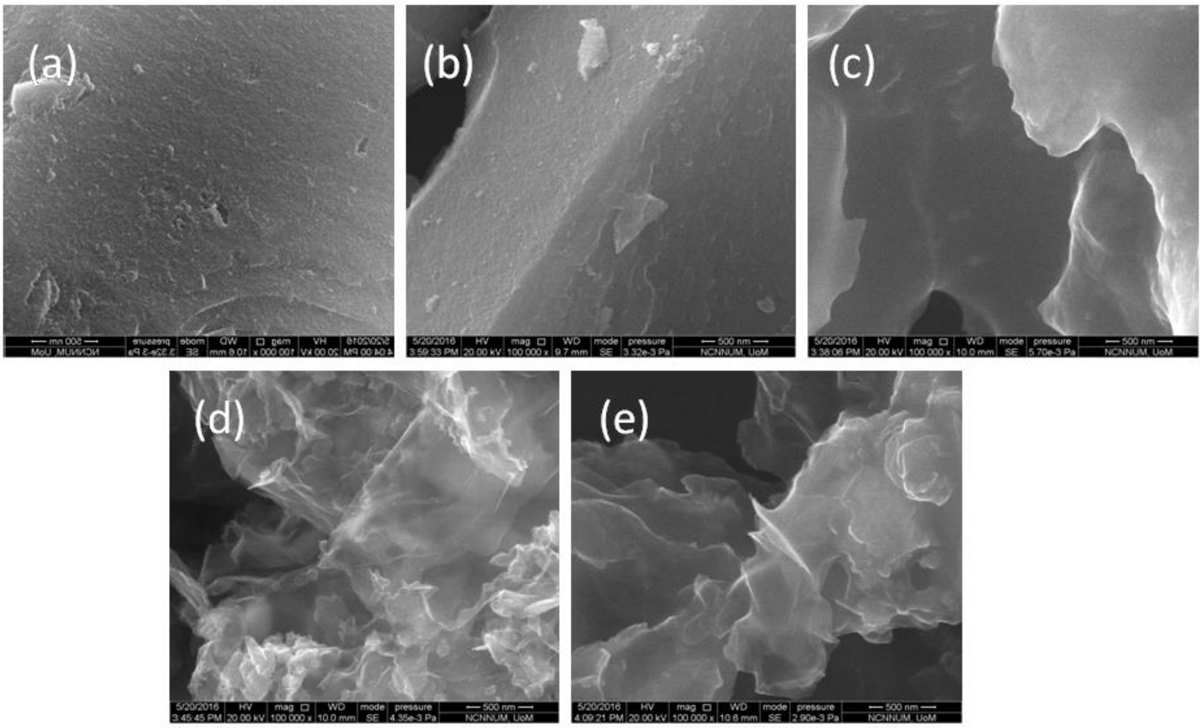

Figure 42: *SEM Images of (a) pure TiO_2, (b) W-doped TiO_2, (c) GO, (d) rGO/TiO_2 and (e) rGO/1W-TiO_2 composite powders.*

Morphological analysis was performed using SEM (**Fig. 42**) and TEM (**Fig. 43**). 1W-TiO_2 showed big crystal like structure (**Fig. 42**) composed of small nanoparticles (NPs). As prepared GO displayed sheet like morphology (**Fig. 42**) which is maintained even after bonding TiO_2 on it. TEM images displayed TiO_2 NPs in the range of 5-10 nm for 1W-TiO_2 (**Fig. 43a**) with an average size of ~8 nm. This value is in good agreement with that obtained from XRD. Nevertheless, these NPs are agglomerated to form big crystals. On the other hand, for rGO/ TiO_2 and rGO/1W-TiO_2, the TiO_2 NPs are well dispersed and are found loaded only on rGO (**Fig. 43b**). No loose NPs was observed in the presence of rGO, thus confirming a good interaction between rGO and TiO_2 as indicated by XPS, Raman and FTIR results. No variation in the size of TiO_2 NPs was seen thus confirming formation of nanocomposite. In HRTEM images (**Fig. 43b and e**), interplanar spacing of 0.35 nm was recorded for NPs assigned to (101) plane of TiO_2 for both pure and composite TiO_2. The rGO/1W-TiO_2 coupling can be clearly seen from the bright field TEM image (**Fig. 43d**) with 1W-TiO_2 nanoparticles embedded in a background of rGO sheets. SAED patterns in **Fig. 43c** illustrates all the distinct diffraction rings corresponding to TiO_2 anatase phase. For 1W-TiO_2, the same diffraction rings are also observed for GO/1W-TiO_2 composite but in diffused form due to the GO wrapped with TiO_2 (**Fig. 43f**). BET surface area is recorded and summarized in **Table 2**. No major variation in the surface area was observed after the formation of GO/TiO_2 composite.

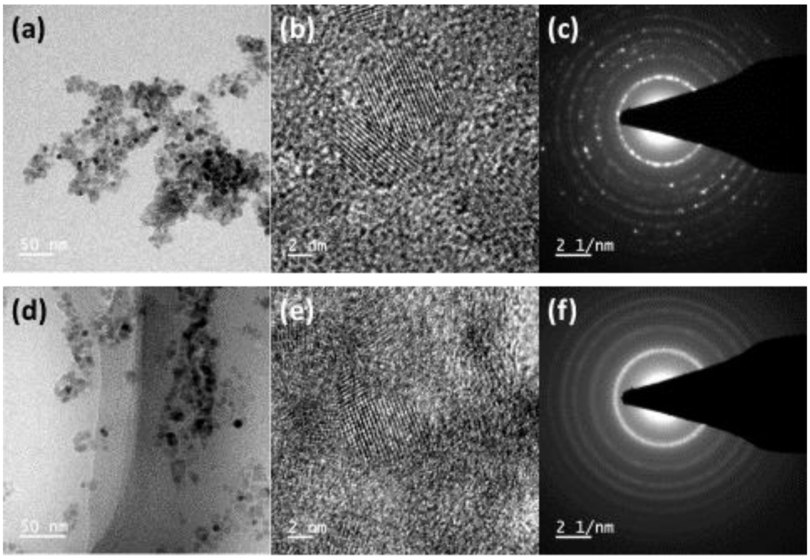

Figure 43: *Bright field TEM image (a) & (d), High resolution TEM image (b) & (e), and SAED pattern (c) & (f) of 1W-TiO_2 and rGO/1W-TiO_2 composite powders respectively.*

Sample name	Surface area (m^2/gm)
TiO_2	80.7 ± 0.2
1W-TiO_2	89.7 ± 0.3
rGO/TiO_2	82.0 ± 0.2
rGO/1W-TiO_2	91.3 ± 0.3

Table 2: *BET surface area of pure TiO_2, W-doped TiO_2, rGO/TiO_2 and rGO/1W-TiO_2 composite powders.*

The recombination of e^- and h^+ pairs plays an important role in controlling the efficiency of the photocatalyst. **Fig. 44a** shows the PL spectra of GO/TiO_2 and rGO/1W-TiO_2 in comparison with pure TiO_2 and 1W-TiO_2. The emission intensity of pure TiO_2 is highest among all the other photocatalysts, indicating the highest efficiency in recombination of electron and hole pairs. The emission intensity dropped drastically in the case of composite material. The photocatalyst rGO/1W-TiO_2 shows lowest emission intensity as compared to all other photocatalysts due to an effective separation of electron and hole pairs. This clearly shows that the electrons, when excited from valence band to the conduction band of W-TiO_2, are immediately transferred to rGO, resulting in the enhanced charge separation.

Time Resolved PL decay spectra (**Fig. 44b**) were monitored to quantify the relevant quenching time scales by exciting TiO_2 and rGO/TiO_2 composite with a 405 nm pulsed diode laser near the band gap energy. The decay curves were fitted by two-exponential decay functions comprising two time components, $\tau1$ and $\tau2$. Fast decay component, $\tau2$, is due to the near band edge relaxation of TiO_2 by free e^- and h^+, while the slow decay component, $\tau1$, arises from the recombination of self-trapped excitons. After the electron- hole pair formation and subsequent charge carrier separation, in competition with recombination, some of the electrons and holes are trapped at various defect sites in lattice or surface (such as oxygen vacancies, surface hydroxyl group and other defects) which form shallow and deep levels within the band gap. These trap charges quenched to the luminescent sites through trap to trap hopping and finally producing the visible luminescence thus contributing to the slow decay component of the PL curve. The values of $\tau1$ and $\tau2$ along with their corresponding fraction f1 and f2 to the total decay, for pure TiO_2, 1W-TiO_2, rGO/TiO_2 and rGO/1W-TiO_2 are reported in **Table 3**. Although the fraction of both the components are similar (~50%), by inclusion of 1W in TiO_2, the decay time of both the components increases as compared to that of TiO_2, and finally results in a higher effective average lifetime. W^{6+} states formed just below the CB are mainly responsible for trapping e^- thus reducing and delaying the recombination process as indicated by PL spectra. On the contrary, by forming a composite with rGO/TiO_2, no change in fast component was observed but the slow component $\tau1$ decreases to 4.16 ns from 5.03 ns (pure TiO_2). Most importantly, the fraction of the total decay corresponding to the slow component reduces significantly from 46% to 18% which lowers the average effective lifetime of the composite with respect to TiO_2. Thus, the faster component related to recombination of free electron and hole dominates the decay curve. This result shows that the electrons before being trapped by the defect sites are transferred to rGO through the channel formed by the interaction between TiO_2 and rGO. A similar decrease in the lifetime value was observed in perovskite/TiO_2 composites due to fast charge extraction from perovskite into TiO2 [157]. For a TiO_2/copolymer and TiO_2/Ag_3PO_4 composites, the same behavior was observed and in both the cases the efficient charge separation was responsible for such a result [158,159]. In the case of rGO/1W-TiO$_2$, the τ1 and τ2 increase in comparison to rGO/TiO$_2$ though both the amounts are identical. As indicated above for 1W-TiO$_2$, the presence of W^{6+} states trap the electrons after the generation prolonging the lifetime for both interband and intraband transitions of exciton. The effective lifetime value recorded for rGO/1W-TiO$_2$ is lower than that of pure TiO$_2$ and 1W-TiO$_2$ suggesting efficient charge transfer from TiO$_2$ to rGO via bonding channels created at the interface.

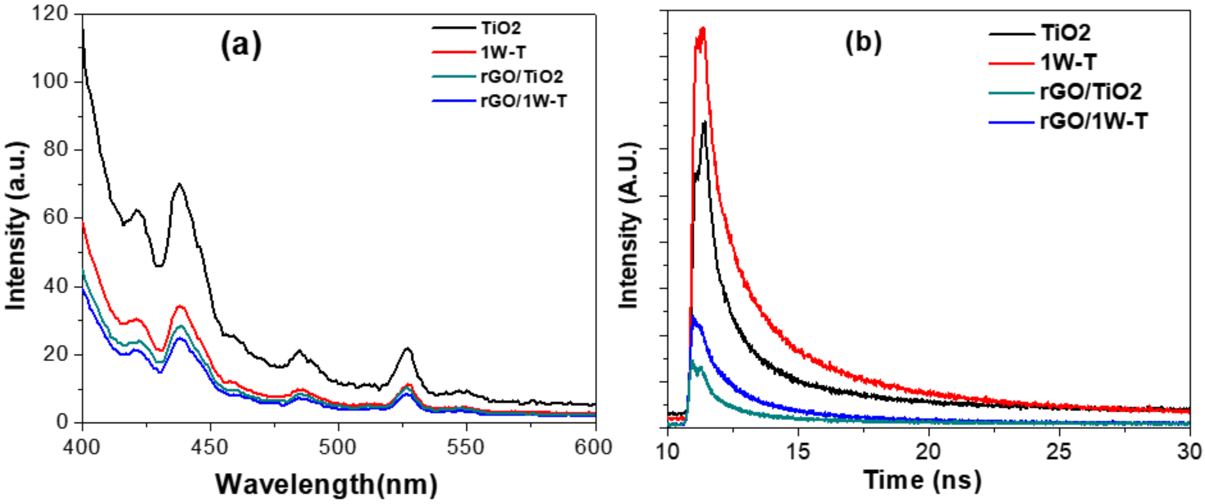

Figure 44: *(a) Photoluminescence emission spectra and (b) Time-resolved photoluminescence decay curve of pure TiO$_2$, W-doped TiO$_2$, rGO/TiO$_2$ and rGO/1W-TiO$_2$ composite powders.*

samples	τ1 (ns)	τ2 (ns)	f1	f2	Average lifetime τ(ns)
TiO2	5.03	0.65	0.46	0.54	2.49
1W-TiO2	6.07	0.73	0.52	0.48	3.33
GO-TiO2	4.16	0.63	0.18	0.82	1.00
GO-1W-TiO2	4.44	1.01	0.19	0.81	1.68

Table 3: *Average Lifetime values along with fitting parameters (τ_1 and τ_2 with their corresponding fraction f1 and f2) of the total decay, for pure TiO$_2$, 1W-TiO$_2$, rGO/TiO$_2$ and rGO/1W-TiO$_2$*

The photocatalytic activity (**Fig. 45**) of rGO/TiO$_2$ nanocomposite is compared with TiO$_2$ and 1W-TiO$_2$. The highest activity is observed for rGO/1W-TiO$_2$ in degrading (87%) p-NP in 3 h While TiO$_2$, rGO/TiO$_2$ and 1W-TiO$_2$ show 29%, 42% and 62%, respectively, in the same period. The photocatalytic activity depends mainly on the surface area, visible light absorption and charge recombination. There is not much difference in the surface area among all the samples, thus it is not the parameter to consider for explaining the differences among samples. Therefore, the observed enhancement in photocatalytic activity in p-NP degradation is due to the red shift of the absorption edge after coupling W-TiO_2 with GO and, most importantly, to the enhanced separation of photogenerated charge carriers by inhibiting the recombination in rGO/1W-TiO_2 samples.

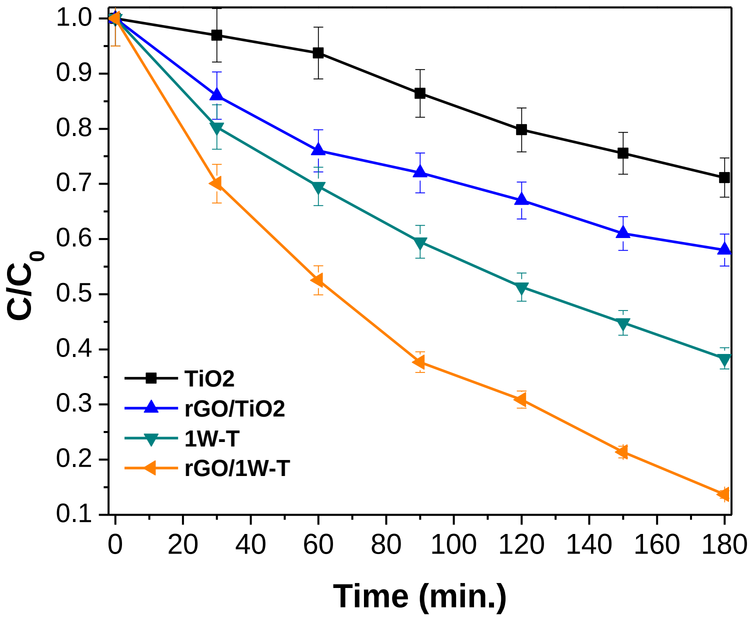

Figure 45: *Comparison of photocatalytic degradation of p-nitrophenol under light irradiation in presence of pure TiO2, W-doped TiO2, rGO/TiO2 and rGO/1W-TiO2 composite powders.*

Upon irradiation of the composite, large numbers of electrons are excited in the conduction band of TiO_2 to form excitons. Most excitons have very short lifetime and thus recombine by direct transition along the band gap, while a small amount of electron and holes travels towards the surface for the photocatalysis reaction. However, during the journey these photogenerated charges are trapped by defects in the bulk or on the surface, where they recombine with little delay as compared to interband recombination. Thus only negligible amounts of electrons-holes are available for the reaction and represent the rate limiting step for the photocatalytic process. This shows that avoiding recombination, via both interband process and defect traps, is necessary. In the 1W- TiO_2/GO composite, W^{6+} acts as the trapping site for electrons and reduce the interband recombination of excitons. On the other hand, the interaction between TiO_2 and GO creates a channel for fast transfer of excited electrons towards the latter before being recombined at the defect traps. The work function of rGO (-4.4eV), lower than the CB of TiO_2 (-4.2eV), also allows injection of electrons from TiO_2 to rGO. So the present system assists not only in trapping but also spatially separating the electrons from TiO_2 to avoid recombination. Enhanced absorption in the visible region and effective charge separation are thus mainly responsible for higher photocatalytic activity. In addition, rGO also plays a role in creating a better dispersion of TiO_2 NPs on the surface. Further, in order to distinguish the effect of visible light absorption and charge separation, different composites of GO and W doped TiO_2 were synthesized by varying the concentration of W (0.1, 0.25, 0.5, 1, and 3 at.%). No major variation in crystal structure or visible light absorption was observed as indicated by XRD pattern and UV-vis spectra of rGO/W-TiO_2 composites. Nevertheless, the intensity of peaks in PL spectra (**Fig. 46a**) diminishes for all the concentrations of W with minimum intensity recorded for rGO/1W-TiO_2 composite. The trend obtained in the composite is exactly similar to that for W-doped TiO_2. In TRPL (**Fig. 46b**), the maximum effective lifetime (1.68 ns) is obtained for rGO/1W-TiO_2 composite. Most importantly, all the composite samples with varying W concentration showed significant decrease in the fraction of slow component due to immediate charge transfer to rGO via a channel created by the interaction. In the case of rGO/1W-TiO_2 composite, the $\tau 1$ is comparable to the values recorded for other concentration of W, but $\tau 2$ increases considerably due to the trapping of electron at W^{6+} resulting in the highest overall lifetime among the W doped rGO/TiO_2 composite.

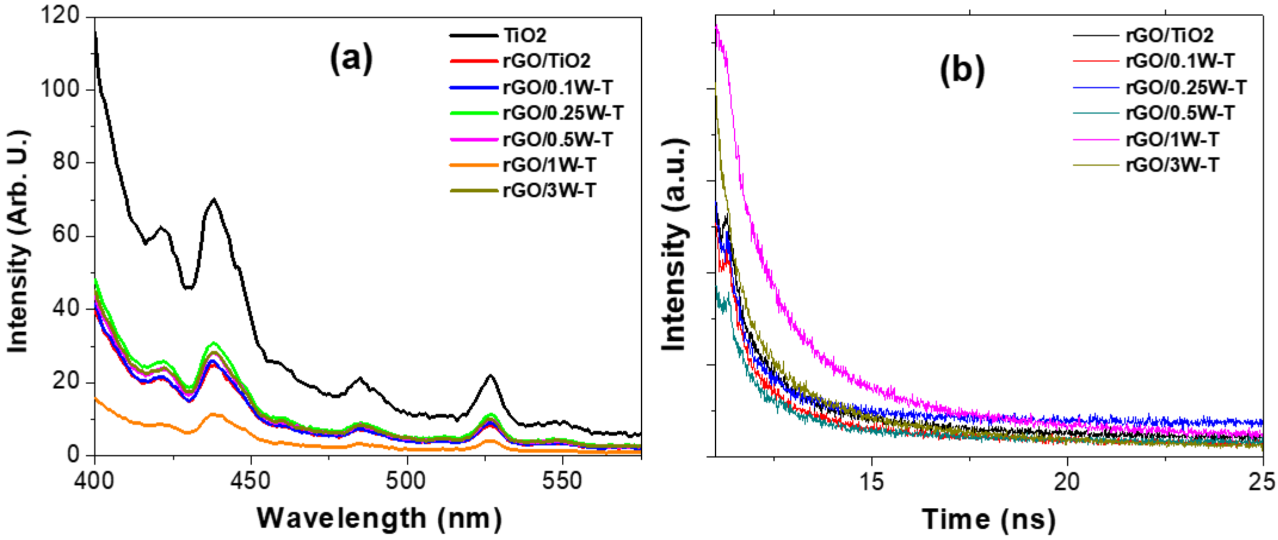

Figure 46: *(a) Photoluminescence emission spectra and (b) Time-resolved photoluminescence decay curve of rGO/W-doped TiO_2 composite powders with different doping concentration of W.*

The photocatalytic activity for the degradation of p-NP for W doped rGO/TiO_2 composite is reported in **Fig. 47**. Among all the composites, rGO/1W-TiO_2 shows the highest photocatalytic activity. rGO/1W-TiO_2 composite showed higher activity than pure TiO_2 mainly due to the fast transfer of excited electrons from TiO_2 to GO. On the other hand, W introduced in the composite is able to act as a trapping site for electron to delay the band gap recombination. Thus implementation of both these features in rGO/1W-TiO_2 creates a synergic effect to efficiently separate the charges and favor transport to the surface for improved photocatalytic activity.

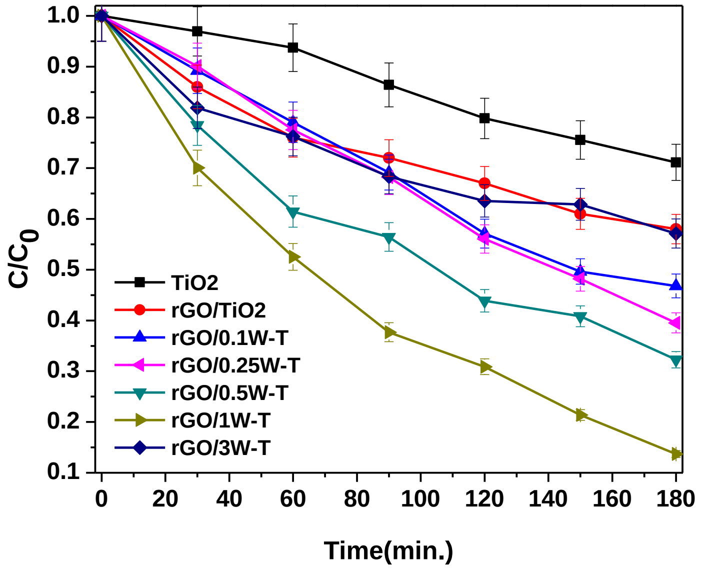

Figure 47: *Comparison of photocatalytic degradation of p-nitrophenol under light irradiation in presence of pure* TiO_2*, rGO/*TiO_2*, and rGO/W-doped* TiO_2 *composite powders with different doping concentration of W.*

4.4 Conclusions

Nano-composite materials made of W-doped TiO_2 and rGO graphene have been synthesized to increase the efficiency of the bare TiO_2 photocatalyst. Several values of W at% concentrations have been used but the best results have been obtained with 1 at.% W doping and weight ratios rGO/1W-TiO_2 of 1:1. UV-Vis, XPS, PL and time resolved PL spectra establish that W^{6+} in TiO_2 lattice creates impurity level just below the minimum of conduction band of TiO_2 to give the band gap of W doped TiO_2 of 3.09 eV, only marginally lower than that of pure TiO_2. W-doping of TiO_2 and electrons transport through channels created by the TiO_2-rGO chemical bonds contribute in a synergetic way to enhance the photocatalytic efficiency of the composite materials. In particular, the photoexcited electrons are trapped by the introduced impurity levels, thus reducing interband recombination, while the new formed bonds with rGO create a channel for fast transfer of excited electrons towards rGO thus avoiding charges recombination on the surface defect sites. The increased photocatalytic activity is demonstrated in photo-degradation tests of p-nitrophenol. The efficiency of 1 at.% W- TiO_2 /rGO results to be 87% as compared to rGO/ TiO_2 (42%), 1W- TiO_2 (62%), and pure TiO_2 (29%).

Chapter 5: Effect of Graphene oxide loading on TiO_2: Morphological, optical, interfacial charge dynamics

Preview: TiO_2 is a well-known photocatalyst studied extensively for photocatalytic degradation of organic pollutants for water treatment. However, high bulk and surface recombination of photo-excited charges is a major drawback it faces. rGO on the other hand, has gained interest as a supporting material for TiO_2 due to its high surface area, superior electron mobility and tunable bandgap. rGO-TiO_2 composites with different GO loading from low to high GO concentration range were synthesized using photoreduction method. The developed composites were tested for photocatalytic degradation of para-Nitrophenol and demonstrated good photocatalytic activity. Among all, the weight ratio, rGOT-3 showed the best performance. Experimental measurements were conducted in order to study and analyse the synthesized composites.

My contribution to this work includes the synthesis of Graphene Oxide (GO) and rGO/TiO_2 composites with different concentrations, performing photocatalytic measurements for the samples along with analysis and plotting of data obtained.

The content of this chapter is adopted from;
A. Yadav, M. Yadav, S. Gupta, Y. Popat, A. Gangan, B. Chakraborty, L.M. Ramaniah, R. Fernandes, A. Miotello, M.R. Press and N. Patel, Carbon 143 (2019), 51-62.
https://doi.org/10.1016/j.carbon.2018.10.090

5.1 Introduction

TiO_2 is one of the most exhaustively studied material as it is a potential candidate for various applications such as photocatalytic degradation of organic pollutants for water treatment, H_2 production by photocatalytic bacteria deactivation, water-splitting, gas sensors, photovoltaics and Li ion batteries [160–164]. TiO_2 gained interest in these applications owing to its low-cost, non-toxic nature, suitable band edge positions, earth-abundance and long-term photo- and chemical stability in all pH media. For photocatalytic application, the efficiency of

TiO_2 is limited due to its wide bandgap, which restricts light absorption within UV range (5% of solar spectrum), and high bulk and surface recombination rates of the produced electron hole pairs. Former limitation can be circumvented by reducing the electronic bandgap of TiO_2 through metal [165] or non-metal doping [166,167], which improves its absorbance in visible spectrum. The latter issue of bulk recombination can be suppressed using high valence dopants (such as W^{6+}) that lead to formation of an impurity level just below the conduction band of TiO_2 and acts as a trap site for electron carriers, thereby improving charge carrier lifetime [168]. On the other hand, formation of heterojunction of TiO_2 with other semiconductors (C_3N_4, WO_3 etc) [169,170], carbonaceous materials (carbon nanotubes, fullerene, graphene, reduced graphene oxide (rGO) and graphene oxide (GO)) and metal nanoparticles has proven to be very effective in decreasing the surface recombination rate [171–173].

Recently, rGO has gained great interest in photocatalytic water-treatment, as a supporting material for TiO_2, owing to its high surface area, superior electron mobility, tuneable bandgap and easily changeable surface properties [174]. It was found that combining rGO with TiO_2 leads to improvement in photo-induced charge separation by transfer of excited electrons to rGO through interface. During the synthesis of composite, the amount of rGO loading and proper coupling at the interface in rGO-TiO_2 composite plays a key role in deciding the photocatalytic performance of the resulting composite. Generally, past literature on rGO-TiO_2 composites are divided into two categories where (1) TiO_2 particle is decorated by a small amount of rGO and (2) TiO_2 particles are well dispersed over 2D rGO sheet. To realize the former strategy, weight ratio between 0.1-5 wt % of rGO were used while for latter case, nearly equal amount of rGO were used. Optimum concentration of rGO is determined in both cases of rGO-TiO_2 composites. Depending upon the size of TiO_2 nanoparticles and the method adopted for synthesis of the composite, the optimum concentration of rGO that shows superior photocatalytic performance also varies. Lower amount of rGO acts as an electron sink over TiO_2 particles to reduce recombination process. In this case, though light is not shielded by rGO, the interaction area between TiO_2 and rGO is at minimum level. Iqbal et al. [175] fabricated rGO-TiO_2 composite using solvothermal method with GO to TiO_2 mass ratios of 0, 2.5, 5 and 10 wt% and found the mass ratio of 5 wt % as optimum ratio for the photodegradation of Rhodamine B dye and phenol due to efficient charge transportation and separation at the interface with enhanced visible light absorption. Liu et al. [176] also reported rGO-TiO_2 composite and observed that superior photodegradation performance is achieved when amount of rGO in the composite is 2 wt% compared to pure TiO_2 and 1 and 5 wt% rGO-TiO_2 composites. Similar study by Yu et al. [177] also demonstrated that when GO amount was controlled to 1wt % in rGO-TiO_2 composite, it has shown highest photocatalytic performance for degradation of methylene blue. Several other reports have also shown that when rGO is combined with TiO_2 to obtain composite with rGO weight ratio in the range of 0.1-10 wt%, then significant improvement towards photocatalytic activity under UV illumination can be achieved [174,178,179]. Using equal amount of rGO and TiO_2 provides better scenario for strong interaction between TiO_2 and rGO in form of Ti-O-C bonds at interface. These bonds not only provides channel for fast transfer of electrons but also create energy levels within the band gap of TiO_2 to improve the visible light absorption. Although better dispersion of TiO_2 is obtained here, provided by higher surface area of rGO, however a portion, also relevant, of light reaching the TiO_2 particle is blocked by surface covering of rGO. Even the surface exposure of TiO_2 to reactant and product of the catalytic reaction is also reduced drastically. Gao et al. [180] reported that GO to TiO_2 weight ratio of 3:2 has the highest degradation rate towards methylene orange under UV irradiation as compared to pure TiO_2 and other weight ratios (0:1 and 0.1:1). Similarly, a microwave-assisted combustion method was developed to synthesize GO-TiO_2 composite with GO to TiO_2 weight ratios between 0.25-2.0 [181]. The weight ratio of 1.5 was found to be the best for degradation of methylene orange dye and beyond this value, absorption and scattering of light takes place by rGO which leads to significant reduction in photocatalytic activity. To avoid the agglomeration, Lee et al. [182] reported that hydrothermally synthesized graphene wrapped TiO_2 composite, using GO and amorphous TiO_2 nanoparticles results in formation of Ti-C bond, which helps in efficient photo-charge transfer from TiO_2 to graphene to enhance the photocatalytic performance. It was noted that graphene wrapping also results in less exposed TiO_2 active sites for photo-oxidation of pollutants and thus reducing the photocatalytic performance. Recently, Williams et al. demonstrated a facile and chemical free reduction process of GO via UV-assisted photoreduction method in presence of TiO_2 nanoparticles which also results in formation of rGO-TiO_2 composite [183]. This provides a simple method to synthesize uniformly dispersed TiO_2 nanoparticles decorated over rGO sheets by just varying the weight ratio of GO to TiO_2. Though extensive research has been carried out in past for both strategies, it is still unclear which range of rGO is best suited for photocatalytic activity. Also, none of them explains the effect of variation of GO loading on the morphological properties, charge dynamics and degree of functionalization of the resulting composite, which was taken up in this work.

Thus, in the present work, rGO-TiO_2 composite is studied in a holistic manner by synthesizing different weight ratio of both the ranges namely 0.001:1, 0.01:1, 0.1:1, 1:1, 3:1 and 10:1. For an intimate interaction between TiO_2 and rGO, photo-reduction technique was used for synthesizing the composite. Effect of weight ratio on the properties of the composite samples were explored using various characterization techniques. The developed composites were tested for photocatalytic degradation of para-Nitrophenol under Xenon and UV irradiations. The reasons for the higher photocatalytic performance of rGO-TiO_2 composites were investigated and explained.

5.2 Experimental Methods

5.2.1 Synthesis of TiO_2, GO and rGO-TiO_2 nanocomposite

TiO_2 nanoparticles were synthesized by sol-gel method using Titanium (IV) n-butoxide ($Ti(OC_4H_9)_4$) as a precursor. In a typical procedure, a mixture of $Ti(OC_4H_9)_4$ with ethanol was prepared to obtain TiO_2 sol. To this precursor sol, a mixture of ethanol, double distilled water (DDW) and HNO_3 was added slowly and stirred for 2 hours for homogeneous mixing. The ratio of titanium butoxide/DDW/ethanol/HNO_3 was maintained at 1/30/20/0.1. After stirring, the solution was kept overnight for gelation, at room temperature. The resulting gel was thoroughly washed with DDW and ethanol followed by drying for 3 hours at 120 ^{0}C in open atmosphere. A pale white TiO_2 powder was obtained which was grinded and calcined at 400 ^{0}C for 2 hours to obtain crystalline TiO_2 powder.

Synthesis of GO was carried out by modified Hummers method, as discussed by Kalambate et al. [149]. The synthesis procedure involves oxidation of graphite using a strong oxidizing agent like $KMnO_4$ along with $NaNO_3$, which acts as supporting oxidizing agent. 1g graphite powder was exfoliated using 48 ml 98% H_2SO_4 in presence of 0.5 g $NaNO_3$ at 0 ^{0}C under ice bath, followed by gradual addition of 5 g $KMnO_4$ in small parts. After the addition of $KMnO_4$, the solution was stirred for 2 hours under water bath at room temperature. The reaction was terminated by addition of 240 ml DDW, followed by 5 ml H_2O_2 (30%) solution. The obtained solution was filtered and washed several times with 10% v/v HCl solution, DDW and ethanol, and later dried under vacuum. The dried powder obtained here is GO.

A composite of the synthesized TiO_2 and GO powders was made by photo-reduction method, as reported by Williams et al. [183]. With this method, aqueous solutions of TiO_2 and GO were made separately and ultrasonicated for one hour. The two dispersion solutions were mixed together and were again ultrasonicated for one hour to obtain homogeneous mixture. The final mixture was irradiated under UV light for 24 hours under constant stirring at room temperature to complete the photo-reduction process. After the process, black powder is obtained which indicates reduction of GO to rGO. The solution is then filtered and washed with water followed by drying under vacuum to obtain rGO-TiO_2 composite. By varying the weight ratio of GO in the aqueous mixture, samples with different rGO:TiO_2 weight ratios (0.001:1, 0.01, 0.1:1, 1:1, 3:1 and 10:1) were prepared and hereafter are denoted by rGOT-0.001, rGOT-0.01, rGOT-0.1, rGOT-1, rGOT-3, rGOT-10, respectively. For all the samples, the weight of TiO_2 was fixed (100 mg) while that of GO was varied.

5.2.2 Materials Characterization

The phase and crystalline structure of all the samples were identified by X-ray diffraction (Rigaku Ultima IV) using Cu Kα radiation (λ = 1.5414 Å) in θ-2θ mode. Optical absorbance of the synthesized samples was determined using UV-Vis-NIR spectrophotometer (Shimadzu) in diffused reflectance mode in the wavelength window of 200 – 800 nm. Transmission electron microscope (TEM, JEM 2100, 200 kV) was used to determine the morphology of all samples. Raman microscopy was used to gain information of the degree of reduction of GO in rGO-TiO_2 composites. Raman spectra were recorded on a HORIBA LabRAM HR 800 spectrometer using 532 nm solid-state laser source with a power of 50mW. FTIR spectroscopy was used to identify the functional groups on GO and rGO-TiO_2 composites using JASCO FT-IR-660 plus spectrometer, operated at room temperature. X-ray photoelectron spectroscopy (XPS) measurement was performed using an AXIS Supra (Kratos Analytical) instrument equipped with a monochromatic Al Kα (1486.6 eV) X-ray source to analyze the surface electronic states and composition. The binding energy (BE) positions were referenced to standard C 1s (284.8 eV) peak for all elements. XPS analysis was performed using ESCApe software from Kratos where the background was corrected using Shirley method. For deconvolution and fitting of XPS peaks, a combination of 50% Lorentzian and 50% Gaussian distribution functions were used. Radiative recombination of photogenerated charge carriers was determined with the help of photoluminescence (PL) emission spectra, measured using a Fluorescence spectrophotometer (Varian, Cary Eclipse) at an excitation wavelength of 385 nm. Time-resolved photoluminescence (TRPL) spectra were obtained using an ISS Chronos BH fluorometer. The charge carriers were excited to higher energy level using excitation pulse of wavelength 405 nm with a pulse width of 70 ps obtained from a pulsed diode laser (Hamamatsu). To obtain PL and TRPL spectra, a homogeneous dispersion of 2 mg powder in appropriate amount of double distilled water was prepared.

5.2.3 Photocatalytic activity measurement

The photocatalytic measurements for water purification was carried out in a lab-made photoreactor assembly. The set up consists of a top-down assembly of 150 W collimated Xenon arc lamp (Hamamatsu) and a borosilicate photoreactor (250 ml) provided with constant stirring system. The distance between source of light and reactor was kept fixed for all the measurements and was measured to be 47 cm. At this distance, the light flux was measured to be 8.6 mW/cm^2. This distance was also found to be ideal to maintain uniform illumination over the samples. The whole setup was kept in dark atmosphere to avoid any errors due to stray lights. For each measurement, 10 mg of photocatalyst was uniformly dispersed in 50 ml p-Nitrophenol (p-NP) solution by ultrasonication for 5 min. In order to separate the adsorption of pollutant over catalyst surface from the photocatalytic degradation [184], prior to photo irradiation, the solution was kept in dark under constant stirring for about 30 min, in order to achieve adsorption/desorption equilibrium between the photocatalyst surface and pollutant in the solution. Once the equilibrium condition was established, the solution was illuminated by light under constant stirring, at room temperature. During photo-catalytic reaction, after an interval of 30 minutes, 5ml of the solution was collected in a quartz cuvette and absorbance spectra was recorded using UV-vis spectrometer (Implen Nano Photometer). A control experiment was also performed by irradiating the pollutant solution under the same conditions, in absence of the photocatalyst. The photo-degradation rate was determined by measuring the variation in characteristic UV-Vis absorbance peak of p-NP at 320 nm with irradiation time. All the samples were tested at least 3 times to establish the consistency of the obtained results.

5.3 Results and Discussion

To understand the effect of loading of GO on TiO_2 and subsequent formation of rGO-TiO_2 composite, samples with different weight ratios of GO:TiO_2 were synthesized such that it covers the whole possible range of GO from low (0.001, 0.01, 0.1) to high ratio (1,3,10). **Fig. 48** displays X-ray diffraction pattern of TiO_2 nanoparticles, GO and the series of rGO-TiO_2 nanocomposites with different weight ratios. XRD pattern of bare GO shows a major diffraction peak around 11.26^o and a minor peak at 43.9° corresponding to the reflections from (002) and (100) planes of GO, respectively, consistent with previous reports [185,186]. XRD pattern of pure TiO_2 displays nine diffraction peaks at 25.3^o, 37.7^o, 48.1^o, 53.8^o, 55.1^o, 62.7^o, 68.8^o, 70.3^o and 75.3^o ascribed to the reflections from (101), (004), (200), (105), (211), (204), (116), (220) and (215) planes, respectively of pure anatase phase. Crystal size of 5-9 nm was calculated from the main peak (25.3^o) of TiO_2 for all the samples. In composite, the peaks assigned to both materials are observed but with different intensities depending on its weight ratio. From the figure, it is clear that as the weight ratio of GO to TiO_2 decreases, the intensity of main characteristic peak of GO at 11.26^0 also decreases, suggesting improvement in reduction of GO to rGO with increasing amount of TiO_2. The existence of both diffraction peaks at 11.26^0 and 43.9° of GO in rGOT-10 and rGOT-3 composite could be ascribed to the absence of sufficient amount of TiO_2 nanoparticles in the composite to reduce GO to rGO. However, when TiO_2 and rGO are in equal amount (rGOT-1), merely a broad signal of both peaks are detected, which implies that TiO_2 nanoparticles are in sufficient quantity to reduce majority of GO to rGO, during photoreduction but not fully. The reduction in the intensity of main characteristic peak at 11.26^0 is attributed to the disruption of stacked (002) planes of GO. On further decreasing the amount of GO in composite, only the peaks attributed to anatase TiO_2 are visible. Furthermore, on comparison of the XRD pattern of all the samples, it is clear that TiO_2 present in the composite exhibits similar diffraction peaks as that of pristine TiO_2, suggesting that only GO is reduced to rGO, while TiO_2 phase remains preserved. This result suggests that GO and rGO-TiO_2 composite both are present in higher range loading, while GO is completely reduced to form rGO-TiO_2 composite in lower range loading.

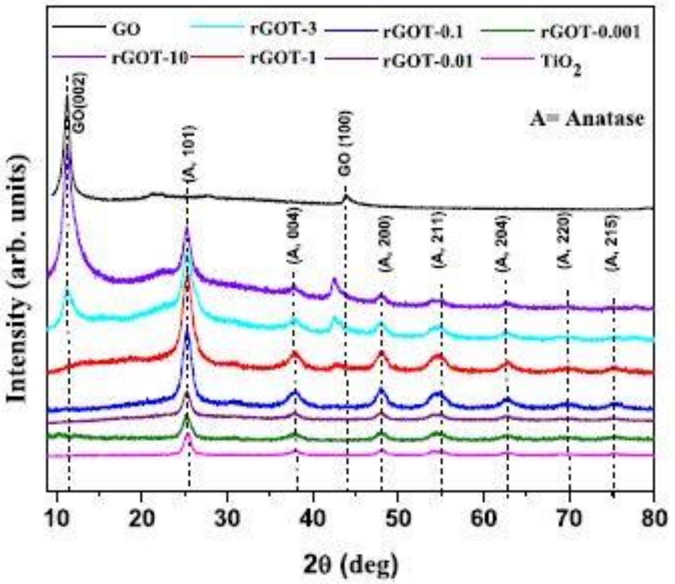

Fig. 48: *XRD pattern of GO, TiO_2 and rGO-TiO_2 nanocomposite with different weight ratios.*

To study the morphological differences between the series of rGO-TiO_2 composites, TEM was used and the corresponding images are presented in **Fig. 49**. **Fig. 49a** shows crumbled structure of bare GO sheet, confirming successful exfoliation of graphite into GO layers. **Fig. 49b** shows that TiO_2 nanoparticles are spherical in shape with a narrow size distribution ranging from 5-8 nm. From the morphological analysis of rGOT-0.001 (**Fig. 49b**) and rGOT-0.1 (**Fig. 49c**), it is revealed that the amount of TiO_2 nanoparticles, as compared to GO, is very high and hence most of the particles can be seen in the form of aggregates rather than uniformly distributed over the surface. Similar morphology is observed for rGOT-0.01 (figure not shown). In the case of rGOT-1 (**Fig. 49d**), although rGO is very well decorated and covered by TiO_2 nanoparticles, but still certain degree of agglomeration of TiO_2 nanoparticles is observed on the surface of rGO sheet. However, the agglomeration is lower as compared to that observed in smaller rGO concentration ratio. TEM images of rGOT-3 (**Fig. 49e**) and rGOT-10 (**Fig. 49f**) show uniform and well-separated TiO_2 nanoparticles decorated on rGO sheets. For lower concentration loading, though TiO_2 nanoparticles mostly covers rGO, they appears agglomerated on the surface, while contrary behaviour is observed for the higher concentration loading. Formation of a composite with uniform distribution over rGO and large spacing between the particles may result in more exposed active sites of TiO_2 for photocatalytic reactions, in contrast to rGO decorated with agglomerated TiO_2 nanoparticles. In addition, even dispersion is more likely to permit formation of an interface between each TiO_2 nanoparticle and rGO which creates a channel for fast charge transfer between them. This is a very important feature to reduce the recombination process during photocatalysis.

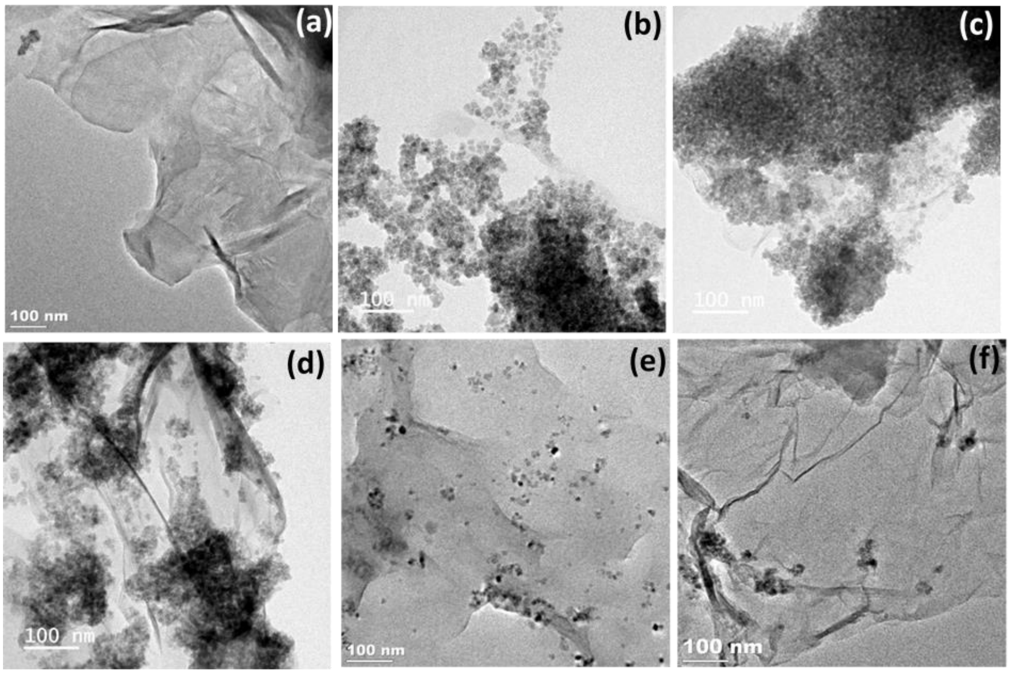

Fig. 49: *TEM images of (a) GO; (b) rGOT-0.001; (c) rGOT-0.1; (d) rGOT-1; (e) rGOT-3; (f) rGOT-10*

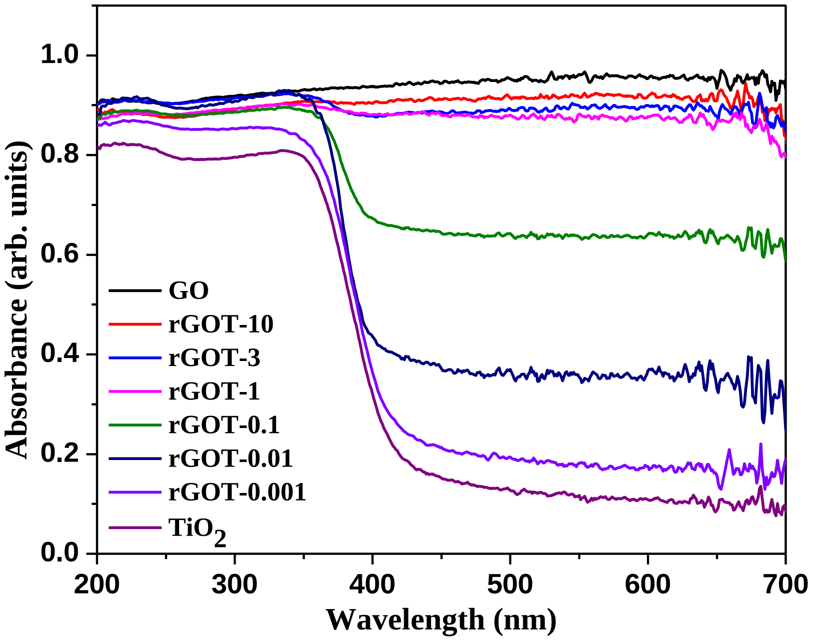

Fig. 50: *UV-Visible absorption spectra (in diffused reflectance mode) of pure* *TiO_2, GO and rGO-TiO_2 nanocomposites with different weight ratio.*

The effect of variation in weight ratio of rGO-TiO_2 composites on their optical properties was studied using UV-Vis absorption spectra in diffuse reflectance mode. From **Fig. 50**, it is evident that TiO_2 possesses an absorption edge at 385 nm corresponding to a band gap of 3.2 eV [187], consistent for anatase phase. On formation of rGO-TiO_2 composite in lower concentration range, there is a very small shift in the absorption edge with significant increase in absorbance throughout the visible range. As the weight ratio of rGO to TiO_2 increases to higher value, absorption of photons in the visible spectrum also increases. This absorption of visible light is mainly attributed to the contributions from GO and rGO whose bandgap varies from 2.2eV to 0.5eV depending on the amount of oxygen containing groups on their surface. On the other hand, a slight red shift in the absorption edge of TiO_2 to 2.9 eV is observed for lower amount of GO. This is mainly due to the formation of impurity levels just above the valence band owing to Ti-O-C bond formation at the interface of TiO_2 and rGO, as confirmed by XPS in later section.

Raman spectroscopy was used to explore the effects of variation in the rGO:TiO_2 weight ratio on ordered and disordered structures of rGO and TiO_2 on surface. Raman spectra of GO, and rGO-TiO2 with high weight ratio (rGOT-1, 3, and 10) are displayed in **Fig. 51** in the range of 900-3000 cm^{-1} wavenumber, while that for graphite and lower weight ratio (rGOT-0.001, 0.01, & 0.1) is presented in **Fig. 52**. For graphite, peak measured at 1341 cm^{-1} and 1568 cm^{-1} (**Fig. 51**) corresponds to D and G band, consistent with previous results [188,189]. D band is assigned to disordered mode, which may arise due to presence of sp^3 defects, disruption of hexagonal graphitic lattice, edge defects and dangling bonds. The observed G band is contributed by phonons of in-plane sp^2 C-C bonds. Raman spectra of unoxidized graphite shows highly intense G band and a weak D band [189] suggesting presence of ordered structure. However, after oxidation of graphite, i.e. formation of GO, an intense D band centred at 1341 cm^{-1} was observed. An increase in relative intensity of D to G band implies disruption of symmetric hexagonal lattice due to introduction of oxygen containing groups (epoxy, hydroxyl & carboxyl). Simultaneous decrease in G band confirms reduction of in plane sp^2 C-C bond and formation of sp^3 bonds in C network with oxygen of epoxy or hydroxyl group. Also, a small shift in G band to higher wavenumber 1597 cm^{-1} indicates the formation of isolated double bond, which resonates at higher frequency compared to G band in graphite [189]. For low range of GO loading, D and G bands are merely visible due to large quantity of TiO_2 on the surface of rGO (**Fig. 52)**. The relative intensity of I_D/ I_G is a good indication for the amount of reduction of GO in the composite. Thus, **Table 4** summarizes the relative ratio of I_D/I_G for all the composite with different weight ratio and GO. In composite, I_D/I_G intensity ratio decreases from 1.17 (GO) to 0.73 (rGOT-0.1) indicating that level of reduction is enhanced with amount of TiO_2. The 2D band observed at higher wavenumber (~2680 cm^{-1}) is sensitive to the stacking of graphene sheets [190]. The peak position of 2D band is located at around 2679 cm^{-1} and 2698 cm^{-1} for single layer and multilayer graphene sheet respectively. The intensity of 2D peak is also inversely proportional to the number of stacking of graphene sheet. In the present case, the 2D band is centred between 2696 and 2700 cm^{-1} for rGOT-1, 10 and GO while only rGOT-3 sample showed the peak position at 2680 cm^{-1} with highest intensity. Thus, 3:1 seems to be the optimum ratio for interaction between TiO2 and GO which leads to disintegration of stacking to form very few number of layers (233), if not single layer. The spectra acquired in lower wavenumber range (100-800 cm^{-1}) for all samples are reported in **Fig. 53**. Raman bands observed at 148 cm^{-1}, 397cm $^{-1}$, 518 cm^{-1} and 640cm^{-1} are assigned to E_g, B_{1g}, A_{1g} and E_{1g} modes of anatase phase of pure TiO_2 nanoparticles (**Fig. 53**).

Samples	**I_D/I_G**	**τ_1 (ns)**	**τ_2 (ns)**	**f_1**	**f_2**	**$\tau_{avg.}$ (ns)**
TiO_2	-	0.370	1.320	0.208	0.792	1.120
rGOT-0.001	Not visible	0.382	1.380	0.296	0.704	1.080
rGOT-0.1	0.730	0.592	1.366	0.322	0.678	1.110
rGOT-1	0.770	0.706	2.720	0.115	0.885	2.480
rGOT-3	0.860	0.855	2.600	0.147	0.853	2.350
rGOT-10	0.880	0.846	1.820	0.231	0.770	1.600
GO	1.170	-	-	-	-	-

Table 4: *Ratio of intensities of D and G band (I_D/I_G) and average lifetime values along with fitting parameters (τ_1 and τ_2 with their corresponding fractions f_1 and f_2) of the total decay, for pure TiO_2, GO and rGO-TiO_2 nanocomposites with different weight ratio.*

Raman spectroscopy of rGO-TiO_2 composite with weight ratio 0.001, 0.01 and 0.1 does not show any significant shift in wavenumber of TiO_2 phase. However, Raman modes of TiO_2 in composites with higher weight ratio (1, 3 and 10) are suppressed due to the low concentration of TiO_2 on the surface as a result of covering by rGO.

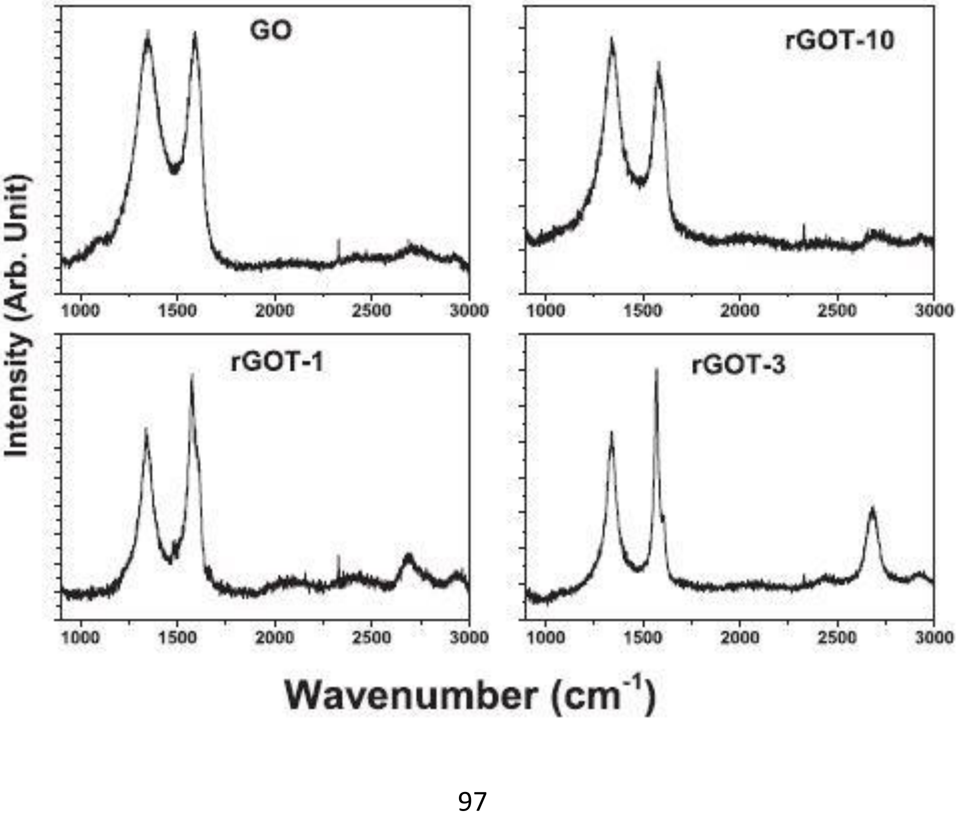

Fig. 51: *Raman spectra of GO and rGO-TiO*$_2$ *nanocomposites in the higher wavenumber region.*

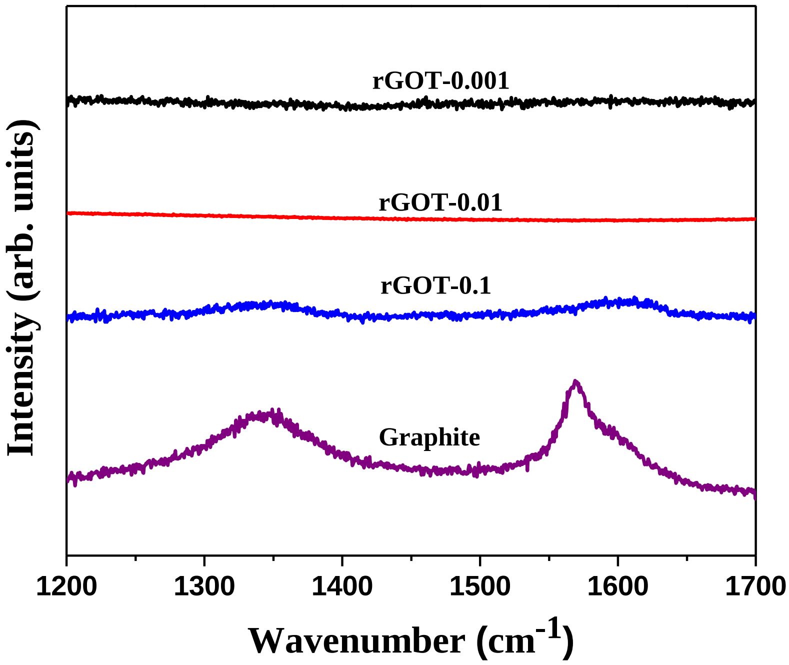

Fig. 52: *Raman spectra of graphite and rGO-TiO*$_2$ *(0.1, 0.01 and 0.001) nanocomposites in the higher wavenumber region.*

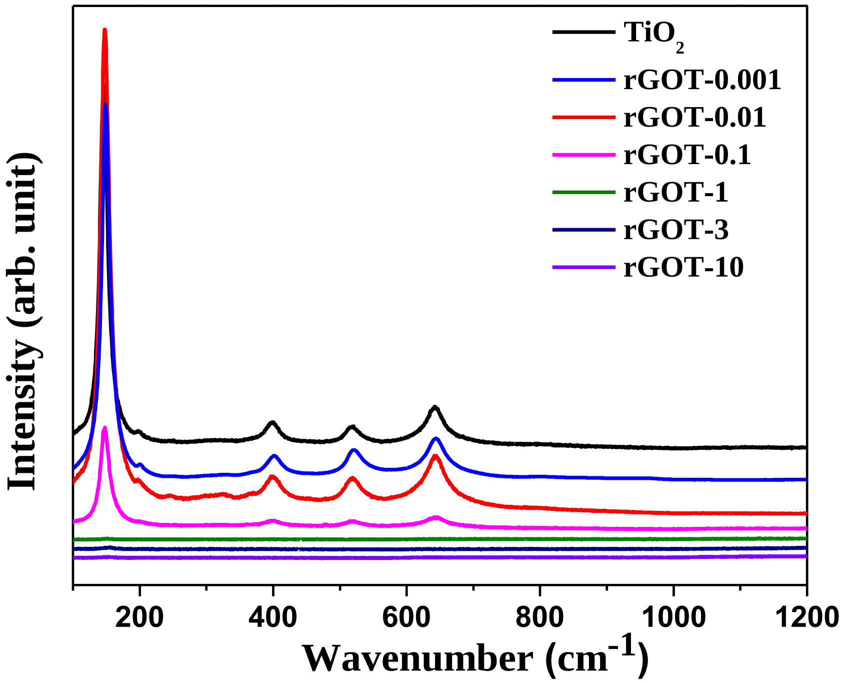

Fig. 53: *Raman spectra of GO and rGO-TiO*$_2$ *nanocomposites in the lower wavenumber region.*

FTIR spectra of GO and rGO-TiO_2 composites are illustrated in **Fig. 54**. In graphene oxide, a broad peak extending from 3700 cm^{-1} to 2700cm^{-1} corresponds to stretching and vibration of O-H bond and intercalated water molecules. The peak at 1614 cm^{-1} is assigned to skeletal vibration of C=C bond of unoxidized graphite. Additionally, the peaks centred at 1718, 1373, 1226, 1026 and 959 cm^{-1} are attributed to vibrations and stretching of C=C, C-OH, C-O-C and C-O (alkoxy) groups, respectively [188,189]. This result confirms that GO surface is mainly covered by hydroxyl, epoxy, carbonyl and carboxylic groups. However, after formation of rGO-TiO_2 composite, there is significant decrease in the peak corresponding to oxygen containing functional groups confirming reduction of GO to rGO and formation of rGO-TiO_2 composite for both the range of loading.

In order to investigate the chemical nature of bonding and interactions at the interface between rGO and TiO_2 after the formation of composite, XPS analysis of all the samples were conducted. The spectra of Ti 2*p* core level for TiO_2 and rGO-TiO_2 composites are shown in **Fig. 55**. For pure TiO_2 (**Fig. 55a**), the two peaks located at 458.5eV and 464.2 eV are assigned to Ti^{4+} state in TiO_2 for Ti $2p_{3/2}$ and Ti $2p_{1/2}$ levels, respectively. Both these peaks are maintained for rGOT-0.001 (**Fig. 55b**) and 0.01 (Figure not shown) where the amount of rGO is low. However, in other rGO-TiO_2 composites, a positive shift by 1.1 to 1.2 eV was observed in both Ti $2p_{3/2}$ and Ti $2p_{1/2}$ levels (**Fig. 55c-f**). This shift is attributed to the strong interaction between rGO and TiO_2 caused by electron transfer from TiO_2 to rGO leading to the formation of Ti-O-C bonds. These Ti-O-C bonds are highly beneficial because they act as a channel for fast transfer of electrons from TiO_2 to rGO during photocatalytic process. For rGOT-10, where amount of rGO is the highest, the signal for Ti is merely detected, thus suggesting complete coverage of TiO_2 with rGO and GO.

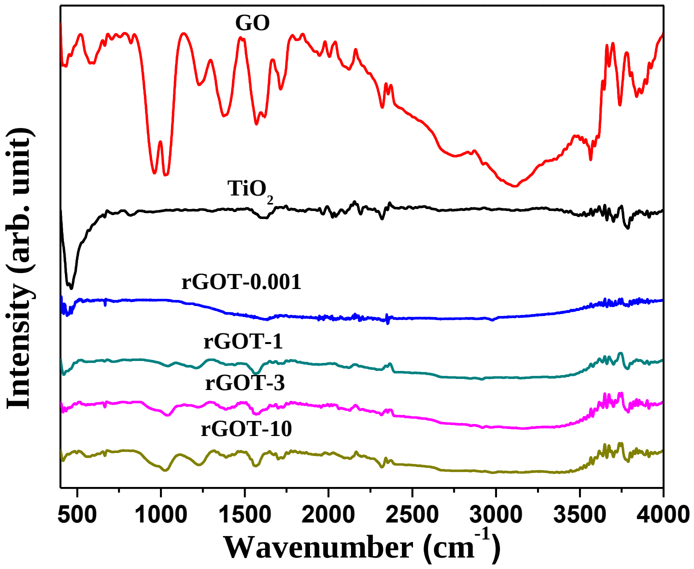

Fig. 54: *FTIR spectra of GO, TiO_2 and rGO-TiO_2 nanocomposites with different weight ratios.*

XPS spectra of C 1*s* level (**Fig. 56**) of GO and the series of rGO-TiO_2 composites are deconvoluted into mainly three peaks with BE 284.8 eV, 286.1 – 286.7 eV and 288.2 – 288.6 eV, corresponding to sp^2 hybridized C-C bond, C-O-C bond and C=O bond, respectively. Comparison between all the composites and GO clearly indicates that after formation of the composite, peaks located at 286.1 – 286.7 eV and 288.2 – 288.6 eV reduces significantly due to removal of oxygen functional groups attached on the surface of GO, in the presence of light and TiO_2 and subsequent conversion to rGO.

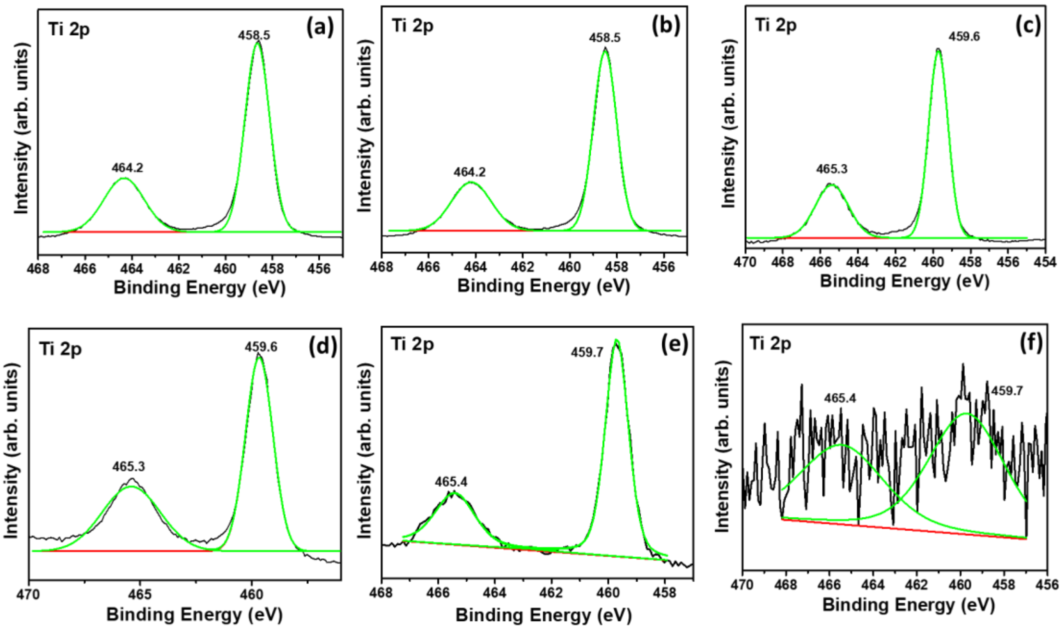

Fig. 55: *XPS spectra of Ti 2p states for (a) TiO_2, (b) rGOT-0.001, (c) rGOT-0.1, (d) rGOT-1, (e) rGOT-3 and (f) rGOT-10.*

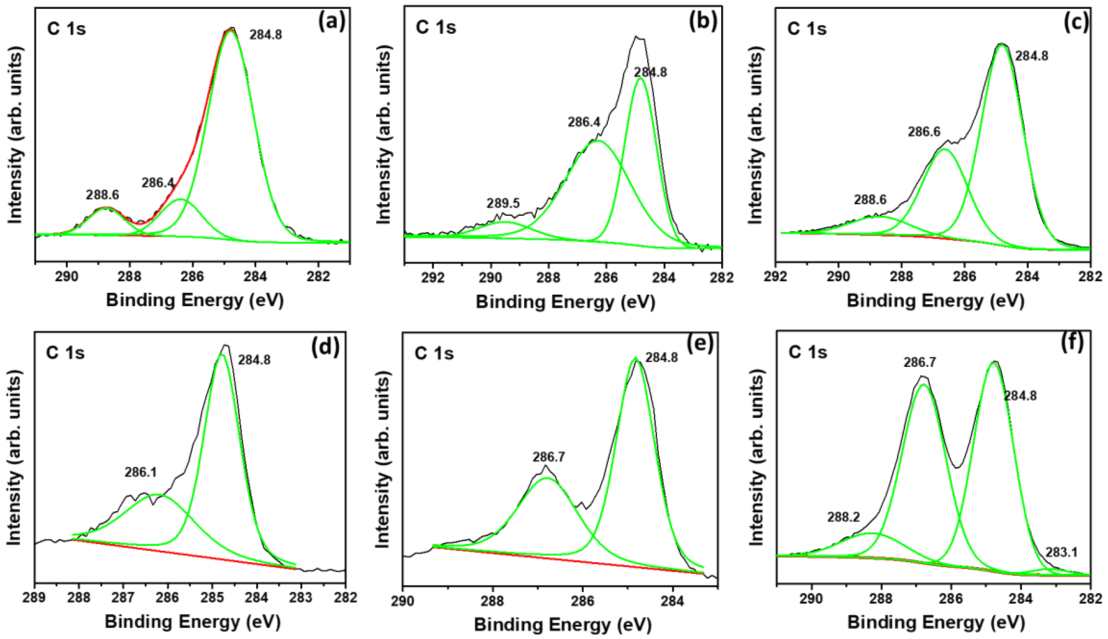

Fig. 56: *XPS spectra of C 1s states for (a) rGOT-0.001, (b) rGOT-0.1, (c) rGOT-1, (d) rGOT-3, (e) rGOT-10 and (f) GO.*

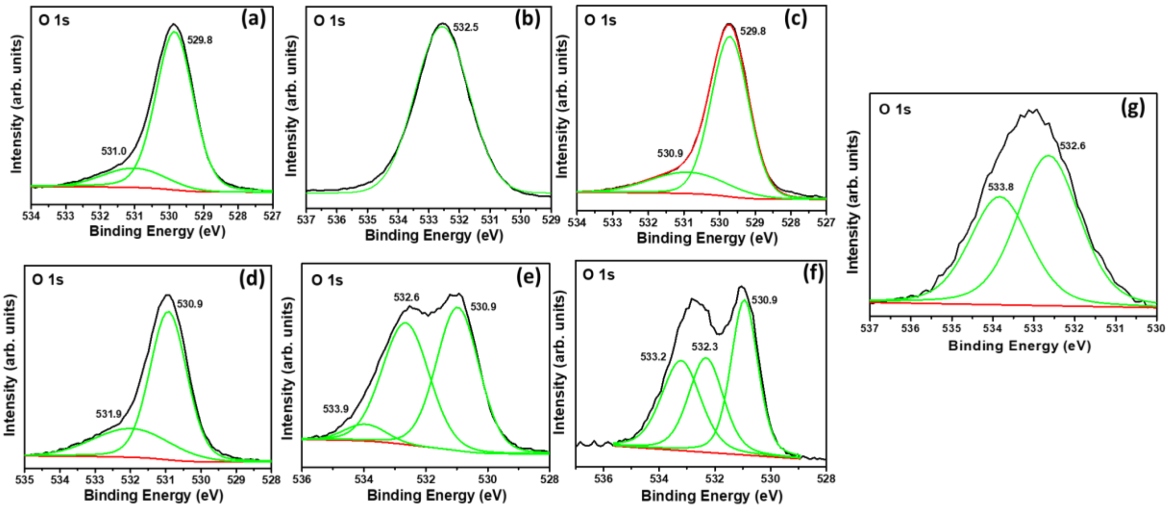

Fig. 57: *XPS spectra of O 1s states for (a) TiO_2, (b) GO, (c) rGOT-0.001, (d) rGOT-0.1, (e) rGOT-1, (f) rGOT-3 and (g) rGOT-10.*

The core level of O 1*s* spectra of TiO_2, GO and all the composites are presented in **Fig. 57**. For pure TiO_2 nanoparticle (**Fig. 57a**), the main peak of O 1*s* can be deconvoluted into two peaks, centred at around 529.8 eV, corresponding to Ti-O-Ti bond [191] and at higher BE 531.0

eV is attributed to the Ti-OH bond. On the other hand, in GO (**Fig. 57b**), single peak located at 532.5 eV is assigned to the presence of hydroxyl and epoxy groups on the surface of GO layer. The intensity of this peak reduces considerably for all the composites except for rGOT-0.001 (**Fig. 57c**) and rGOT-0.01 (Figure not shown), where it is not visible. This again confirms that all oxygen containing groups on the surface of GO are reduced by introducing TiO_2 and the degree of reduction increases with increasing the TiO_2 concentration. For the sample with lower weight ratio (rGOT-0.001 and rGOT-0.01), the two peaks in O 1*s* level are exactly similar to that found in case of pure TiO_2. On the contrary, for composites with other weight ratios i.e. rGOT-0.1 (**Fig. 57d**), rGOT-1 (**Fig. 57e**) and rGOT-3 (**Fig. 57f**), the peak attributed to O in TiO_2 at 530.9 eV shows a positive shift of 1.1eV, similar to Ti 2*p* level. Therefore, it again validates the presence of strong bonding between rGO and TiO_2 created by electron transfer from latter to former. This peak of TiO_2 is completely absent in O 1*s* level of highest weight ratio rGOT-10 (**Fig. 57g**), suggesting absence of TiO_2 on the surface owing to complete coverage by GO. Additional peak is detected at 533.2-533.3eV for higher concentration range of GO which is, after deconvolution, is assigned to Ti-O-C bond formed at interface of TiO_2 and rGO. No signature peak due to Ti-C bond with BE at 460.2 eV and 283.7 eV is seen upon deconvolution of Ti 2p and C 1s level [192,193] respectively, thus eliminating the possibility of Ti-C bond formation at the interface. This shows that TiO_2 nanoparticles interact with GO by forming Ti-O-C bond with oxygen containing group on the surface of GO and not directly with graphene sheet. This channel in the form of Ti-O-C is highly useful for electron transfer during photocatalytic reaction. XPS results indicates that for lower GO loading (rGOT-0.001 and 0.01), TiO_2 is mainly present on the surface of the composite and even if interaction between rGO and TiO_2 occurs, this is not with the TiO_2 nanoparticles present on the surface. On the other hand, for higher GO loading, TiO_2 nanoparticles on the surface display clear interaction with rGO present in form of Ti-O-C bond. At highest loading (rGOT-10), TiO_2 is mostly wrapped by the GO sheets.

From the results so far, it is now established that photo-reduction process helps in formation of rGO-TiO_2 composite and a channel is created in the form of Ti-O-C bond for fast transfer of electrons. This intimate interaction between TiO_2 and rGO through Ti-O-C bond is expected to hinder the recombination process in TiO_2. To investigate the recombination process in rGO-TiO_2 composites, photoluminescence (PL) studies were carried out. PL spectra (**Fig. 58a**) of all the composite samples including TiO_2 shows four peaks around 420, 438, 485 and 526 nm. The two peaks at 420 and 438 nm are due to relaxation from self-trap states whereas other two peaks at 485 and 526 nm are due to interband transitions [151]. From the PL spectra, it is revealed that as the rGO:TiO_2 ratio increases, peak intensity decreases and reaches a minimum for rGOT-10. The reduction in the peak intensity of PL spectrum confirms that addition of rGO reduces the recombination process in TiO_2 by immediate electron transfer from TiO_2 to rGO via Ti-O-C bond [194]. To further confirm this result, time-resolved photoluminescence (TRPL) studies were performed for all the samples.

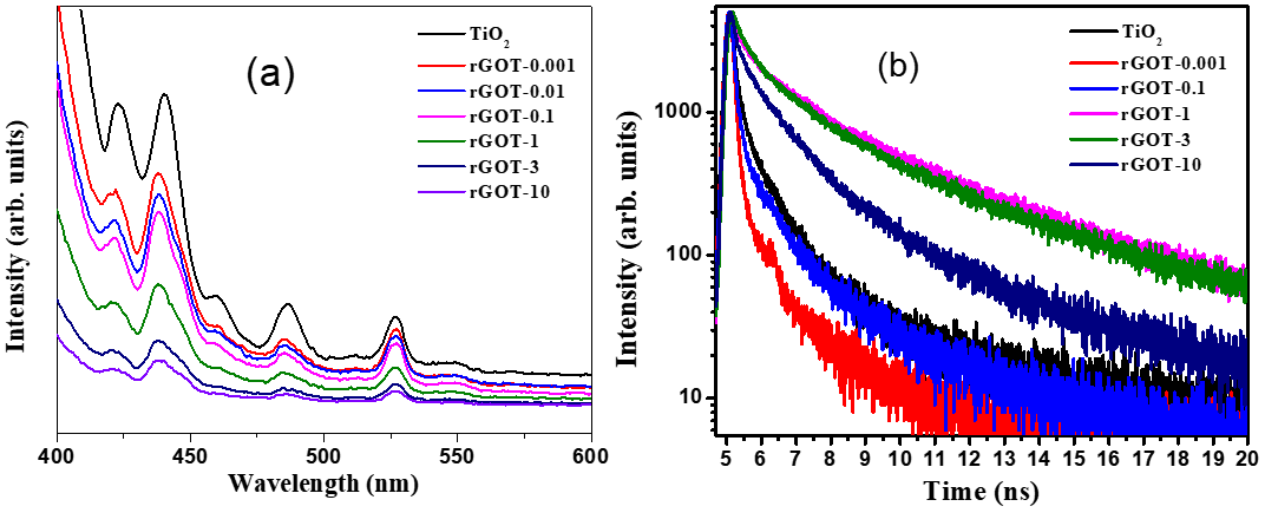

Fig. 58: *(a) Photoluminescence emission spectra and (b) Time-resolved photoluminescence decay curve of pure* TiO_2 *and rGO-*TiO_2 *nanocomposites with different weight ratio.*

Fig. 58b shows the TRPL decay curves measured for an integrated value of PL for pristine TiO_2 and rGO-TiO_2 composites. The decay curves are fitted by two-exponential decay functions comprising two time components, τ_1 and τ_2 corresponding to fast and slow decay components respectively. The logarithmic scale does make the result look like a stretched exponential but due to the relatively low stretching exponent ($\beta << 0.5$), the fitting was done by bi-exponential decay functions. The fast component arises by electron and hole relaxation near band edge of TiO_2 and slow component originates from recombination of excitons which are self-trapped at various defect sites in lattice or surface (such as oxygen vacancies, surface hydroxy group and other defects). The values of these components with the corresponding fractions are summarized in **Table 4** along with the average life time value. In pure TiO_2, the average lifetime of 1.12 ns is mainly dominated by slow component with fraction of 79% as compared to fast component (21%). For lowest GO loading (rGOT-0.001) the time component values are nearly same but fraction of slow component decreases to 70% as compared to 79% of TiO_2 which results in slight decrease of overall lifetime to 1.084 ns. Similar decrease in average lifetime is also observed for rGOT-0.1 where the fraction of τ_2 further decreases to

67.8% but the value of τ_1 increases to 0.592 ns in comparison to TiO_2 (0.370 ns). TiO_2 nanoparticles are in form of agglomerated clusters for lower ratio GO loading, where only few nanoparticles on the outside of cluster interact with GO to form rGO-TiO_2 composite. In these interacting TiO_2 nanoparticles, photo-generated electrons before being trapped by the defect sites are transferred to rGO, leading to decrease in fraction of slow component. But majority of TiO_2 nanoparticles are not in contact with rGO, thus the overall lifetime is slightly lower or close to that of TiO_2. In case of the high range GO loading, mainly for rGOT-1 and rGOT-3, the average lifetime value is more than doubled than that of TiO_2 owing to the increase in τ_1 and τ_2 values by more than two times. This increase in lifetime values can be directly linked to the formation of Ti-O-C bond between TiO_2 and rGO, found for only higher ratio GO loading. Each TiO_2 nanoparticle is well dispersed on 2D sheet forming distinct interfacial channel with rGO in form of Ti-O-C bond. Since conduction band minima of TiO_2 (-4.2 eV) is higher than the work function of rGO (-4.4 eV), this Ti-O-C bond acts as a channel to immediately transfer the electrons from TiO_2 to rGO after its photo-generation. PL and TRPL results suggest that interaction between TiO_2 and rGO is an important factor to reduce recombination process in rGO-TiO_2 composite.

5.3.1 Photocatalytic activity

To investigate the effect of loadings variation of GO in rGO:TiO_2 towards their photocatalytic performance, photodegradation of p-NP was carried out. For all measurements, the amount of TiO_2 was kept constant (2.5 mg), so as to ensure that the amount of photocatalyst is same in all the samples. **Fig. 59a** shows the graph of photocatalytic degradation of p-NP under Xenon light irradiation for pure TiO_2 and rGO-TiO_2 composites. It is evident that rGO-TiO_2 composites show better photocatalytic activity as compared to unsupported pure TiO_2, irrespective of the weight ratio value. One can observe that as the weight ratio is increased, the photo-degradation efficiency increases until the value becomes 3:1. On further increasing the amount of GO (rGOT-10), photoactivity starts decreasing. This implies that rGOT-3 with GO:TiO_2 weight ratio of 3:1 portrays the most suitable scenario that assists in improving the photocatalytic performance by 3.5 times as compared to pure TiO_2.

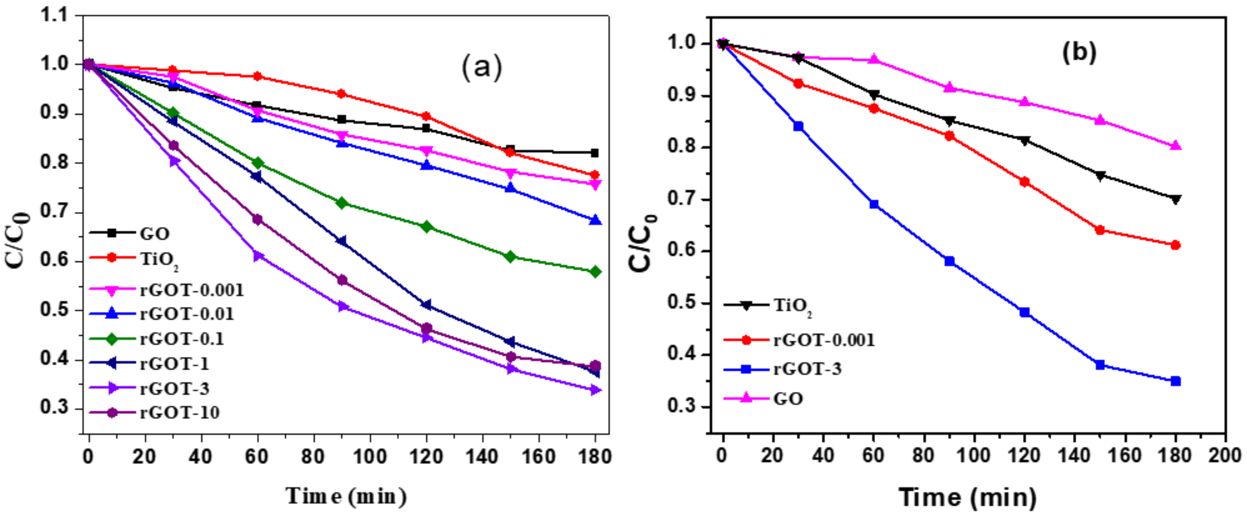

Fig. 59: *Comparison of photocatalytic degradation of p-NP under (a) Xenon irradiation and (b) UV light irradiation for pure* TiO_2*, GO and rGO-*TiO_2 *nanocomposites.*

To understand the reasons for better photocatalytic performance of rGO-TiO_2 composites, rGOT-3 in particular, one need to understand the differences in pristine TiO_2 and the composite samples. Two major modifications take place in the properties of composite samples when compared to pure TiO_2: (a) increase in the absorption of visible light spectrum and (b) decrease in the recombination of photogenerated charge carriers. The presence of rGO with a bandgap less than 2.2 eV is mainly responsible for absorption of visible light, as confirmed by UV-Visible spectroscopy. Additionally, in composite samples, marginal narrowing of TiO_2 bandgap was also observed, which is due to the formation of Ti-O-C level above the VB. This phenomenon also contributes to the improved utilization of visible spectrum. The reduced recombination rate is a consequence of the fast electron transfer from TiO_2 to rGO at the interface of the composite. According to XPS results, strong interaction between TiO_2 and rGO is developed at the interface due to the formation of Ti-O-C bonds. The conduction band minimum of TiO_2 (-4.2 eV) is higher than the work function of rGO (-4.4 eV) which assists the fast transfer of electrons from TiO_2 to rGO through interfacial channel to reduce the recombination rate as also confirmed by PL and TRRL spectroscopy.

To identify which of the two factors, absorption of visible spectrum or decrease in recombination rate, is dominant in improving the photocatalytic performance, more experiments were performed. As rGO is a low bandgap material, it is mainly responsible for enhancement in absorbance of visible spectrum in the composite samples. In order to investigate the possibility that GO absorbs visible light under xenon lamp and the enhancement in rGO:TiO_2 composite is due to extended absorption in visible region, the photo-degradation tests were carried out under UV light irradiation, as shown in **Fig. 59b**. In these measurements also, the amount of TiO_2 was kept constant (2.5 mg) to make a fair comparison. Even under UV irradiation, rGOT-3 shows the highest activity, similar to that under Xenon irradiation. This confirms the fact that TiO_2 is the dominant photocatalyst in the composite and visible light absorption is not the main reason for enhancement in their photocatalytic performance. Thus, charge separation at the interface is the major factor controlling the photocatalytic performance in rGO-TiO_2 composites. In rGOT-3, the amount of GO is 3 times that of TiO_2. This raises a concern that the observed photocatalytic activity can also have contributions from the excess amount of GO and not purely due to enhanced charge separation at the interface. To shed more light on this concern, GO powder in an amount equal to thrice the value of TiO_2 (i.e. 7.5 mg) was tested individually for photo-degradation under UV and Xenon light, as shown in **Fig. 59b and 59a** respectively. On comparing the activity graphs of rGOT-3 and GO, clear difference in their photo-degradation activity is observed, which indicates that enhancement in photoactivity is purely due to the interaction between rGO and TiO_2 at the interface, rather than due to excess amount of GO.

This result also indicates that higher GO loading (rGOT-1, 3 and 10) displays significantly improved photocatalytic activity as compared to lower GO loading (rGOT-0.001, 0.01 and 0.1). TEM and XPS results shows that for higher GO loading TiO_2 nanoparticles are well dispersed on the 2D sheet to form distinct interfacial channel with rGO in the form of Ti-O-C bond, for fast electron transfer. This effect is optimum for weight ratio of 3:1 thus leading to highest degradation rate with minimum recombination processes. For highest loading (rGOT-10), slight decrease in the activity is observed which is due to the wrapping of TiO_2 nanoparticles by excess amount of GO present in the composite as evidenced by the absence of TiO_2 peaks in XPS and Raman spectra of the surface. The surface coverage not only prevents light to reach on TiO_2 but also avoids the interaction between TiO_2 active sites and organic pollutants leading to reduce activity. In case of lower GO loading, TiO_2 nanoparticles are mostly in aggregate state on the surface out of which only fewer nanoparticles are able to interact with GO and form Ti-O-C channel for electron transfer. Thus all the above results are able to clarify the role played by the formation of interface between rGO and TiO_2 and establish as the most important factor in rGO-TiO_2 composite.

5.4 Conclusion

rGO-TiO_2 composites with different GO loading from low to (rGOT-0.001, rGOT-0.01 and rGOT-0.1) to high GO (rGOT-1, rGOT-3 and rGOT-10) concentration range were synthesized using photoreduction method to investigate the effect of GO loading on morphological, interfacial, structural, optical and electron transfer dynamics in resultant composite. The following differences in various properties are listed below.

Techniques	High concentration (rGOT-1, 3 and 10)	Low concentration (rGOT-0.001, 0.01and 0.1)
XRD, Raman, FTIR, XPS	Incomplete reduction of GO to rGO due to insufficient amount of TiO_2 nanoparticles.	Complete reduction to rGO.
TEM	Well dispersed TiO_2 nanoparticles on rGO sheets.	Agglomerated clusters of TiO_2 nanoparticles covering over rGO.
XPS	Each nanoparticle is strongly interacting with rGO in form of Ti-O-C bond at interface.	No visible sign of Ti-O-C bond is observed.
UV-Vis	Visible light absorption in whole range due to presence of low band gap rGO and GO.	Slight red shift in the absorption edge of TiO_2.
PL, TRPL	The amount of recombination processes significantly reduced with prolonged carrier lifetime due to fast transfer of electron through Ti-O-C channel.	Amount of recombination process is lower than TiO_2 nanoparticles but carrier lifetime slightly decreases.

All the above mentioned properties led to higher photocatalytic activity for degradation of phenol for higher concentration GO loading as compared to TiO_2 as well as lower range composites. Among all, the weight ratio, rGOT-3 showed the best performance under both Xenon and UV lamp owing to better dispersion of each nanoparticles which allows to form strong interaction with rGO creating Ti-O-C channel at interface. Marginal decrement in activity at the highest weight ratio of 10:1 is due to excess amount of GO which results in wrapping of TiO_2 active sites for photo reaction as well as blocking of light.

Chapter 6: WO_3 nanostructures produced by pulsed laser deposition for solar photocatalytic water remediation

Preview: The increasing interest for addressing photocatalyst materials towards an effective application under direct sunlight is an important topic in materials science. We present here an investigation of monoclinic tungsten trioxide (m-WO_3) coatings fabricated by pulsed laser deposition (PLD), with the aim of providing a nanostructured photocatalyst capable of working with concentrated sunlight and exhibiting good stability in acidic environment. The photocatalytic activity was evaluated in both direct photocatalysis and photo-Fenton mode for Methylene Blue (MB) dye degradation under artificial light and concentrated solar light from a parabolic dish concentrator (PDC). The results were analysed and demonstrated good photocatalytic activity under photo-Fenton conditions with best activity in pH 4. A detailed study is reported ahead.

Being the main author of this to-be published work, my contribution includes the fabrication of m-WO3 coatings, performing photocatalytic measurements in the lab as well as with the PDC system, material characterization and drafting the manuscript.

6.1 Introduction

The population growth and the consequent increase of industrial activities have been directly affecting the environmental behavior [195,196]. Water quality is a matter of important concern due the observation of the decrease in the number of available potable water sources [197]. Precautions and strong environmental actions such as forests restructuring and conservation have been attempting to sustain weather equilibrium and water quality [198–200]. On the other hand, contaminated water residuals from industrial activities require constant development of remediation measures as far as new chemical processes are employed [201,202]. Some scientific and technological developments in terms of products still present a technological gap neglecting the complete life cycle chain and not taking into consideration proper predictions to the direct and indirect effects that can impact water quality and consequently the environment [203,204]. In terms of contaminated water remediation, for the last 40 years, a field of industrial research has been employing advanced oxidation processes

(AOP) for the removal of recalcitrant agents present in water. AOPs present the properties to form highly reactive chemical species to convert organic molecules into inorganic carbon by mineralizing them [205]. Solutions in terms of AOPs have received special attention to applications employing heterogeneous photocatalysis which are capable of generating oxidizing radicals by light exposure [206,207]. Heterogeneous routes are presented as interesting solutions due to the enhanced possibility of controlling reaction rates using a supported catalyst, which can be inserted or removed immediately during a reaction, thereby demonstrating advantages when compared to homogeneous routes, which require post processing treatments for the catalyst removal [13].

The possibility to use semiconductor materials as catalysts have been investigated with special attention, for example, TiO_2 as a catalyst material [174,208], when employed in anatase form, presents high photoactivity in presence of UV light. Its photoexcitation properties show activation in the range between 300 to 388 nm [209]. However, the use of artificial light sources to activate the photocatalytic effect is commonly mentioned with the counterpoint that this type of illumination procedure turns the decontamination process economically ineffective [150,151,210–212]. Other materials such as ZnO, Fe_2O_3, CdS, GaP, Co_3O_4, ZnS are also presented in the literature with approaches looking for the possibility of using the solar light as the activation source [84,87,94,107,213–216]. Since the late 80's, solar installations have been designed to water remediation, initially developed for the use of mirrors capable of reflecting UV light, by polished anodized aluminum coated with acrylic polymers, which turn the processing expensive [217,218]. Engineering configurations for solar mirrors were also developed, in terms of concentrating and non-concentrating solar systems [219]. The use of commercial silver coated glass mirrors also gained interest as long as the photocatalytic materials were able to perform absorption of solar light in the near UV and visible spectrum [220–222]. An important number of literatures report the combined use of both concentrating and non-concentrating solar systems with advancements over the benchmark commercial TiO_2 evidencing improvements towards the activation of photocatalyst reducing the need of artificial light sources [223–229]. Thus, it is of utmost importance to explore different photocatalysts apart from TiO_2 for solar applications.

In this context, semiconductors with promising possibilities to be employed as photocatalysts capable of being activated by sunlight and explored in a variety of applications in the literature are tungsten (W) and tungsten oxide based materials [230–235]. Their properties present the possibility to work in the near-UV light range, since the bandgap of tungsten oxide (WO_3) is at 2.6 eV, meaning a photoactivation in the range of 474 nm.

Moreover, Pourbaix diagrams presented for tungsten oxides demonstrate a favorable stable catalytic activity under acidic pH conditions, which is a general rule in industrial processes [236].

Important investigations were published comprising of the features possible for WO_3 applications, such as special coating to promote adsorbance [237], sensors [238–243], electrochromic devices [244,245] and photoanodes [246–251]. It is also observed that employing tungsten oxide structures as photocatalysts for water remediation can be explored [252–257]. Initial researches have pointed out positively the employment of such materials. Furthermore, advances on the employment of fabrication methods such as Pulsed Laser Deposition (PLD) can lead to novelties in terms of controlled crystallinity, film thickness and morphology along with the possibility of obtaining 3D hierarchical nanostructures [258–262] by varying the parameters such as the laser fluence, deposition pressure and gas assistance. The combined innovation of producing photocatalysts with controlled properties and its use under natural light source can be the alternative to explore water remediation under solar exposure.

In this work we propose the fabrication by PLD of a monoclinic nanostructured "flower-shape like" tungsten oxide (WO_3) coating with the features to work under near UV-visible light absorbance, stable in acidic environments and capable of working with a low-cost solar concentration apparatus. The deposition was performed in oxygen atmosphere with the PLD target made of metallic tungsten powder pressed with boric acid which served the purpose of a binding agent. The deposited samples were later thermally annealed to obtain the monoclinic WO_3 phase. The m-WO_3 coatings were tested as photocatalysts for degradation of Methylene Blue (MB) as a model pollutant under photo-Fenton reactions. The validation studies were performed in lab scale with artificial visible light lamps and upon optimization were tested for scaling process in a solar parabolic dish concentrator (PDC) type system under natural sunlight.

6.2 Experimental

6.2.1 Synthesis

Tungsten metallic (W) and boric acid (H_3BO_3) powders were mixed in an appropriate ratio and the prepared mixture was compressed in the form of a disc to be used as a target for the deposition of tungsten oxide coatings by PLD. A KrF excimer laser (Lambda Physik) with an operating wavelength of 248 nm, pulse duration of 25 ns, and repetition rate of 20 Hz was used for deposition. The fluence of the laser was always maintained at 4.5 J/cm^2 for ablation. The PLD apparatus details and the mechanisms involved in the laser matter interactions are presented in our past reports [60,105,263]. The PLD chamber was evacuated up to a base pressure of 10^{-6} mbar prior to all the depositions. Deposition of the coatings were carried out in an oxygen atmosphere at pressures of 1.5 x 10^{-2} mbar. The target to substrate distance was fixed at 4.5cm with the substrate positioned parallel to the target and the number of pulses used were 10k. The coatings were deposited on glass and Si at room temperature. Thermal annealing of the deposited coating was carried out in air at 600ºC for 8 h with a heating rate of 5 ºC/min.

6.2.2 Characterization

A Scanning Electron Microscope (SEM-FEG, JSM 7001F, JEOL) with 20keV electron beam energy equipped with energy dispersive spectroscopy analysis (EDS, INCA PentaFET-x3) was used for examining the surface morphologies of all the samples prepared by PLD. Structural characterization was performed using X-Ray Diffractometer (XRD) with Cu K_{α} radiation (λ = 1.5414 Å). Micro-Raman spectroscopy was performed using a Labram Aramis Jobin-Yvon Horiba μ-Raman system equipped with a He-Ne laser source (632nm). Absorption spectra were obtained with UV-VIS-NIR absorption spectrophotometer (Varian Cary 5000 UV-VIS-NIR absorption spectrophotometer).

6.2.3 Photocatalytic activity

The photocatalytic activity of the synthesized samples were evaluated by studying the degradation of model MB dye solutions in presence of H_2O_2 and light. 30ml of MB dye (10 ppm) mixed with 1ml of H_2O_2 (1M), as an oxidizing agent, in an aqueous solution was used for degradation by photo-Fenton reaction. The catalyst coatings (prepared on glass slide of area 2.5 × 7.5 cm) were dipped in the above prepared MB dye solution and kept in the dark for 30 mins at constant stirring to establish adsorption equilibrium between the solution and the catalyst surface. After dark reading, a tungsten lamp (225W) emitting mostly visible light was used as the light source. 1ml of MB dye solution was collected after fixed intervals of time during the reaction to study the amount of degradation by measuring the UV-Vis absorption spectra and analyzing the characteristic peak of MB at 664 nm. All the photocatalysis experiments were performed at room temperature. CO_2 evolution was followed in selected experiments by an IR sensor (COZIR Wide range 5) placed in proximity of the solution surface. Note that since the reactor is open, the measurement is not quantitative, but can only show a variation in the atmospheric level of CO_2.

6.2.4 Solar Concentrator photocatalytic measurements

The solar scaling-up experimentation was performed by studying the degradation of MB dye as model pollutant in the same concentration as the lab experiments. At this time, instead of 30 ml, degradation of 2 liters of 10 ppm MB dye solution was tested for each of the four different solar experimental conditions: 1) Concentrated sunlight + WO_3 catalyst + 0.6 ml of H_2O_2 (corresponding to concentration of 0.1M) as the oxidizing agent for photo-Fenton reaction, 2) Concentrated sunlight + 0.6 ml of H_2O_2, 3) Concentrated sunlight + WO_3 catalyst and 4) Concentrated sunlight exposure only. Regarding H_2O_2, the concentration of H_2O_2 employed in laboratory experiments was 1M (Molar), in the solar concentrator experiments, due to an observation of a dominant process regarding the direct photocatalysis of H_2O_2 by solar light photons, the concentration was reduced to 0.1M (10 times less). The WO_3 catalyst material was deposited on a glass slide with dimensions of 7.5 x 2.5 cm, the weight of the catalyst was approximately 4 mg on each glass slide. The glass slides were inserted inside a quartz glass tube of approximately 150 ml volume that was used as the reactor to be focused towards the reflected sunlight. The quartz tube was sealed at one end and closed by a three-port lid on the other end. One port hosts a thermocouple for temperature monitoring, and the other two ports are the inlet and outlet for the MB solution circulation. A pumping system was used to promote the circulation of the solution provided by a diaphragm pumping system with volume flow rate of 5 L/h. The tubing circuit was polyamide pipes connected to a cooler with monitored temperature.

The solar concentrator apparatus setup employed was designed, built and patented by IdEA group from the University of Trento [264], the setup has low operation and maintenance costs and consists of an automatic tracker (PDC) with 5 m diameter, with the focus located at 2.5 m distant from the mirrors. It is designed to assemble a maximum of 24 coated silver glass mirrors in individual segments (each of 0.76 m^2 area), providing a concentration factor of up to 870x on a circular spot of approximately 5.8 cm diameter [265]. **Fig. 60** presents the working scheme and the solar apparatus used in the work. The solar intensity was constantly measured using a pyrheliometer (Kipp & Zonnen CHP1). In this study, to compare the prevalence effects between the concentrated sunlight and the H_2O_2 concentration, only one module of mirror was mounted on the system. 1 ml of MB dye in circulation solution was collected every 30 minutes. All the photocatalysis experiments were performed at controlled temperature range between 20 and 30 °C.

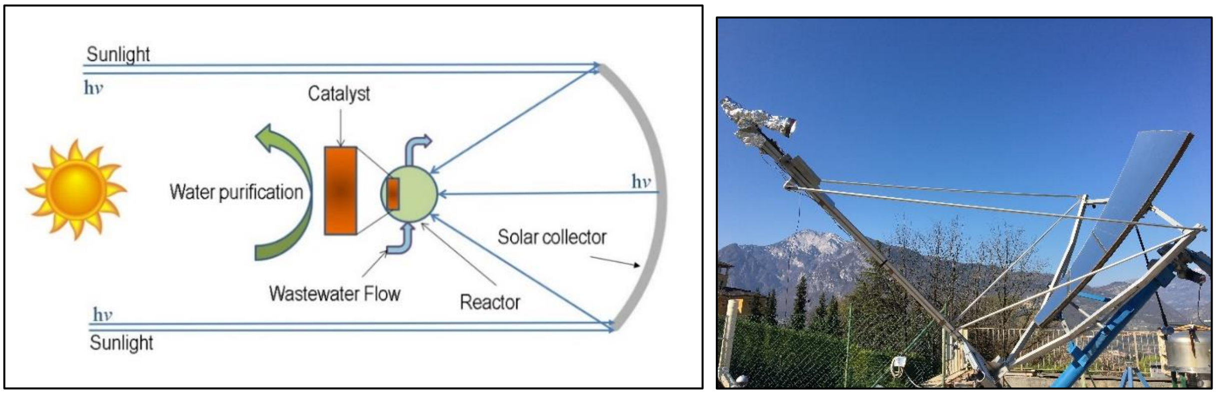

Figure 60: *concentration scheme* [94] *and solar apparatus for solar water purification used in this work.*

6.3 Results and Discussions

The as-deposited (AD) as well as the AN600 coatings were studied by SEM to get insights on the surface morphologies and the changes that occur up on annealing. The AD sample **(Fig 61a and 61b)** shows particle like morphology with a varied particle size distribution from tens of nanometer to few micrometer. This kind of morphology is expected owing to the phase explosion process which comes close to the thermodynamic critical temperature upon irradiating with high laser fluence. On the other hand, AN600 sample **(Fig 61c and 61d)** shows the particle like morphology evolve into well-grown flower-like structures depicting completely different morphology.

The absorption spectra were acquired for the as-deposited and AN600 (WO_3) samples in the range of 350-600 nm (**Fig. 62**). AN600 (WO_3) sample shows a clear absorption edge with an absorption maxima around 472 nm which is in line with the absorption of WO_3 samples reported in literature.

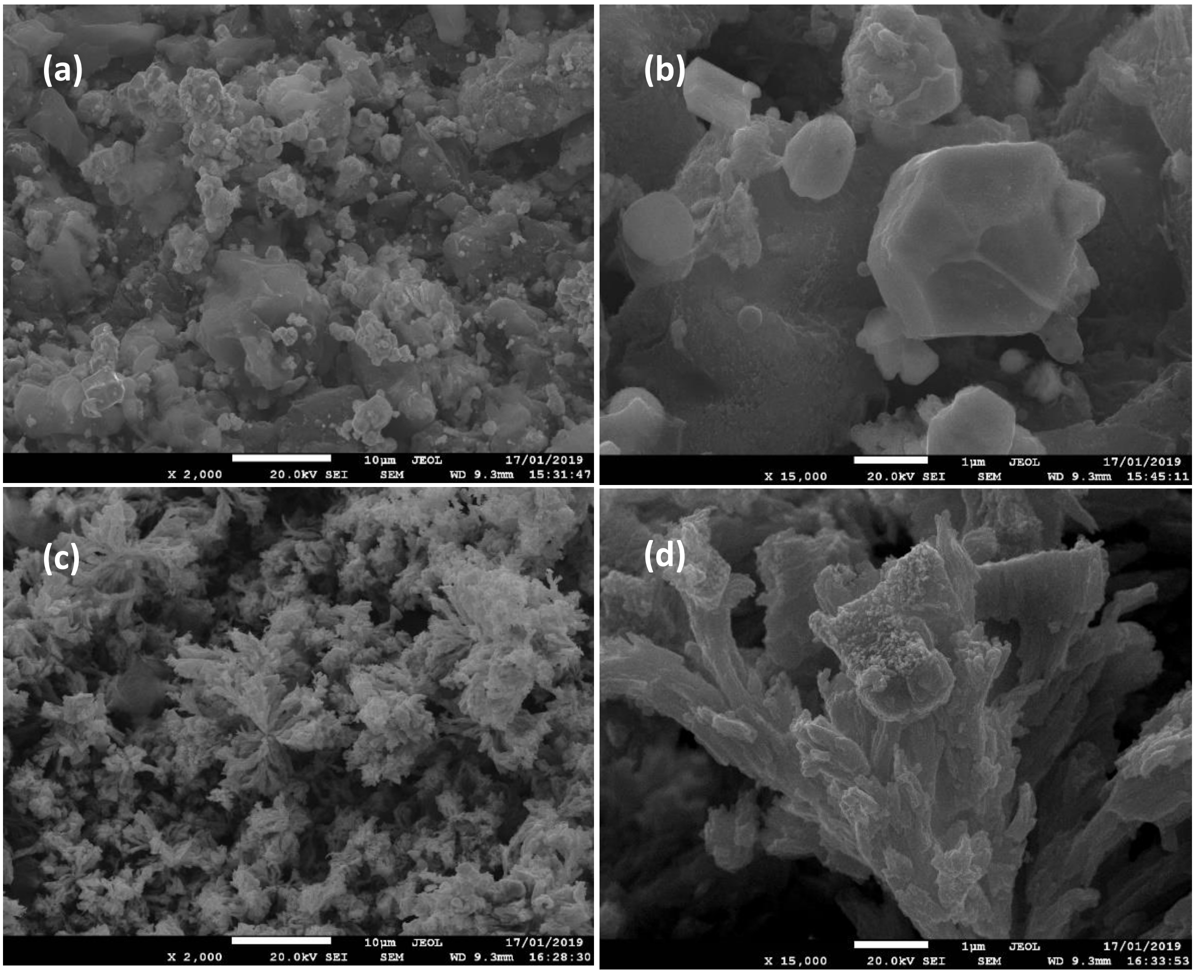

Figure 61: *SEM images of (a & b) as-deposited [AD] samples, (c & d) of AN600 samples.*

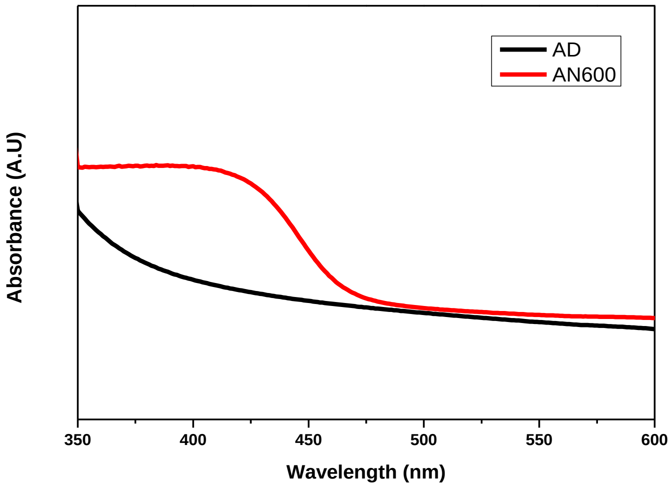

Figure 62: *Absorption spectra for as-deposited and AN600 samples.*

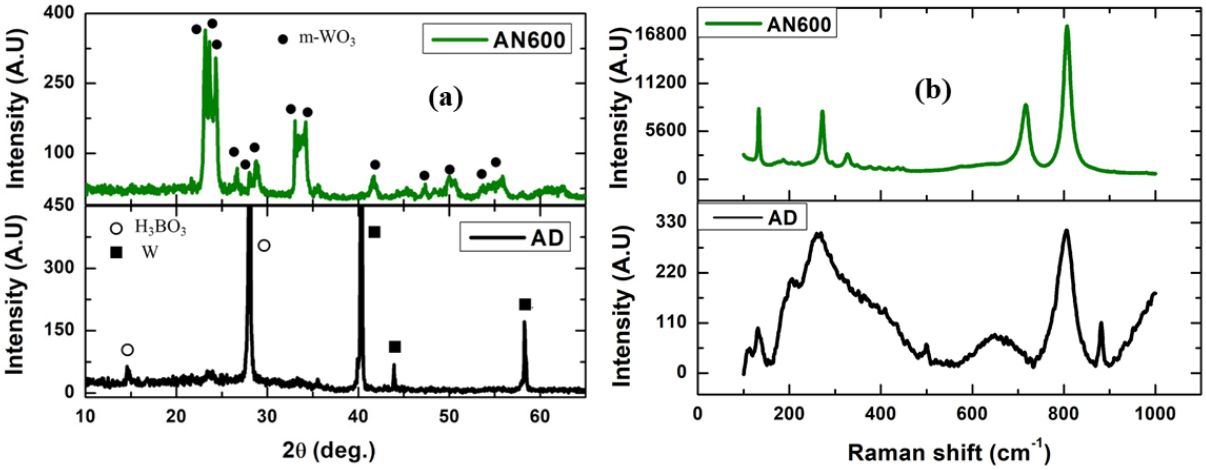

Figure 63: *a) XRD spectra and b) Raman spectra for as-deposited (AD) and AN600 samples.*

XRD measurements were also done on the as-deposited (AD) and annealed sample (AN600) to identify the crystal structure and the XRD spectra are shown in **Fig 63a**. The XRD pattern for AD coating shows H_3BO_3 and metallic tungsten (W) peaks. No other phases were detected in the sample thereby maintaining the same composition as that of the PLD target. On annealing at 600°C, all the displayed peaks are associated to monoclinic WO_3 phase (JCPDS Card No. 43-1035) with no other phase present. Micro-Raman spectra were acquired to investigate the presence of tungsten oxide phase and the spectra for as-deposited (AD) and AN600 samples are shown in **Fig. 63b**. The Micro-Raman spectra of AD coating and the sample annealed in air at 600°C are reported in the range of 100 to 1000 cm^{-1}. The broad nature of the peaks with low intensities in AD sample indicate the amorphous nature of the film. Upon annealing at 600°C, the peaks are intensified and are well matched with the monoclinic phase of WO_3. The peaks at 716 and 806 cm^{-1} correspond to the ν(O-W-O) mode of WO_3 while the peaks at 271 and 327 cm^{-1} are due to bending vibration δ(O-W-O) [266].

The effectiveness of the synthesized tungsten oxide coating (AN600) as a photocatalyst was studied by using it for degradation of model MB dye through a photo-Fenton reaction involving H_2O_2. The variation in the MB dye concentration as a function of irradiation time was measured by monitoring the variation in the characteristic absorption peak at 664 nm. Adsorption is the major prerequisite condition for any heterogeneous catalytic reaction, thus all the catalyst coatings were kept stirring in the dye solution under dark for 30 min.

The photocatalytic degradation was performed for separate degradation of MB dye, (1) in presence of light only, (2) with added H_2O_2 and light, (3) with coating annealed at 600˚C and light, and (4) combination of all three (H_2O_2, light and catalyst) [**Fig. 64**]. In 120 mins, the degradation of MB dye in light is only 34% which increases to 51% after inclusion of H_2O_2. Finally adding tungsten oxide coating along with H_2O_2 and light the degradation reaction is almost completed (about 96%) in 120 mins. This indicates that the catalyst coating follows photo-Fenton reaction by generation of $OH^•$ radicals by dissociation of H_2O_2. Most importantly, the catalyst coating is also able to degrade 74% of MB dye in absence of H_2O_2. This suggests that the tungsten oxide catalyst coating also works as a pure photocatalyst which might be able to generate hydroxide radicals from adsorbed H_2O on the surface. Although the involvement of H_2O_2 is very useful, the catalyst coating can however also be utilized without H_2O_2. CO_2 emission measurements were also done for the experiments involving the catalyst (with and without H_2O_2) and the CO_2 emission graphs are reported below **(Fig. 65a & 65b)**. The added confirmation of photo-Fenton and photocatalysis without H_2O_2 experiments are clearly given by the evolution of CO_2 as soon as light is irradiated on the catalyst coating. The $OH^•$ radicals generated in both the cases mineralize the MB dye giving CO_2 as the by-product.

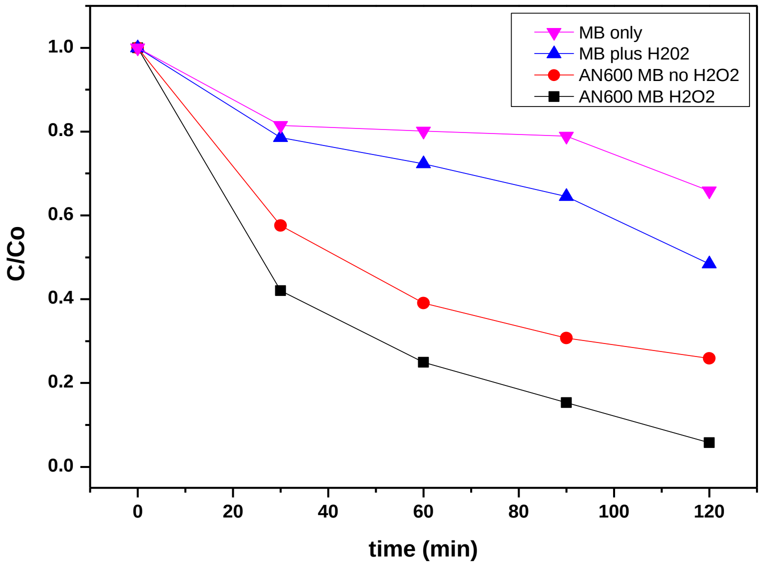

Figure 64: *Percentage degradation of MB dye after 120mins in presence of AN600 coating, H_2O_2 and visible light.*

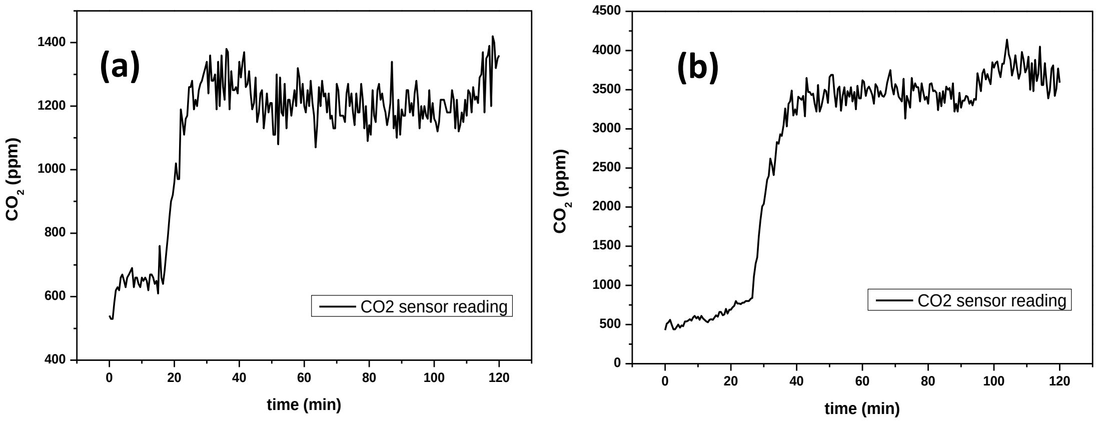

Figure 65: *CO$_2$ evolution during MB degradation by AN600 sample (a) in presence of visible light without H$_2$O$_2$ (b) in presence of H$_2$O$_2$ and visible light.*

The photocatalytic activity of MB dye was also tested in presence of WO$_3$ coatings (AN600) in different pH (**Fig. 66**). The best activity was seen for pH 4 which is as expected because photo-Fenton reactions as well as WO$_3$ catalyst both have ideal/stable conditions in the pH range 3-5.

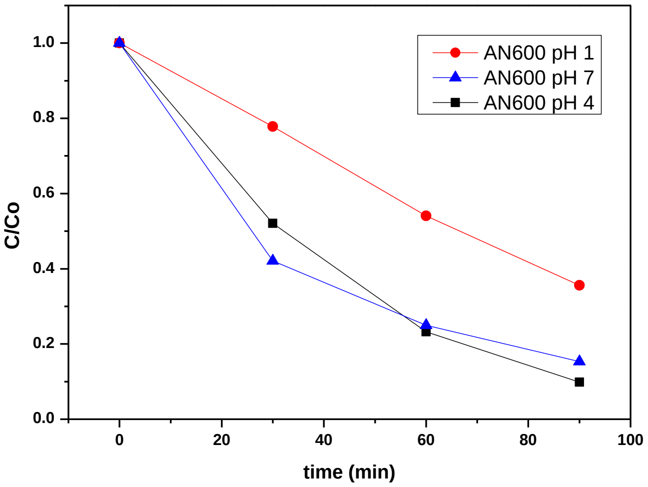

Figure 66: *Effect of pH on photocatalytic degradation of MB by AN600 sample in presence of H$_2$O$_2$ and visible light.*

In the solar concentrator experimental setup, the role of light, H$_2$O$_2$ and catalyst, in catalytic degradation was evaluated in the same way as in the lab scale photocatalytic degradation by performing the separate degradation of MB dye, (1) in presence of concentrated light only, (2) with added H_2O_2 and concentrated light, (3) with coating annealed at 600˚C and concentrated light, and (4) combination of all three (H_2O_2, concentrated light and catalyst) [**Fig. 67**]. In 120 mins, the degradation of MB dye in light is about 54% which increases to 63% after inclusion of H_2O_2. Finally adding tungsten oxide coating along with H_2O_2 and light the degradation occurs significantly higher with about 85% degradation in 120 mins. This indicates that the catalyst coating follows photo-Fenton reaction by generation of $OH^{\bullet}$ radicals by dissociation of H_2O_2.

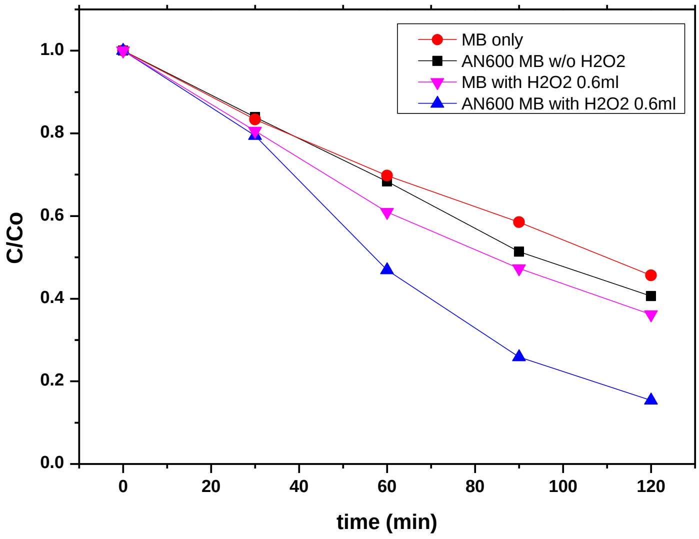

Figure 67: *Percentage degradation of MB dye after 120mins under concentrated sunlight in presence of AN600 coating and* H_2O_2*.*

6.4 Conclusions

m-WO_3 nanostructured coatings were prepared by PLD for photocatalytic application for the first time to our knowledge. PLD targets were prepared by a mixture of metallic W and H_3BO_3. The as-deposited (AD) samples were thermally annealed at 600 °C for forming monoclinic phase of "flower-shape like" nanostructured WO_3 coating. The WO_3 nanostructured coatings were tested for photocatalytic MB dye degradation and the coatings showed enhanced photocatalytic degradation of MB dye under photo-Fenton conditions. The enhanced photoactivity can be attributed to the surface morphology that provides high surface area thereby acting as an efficient adsorber that allows an enhanced interaction between the dye molecules and the active sites for photocatalytic reactions. Solar scaling-up experiments were employed to eliminate the use of an artificial source of light thereby making the whole process economically efficient for low-cost industrial applications. The WO_3 coatings showed good results in the solar PDC setup under photo-Fenton conditions thus expanding the outreach of the synthesized coatings. This work turns into a promising possibility for further photocatalytic studies on WO_3 coatings fabricated by PLD under concentrated sunlight thereby moving towards the use of free, renewable solar energy.

Chapter 7: Pulsed laser deposition of nickel oxide films with improved optical properties to functionalize solar light absorbing photoanodes and very low overpotential for water oxidation catalysis

Preview: Transition metal oxide coatings of nickel oxide show good electrochemical activity as photoanodes for Oxygen Evolution Reaction (OER). Pulsed Laser Deposition (PLD) was used to fabricate nanostructured NiOx coatings of different morphologies, namely compact and porous. Electrochemical measurements were performed on both the morphologies along with optical measurements to evaluate the use as co-catalysts on solar absorbers in photoelectrochemical cell (PEC). A detailed study of different film thicknesses, morphologies and in-depth electrochemical measurements are reported in this chapter.

My contribution to this work includes the Pulsed Laser Deposition of thin NiOx coatings and the electrochemical measurements and its analysis/interpretation.

The content of this chapter is adopted from;

Alberto Mazzi, Michele Orlandi, Nicola Bazzanella, Yaksh J. Popat, Luca Minati, Giorgio Speranzaa and Antonio Miotello, Materials Science in Semiconductor Processing 97 (2019), 29-34. https://doi.org/10.1016/j.mssp.2019.02.036

7.1 Introduction

NiO_x based materials are employed in a variety of applications: mesoporous NiO is widely used as a photocathode material in dye-sensistized solar cells and photoelectrosynthetic cells [267–271], the $Ni(OH)_2$/NiOOH hydroxide/oxyhydroxide system is found in rechargeable batteries [272], the electrochromic behavior of NiO/$Ni(OH)_2$/NiOOH thin films is exploited in smart windows and displays [273–276]. Both the hydroxide and the oxyhydroxide are reported to be good water oxidation catalysts (WOC) [277,278], with an onset overpotential of about 400 mV in the case of pure nickel oxides [279,280]. The catalytic performance of nickel oxide are significantly improved through the incorporation of iron, with an overpotential of 280 mV at 10 mA cm^{-2} and a 40 mV/decade Tafel slope [280,281].

The development of cheap, efficient and scalable materials as WOC is crucial in the technology of electrochemical water splitting and even more for the photoelectrochemical version [89]. The oxygen evolution reaction (OER) is indeed a kinetically slow process, requiring the exchange of four carriers to produce one oxygen molecule. Among inorganic heterogeneous catalysts, noble metal based materials as IrO_x and RuO_x are currently considered as a benchmark for WOC performance in acidic media [282], with as small an overpotential as 190 mV at 1 mA cm^{-2} for amorphous iridium oxide [283]. On the other hand, in recent years, amorphous transition metal oxides based on iron, cobalt and nickel gained increasing attention because of their stability and promising performances as WOC in alkaline media [277,278,284–286]. When WOCs are applied as co-catalysts for the functionalization of semiconductor-based photoanodes, they need to match additional requirements in order to effectively improve the photoelectrode performance. Once the thermodynamics of the photoanode/WOC system are favorable, the morphology of the WOC becomes crucial: porous layers permeable to ions favor the formation of adaptive junctions [287] and, depending on the dimensions and roughness, may exhibit high transmittance in the visible range, due to reduced reflectance and/or quantum confinement [288,289]. Both these features generally improve photoelectrochemical cell (PEC) performance, by enhancing charge-separation and reducing non-effective light absorption by the WOC layer [290].

A nanosized porous morphology would thus allow to obtain high catalytic performance with a minimal amount of catalyst. This is of crucial importance in the case of amorphous NiO_x used as a WOC. In fact, nickel oxide is well known as an anodic electrochromic material, becoming black at moderate positive biasing [275].

Pulsed laser deposition (PLD) is a thin-layer fabrication method based on the ablation of a target material by high fluence laser pulses, followed by deposition of the ablated material on a substrate. Several key parameters (laser fluence, background atmosphere composition, pressure, substrate temperature, target-to-substrate distance, number of pulses) can be adjusted to control structure and morphology of the deposited material at the nanometric scale [291–294]. It is worth noting that this can be achieved while keeping the material amorphous, which is known to greatly enhance catalysis performance in several metal-oxides, among which NiO_x [277]. PLD is thus an ideal instrument to fine-tune optical and catalytic properties of materials.

In this investigation, Nickel oxides coatings were deposited through PLD on fluorine-doped tin oxide (FTO) transparent conducting layers. Depositions at 300°C (DEP300) or at room temperature followed by post-deposition annealing at 300°C (AN300) led to very different morphologies, compact and highly porous respectively. The obtained catalyst layers were characterized through scanning electron microscopy (SEM), X-ray photoelectron spectroscopy (XPS) and Raman spectroscopy. Optical properties were investigated by UV-VIS-NIR spectrophotometry and the electrocatalysis performance as WOC was evaluated by voltammetry and Tafel analysis.

7.2 Materials and Methods

Thin, porous Ni oxide coatings were deposited through PLD on FTO-coated glass electrodes. The substrates were cut as 15×25 mm slides and cleaned by successive ultrasonic treatments in acetone and 2-propanol. The PLD process was carried out in a vacuum chamber, by focusing a KrF excimer laser beam (Lambda Physik LP 220i) on a pure nickel target (Sematrade, 99.95%). The laser was operated with a wavelength of 248 nm, pulse duration of 20 ns, repetition rate of 20 Hz, and laser fluence of 2.0 J cm^{-2}. The substrates were placed at a distance of 5.5 cm from the target surface, parallel to it. The PLD chamber was evacuated prior deposition to a background pressure of 10^{-4} Pa. Nickel oxides were obtained by applying an oxygen controlled flux with equilibrium pressure of 45 Pa during the deposition process. Further details of the PLD setup are available elsewhere [60]. Films of different thickness were obtained by changing the number of laser pulses, between 2,000 (2k) and 20,000 (20k). The substrate temperature was either room temperature or 300°C (samples indicated as RT and DEP300, respectively). In the case of deposition at room temperature, in order to obtain a stable electrochemical response, a post-deposition treatment at 300°C for 2h in air was required (AN300).

Scanning electron microscopy (SEM) analyses were performed with a SEM-FEG JSM-7001F JEOL microscope, operated at 20 keV electron beam energy. The XPS measurements were carried out using a Kratos Axis DLD Ultra. Wide scans were acquired in the binding energy (BE) energy range 1200–0 eV using a 160 eV pass energy, while high resolution core line spectra were performed setting the analyzer pass energy at 20 eV and the energy step at 0.05 eV. Spectra were analyzed using a home-made software based on R platform.

The vibrational modes and short-range order of the coatings deposited on FTO substrates were studied via Raman spectroscopy, using a Labram Aramis Jobin- Yvon Horiba micro-

Raman apparatus equipped with a He-Ne laser source (632.8 nm). The optical properties and the electrochromism of NiO_x coatings were analyzed with a Varian Cary 5000 UV-VIS-NIR absorption spectrometer. The electrochemical measurements were performed using a Gamry potentiostat/galvanostat/ZRA Interface 1000 in a three-electrode cell configuration. The experimental setup included a saturated calomel electrode (SCE, 0.244 V vs. standard hydrogen electrode SHE) used as reference electrode, a Pt-mesh as counter-electrode and a 150 ml 1.0 M KOH solution as electrolyte. The geometric area of FTO/NiO_x electrodes under analysis was 1 cm^2. A conductive copper-based adherent tape was applied to a bare portion of FTO to provide a good electric contact with the electrode holder. All the electrochemical measurements were performed in static solution. Cyclic voltammetries (CV) were collected at 100 mV s^{-1} while linear-sweep voltammetries (LSV) were collected at a 10 mV s^{-1} scan rate. iR drop compensation was applied only for LSVs. Electrochemical potentials reported in this paper are relative to the reversible hydrogen electrode (RHE), with pH correction, unless otherwise indicated:

$$E_{\mathrm{RHE}} = E_{\mathrm{applied}} + 0.244\ \mathrm{V} + 0.059\, pH.$$

7.3 Results and Discussion

PLD technique is based on the laser ablation of a solid target and on the deposition of the ablated material on a substrate after a short flight in vacuum or in a reactive atmosphere. In the case of the nanosecond laser ablation of metals, material removal occurs through thermal processes, mainly vaporization and phase explosion [295,296]. In our case, given the relatively low laser fluence of 2.0 J cm^{-2}, it is reasonable to expect that the ablation process mainly proceeds through vaporization. The relatively high oxygen pressure in the PLD process (45 Pa) results in a collisional regime of the ablated material [297], which also combines with oxygen through chemical reactions. The collisional processes are expected to contribute significantly to nanoparticle (NP) formation in the ablation plume, which are then deposited on the substrate.

The two synthesis routes, DEP300 and AN300, were designed to provide a different film morphology, but with the same amount of catalyst. Indeed, in the PLD process, the ablation yield depends on laser parameters and on the thermophysical quantities of the target material [298], while the deposition rate is also related to the eventual presence of a gas atmosphere and to the geometrical parameters of the experimental setup. The substrate temperature, on the other hand, mainly affects the cooling process of the ablated high temperature material (vapor and NPs) that strikes the substrate surface. Thus, keeping constant all parameters except the substrate temperature, the quantity of deposited material will not change. Due to the higher substrate temperature in the case of DEP300 compared to AN300, the nanostructures that aggregate to the substrate surface undergo a slower cooling process. Indeed, similarly to our recent results obtained with iron oxide [294], AN300 shows a highly porous morphology, compared to DEP300, since in the latter case the slower cooling allows some particle mobility and agglomeration.

Top-down SEM images shown in **Fig. 68** are consistent with this interpretation. We can see in **Fig. 68 (b) and (d)** that both DEP300 2k and AN300 2k (2k=2,000 laser pulses) resulted in a complete covering of the FTO layer with nickel oxides. In particular, in the case of DEP300, the morphology we observe is compatible with an assembled-NPs coating, while AN300 shows smaller scale nanostructures with a higher porosity.

The difference in film morphology obtained through the two processes is more evident in **Fig. 69**, which shows a cross-section view of DEP300 20k (a) and AN300 20k (b) (20k=20,000 laser pulses) deposited on flat silicon substrates. While DEP300 appears as a compact film of agglomerated nanoparticles, AN300 shows a foamy structure. Film thickness in the case of DEP300 20k is estimated between 50 and 100 nm; on the other hand it is hard to univocally define the thickness of AN300 20k, due to the enhanced porosity. Anyway, as an order of magnitude, we can say that AN300 is 5–10 times more thick compared to DEP300. Given that the same amount of catalyst was deposited on both electrodes, we assume that AN300 is 5–10 times macroscopically less dense than DEP300, providing a higher catalyst–electrolyte active surface and a better ion permeability.

The short-range order of the nickel oxides films was studied through Raman spectroscopy. In **Fig. 70**, we can see the Raman spectra of FTO/ NiO_x electrodes, collected with a 632.8 nm wavelength He-Ne laser source, focused on the catalyst surface through a 100× confocal microscope objective. We also compare the spectra with that of a bare FTO surface. We can see that all the features in the spectra of both DEP300 20k and AN300 20k are compatible with the Raman response of the underlying FTO layer, proving the largely amorphous nature of the catalyst thin films.

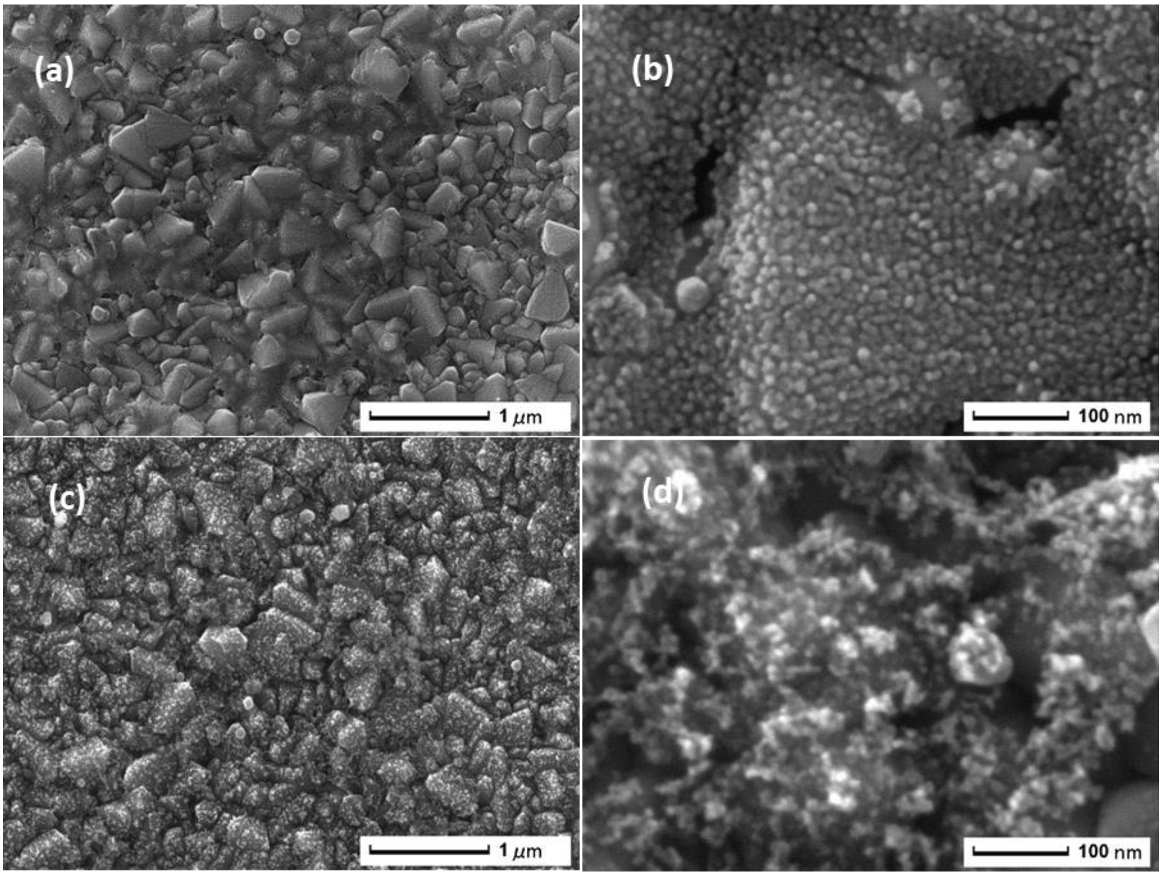

Figure 68: *SEM top-down images of NiO_x thin films deposited on FTO substrates at different magnifications: (a) and (b) DEP300 2k, (c) and (d) AN300 2k. The jagged morphology of the underlying FTO layer at a scale of hundreds of nanometers is clear in (a) and (c). NiO_x nanoparticles have a typical size of $\lesssim$10 nm, with an irregular shape in the case of AN300.*

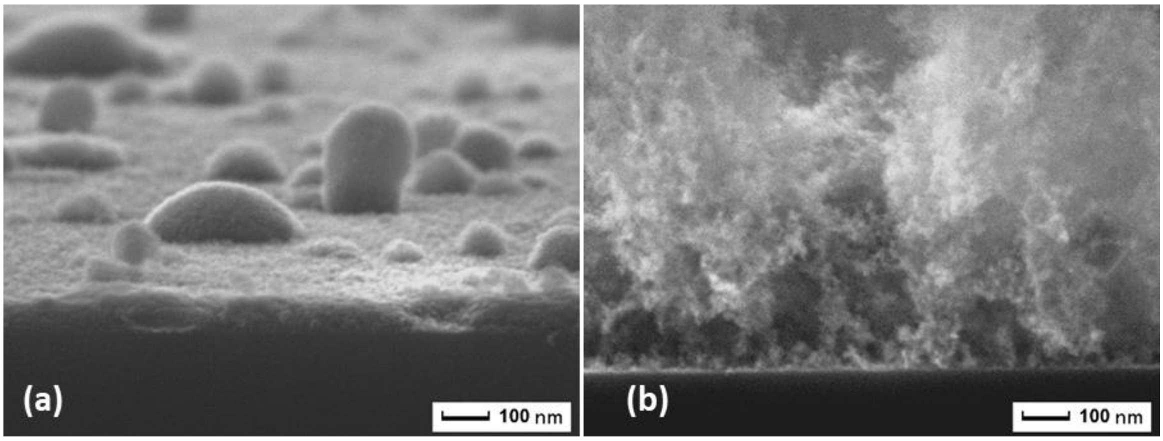

Figure 69: *SEM cross-section images of thick catalyst layers deposited on flat silicon slides. (a) DEP300 20k and (b) AN300 20k.*

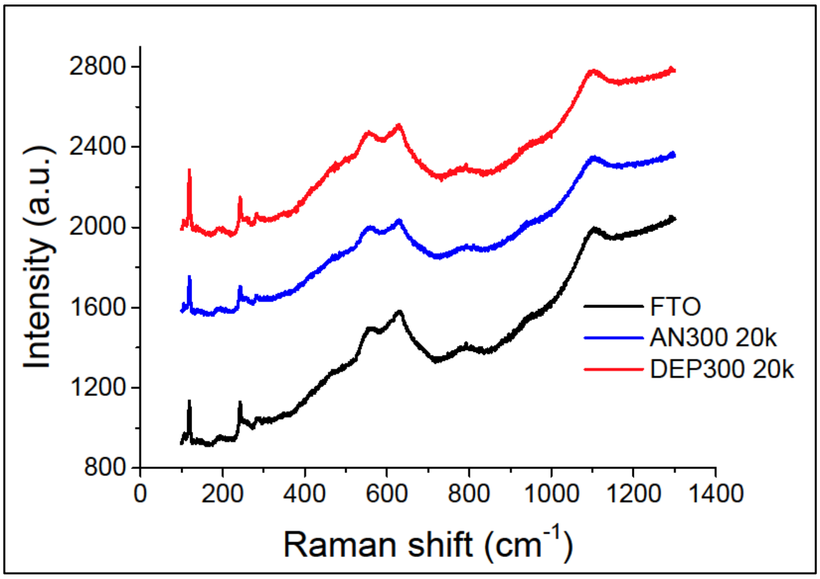

Figure 70: *(Color online) Raman spectra of AN300 20k and DEP300 20k compared to that of bare FTO. Nickel oxides thin films show an amorphous phase in both cases.*

In **Fig. 71**, we analyze more in detail the region around 1100 cm^{-1}, where the main band of NiO, related to a two-phonon process [299,300], should emerge. We prove that the peaks in DEP300 20k and AN300 20k close to 1100 cm^{-1} are only due to a FTO band since, when the FTO spectrum is subtracted, the peak is fully removed. No peaks attributable to nickel oxide crystallites were present also in the case of the 2k series [301].

XPS analysis of DEP300 2k and AN300 2k revealed the presence of either $Ni(OH)_2$ or NiOOH as the main phase. The Ni $2p_{3/2}$ peak observed at 855.5 eV, together with the satellite peak at 861.0 eV, can be attributed to both $Ni(OH)_2$ and NiOOH, within the experimental errors [302]. Moreover, the peak at 853.9 eV was assigned to the presence of NiO, whose $2p_{3/2}$ peak should appear at 854.5±0.9 eV [302]. The XPS signals of DEP300 2k and AN300 2k around the Ni $2p_{3/2}$ region, together with the complete survey of the XPS spectra are shown in **Fig. 72**.

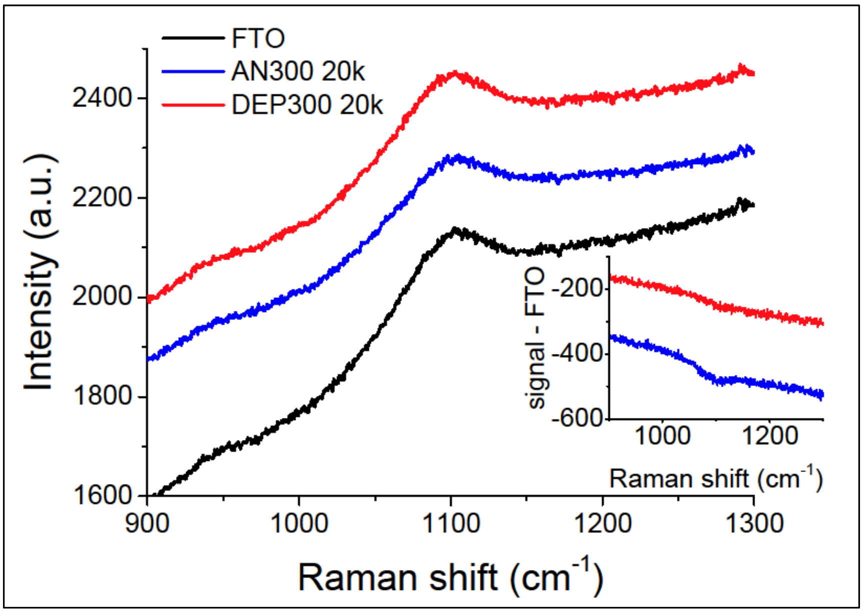

Figure 71: *Raman spectra of AN300 20k and DEP300 20k deposited on FTO, compared to that of a bare FTO substrate. In the inset, the FTO background was subtracted to the* NiO_x *spectra.*

In view of the application of nickel oxides thin films to functionalize water oxidation photoanodes, we characterized the optical features of our FTO/NiO_x electrodes through UV-VIS-NIR spectrophotometry. Absorbance and transmittance spectra were acquired using a bare glass/FTO electrode as a reference. The samples were backside illuminated, so that light reflection from the flat glass surface can be assumed to be the same on all samples. **Fig. 73 (a)** shows the absorbance spectra of DEP300 and AN300 from both the 2k and 20k series. The optical features of the nickel oxide thin films were studied, referring to that of NiO, $Ni(OH)_2$ and NiOOH [303,304], the possible phases identified through XPS analysis.

Nickel monoxide, NiO, is a charge-transfer insulator, with an optical bandgap of about 4 eV [303,305]. NiO is intrinsically prone to structural defects, usually presenting an excess of oxygen [303], whose amount determines the actual NiO optical features [299,303]. $Ni(OH)_2$ is an n-type semiconductor, with an optical bandgap usually measured between 3.6 and 3.9 eV [304]. Finally, NiOOH, is a p-type semiconductor and its optical bandgap is of about 1.7–1.8 eV [304].

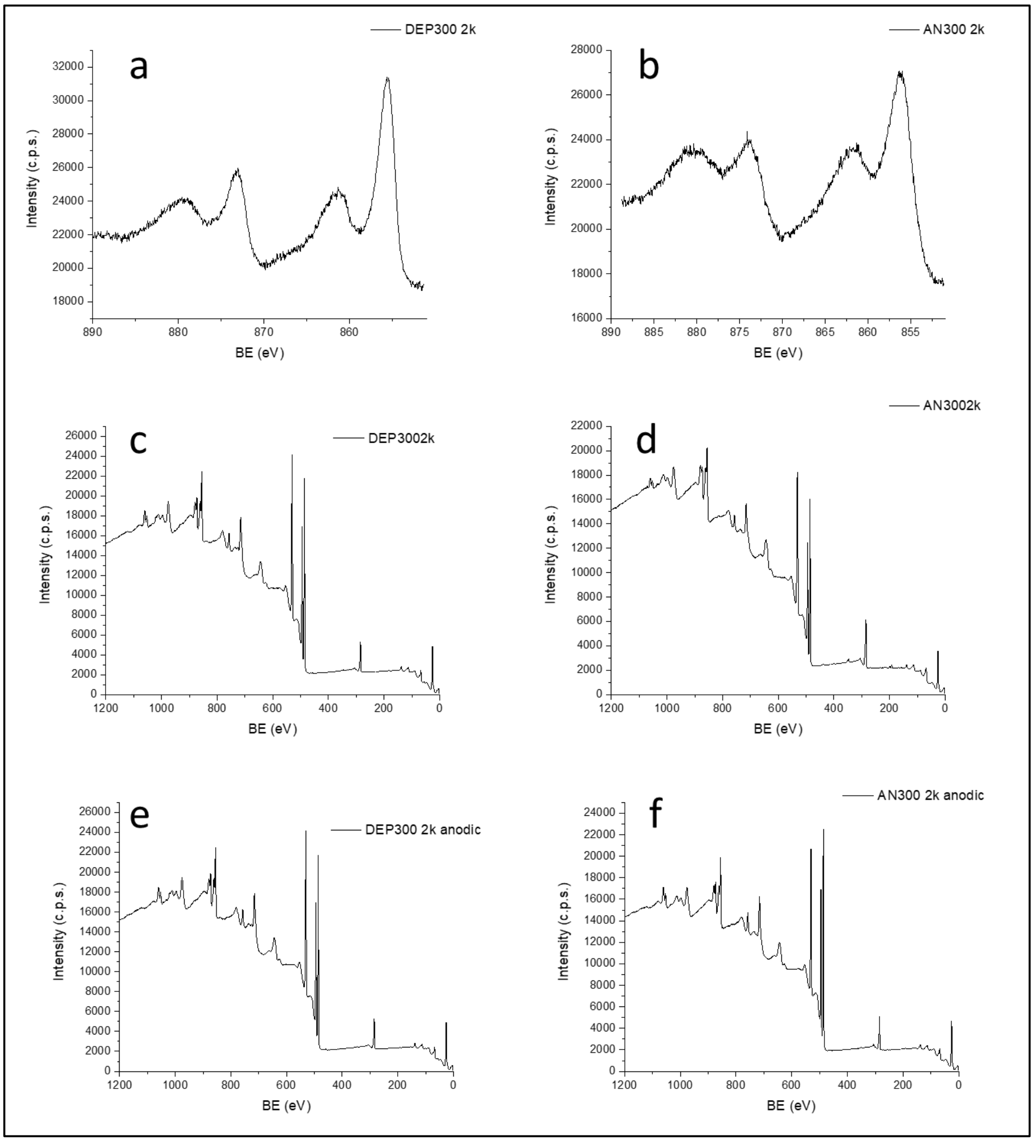

***Figure 72:** XPS spectra of nickel oxide thin films deposited on silicon slides. Panels (a) and (b) show the Ni $2p_{3/2}$ region of DEP300 2k and AN300 2k, respectively. Plots in (c), (d), (e) and (f) show the Survey spectra of DEP300 2k, AN300 2k, DEP300 2k after anodic treatment and AN300 2k after anodic treatment.*

Through the Tauc analysis of the absorption edge region, we evaluated the optical bandgap of the Ni oxide thin films for direct transitions. In particular, the quantity $(Ah\nu)^2$ was plotted as a function of the photon energy, where A is the absorbance, directly proportional to the absorption coefficient. The linear fit of the Tauc relation allowed us to evaluate the optical bandgap of DEP300 20k and AN300 20k as 3.6 eV and 3.7 eV, respectively, with 0.1 eV uncertainty. The contribution of NiOOH is probably too low to be detected. The same analysis on the films from the 2k series gave comparable results, but with a lower accuracy due to the worse signal to noise ratio.

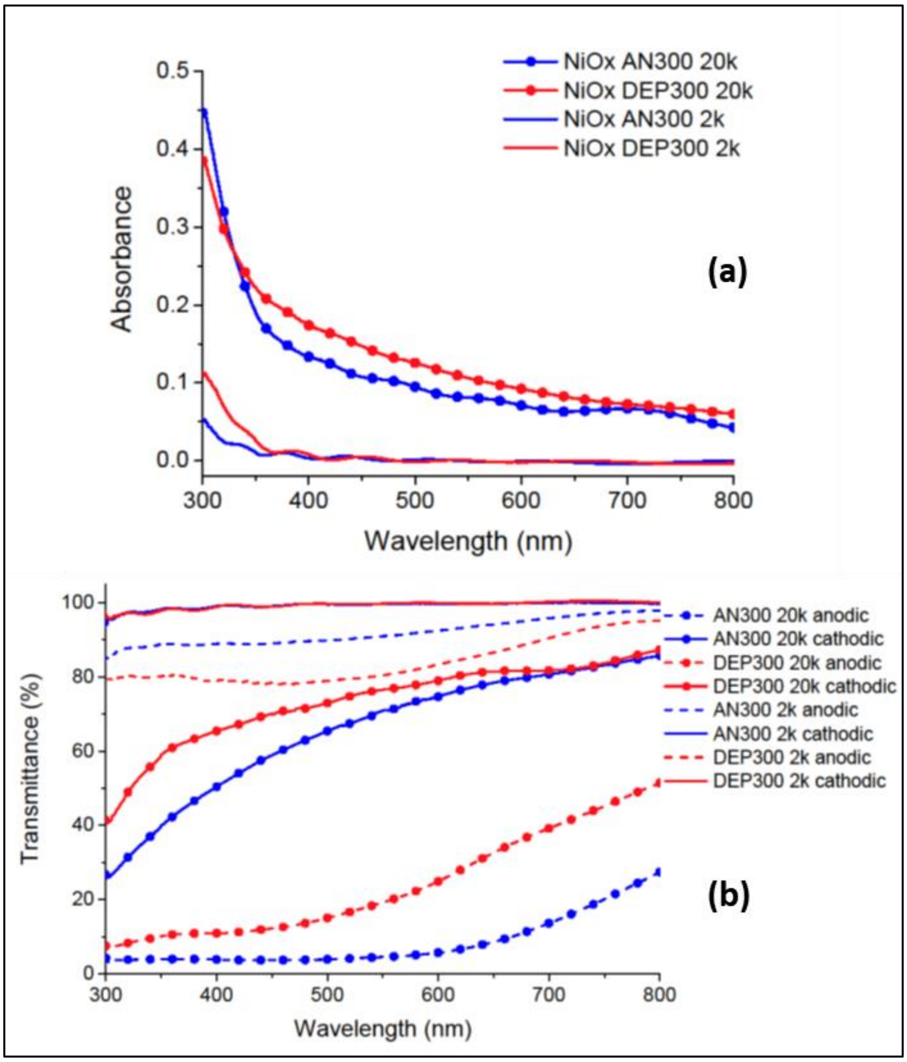

Figure 73: *(a) Absorption spectra of AN300 and DEP300 from both 2k and 20k series. (b) Transmittance spectra of AN300 and DEP300 from 2k and 20k series, after electrochemical measurements under anodic or cathodic biasing.*

The absorption measurements were repeated on the same electrodes after usage in an electrochemical cell. The glass/FTO/NiO_x electrodes were operated alternatively at anodic or cathodic biasing in 1 M KOH solution. First, 30 voltammetry cycles were run in order to obtain a stable response, in the range $0 \div 0.7$ V and $0 \div -1.8$ V vs. saturated calomel electrode (SCE) in the case of anodic or cathodic measurements, respectively. Then a short chronoamperometry measurement was performed for 5 minutes at 0.7 V or -1.8 V vs. SCE for anodic or cathodic conditions, respectively, providing a current density of the order of 10 mA cm^{-2}. These measurements were carried out without applying iR compensation.

In **Fig. 73 (b)**, we show the transmission spectra of the Ni oxide thin films after anodic or cathodic measurements described above. Transmittance was calculated as $T = 10^{-A}$ and expressed as a percentage. The spectra obtained from the 20k series allowed us to evaluate the change in the optical bandgap associated to the electrochromic transition of Ni oxide. Under anodic biasing, the Ni oxides film becomes colored, absorbing more than 60% or 85% in the case of DEP300 20k or AN300 20k, respectively (see dashed curves with markers in **Fig. 73 (b)**). In this condition, the optical bandgap is reduced to 1.6÷2.0 eV, indicating oxidation of $Ni(OH)_2$ to NiOOH, in agreement with the Bode reaction scheme [306]. The redox process between the states Ni^{2+} and Ni^{3+} is reversible, so that under cathodic biasing, the Ni oxide film becomes bleached, showing a bandgap of 3.5÷3.6 eV, attributable to the nickel hydroxide phase. The results of Tauc analysis are summarized in **Table 5**.

	E_G (as synthesized), eV	E_G (anodized), eV	E_G (cathodized), eV
DEP300 20k	3.6 ± 0.1	1.96 ± 0.02	3.6 ± 0.2
AN300 20k	3.7 ± 0.1	1.55 ± 0.02	3.5 ± 0.1

***Table 5:** Optical bandgap of the Ni oxide thin films obtained from absorption measurements through the Tauc analysis. The results obtained after anodic and cathodic measurements give information about the electrochemical processes occurred in the Ni oxides thin film.*

The same behavior was observed in the electrodes from the 2k series, while the quantitative evaluation of the optical bandgap was affected by a large error due to the reduced film thickness, especially in the case of the bleached phase. It is worth noting that, while the 20k series catalysts show a very poor transmittance in the visible range under anodic conditions, the thin films from the 2k series present a transmittance of about 80% or 90% in the whole visible range in the case of the compact or porous film, respectively.

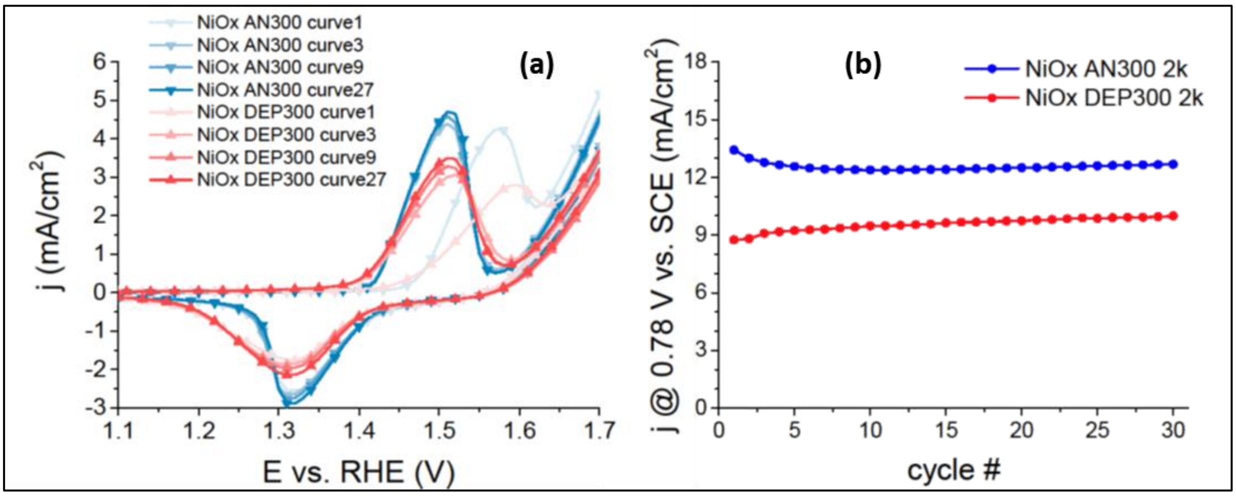

***Figure 74**: (a) Cyclic voltammetry curves. (b) Current density versus cycle.*

The electrocatalysis performance of the materials towards the OER was evaluated in terms of overpotentials and Tafel slopes. A set of about 30 anodic CVs was performed to ensure a stable response of the electrochemical setup (**Fig. 74 (a) and (b)** show CV curves and current density versus cycle number, respectively), followed by *iR* compensated LSVs (**Fig. 75**). A precatalytic oxidation peak, accompanied by the corresponding reduction process in the reverse scan, features prominently in the CVs in **Fig. 74 (a)**. This is assigned to the $Ni(OH)_2$/NiOOH redox couple [278], in agreement with literature and confirming XPS results.

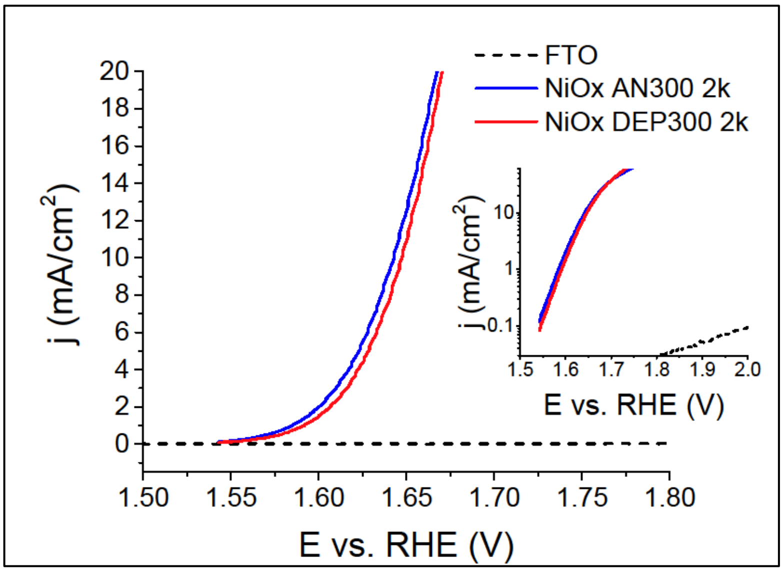

***Figure 75:** $j - V$ curves of thin catalyst films deposited on FTO. In the inset we show the Tafel plot. The black, dashed line was obtained with a bare FTO electrode, as reference.*

Overpotentials (η) at two selected current-density (J) values (1 and 10 mA cm^{-2}) were extracted from these curves: the first approximates the beginning of the catalytic process and is useful for literature comparison, while the second is of interest for WOC to be applied in PECs [282]. Tafel plots are shown in **Fig. 75**, inset. All data are reported in **Table 6**.

	η @ $J = 1$ mA cm^{-2} (mV)	η @ $J = 10$ mA cm^{-2} (mV)	Tafel slope (mV/decade)
AN300 2k	355 ± 1	413 ± 1	62 ± 0.3
DEP300 2k	362 ± 1	418 ± 1	59 ± 0.1

***Table 6:** Selected electrode metrics for DEP300 and AN300 operated as WOC.*

The results of LSV measurements obtained with thicker catalyst films (20k series) are reported in **Fig. 76** and the metrics of the two series as WOC are summarized in **Table 7**. Since the thicker films are both less active and less transparent, they will not be discussed further.

With a comparable Tafel slope and slightly better overpotentials, AN300 can be considered a better WOC compared to DEP300. According to a recent report [280], iron incorporation can play a critical role in determining NiO_x electroactivity. In our case however, this can be excluded since XPS (**Fig. 72 e, f**) shows no trace of iron after electrochemical experiments.

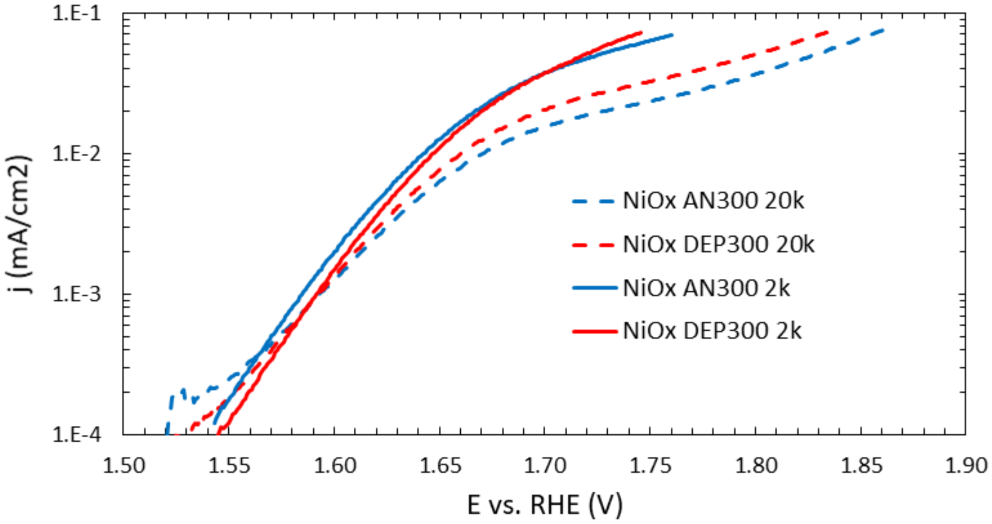

Figure 76: *Tafel plot of thick catalyst films (20k series) compared with thin films (2k series) deposited on FTO. The catalytic performance is not limited by the amount of catalyst and thicker films show lower currents possibly due to the increased resistivity of nickel oxide film.*

	η @ J = 1 mA cm^{-2} (mV)	η @ J = 10 mA cm^{-2} (mV)	Tafel slope (mV/decade)
AN300 20k	362 ± 1	441 ± 1	71 ± 0.5
DEP300 20k	362 ± 1	427 ± 1	66 ± 0.5
AN300 2k	355 ± 1	413 ± 1	62 ± 0.3
DEP300 2k	362 ± 1	418 ± 1	59 ± 0.1

Table 7: *Comparison of electrode metrics for DEP300 and AN300 from 20k and 2k series, operated as WOC.*

7.4 Conclusions

The porous structure obtained here exhibits a very high (90%) optical transmittance in the visible-range, even under anodic conditions, while also showing good performance as WOC, with overpotentials and Tafel slopes on-par with some of the best results for amorphous NiO_x in recent literature [278,285]. Both these features are important in view of the application of NiO_x as OER co-catalysts in photoanodes for PEC technology. The high transmittance in particular provides a solution to the problem of parasitic light absorption, which to date prevented the effective use of Ni oxides for photoanode functionalization. Thus, the functionalization of absorber materials to realize such a photoanode will be the natural extension of this work, as well as the extension to mixed-metal oxide species which are known to be intrinsically more active [286,307]. PLD proves to be a highly versatile fabrication technique to control morphology at the nanoscale, thus allowing the tuning of functional properties which critically depend on it. By varying the substrate temperature during deposition, NiO_x morphologies ranging from a compact NPs-assembled layer to a porous coating can easily be obtained, while keeping the material substantially amorphous, an important feature for several catalysis applications.

Chapter 8: Alkaline water oxidation studies on mixed metal oxide thin films deposited by pulsed laser deposition

Preview: Mixed metal oxide coatings were synthesized by Pulsed Laser Deposition (PLD) as water oxidation catalysts for OER. Boron was added to the films to study its influence in the electrochemical performance of the films. The synthesized coatings exhibited superior electrochemical activity compared to single oxide coatings and mixed metal oxide coatings without boron. The role of boron, iron and cobalt was systematically investigated through in-depth characterization and electrochemical measurements.

My contribution to this work includes the synthesis of all the coatings, performing electrochemical measurements along with other characterizations, interpreting the data/results obtained and preparation of the final manuscript.

8.1 Introduction

The rapid industrialization coupled with population explosion has put tremendous stress on the existing energy sources of the planet. Hence, it is important to look for alternate renewable energy carriers like hydrogen to sustain the current as well as future energy needs. Currently, hydrogen production occurs mainly through steam reforming of natural gas, a process leading to high emission of greenhouse gases along with its fossil fuel dependence. Electrochemical water splitting has been considered as one of the promising techniques for sustainable production of H_2 and O_2 owing to simple nature of the process along with no harmful gas emission and high conversion efficiency. Oxygen Evolution Reaction (OER), however, requires a large overpotential to overcome the significant kinetic barrier associated with the exchange of four electrons and thus shows very slow kinetics. Hence, electrocatalysts are required in this process to reduce the overpotential and improve the efficiency of the process. Metal oxides are generally more stable for water oxidation reactions compared to metals due to their resistance in getting oxidized even further [308]. Iridium oxide (IrO_2) and ruthenium oxide (RuO_2) catalysts are reported to be one of the best OER electrocatalysts [309]. However, as they belong to the rare inert group of catalysts and are scarcely available [310], efforts have been made to synthesize electrocatalysts which are abundant and made up of cheap scalable materials. Transition metal oxides of Fe and Co are extensively studied for photocatalytic and electrocatalytic water oxidation respectively, due to their earth abundance and low cost.

Nanostructured α-Fe_2O_3 thin films have been investigated as photoanode in photoelectrochemical water splitting [311]. Iron oxide catalysts (α-Fe_2O_3) synthesized by Pulsed Laser Deposition functionalized on ITO surfaces showed stable photocurrents at relatively low overpotentials for electrochemical water splitting [312]. Reduced graphene oxide wrapped ITO@Fe_2O_3 core-shell nanowire arrays served as photoanode showed promising results for making Fe_2O_3 composites for future water splitting applications [313]. Porous amorphous Fe_2O_3 films synthesized by PLD opened up the possibility of functionalizing solar absorbers with iron oxide thin films as efficient photo-electrocatalysts [294]. Synthesis of mesoporous Co_3O_4 via nanocasting route and different nanostructures of Co oxide by facile hydrothermal method as Oxygen Evolution Catalysts (OECs) demonstrated the role of morphology in electrochemical water splitting [314,315]. Light and inexpensive nanostructured Co_3O_4 clusters in mesoporous silica efficiently produced oxygen by electrochemical water splitting thereby providing an alternative to the noble IrO_2 [310]. Cobalt oxide catalysts are generally quite active for OER in the alkaline medium [316–318]. Owing to the advancements in the electrochemical studies on cobalt and iron based oxides, research progressed towards electrochemical water splitting using mixed oxide OEC's of cobalt and iron. $CoFe_2O_4$ nanoparticles (NPs) synthesized by facile hydrothermal method and attached on 3D carbon fiber papers exhibits efficient, cost effective and durable oxygen evolution along with its bifunctional electrocatalysis as both OER and HER catalyst [319]. Hybrid nanorod arrays of porous $CoFe_2O_4$/C supported on nickel foam treated with polyaniline exhibited low overpotentials and high stability as OEC in alkaline medium [320]. $CoFe_2O_4$ nanoparticles supported over nitrogen-sulphur doped 3D rGO displayed similar electrocatalytic activity as that of RuO_2/C catalyst with high durability in alkaline medium [321]. These recent advances on Cobalt ferrite ($CoFe_2O_4$) and its composites however has a drawback. $CoFe_2O_4$ nanoparticles are generally synthesized by chemical methods and then supported on different optimized substrates like rGO, which makes it a two-step synthesis procedure. To tackle this problem, it is imperative to have a synthesis/fabrication process which enables the direct deposition of $CoFe_2O_4$ nanoparticles on different substrates in a single step thereby eliminating the need for separate synthesis of $CoFe_2O_4$ nanoparticles. Pulsed Laser Deposition (PLD), gives an immense control over the synthesis of heterogenous catalysts by varying the deposition parameters like gas pressure, film thickness, fluence etc. to get different nanostructured morphologies with good adhesion [83,105,322]. Various metal oxide catalysts have been synthesized by PLD as water oxidation catalyst (WOC) [312,323–325]. 3D hierarchical porous/urchin nanostructured Co_3O_4 coating synthesized by using boric acid in the initial mixture displayed excellent photocatalytic activity towards degradation of MB dye [87]. Similar approach was used for synthesizing 3D hierarchical iron oxide nanostructures where boric acid was used as a source of boron and the resultant films degraded MB dye with good efficiency [107]. Recently published CoFe2O4/CoO hierarchical-type nanostructured coating synthesized with the inclusion of boron exhibited superior photocatalytic activity compared to the single oxide hierarchical coatings of iron oxide and urchin-like Co_3O_4 respectively [326]. In view of the enhanced photocatalysis seen by inclusion of boron, primarily in the outer shell of the nanoparticles, it would be interesting to study its effect on the electrochemical performance of the films active as WOC.

In this paper, we synthesize mixed metal oxide coatings on FTO substrates as a WOC for oxygen evolution reaction (OER). The coatings were synthesized by PLD with targets comprising of a mixture of metallic Fe, Co and boric acid (H_3BO_3). The synthesis protocol is adopted from our past work [326]. Boron was intentionally included in the initial mixture to study its influence on the coatings. The synthesized coatings were characterized thoroughly for in-depth analysis. The mixed metal oxide coating shows excellent electrocatalytic activity with a low overpotential of 315mV for 10mA/cm^2 along with a Tafel slope of 31.5 mV/dec, displaying high stability and recyclability in alkaline medium with almost no deterioration. The electrochemical performance of mixed metal oxide coatings show superior electrochemical activity in OER compared to the single oxide coatings of FeOx and CoOx owing to the formation of stable active species. The coatings synthesized in absence of boron show reduced OER activity indicating that the presence of boron enhances the electrochemical performance of the catalyst coatings. The detailed study and analysis on the structural and electrochemical properties are discussed ahead.

8.2 Experimental

8.2.1 Synthesis

Fe metallic, Co metallic and boric acid (H_3BO_3) powders were mixed in molar ratio of 1:1:1 and the prepared mixture was compressed in the form of a disc to be used as a target for the deposition of CoFeOx coatings by PLD. A KrF excimer laser (Lambda Physik) with an operating wavelength of 248 nm, pulse duration of 25 ns, and repetition rate of 20 Hz was used for deposition. The fluence of the laser was always maintained at 3 J/cm^2 for ablation. The PLD deposition apparatus details and the mechanisms involved in the laser matter interactions are presented in our past reports [60,327]. The PLD chamber was evacuated up to a base pressure of 10^{-6} mbar prior to all the depositions. Deposition of the coatings were carried out in an Argon atmosphere at a pressure of 1.5 x 10^{-2} mbar. The target to substrate distance was fixed at 4.5cm with the substrate positioned parallel to the target. The coatings were deposited on FTO, borosilicate glass and Si at room temperature and the number of pulses deposited were 10k. Thermal annealing of the deposited coatings were carried out in air at 200 ºC, 400 ºC and 600ºC for 5 h with a heating rate of 5 ºC/min.

8.2.2 Characterization

Scanning Electron Microscope (SEM-FEG, JSM 7001F, JEOL) at 20keV electron beam energy equipped with energy dispersive spectroscopy analysis (EDS, INCA PentaFET-x3) were used for examining the surface morphologies of all the samples prepared by PLD. Transmission Electron Microscopy (TEM) and High resolution TEM (HR-TEM) analyses were performed with a JEOL 2100F Cs-corrected analytical FEG TEM with an accelerating voltage of 200 kV equipped with an energy-dispersive X-ray spectrometer (EDS). Images were analyzed using Digital Micrograph software from Gatan. Copper grids (300 mesh) with Holy-carbon film were used as substrate to prepare samples for TEM analysis. Structural characterization was performed using X-Ray Diffractometer (XRD, Rigaku Miniflex) with Cu K_α radiation (λ = 1.5414 Å) in 2θ- θ configuration, with a step size of 0.05 deg and a scan rate of 1 deg/min. Micro-Raman spectroscopy was performed using a Labram Aramis Jobin-Yvon Horiba μ-Raman system equipped with a He-Ne laser source (632nm). The surface composition and chemical states of each element present in the sample were analysed with X-ray Photoelectron Spectroscopy (XPS) using a PHI 5000 Versa II instrument equipped with a monochromatic Al K_α (1486.6 eV) X-ray source and a hemispherical analyser. Appropriate electrical charge compensation was required to perform the XPS analysis.

8.2.3 Electrochemical measurements

Electrochemical measurements were performed using a Gamry potentiostat/Galvanostat/ZRA interface 1000 in a three-electrode cell composed of Saturated Calomel Electrode (SCE, 0.244 V vs. Standard Hydrogen Electrode) as reference, Pt mesh as counter electrode and 1M KOH solution (pH 14) as electrolyte. Catalysts deposited on Fluorine doped Tin Oxide (FTO) glass substrates [1cm^2] were used as working electrodes. Initially, Cyclic Voltammetry (CV) scans were performed on the samples to remove the impurities and stabilize the current. Linear Sweep Voltammetry (LSV) was carried out with iR compensation to reach the current density greater than 10 mA/cm^2. The LSV measurements were done at a scan rate of 10 mV/s while the CV measurements were done at a scan rate of 100 mV/s. Finally, Chronoamperometry (CA) measurements were performed on the samples to check the stability of the catalysts for water oxidation reactions. Electrochemical impedance spectroscopy (EIS) was performed in the frequency range of 2 MHz to 10 Hz with an input sinusoidal wave of amplitude 50 mV. EIS data was fit using Echem Analyst software from Gamry to obtain the equivalent electrical circuits. Determination of the electrochemical surface area (ESA) was carried out by calculating the double layer capacitance (C_{DL}) from CV scans in the non-Ohmic potential region of -0.20 V to 0.10 V (vs Hg/HgO), at increasing scan rates. The graph of difference in cathodic and anodic current densities at -0.05 V was plotted against the respective scan rates to determine the value of C_{DL}.

8.3 Results and Discussions

The as-deposited (AD) as well as the coatings annealed at different temperatures in air were studied by SEM to get insight on the surface morphologies and the changes that occur on annealing. The AD sample **(Fig 77a)** shows particle like morphology with a varied particle size distribution from tens of nanometer to a few micrometers. This kind of morphology is expected owing to the phase explosion process which occurs when the target surface comes close to the thermodynamic critical temperature upon irradiating with high laser fluence. Moreover, the particles seem to have a core-shell structure with the core made up of heavy elements like Fe and Co while the shell comprises of lighter elements, mainly boron. This core-shell morphology is preserved even at 200ºC (**Fig. 77b**) and 400ºC (**Fig. 77c**). The topography of the particles completely change upon annealing in air at 600ºC (**Fig. 77d**). At 600ºC, the shell disintegrates leading to the formation of small nanowires (NWs) on the surface of the particles which leads to complete transformation from spherical particulates to urchin-like hierarchical structures with vertically grown nanowires (NWs) from surface of the particulates. The length and diameter of the NWs vary from 0.5 to 1 µm and 10-30 nm, respectively. The formation of these hierarchical nanostructured coatings at temperatures above 500 ºC is also reported in our previous work [326]. Annealing at 600°C essentially produced two kinds of morphology, hierarchical (petal like) and urchin like nanowires. As mentioned in chapter 3 in the description of SEM images, there is about 10% contribution from petal like morphology. In **Fig. 77d**, the image shown is completely urchin-like which is the case for most of the particles while **Fig. 21g** shows the hierarchical morphology.

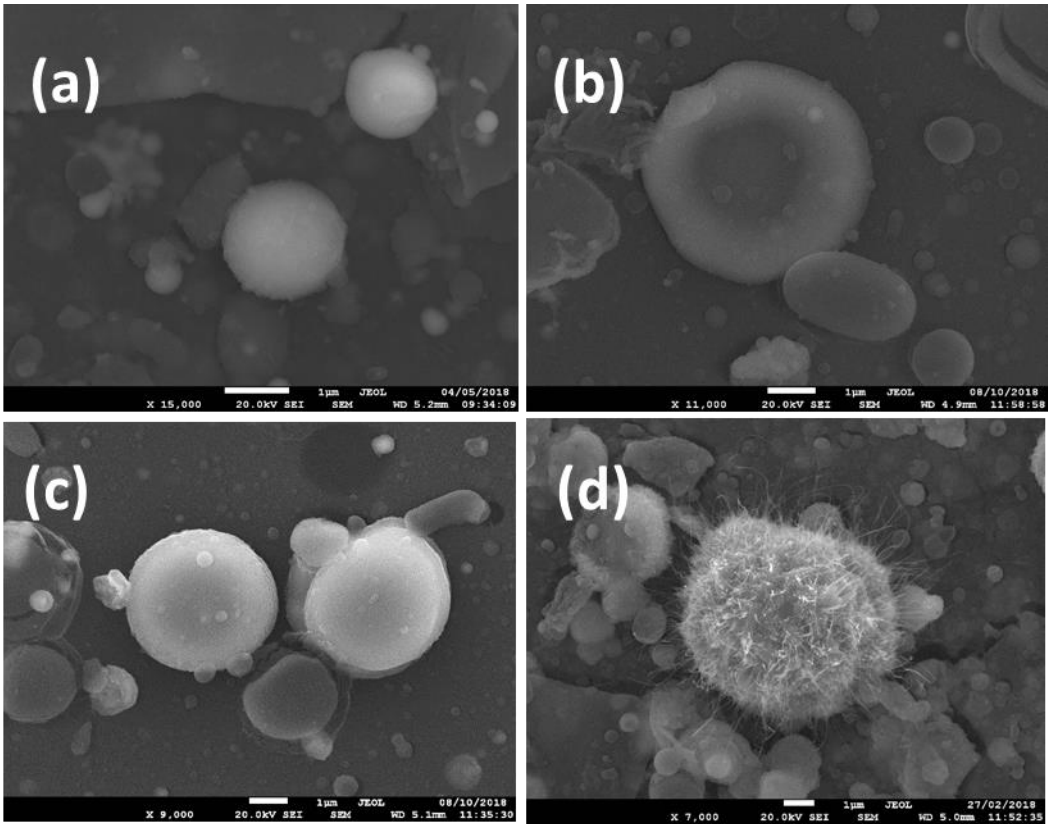

***Figure 77:** SEM images of [a] as-deposited (AD), [b] AN200, [c] AN400 and [d] AN600 samples*

Micro-Raman spectroscopy was performed on the as-deposited and the annealed samples in the range of 150 to 800 cm^{-1} (**Fig. 78a**), where signature vibrations due to metal oxides are located. The AD and AN200 coatings display broad Raman spectra indicating that the films are mostly in the amorphous state. On annealing at 400˚C, Raman peaks at 184 cm^{-1} pertinent to F_{2g} mode of CoO phase [109] and 290 cm^{-1} assigned to E_g mode of α-Fe_2O_3 phase [110] are observed. The deconvoluted peaks observed at 453,586 and 658 cm^{-1} upon annealing at 600˚C display a red shift to 462, 607 and 678 cm^{-1} respectively. The peaks centered at 462 cm^{-1} and 678 cm^{-1} can be assigned to T_{1g} and A_{1g} mode of spinel $CoFe_2O_4$ phase as well as to E_g and A_{1g} mode of CoO phase [108,109] while the peak at 607 cm^{-1} is attributed to A_{1g} mode of vibration of spinel $CoFe_2O_4$ phase. Further confirmation of these phases were carried out by XRD and XPS.

To identify the phases in the as-deposited and annealed coatings, XRD was performed and reported in **Fig. 78b**. XRD pattern was acquired to mainly investigate the crystallinity of the particulates on the coating surface. For AD coating, the peaks centered at 44.2^{o} and 44.9^{o} are assigned to metallic Co and Fe, respectively, while the peaks observed at 54.6^{o} and 56.4^{o} correspond to α-Fe_2O_3 phase (JCPDS-24-0072). On annealing at 200^{o}C, an additional sharp peak at 47.7^{o} is observed, which corresponds to $CoFe_2O_4$ phase (JCPDS-22-1086). This peak intensifies at 400^{o}C along with the appearance of more small peaks corresponding to Co metal and Fe2O3 phases, indicating crystallization of the sample due to heating. On further annealing (AN600 sample), complete crystallization occurs[3], and more peaks related to $CoFe_2O_4$ phase are observed.

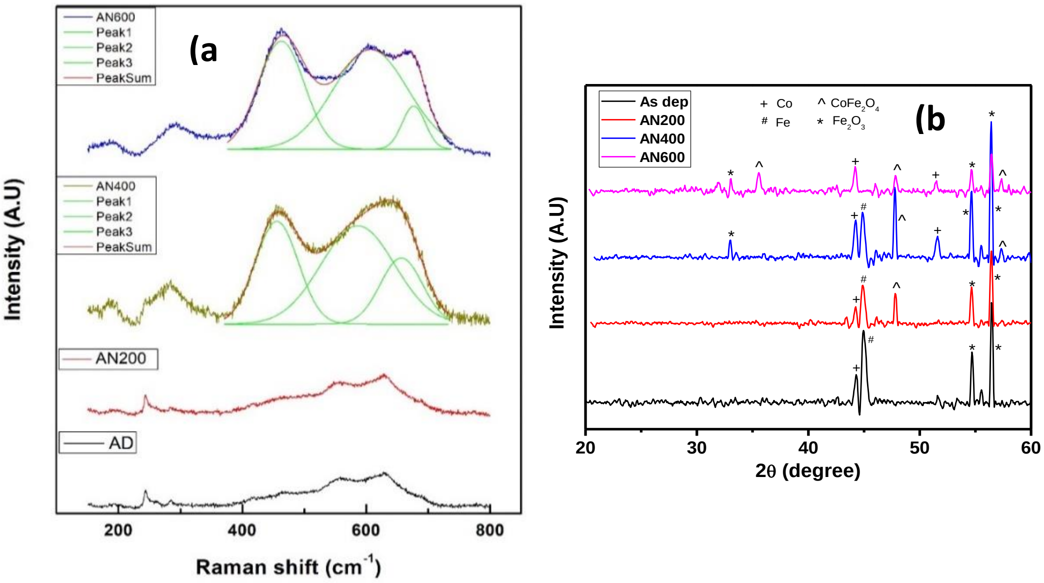

Figure 78: *a) Raman spectra and b) XRD spectra for as-deposited and annealed samples.*

The elemental survey scan of XPS detects elements such as Co, Fe, B and O along with residual carbon for all the samples. Focused scan of Fe_{2p} level (**Fig 79a**) shows existence of two distinct peaks attributed to $2p_{3/2}$ and $2p_{1/2}$ levels for all the coatings. The deconvolution of $2p_{3/2}$ levels for AD and AN200 films exhibit two peaks at 711.1 and 712.1 eV with a satellite peak at 724.5 eV, indicating the presence of Fe^{3+} oxidation state on the surface. In case of AN400 and AN600 samples, a peak at 710.7 eV corresponding to $CoFe_2O_4$ phase emerges along with a peak centered at 712.3 eV, corresponding to $FeBO_3$ phase [328]. It must be noted that no signal due to Fe^{2+} is detected in the XPS spectra. In Co 2p XPS spectra of AD and AN200 samples (**Fig. 79b**), the broad peak due to $2p_{3/2}$ level can be deconvoluted into three peaks centred at 780.9 eV, 782.0 eV and 786.0 eV, corresponding to Co in Co2+ oxidation states [329,330]. In case of AN400, the peak centred at 780.8eV increases in intensity due to the formation of $CoFe_2O_4$ phase [331]. When annealed further to 600°C, the peak positions do not change but area under the peak increases. The core-level spectra of B 1s in AD sample (**Fig. 79c**) shows a single peak centred at 192.0 eV corresponding to both B_2O_3 and $FeBO_3$ phases [332,333]. B 1s spectra in AN200 and AN400 samples denote the same peaks. On further annealing at 600°C, the spectra can be deconvoluted to two peaks centered at 191.5 eV and 192.5 eV due to segregation of $FeBO_3$ and B_2O_3 phases. The XPS spectra of O 1s (**Fig. 79d**) for AD and AN200 coatings are mainly composed of a single broad peak at 531.6 eV corresponding to Fe^{3+}/Co^{2+} and B_2O_3 species. On further annealing at 400°C, three peaks are observed at 529.9eV, 531eV and 532.4eV corresponding to O in metal oxides, $FeBO_3$ and B_2O_3 phases, respectively. The dominant peak is of the $FeBO_3$ species indicating the maximum contribution of this species at this temperature. Annealing at 600°C results in the same peaks as in AN400 but with reduced $FeBO_3$ peak concentration and the dominant peak being the one coming from the metal oxide species.

a) Fe 2p:

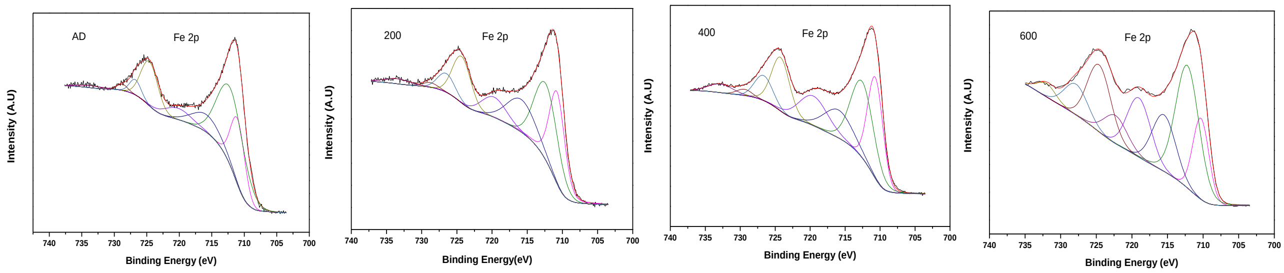

b) Co 2p:

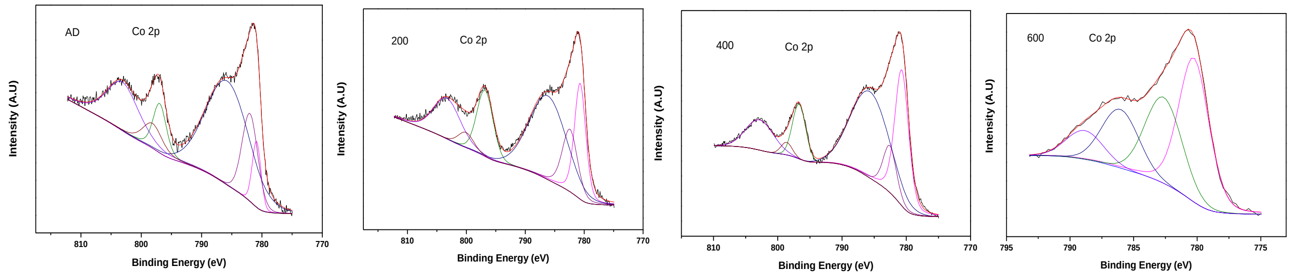

c) B 1s

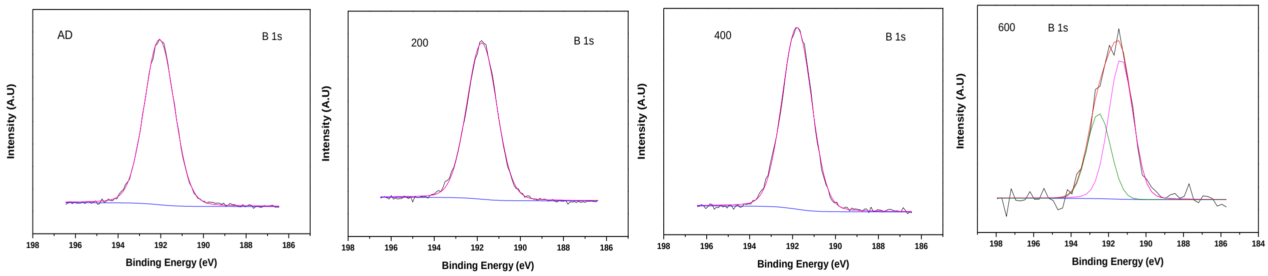

d) O 1s

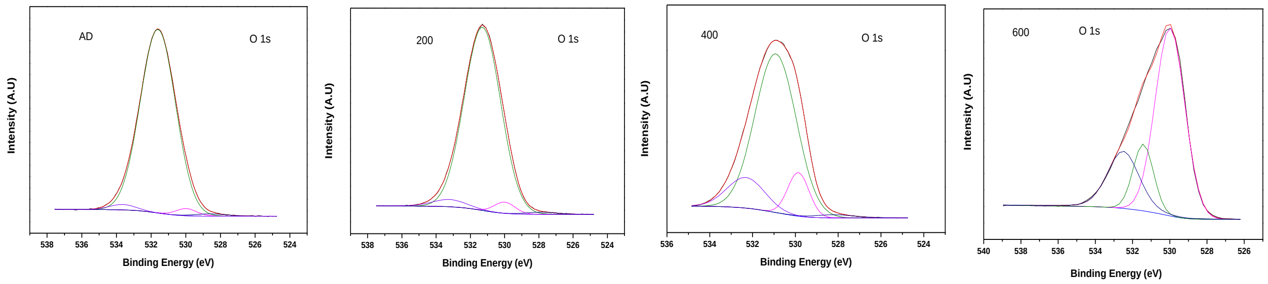

Figure 79: *XPS spectra of a) Fe 2p b) Co 2p c) B 1s d) O 1s levels for as-deposited and annealed samples.*

As XPS is a surface sensitive technique, the above results could only identify the surface oxides and no metallic peaks were detected, as was seen from XRD data. The signature of CoFe2O4 phase is observed in AN400 and AN600 samples, matching well with XRD results. Additionally, the phases of $FeBO_3$ and B2O3 are observed, suggesting existence of oxy-boride species in the films. The XPS results are in good agreement with the Micro-Raman and XRD results thereby confirming the main phases present in the coatings.

It was seen that AD and AN200 films do not show distinct formation of $CoFe_2O_4$ phase. Hence, AN 400 and AN600 samples were chosen to perform HR-TEM analysis and the results are shown in **Fig. 80**. AN400 clearly demonstrates the core-shell structure of the particles which is seen by the dark contrast of the core with the shell surrounding it (layer of light contrast) [**Fig. 80a**]. The shell is mostly comprised of lighter elements mainly boron with a thickness typically in the range of few nanometres depending on the particle size. A d-spacing of 0.21nm ascribed to (004) planes of $CoFe_2O_4$ phase [326] is clearly visible in the HRTEM image (**Fig 80b**). Fast-Fourier Transform (FFT) (**Inset of Fig. 80b**) of this particle can also be indexed to $CoFe_2O_4$ phase. **Fig. 24a** shows the HRTEM image of a representative NW from the hierarchical urchin like structures of AN600. The surface of the NW shows a set of three d-spacings of 0.14, 0.21 and 0.29 nm (**Fig. 24b),** where 0.14 nm and 0.29 nm are ascribed to (044) and (022) planes of $CoFe_2O_4$ phase (JCPDS file: 22-1086) whereas d-spacing of 0.21nm is common to that of (002) planes of CoO phase (JCPDS file: 75-0533) as well as (004) plane of $CoFe_2O_4$ phase. FFT (**Fig. 24c**) of this NW can be perfectly indexed to $CoFe_2O_4$ and CoO phases. On the basis of these results, it becomes clear that AN400 is comprised of $CoFe_2O_4$ phase only, along with surface residual oxides, while AN600 comprises of $CoFe_2O_4$ as well as CoO phases. Thus, the heat treatment causes crystallization of the sample to form $CoFe_2O_4$ phase at 400 °C but on heating further, secondary phases start erupting, as observed in AN600 film.

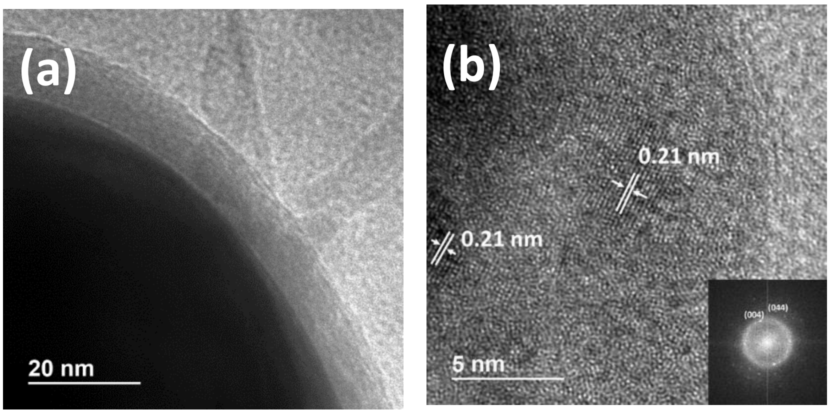

Figure 80: *(a) TEM and (b) HR-TEM images of AN400 sample.*

All the films deposited on FTO electrodes were tested for electrochemical water oxidation in a three-cell configuration. Before measurements, the electrodes were subjected to cyclic voltammetry cycles in the potential range of -0.24 V to 1.76 V (V vs. SCE) in order to obtain a stable response and to remove eventual surface impurities. iR-corrected linear polarization curves of all the films (as-deposited and annealed) and RuO2 nanoparticles are shown in **Fig. 81a** and the values obtained from these curves are summarized in **Table 8**. The best results are obtained for AN400 sample with an overpotential of 315mV at 10 mA/cm^2, which is much lower than other samples, including RuO2 (370 mV/dec). AN400 also shows the lowest Tafel slope value of 31.5 mV/dec, while AN600 exhibits the highest Tafel slope of 65.8 mV/dec. To understand the reasons for higher electrochemical performance of AN400 film, various electrochemical characterizations were performed.

Identification of the in-situ formed redox species was done by performing slow CV scans in the pre-OER potential region (**Fig. 81c**). In the first cycle of anodic scan for AN400, two oxidation peaks were observed, where the first peak has a shoulder at 1.21 V (vs RHE) while the second peak is at 1.31 V (vs RHE). The occurrence of first peak indicates formation of Co^{3+} species in the form of CoOOH on the surface of the film which then gets converted to Co^{4+} (CoO_2) at further oxidation potential [315]. In the reverse scan, one can see only one peak corresponding to reduction of CoO_2, indicating that the formation of CoOOH species is an irreversible reaction. This is also evident from the successive scan, where only one peak of CoO_2 species is seen, confirming that all the CoOOH is now converted to stable oxide. Similar phenomenon is also observed for AN200 film (**Fig. 81d**), but the intensities of oxidation and reduction peaks are much lower, suggesting less formation of active Co oxides. On the other hand, this oxide formation is not observed for AD as well as AN600 films (**Fig. 81d**). This clearly shows that CoO_2 phase is the active species responsible for facilitating OER and hence AN400 sample shows the best performance.

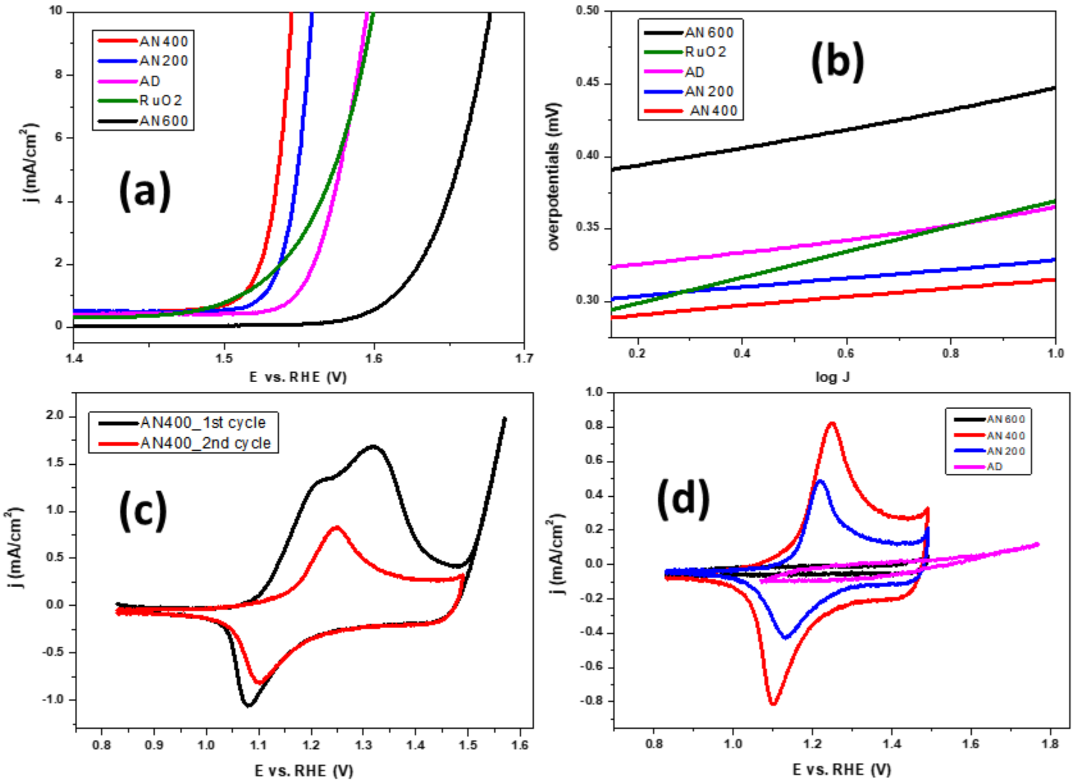

Figure 81: *a) LSV curves with iR compensation and b) Tafel plots for as-deposited, annealed samples and RuO_2, c) first two cycles of slowscan CV curves for AN400 sample and d) slowscan CV curves for as-deposited and annealed samples.*

Sample	**Overpotentials**		**Tafel slope b (mV/dec)**
	η (1 mA/cm^2)	η (10 mA/cm^2)	

AD	317mV	365mV	41.7 ± 0.2
AN200	296mV	329mV	31.9 ± 0.2
AN400	**281mV**	**315mV**	**31.5 ± 0.2**
AN600	384mV	447mV	65.8 ± 0.3
RuO_2	283mV	370mV	88.3 ± 0.2

Table 8: *Overpotentials (η) and Tafel slopes (b) for as-deposited, annealed samples and RuO_2.*

The graphs shown in **Fig. 81a** does not represent the intrinsic activity of the films and is influenced by the contributions from surface area. Electrochemical surface area (ESA) of the films was estimated indirectly by determining the value of double layer capacitance (C_{DL}). **Fig. 82** demonstrates the CV curves for all the films at increasing scan rates. From these graphs, the difference between the cathodic and anodic current densities was calculated and plotted against respective scan rates, to determine the value of C_{DL}. As seen in **Fig. 83**, the value of C_{DL} and hence the ESA is the highest for AN600 while that of other films are more or less the same. This result matches well with the SEM images where AD, AN200 and AN400 films show similar particulate morphology while AN600 showed formation of NWs on the surface. Owing to these NWs, AN600 presents more surface area for adsorption of reactant species from the electrolyte. However, due to the lack of formation of active oxides on the surface, these reactant species are not converted to oxygen. Thus, in spite of higher ESA, AN600 shows poor OER performance. On the other hand, despite having similar ESA as AN200 and AD films, AN400 shows the highest OER rate which can be attributed to the highest amount of formation of active oxides amongst all the coatings as evident by the intense oxidation peak observed in **Fig 81d**. This presents a possibility to further improve the OER performance of AN400 film by tuning the morphology to obtain higher ESA.

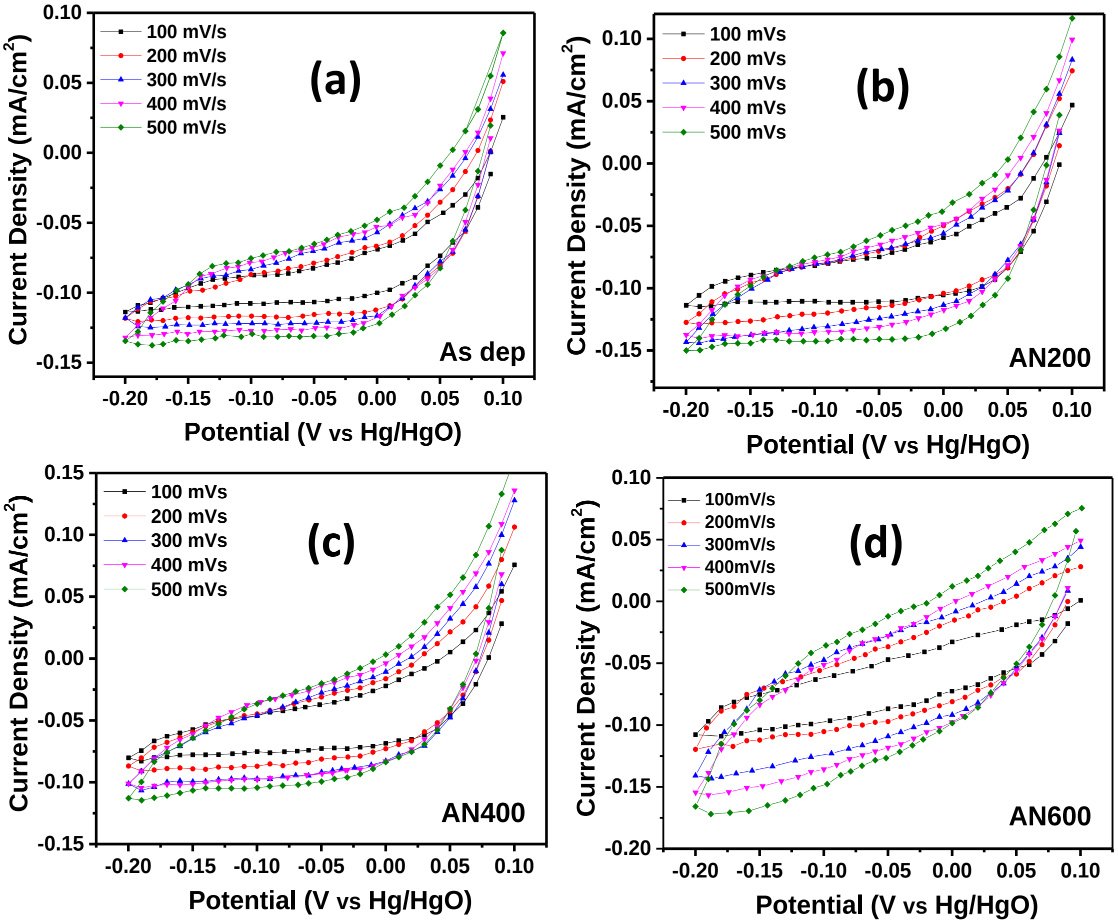

Figure 82: *(a-d) CV curves for as-deposited and annealed samples at increasing scan rates.*

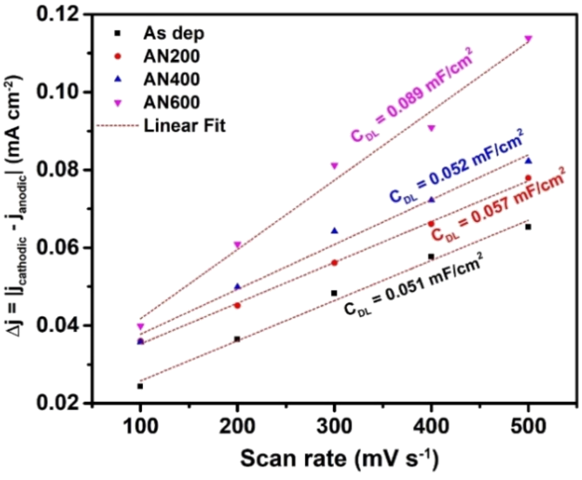

Figure 83: *Plot representing the difference in cathodic and anodic current density against the scan rate to determine* C_{DL} *for as-deposited and annealed samples.*

Another factor that can affect the performance of a catalyst is the charge transfer resistance (Rct) across the electrode/electrolyte interface. Rct was determined by electrochemical impedance spectroscopy (EIS) using an equivalent circuit model of two resistances and a constant phase element to fit the obtained Nyquist plots. **Fig. 84** shows the obtained Nyquist plots for all the samples at two different potentials of 0 V and 0.1 V (vs OCP), while the corresponding resistance values are tabulated in **Table 9**. It can see that the Rct value decreases on increasing the applied potential. However, the maximum decrease in Rct is observed for AN400 sample, which also shows the lowest overpotential, supporting our results. On the other hand, the decrement in Rct value for AN600 sample is very minimal, suggesting that under applied potential, it offers higher resistance for transfer of charges across the interface. It must be noted that the value of Rct is smallest in case of AD films, which could be due to its metallic nature.

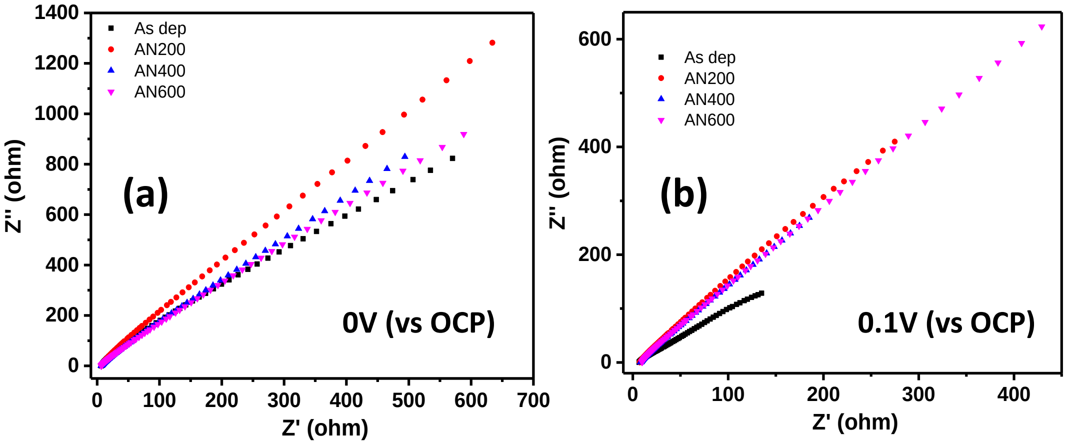

Figure 84: *EIS graphs for as-deposited and annealed samples at (a) 0 V and (b) 0.1 V respectively.*

At 0 V (vs OCP):

Samples	**R soln (Ω)**	**R ct (Ω)**
As dep	6.30	$2.642 * 10^3$
AN200	7.03	$6.933 * 10^3$
AN400	7.98	$5.954 * 10^3$
AN600	9.04	$5.082 * 10^3$

(a)

At 0.1 V (vs OCP):

Samples	**R soln (Ω)**	**R ct (Ω)**
As dep	5.94	$0.979 * 10^3$
AN200	6.91	$3.514 * 10^3$
AN400	7.93	$2.865 * 10^3$
AN600	8.95	$4.060 * 10^3$

(b)

Table 9: *Charge transfer resistance (Rct) values for as deposited and annealed samples at a) 0 V and b) 0.1 V respectively.*

So far, it is well-established that AN400 film shows the best performance, owing to in-situ formation of large number of active Co^{4+} species, highest intrinsic activity of each site and also the improved charge transfer resistance. To illustrate the roles of Co, Fe and B in the film, the performance of AN400 was compared with that of single oxide films of CoOx and FeOx (containing boron) and mixed oxide film deposited without boron (termed as AN400_2). It must be noted that these single oxide films were also deposited with exactly the same experimental conditions as that of AN400 film. AN400 film shows much superior electrochemical activity (**Fig. 85a**) and lower Tafel slope (**Fig. 85b**) compared to the single oxide and AN400_2 films. To achieve the current density of 10 mA/cm^2, overpotentials of 315 mV, 406 mV, 492 mV and 421 mV were obtained for An400, CoOx, FeOx and AN400_2 films, respectively (**Table 10**), indicating that the combination of Co, Fe and B together yields the best performance. To isolate the roles of Co, Fe and B, CV scans were recorded for AN400, CoOx, FeOx and AN400_2 films at a scan rate of 2 mV/s **(Fig. 85c).** On comparing the two mixed oxide films, AN400 and AN400_2, one can see that boron free sample (AN400_2) shows no redox peaks, while the sample with boron (AN400) shows prominent reversible redox peaks, corresponding to transformation of Co from Co^{3+} to higher oxidation states. This implies that the role of boron is to assist in formation of Co^{3+} states on the surface of the film. It has been reported that in case of Co-B films, B acts as the sacrificial element by donating electrons to Co, thereby protecting it from forming stable oxides. In the present case, boron plays a similar role of preventing complete oxidation of Co and assisting it in forming Co^{3+} species on the surface. To illustrate the role of Fe, CV scans of AN400 is compared with that of CoOx and FeOx films. The first anodic cycle for CoOx shows a main oxidation peak at 1.15 V (vs. RHE) along with two secondary shoulders at at 1.07 V (vs. RHE) and 1.25 V (vs. RHE). During the reverse scan, a very small reduction peak is observed at 1.05 V (vs. RHE), indicating a quasi-reversible reaction. The successive scan displays no oxidation and reduction peaks, indicating that the oxidised species are not regenerated again. Thus, CoOx coatings show no stable active species and hence exhibit inferior electrochemical activity for OER. FeOx, on the other hand, shows no redox peaks in both the cycles, suggesting that Fe doesn't undergo any oxidation in this potential regime and hence lacks active sites for catalysing water oxidation, thereby displaying the worst OER performance. Only in the case of AN400 film, the redox peaks corresponding to the active Co^{4+} species are present consistently in all CV scans. This indicates that the oxidation chemistry of mixed oxide catalyst (AN400) containing Co and Fe is completely different than that of single oxides of Co and Fe, under applied anodic potentials. Co oxide alone fails to regenerate oxide species on its surface, but the presence of Fe helps it in forming reversible species of Co in higher oxidation state, which in turn facilitates water oxidation reaction. Thus, in case of mixed oxide film (AN400), the role of B is to assist Co in forming Co^{3+} species which further transform to higher oxidation states, while Fe helps it in regenerating these species in successive cycles.

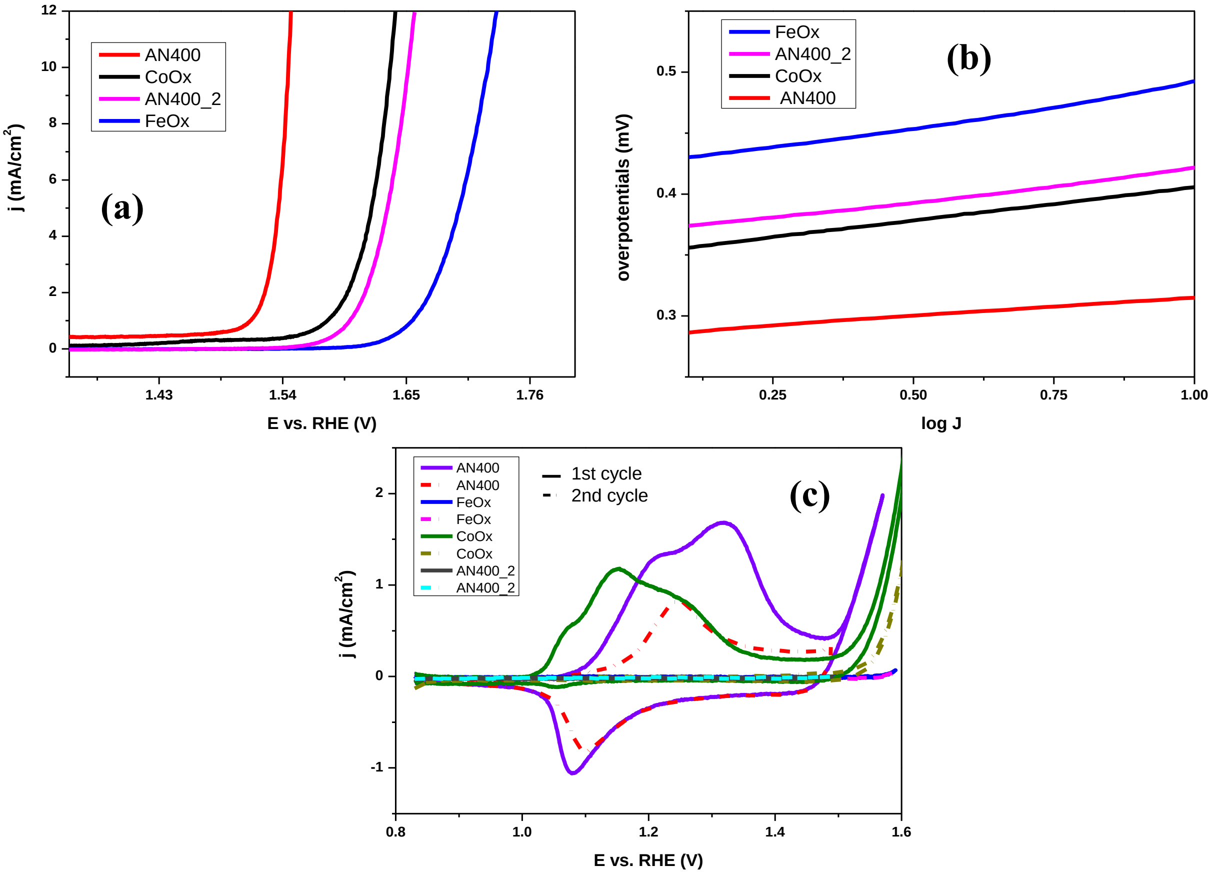

Figure 85: *a) Comparison of LSV curves with iR compensation, b) Tafel slopes and c) slowscan CV curves for AN400, FeOx, CoOx and AN400_2 samples.*

Sample	**Overpotentials**		**Tafel slope b (mV/dec)**
	η (1 mA/cm^2)	η (1 mA/cm^2)	
AN400	281mV	315mV	31.5
CoOx	350mV	406mV	55.4
FeOx	425mV	492mV	66.0
AN400_2	370mV	421mV	46.9

Table 10: *Overpotentials (η) and Tafel slopes (b) for AN400, CoOx, FeOx and AN400_2 films respectively.*

To further elucidate the difference between mixed oxide and single oxide films, C$_{DL}$ values were determined for CoOx and FeOx films (**Fig. 86**). The value of C$_{DL}$ and hence the ESA for CoOx film is the same as that obtained for AN400 film (0.052 mF/cm2), while FeOx exhibits a lower C$_{DL}$ value of 0.045 mF/cm2. This implies that the number of active adsorption sites in

CoOx is the same as in AN400 film, which is understood as Co is the active site in both samples. However, despite having similar ESA, as the adsorbed species in CoOx undergo oxidation and fail to regenerate, they do not show the same performance as AN400 film.

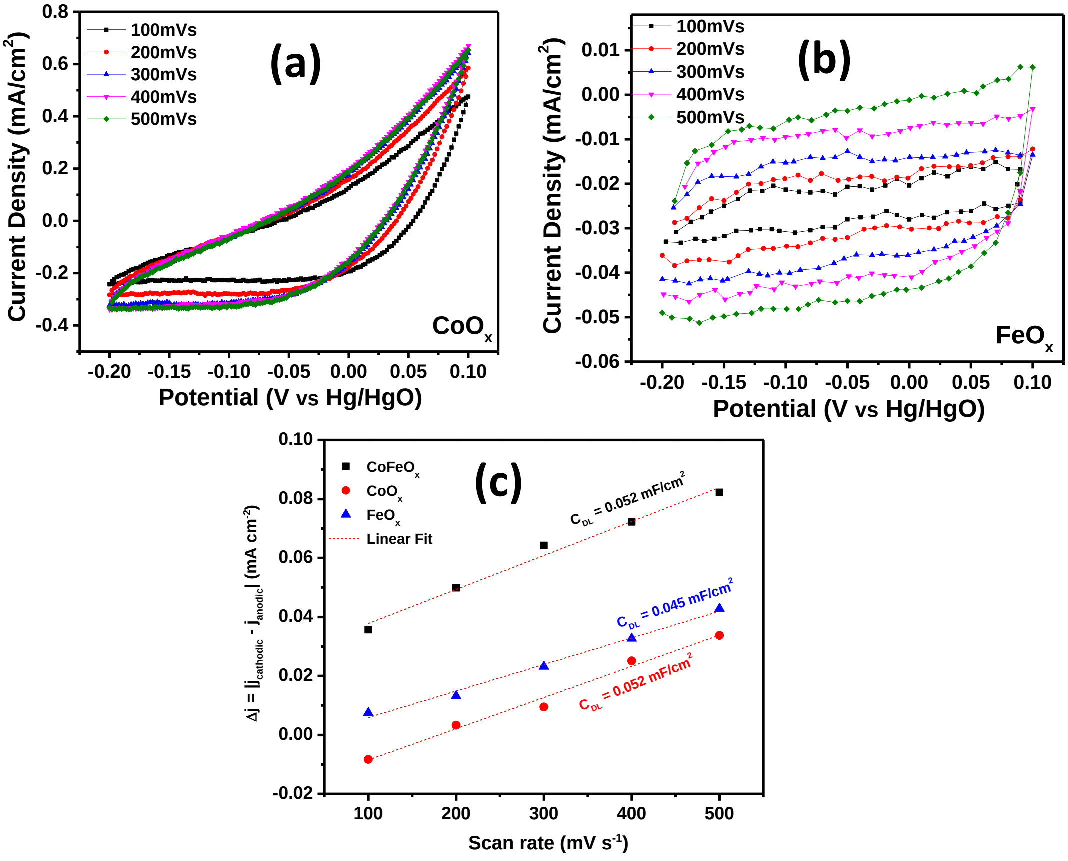

Figure 86: *CV curves for (a) CoOx and (b) FeOx at increasing scan rates, (c) Plot representing the difference in cathodic and anodic current density against the scan rate to determine* C_{DL}

To obtain better understanding of the changes in chemical states of the mixed oxide film due to water oxidation reaction, XPS studies were performed on AN400 film after OER (**Fig. 87**). Post OER, Co 2p state shows a prominent peak at 780.1 eV, which is attributed to the formation of Co^{3+} species in CoOOH, consistent with the results obtained from CV measurements while the peaks at 786.1 and 796.4 eV correspond to the satellite features of Co in Co^{2+} oxidation state. O 1s spectra for post-OER AN400 film also shows an increase in the peak intensity associated with OOH group (529.5 eV). As per previous reports, Fe compounds are easier to form OOH-like species and the Fe in CoFeOx catalyst plays a significant role in promoting the formation and stabilizing the OOH-like species [334]. A higher concentration of OOH-like species leads to superior OER performance. For Fe 2p state, the peak at 711.0 eV corresponding to Fe^{3+} species shows an increase in intensity for post-OER sample. This peak was also observed in as prepared sample, indicating that Fe was in high oxidation state (Fe^{3+}) even before OER measurements. In case of B 1s state, post-OER film shows a single peak at 191.6 eV, ascribed to B_2O_3, as also observed in pristine films before OER.

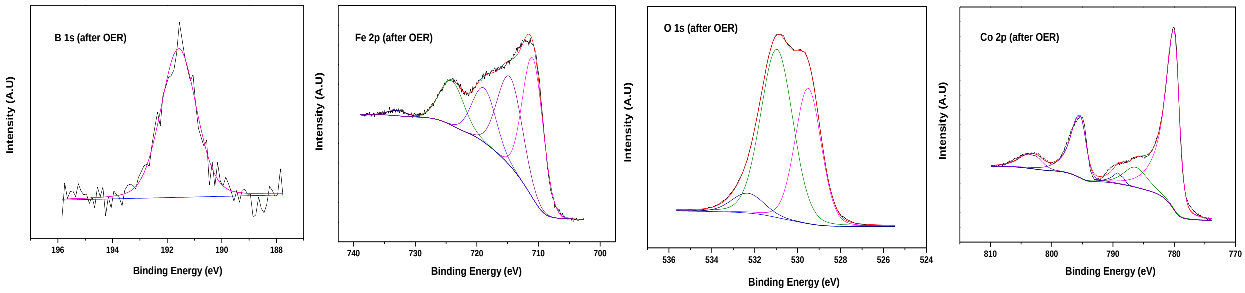

Figure 87: *XPS spectra of Fe 2p, Co 2p, B 1s and O 1s levels for AN400 sample after OER.*

It is of paramount importance to study the stability and recyclability of these coatings for practical applications in the industry. For stability tests, chronoamperometric measurements were done on AN400 film for 12 hrs (**Fig. 88a**). The film displays high stability and produces an almost constant current density of 20mA/cm^2 at 1.97 V vs. RHE. CoFeOx coatings were also tested for its recyclability by performing cyclic voltammetries for 1000 cycles in 1M KOH solution. The films show excellent results with no signs of deterioration even after the 1000th cycle (**Fig. 88b**), thereby making the coatings completely suitable for industrial applications.

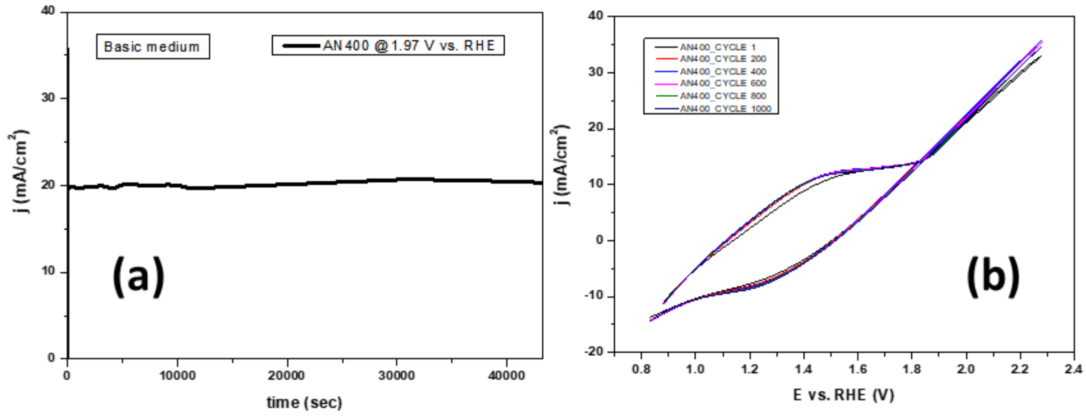

Figure 88: *a) Chronoamperometric measurement demonstrating the stability of AN400 coatings for 12hrs and b) recyclability test by performing cyclic voltammetries on AN400 coating for 1000 cycles.*

8.4 Conclusions

Mixed metal oxide coatings were successfully synthesized by Pulsed Laser Deposition (PLD) as coatings for electrochemical applications. An in-depth characterization consisting of SEM, XRD, Micro-Raman, XPS and TEM were performed for structural and elemental characterization. The synthesized coatings showed excellent electrochemical performance towards water oxidation reactions with an overpotential of 315mV at 10 mA/cm^2, along with a tafel slope of 31.5 mV/dec. The mixed metal oxide films also exhibit superior electrochemical activity compared to single oxide counterparts of CoOx and FeOx respectively. Similarly prepared coatings but without the presence of boron were synthesized to understand the role of boron in enhancing the electrochemical activity. Coatings without boron show an inferior electrochemical activity with high overpotentials of 421mV at 10 mA/cm^2 respectively, with tafel slope of 46.9 mV/dec. The films with boron form stable active oxides which convert the reactant species to oxygen thereby enhancing the electrochemical activity towards OER. Stability and recyclability tests done on mixed metal oxide coatings make it even more appealing for industrial applications due to their non-deteriorating behavior and excellent recyclability.

Conclusions and Future work

a) Environment

In today's world, the availability of clean drinking water throughout the globe is one of the most important aspects to be resolved. Water scarcity due to uneven distribution of water has resulted in escalation of the problem. On the other hand, pollution of water due to industrialization followed by the deficiency of proper wastewater management facilities adds to the existing crisis. The common techniques of wastewater purification namely filtration and adsorption are expensive and they generate secondary products which are toxic in nature thereby contributing to the water pollution. Chlorination is an effective technique but the by-products obtained have carcinogenic and mutagenic effects on human health. A promising methodology for water purification is photocatalysis, an Advanced Oxidation Process (AOP) that can completely mineralize the organic pollutants to inorganic ions without adding harmful chemicals to the surroundings. AOP reactions are very effective due to the generation of strong oxidizing agents such as hydroxyl radicals which can be produced by the photocatalyst upon direct activation by sunlight. An ideal photocatalyst should be made up of cheap, environmentally friendly and abundant material which has high surface area and an energy band gap such that it absorbs much of the solar spectrum. Along with high absorption, it is important that the photocatalyst has low recombination rate of photogenerated electron-hole pairs so that they can be utilized for the photocatalysis reactions without getting recombined. However, these properties of a photocatalyst are ideal. In reality, the photocatalysts have drawbacks which inhibit the effective degradation of pollutant. Hence, researchers adopt different strategies like doping, forming composites, varying the morphology etc. to meet the needs of an ideal photocatalyst demonstrating effective photocatalysis with the least amount of time to completely mineralize the pollutant under consideration.

In this thesis, different strategies have been studied in depth with various photocatalysts for degradation of organic pollutants. $CoFe_2O_4/CoO$ hierarchical urchin like nanostructured coatings were synthesized by Pulsed Laser Deposition (PLD) for degradation of Methylene Blue (MB) dye. These coatings exhibited a) high surface area due to the urchin like structures, b) enhanced visible light absorption due to low energy band gap of CoO and c) reduced recombination of photogenerated charges due to Z-scheme heterojunction formed between $CoFe_2O_4$ and CoO. All these optimizations led to superior photocatalytic activity of the synthesized $CoFe_2O_4/CoO$ photocatalyst. The effect of doping and forming composites were also tested by synthesizing nanocomposites of tungsten doped TiO_2 and reduced Graphene Oxide (rGO). The synthesized W-TiO_2/rGO photocatalyst displayed excellent activity towards degradation of para-Nitrophenol (p-NP). W-doping of TiO_2 resulted in an impurity level below the minimum conduction band of TiO_2 acting as a trap for photoexcited electrons thereby reducing the interband recombination. On the other hand, rGO formed channels with TiO_2 for fast transfer of excited electrons towards rGO which in turn reduced the surface recombination and enhanced the photocatalytic efficiency of the composite. The rGO/TiO_2 composite was studied in detail in our next work with experimental analysis for better understanding of the optical and morphological properties along with charge dynamics. Different composites were synthesized using various weight ratios of rGO and TiO_2. rGOT-3 (rGO/TiO_2 weight ratio of 3) showed the best photocatalytic activity towards degradation of p-NP owing to better dispersion of each TiO_2 nanoparticles which allowed to form strong interaction with rGO creating Ti-O-C channel at interface. The resulting high optical absorption coupled with high mobility Ti-O-C channels assisted in charge separation through fast transfer of electrons at the interface from TiO_2 to rGO.

These research activities can be considered as an important step towards fabrication of an ideal photocatalyst with highest efficiency. However, one vital step towards making the whole process renewable and sustainable is to test the synthesized catalyst in direct sunlight. WO_3 coatings synthesized by PLD were evaluated for photocatalytic measurements of MB dye under artificial visible lamps and tested in a solar parabolic dish concentrator (PDC) type system under natural sunlight. The coatings demonstrated enhanced photocatalytic degradation under photo-Fenton conditions due to the flower-like surface morphology that provided high surface area allowing an enhanced interaction between the dye molecules and the active sites for photocatalytic reactions. Moreover, the WO_3 coatings exhibited the best photocatalytic activity at pH 4, thus showcasing a high potential for industrial applications in acidic environments.

The future work includes testing the $CoFe_2O_4$/CoO and W-TiO_2/rGO photocatalysts under concentrated sunlight. Also, it would be interesting to deposit the metal oxide photocatalysts on different substrates like activated carbon or graphene during PLD and study its effect. Powder catalysts are less stable and tend to agglomerate leading to reduced photocatalytic activity. Hence, synthesis/fabrication of different metal oxide photocatalysts using PLD would be an interesting endeavour involving doping and composite strategies.

b) Energy

Fossil fuels are facing an immediate threat of depletion which could disrupt the energy driven activities of the whole world. Moreover, the emissions of greenhouse gases from fossil fuel burning have resulted in major climatic changes affecting not only the atmosphere but also the aquatic as well as terrestrial ecosystems. These reasons have prompted the need for an efficient and renewable energy source which is clean and contributes to a carbon neutral economy. Hydrogen has emerged as one of the most promising renewable energy carriers due to its high gravimetric energy density and zero emission of greenhouse gases. However, hydrogen is not available in free form on our planet and mainly exists in compounds such as hydrocarbons, chemical hydrides and water. At present, most of the hydrogen production occurs via steam reforming of natural gas, an energy intensive process relying on non-renewable energy sources with the release of enormous amounts of greenhouse gases. Thus, it is important to look for alternatives for production of hydrogen through a clean process. Electrochemical and photoelectrochemical water splitting are promising techniques for producing renewable H_2 given the simple nature of the process along with no harmful gas emission and high conversion efficiency. The produced hydrogen can be directly used in a fuel cell to generate electricity with water as the by-product, thus, making the whole hydrogen energy cycle environmentally green and sustainable.

The catalysts used in the electrochemical cell like Pt and Pd are noble elements and hence suffer from high cost and less abundance hindering their implementation on an industrial scale. Researchers have been developing new catalysts as anodes and cathodes, made up of cheap, economical and scalable materials demonstrating high catalytic activity for H_2 production with high efficiency and low overpotentials. In this thesis, we reported deposition of nickel oxide films by Pulsed Laser Deposition (PLD) exhibiting good electrochemical activity as water oxidation catalysts (WOC’s). The synthesized films showed high optical transmittance paving way for use in functionalizing solar light absorbing photoanodes for photoelectrochemical (PEC) technology. In the final work, we fabricated mixed metal oxide coatings by PLD as efficient WOC for oxygen evolution reaction (OER). The addition of boron lead to enhanced catalytic activity of the coatings due to the reduction in kinetic barrier for formation of active oxide species, a key step in determining the electrochemical performance. The mixed metal oxide coatings also displayed superior activity for OER compared to single metal oxide coatings. This work opens up interesting possibilities of enhancing the catalytic activity by inclusion of boron.

The future work includes testing the synthesized mixed metal oxide and nickel oxide films as co-catalysts over solar absorbers in PEC cell. It will also be interesting to deposit mixed metal oxide coatings of different transition metals and study their electrochemical activity with and without the presence of boron.

References

[1] Wikipedia, Water distribution on Earth, (n.d.). https://en.wikipedia.org/wiki/Water_distribution_on_Earth#/media/File:Earth's_water_distribution.svg.

[2] S. Malato, P. Fernández-Ibáñez, M.I. Maldonado, J. Blanco, W. Gernjak, Decontamination and disinfection of water by solar photocatalysis: Recent overview and trends, Catal. Today. 147 (2009) 1–59. doi:https://doi.org/10.1016/j.cattod.2009.06.018.

[3] Elizabeth Hameeteman, Future Water (In)Security: Facts, Figures, and Predictions, Global water institute, (2013).

[4] A.S. Richey, B.F. Thomas, M.-H. Lo, J.T. Reager, J.S. Famiglietti, K. Voss, S. Swenson, M. Rodell, Quantifying renewable groundwater stress with GRACE, Water Resour. Res. 51 (2015) 5217–5238. doi:doi:10.1002/2015WR017349.

[5] Peter BUREK et. al, Water Futures and Solution - Fast Track Initiative (Final Report), 2016. http://pure.iiasa.ac.at/13008.

[6] Fifth Assessment Report on Climate Change: The Physical Science Basis, 2013. https://www.ipcc.ch/report/ar5/wg1/technical-summary/.

[7] S.D. Richardson, Water Analysis: Emerging Contaminants and Current Issues, Anal. Chem. 81 (2009) 4645–4677. doi:10.1021/ac9008012.

[8] T. Wintgens, F. Salehi, R. Hochstrat, T. Melin, Emerging contaminants and treatment options in water recycling for indirect potable use, Water Sci. Technol. 57 (2008) 99–107. doi:10.2166/wst.2008.799.

[9] UN World Water Development Report, Wastewater: The Untapped Resource, 2017.

[10] United Nations - Water Policy Brief: Water Quality, 2011.

[11] World Urbanization Prospects: 2018 revision, 2018.

[12] P.V.A. Padmanabhan, K.P. Sreekumar, T.K. Thiyagarajan, R.U. Satpute, K. Bhanumurthy, P. Sengupta, G.K. Dey, K.G.K. Warrier, Nano-crystalline titanium dioxide formed by reactive plasma synthesis, Vacuum. 80 (2006) 1252–1255. doi:https://doi.org/10.1016/j.vacuum.2006.01.054.

[13] M.N. Chong, B. Jin, C.W.K. Chow, C. Saint, Recent developments in photocatalytic water treatment technology: A review, Water Res. 44 (2010) 2997–3027. doi:10.1016/j.watres.2010.02.039.

[14] C.Y. Yang, B.H. Cheng, S.S. Tsai, T.N. Wu, M.C. Lin, K.C. Lin, Association between chlorination of drinking water and adverse pregnancy outcome in Taiwan., Environ. Health Perspect. 108 (2000) 765–768. doi:10.1289/ehp.00108765.

[15] J. Lu, T. Zhang, J. Ma, Z. Chen, Evaluation of disinfection by-products formation during chlorination and chloramination of dissolved natural organic matter fractions isolated from a filtered river water, J. Hazard. Mater. 162 (2009) 140–145. doi:https://doi.org/10.1016/j.jhazmat.2008.05.058.

[16] K. Singh, S. Arora, Removal of Synthetic Textile Dyes From Wastewaters: A Critical Review on Present Treatment Technologies, Crit. Rev. Environ. Sci. Technol. 41 (2011) 807–878. doi:10.1080/10643380903218376.

[17] Catalytic degradation of methylene blue in aqueous solutions over Ni- and Co- oxide systems ,

Open Chem. . 9 (2011) 1000. doi:10.2478/s11532-011-0086-7 .

[18] M. Pelaez, N.T. Nolan, S.C. Pillai, M.K. Seery, P. Falaras, A.G. Kontos, P.S.M. Dunlop, J.W.J. Hamilton, J.A. Byrne, K. O'Shea, M.H. Entezari, D.D. Dionysiou, A review on the visible light active titanium dioxide photocatalysts for environmental applications, Appl. Catal. B Environ. 125 (2012) 331–349. doi:https://doi.org/10.1016/j.apcatb.2012.05.036.

[19] S. Banerjee, S.C. Pillai, P. Falaras, K.E. O'Shea, J.A. Byrne, D.D. Dionysiou, New Insights into the Mechanism of Visible Light Photocatalysis, J. Phys. Chem. Lett. 5 (2014) 2543–2554. doi:10.1021/jz501030x.

[20] S. Banerjee, D.D. Dionysiou, S.C. Pillai, Self-cleaning applications of TiO2 by photo-induced hydrophilicity and photocatalysis, Appl. Catal. B Environ. 176–177 (2015) 396–428. doi:https://doi.org/10.1016/j.apcatb.2015.03.058.

[21] K. Elizardo, Fighting pollution with hydrogen peroxide, Pollut. Eng. 23 (1991) 106–109. https://www.scopus.com/inward/record.uri?eid=2-s2.0-0026223942&partnerID=40&md5=972e5e7d035a8549bbc95ef577ac87e4.

[22] M. Pera-Titus, V. García-Molina, M.A. Baños, J. Giménez, S. Esplugas, Degradation of chlorophenols by means of advanced oxidation processes: a general review, Appl. Catal. B Environ. 47 (2004) 219–256. doi:https://doi.org/10.1016/j.apcatb.2003.09.010.

[23] R. Andreozzi, V. Caprio, A. Insola, R. Marotta, Advanced oxidation processes (AOP) for water purification and recovery, Catal. Today. 53 (1999) 51–59. doi:https://doi.org/10.1016/S0920-5861(99)00102-9.

[24] C. von Sonntag, Advanced oxidation processes: mechanistic aspects, Water Sci. Technol. 58 (2008) 1015—1021. doi:10.2166/wst.2008.467.

[25] S. Guo, G. Zhang, J. Wang, Photo-Fenton degradation of rhodamine B using Fe2O3–Kaolin as heterogeneous catalyst: Characterization, process optimization and mechanism, J. Colloid Interface Sci. 433 (2014) 1–8. doi:10.1016/J.JCIS.2014.07.017.

[26] S.H. Bossmann, E. Oliveros, S. Göb, S. Siegwart, E.P. Dahlen, L. Payawan, M. Straub, M. Wörner, A.M. Braun, New Evidence against Hydroxyl Radicals as Reactive Intermediates in the Thermal and Photochemically Enhanced Fenton Reactions, J. Phys. Chem. A. 102 (1998) 5542–5550. doi:10.1021/jp980129j.

[27] A.M. Jr., Application of Different Advanced Oxidation Processes for the Degradation of Organic Pollutants, in: S.C. Oliveira (Ed.), IntechOpen, Rijeka, 2013: p. Ch. 6. doi:10.5772/53188.

[28] J.J. Pignatello, E. Oliveros, A. MacKay, Advanced Oxidation Processes for Organic Contaminant Destruction Based on the Fenton Reaction and Related Chemistry, Crit. Rev. Environ. Sci. Technol. 36 (2006) 1–84. doi:10.1080/10643380500326564.

[29] F.J. Benitez, J. Beltran-Heredia, J.L. Acero, F.J. Rubio, Chemical Decomposition of 2,4,6-Trichlorophenol by Ozone, Fenton's Reagent, and UV Radiation, Ind. Eng. Chem. Res. 38 (1999) 1341–1349. doi:10.1021/ie980441f.

[30] N. Young, P. Fairley, V. Mohan, C. Jumeaux, A study of hydrogen peroxide chemistry and photochemistry in tea stain solution with relevance to clinical tooth whitening, J. Dent. 40 (2012) e11–e16. doi:https://doi.org/10.1016/j.jdent.2012.07.016.

[31] World Energy Balances Overview, 2019.

[32] P. Murphy, Solar Update, in Solar Heating and Cooling Programme, 2015.

[33] N.S. Lewis, D.G. Nocera, Powering the planet: Chemical challenges in solar energy utilization, Proc. Natl. Acad. Sci. 103 (2006) 15729 LP-15735. doi:10.1073/pnas.0603395103.

[34] International Energy Outlook, 2017.

[35] Global Energy Statistical Yearbook, 2019.

[36] World Energy Outlook, 2018.

[37] AR5 Synthesis Report: Climate Change, 2014.

[38] AR4 Synthesis Report: Climate Change, 2007.

[39] AR5 Climate Change: Mitigation of Climate Change, 2014.

[40] B. Kumar, M. Llorente, J. Froehlich, T. Dang, A. Sathrum, C.P. Kubiak, Photochemical and Photoelectrochemical Reduction of CO2, Annu. Rev. Phys. Chem. 63 (2012) 541–569. doi:10.1146/annurev-physchem-032511-143759.

[41] D.H. Won, C. hyuck Choi, J. Chung, S. Ihl Woo, Photoelectrochemical production of formic acid and methanol from carbon dioxide on metal-decorated CuO/Cu2O-layered thin films under visible light irradiation, Appl. Catal. B Environ. s 158–159 (2014) 217–223. doi:10.1016/j.apcatb.2014.04.021.

[42] E.P. Murray, T. Tsai, S.A. Barnett, A direct-methane fuel cell with a ceria-based anode, Nature. 400 (1999) 649–651. doi:10.1038/23220.

[43] P. Kedzierzawski, J. Augustynski, Poisoning and Activation of the Gold Cathode during Electroreduction of CO 2 , J. Electrochem. Soc. . 141 (1994) L58–L60. http://jes.ecsdl.org/content/141/5/L58.abstract.

[44] A. Mazzi, Modeling and production of metal nanoparticles through laser ablation and applications to photocatalytic water oxidation, University of Trento, 2017.

[45] Lionel Vayssieres, On Solar Hydrogen & Nanotechnology, Wiley & sons, 2010.

[46] A. Kudo, Y. Miseki, Heterogeneous photocatalyst materials for water splitting, Chem. Soc. Rev. 38 (2009) 253–278. doi:10.1039/B800489G.

[47] Y.-P. Yuan, L.-W. Ruan, J. Barber, S.C. Joachim Loo, C. Xue, Hetero-nanostructured suspended photocatalysts for solar-to-fuel conversion, Energy Environ. Sci. 7 (2014) 3934–3951. doi:10.1039/C4EE02914C.

[48] M. Wang, L. Chen, L. Sun, Recent progress in electrochemical hydrogen production with earth-abundant metal complexes as catalysts, Energy Environ. Sci. 5 (2012) 6763–6778. doi:10.1039/C2EE03309G.

[49] G. Sharma, A. Upadhyay, D. Behara, S. Sivakumar, R. Pala, 16 Photoelectrochemical Approaches to Solar-H2 Generation: Processes, Technologies, and Challenges, in: 2017: pp. 691–716. doi:10.1201/9781315153209-17.

[50] Wikipedia-Fuel cell, (n.d.). http://en.wikipedia.org/wiki/Fuel-cell.

[51] Arunprasanth Sakthivel, Fuel Cell is an Entity of Modern Grids- RTDS Technologies, (2017). https://www.rtds.com/hot-topic-fuel-cell-model/.

[52] R. Brook, Sol-gel technology for thin films, fibers, preforms, electronics and specialty shapes. Edited by L. C. Klein. Noyes Publications, New Jersey, USA 1988. xxi, 407 pp., bound, US$72.– 1SBN 0-8155-1154-X, Adv. Mater. 1 (1989) 309. doi:10.1002/adma.19890010816.

[53] Yosry A. Attia, ed., Sol-Gel Processing and Applications, n.d.

[54] David Levy; Marcos Zayat, ed., The Sol-Gel Handbook, 2015.

[55] Tessy Maria López; David Avnir; Michel Aegerter, ed., Emerging Fields in Sol-Gel Science and

Technology, n.d.

[56] S. Thiagarajan, Facile Methodology of Sol-Gel Synthesis for Metal Oxide Nanostructures, in: A.S. and D.V.E.-U. Chandra (Ed.), IntechOpen, Rijeka, 2017: p. Ch. 1. doi:10.5772/intechopen.68708.

[57] J. Livage, D. Ganguli, Sol–gel electrochromic coatings and devices: A review, Sol. Energy Mater. Sol. Cells. 68 (2001) 365–381. doi:https://doi.org/10.1016/S0927-0248(00)00369-X.

[58] Michel A. Aegerter ; Martin Mennig, ed., Sol-Gel Technologies for Glass Producers and Users, n.d.

[59] A. Miotello, R. Kelly, Laser-induced phase explosion: new physical problems when a condensed phase approaches the thermodynamic critical temperature, Appl. Phys. A. 69 (1999) S67–S73. doi:10.1007/s003399900296.

[60] M. Bonelli, C. Cestari, A. Miotello, Pulsed laser deposition apparatus for applied research, Meas. Sci. Technol. 10 (1999) 27–30. doi:10.1088/0957-0233/10/3/024.

[61] A. Santini, Synthesis and characterization of nanostructures for catalysis, University of Trento, 2012.

[62] Zakaria El Koura, Solar water splitting for hydrogen production: development of photocatalysts based on earth abundant and biocompatible materials (TiO2 and Fe2O3), University of Trento, 2016.

[63] The Prashant Kamat Laboratory, Raman Spectroscopy, n.d. https://www3.nd.edu/~kamatlab/facilities_spectroscopy.html#Pos7.

[64] Ms. Smith, X-Ray Diffraction by Crystals, AP Chemistry, (n.d.). https://sites.google.com/a/hartdistrict.org/ms-smith/home/modern-solid-materials/chapter-11-intermolecular-forces-and-liquids-and-solids/11-5-x-ray-diffraction-by-crystals.

[65] Jason Grebenkemper, Chemistry, Powder X-ray Diffraction, n.d. https://chem.libretexts.org/link?314.

[66] Tony Owen, Fundamentals of modern UV-visible spectroscopy, 2000.

[67] C. Lei, M. Pi, B. Cheng, C. Jiang, J. Qin, Fabrication of hierarchical porous ZnO/NiO hollow microspheres for adsorptive removal of Congo red, Appl. Surf. Sci. 435 (2018) 1002–1010. doi:https://doi.org/10.1016/j.apsusc.2017.11.201.

[68] M. Fang, G. Dong, R. Wei, J.C. Ho, Hierarchical Nanostructures: Design for Sustainable Water Splitting, Adv. Energy Mater. 7 (2017) 1700559. doi:10.1002/aenm.201700559.

[69] Z. Ren, Y. Guo, C.-H. Liu, P.-X. Gao, Hierarchically nanostructured materials for sustainable environmental applications , Front. Chem. . 1 (2013) 18. https://www.frontiersin.org/article/10.3389/fchem.2013.00018.

[70] A. Meng, B. Zhu, B. Zhong, L. Zhang, B. Cheng, Direct Z-scheme TiO2/CdS hierarchical photocatalyst for enhanced photocatalytic H2-production activity, Appl. Surf. Sci. 422 (2017) 518–527. doi:https://doi.org/10.1016/j.apsusc.2017.06.028.

[71] Q. Wang, H. Zhou, X. Liu, T. Li, C. Jiang, W. Song, W. Chen, Facet-dependent generation of superoxide radical anions by ZnO nanomaterials under simulated solar light, Environ. Sci. Nano. 5 (2018) 2864–2875. doi:10.1039/C8EN01008K.

[72] K. Cao, L. Jiao, H. Liu, Y. Liu, Y. Wang, Z. Guo, H. Yuan, Lithium-ion Batteries: 3D Hierarchical Porous α-Fe2O3 Nanosheets for High-Performance Lithium-Ion Batteries (Adv. Energy Mater. 4/2015), Adv. Energy Mater. 5 (2015). doi:10.1002/aenm.201570020.

[73] Z. Wang, D. Chu, L. Wang, L. Wang, W. Hu, X. Chen, H. Yang, J. Sun, Facile synthesis of hierarchical double-shell WO3 microspheres with enhanced photocatalytic activity, Appl. Surf. Sci. 396 (2017) 492–496. doi:https://doi.org/10.1016/j.apsusc.2016.10.181.

[74] A.J. Mieszawska, R. Jalilian, G.U. Sumanasekera, F.P. Zamborini, The Synthesis and Fabrication of One-Dimensional Nanoscale Heterojunctions, Small. 3 (2007) 722–756. doi:10.1002/smll.200600727.

[75] P. Xu, X. Shen, L. Luo, Z. Shi, Z. Liu, Z. Chen, M. Zhu, L. Zhang, Preparation of TiO2/Bi2WO6 nanostructured heterojunctions on carbon fibers as a weaveable visible-light photocatalyst/photoelectrode, Environ. Sci. Nano. 5 (2018) 327–337. doi:10.1039/C7EN00822H.

[76] S.G. Penn, L. He, M.J. Natan, Nanoparticles for bioanalysis, Curr. Opin. Chem. Biol. 7 (2003) 609–615. doi:https://doi.org/10.1016/j.cbpa.2003.08.013.

[77] O. Hayden, R. Agarwal, C.M. Lieber, Nanoscale avalanche photodiodes for highly sensitive and spatially resolved photon detection, Nat. Mater. 5 (2006) 352. https://doi.org/10.1038/nmat1635.

[78] K.-B. Lee, S. Park, C.A. Mirkin, Multicomponent Magnetic Nanorods for Biomolecular Separations, Angew. Chemie Int. Ed. 43 (2004) 3048–3050. doi:10.1002/anie.200454088.

[79] A.K. Salem, P.C. Searson, K.W. Leong, Multifunctional nanorods for gene delivery, Nat. Mater. 2 (2003) 668. https://doi.org/10.1038/nmat974.

[80] Z. Zhao, W. Zhang, X. Lv, Y. Sun, F. Dong, Y. Zhang, Noble metal-free Bi nanoparticles supported on TiO2 with plasmon-enhanced visible light photocatalytic air purification, Environ. Sci. Nano. 3 (2016) 1306–1317. doi:10.1039/C6EN00341A.

[81] C. Cheng, A. Amini, C. Zhu, Z. Xu, H. Song, N. Wang, Enhanced photocatalytic performance of TiO2-ZnO hybrid nanostructures, Sci. Rep. 4 (2014) 4181. https://doi.org/10.1038/srep04181.

[82] H. Han, F. Riboni, F. Karlicky, S. Kment, A. Goswami, P. Sudhagar, J. Yoo, L. Wang, O. Tomanec, M. Petr, O. Haderka, C. Terashima, A. Fujishima, P. Schmuki, R. Zboril, α-Fe2O3/TiO2 3D hierarchical nanostructures for enhanced photoelectrochemical water splitting, Nanoscale. 9 (2017) 134–142. doi:10.1039/C6NR06908H.

[83] T. Warang, N. Patel, A. Santini, N. Bazzanella, A. Kale, A. Miotello, Pulsed laser deposition of Co3O4 nanoparticles assembled coating: Role of substrate temperature to tailor disordered to crystalline phase and related photocatalytic activity in degradation of methylene blue, Appl. Catal. A Gen. 423–424 (2012) 21–27. doi:https://doi.org/10.1016/j.apcata.2012.02.037.

[84] R. Edla, N. Patel, Z. El Koura, R. Fernandes, N. Bazzanella, A. Miotello, Pulsed laser deposition of Co3O4 nanocatalysts for dye degradation and CO oxidation, Appl. Surf. Sci. 302 (2014) 105–108. doi:https://doi.org/10.1016/j.apsusc.2013.10.174.

[85] F. Majid, S. Riaz, A. Naseer, S. Naseem, Structural and Magnetic Properties of BiFe1-xMnO3 Thin Films, Mater. Today Proc. 2 (2015) 5748–5753. doi:https://doi.org/10.1016/j.matpr.2015.11.122.

[86] T. Warang, N. Patel, R. Fernandes, N. Bazzanella, A. Miotello, Co3O4 nanoparticles assembled coatings synthesized by different techniques for photo-degradation of methylene blue dye, Appl. Catal. B Environ. 132–133 (2013) 204–211. doi:https://doi.org/10.1016/j.apcatb.2012.11.040.

[87] R. Edla, N. Patel, M. Orlandi, N. Bazzanella, V. Bello, C. Maurizio, G. Mattei, P. Mazzoldi, A. Miotello, Highly photo-catalytically active hierarchical 3D porous/urchin nanostructured Co3O4 coating synthesized by Pulsed Laser Deposition, Appl. Catal. B Environ. 166–167 (2015) 475–484. doi:https://doi.org/10.1016/j.apcatb.2014.11.060.

[88] L. Liao, Q. Zhang, Z. Su, Z. Zhao, Y. Wang, Y. Li, X. Lu, D. Wei, G. Feng, Q. Yu, X. Cai, J. Zhao, Z. Ren, H. Fang, F. Robles-Hernandez, S. Baldelli, J. Bao, Efficient solar water-splitting using a nanocrystalline CoO photocatalyst, Nat. Nanotechnol. 9 (2013) 69. https://doi.org/10.1038/nnano.2013.272.

[89] P.C.K. Vesborg, T.F. Jaramillo, Addressing the terawatt challenge: scalability in the supply of chemical elements for renewable energy, RSC Adv. 2 (2012) 7933–7947. doi:10.1039/C2RA20839C.

[90] M.D. Bhatt, J.S. Lee, Recent theoretical progress in the development of photoanode materials for solar water splitting photoelectrochemical cells, J. Mater. Chem. A. 3 (2015) 10632–10659. doi:10.1039/C5TA00257E.

[91] M. Orlandi, A. Mazzi, G. Arban, N. Bazzanella, P. Rudatis, S. Caramori, N. Patel, R. Fernandes, C.A. Bignozzi, A. Miotello, On the effect of Sn-doping in hematite anodes for oxygen evolution, Electrochim. Acta. 214 (2016) 345–353. doi:https://doi.org/10.1016/j.electacta.2016.08.046.

[92] P. Shao, J. Tian, B. Liu, W. Shi, S. Gao, Y. Song, M. Ling, F. Cui, Morphology-tunable ultrafine metal oxide nanostructures uniformly grown on graphene and their applications in the photo-Fenton system, Nanoscale. 7 (2015) 14254–14263. doi:10.1039/C5NR03042K.

[93] M. Orlandi, N. Filosa, M. Bettonte, M. Fendrich, M. Girardini, T. Battistini, A. Miotello, Treatment of surfactant-rich industrial wastewaters with concentrated sunlight: toward solar wastewater remediation, Int. J. Environ. Sci. Technol. 16 (2019) 2109–2114. doi:10.1007/s13762-018-2099-7.

[94] M. Fendrich, A. Quaranta, M. Orlandi, M. Bettonte, A. Miotello, M.A. Fendrich, A. Quaranta, M. Orlandi, M. Bettonte, A. Miotello, Solar Concentration for Wastewaters Remediation: A Review of Materials and Technologies, Appl. Sci. 9 (2018) 118. doi:10.3390/app9010118.

[95] H. Zhang, R. Hou, Z.-L. Lu, X. Duan, A novel magnetic nanocomposite involving anatase titania coating on silica-modified cobalt ferrite via lower temperature hydrolysis of a water-soluble titania precursor, 2009. doi:10.1016/j.materresbull.2009.06.003.

[96] T.J. Castro, S.W. da Silva, F. Nakagomi, N.S. Moura, A. Franco, P.C. Morais, Structural and magnetic properties of ZnO–CoFe2O4 nanocomposites, J. Magn. Magn. Mater. 389 (2015) 27–33. doi:https://doi.org/10.1016/j.jmmm.2015.04.036.

[97] J.L. Domínguez-Arvizu, J.A. Jiménez-Miramontes, J.M. Salinas-Gutiérrez, M.J. Meléndez-Zaragoza, A. López-Ortiz, V. Collins-Martínez, Optical properties determination of NiFe2O4 nanoparticles and their photocatalytic evaluation towards hydrogen production, Int. J. Hydrogen Energy. 42 (2017) 30242–30248. doi:https://doi.org/10.1016/j.ijhydene.2017.09.180.

[98] J. Deng, Y. Shao, N. Gao, C. Tan, S. Zhou, X. Hu, CoFe2O4 magnetic nanoparticles as a highly active heterogeneous catalyst of oxone for the degradation of diclofenac in water, J. Hazard. Mater. 262 (2013) 836–844. doi:https://doi.org/10.1016/j.jhazmat.2013.09.049.

[99] Y. Zeng, N. Guo, Y. Song, Y. Zhao, H. Li, X. Xu, J. Qiu, H. Yu, Fabrication of Z-scheme magnetic MoS2/CoFe2O4 nanocomposites with highly efficient photocatalytic activity, J. Colloid Interface Sci. 514 (2018) 664–674. doi:https://doi.org/10.1016/j.jcis.2017.12.079.

[100] C. Haw, W. Chiu, S. Abdul Rahman, P. Khiew, S. Radiman, R. Abdul Shukor, M.A.A. Hamid, N. Ghazali, The design of new magnetic-photocatalyst nanocomposites (CoFe2O4–TiO2) as smart nanomaterials for recyclable-photocatalysis applications, New J. Chem. 40 (2016) 1124–1136. doi:10.1039/C5NJ02496J.

[101] S. Huang, Y. Xu, M. Xie, H. Xu, M. He, J. Xia, L. Huang, H. Li, Synthesis of magnetic CoFe2O4/g-C3N4 composite and its enhancement of photocatalytic ability under visible-light, Colloids Surfaces A Physicochem. Eng. Asp. 478 (2015) 71–80.

doi:https://doi.org/10.1016/j.colsurfa.2015.03.035.

[102] L. Gan, L. Xu, K. Qian, Preparation of core-shell structured CoFe2O4 incorporated Ag3PO4 nanocomposites for photocatalytic degradation of organic dyes, Mater. Des. 109 (2016) 354–360. doi:https://doi.org/10.1016/j.matdes.2016.07.043.

[103] L. Jing, Y. Xu, S. Huang, M. Xie, M. He, H. Xu, H. Li, Q. Zhang, Novel magnetic CoFe2O4/Ag/Ag3VO4 composites: Highly efficient visible light photocatalytic and antibacterial activity, Appl. Catal. B Environ. 199 (2016) 11–22. doi:https://doi.org/10.1016/j.apcatb.2016.05.049.

[104] G. He, J. Ding, J. Zhang, Q. Hao, H. Chen, One-Step Ball-Milling Preparation of Highly Photocatalytic Active CoFe2O4–Reduced Graphene Oxide Heterojunctions For Organic Dye Removal, Ind. Eng. Chem. Res. 54 (2015) 2862–2867. doi:10.1021/ie504706w.

[105] A. Miotello, N. Patel, Pulsed laser deposition of cluster-assembled films for catalysis and the photocatalysis relevant to energy and the environment, Appl. Surf. Sci. 278 (2013) 19–25. doi:https://doi.org/10.1016/j.apsusc.2012.11.073.

[106] G. Panaccione, I. Vobornik, J. Fujii, D. Krizmancic, E. Annese, L. Giovanelli, F. Maccherozzi, F. Salvador, A. De Luisa, D. Benedetti, A. Gruden, P. Bertoch, F. Polack, D. Cocco, G. Sostero, B. Diviacco, M. Hochstrasser, U. Maier, D. Pescia, C.H. Back, T. Greber, J. Osterwalder, M. Galaktionov, M. Sancrotti, G. Rossi, Advanced photoelectric effect experiment beamline at Elettra: A surface science laboratory coupled with Synchrotron Radiation, Rev. Sci. Instrum. 80 (2009) 43105. doi:10.1063/1.3119364.

[107] R. Edla, A. Tonezzer, M. Orlandi, N. Patel, R. Fernandes, N. Bazzanella, K. Date, D.C. Kothari, A. Miotello, 3D hierarchical nanostructures of iron oxides coatings prepared by pulsed laser deposition for photocatalytic water purification, Appl. Catal. B Environ. 219 (2017) 401–411. doi:https://doi.org/10.1016/j.apcatb.2017.07.063.

[108] S. Akhtar, W. An, X. Niu, K. Li, S. Anwar, K. Maaz, M. Maqbool, L. Gao, Toxicity of PEG-Coated CoFe2O4 Nanoparticles with Treatment Effect of Curcumin, Nanoscale Res. Lett. 13 (2018) 52. doi:10.1186/s11671-018-2468-7.

[109] X. He, X. Song, W. Qiao, Z. Li, X. Zhang, S. Yan, W. Zhong, Y. Du, Phase- and Size-Dependent Optical and Magnetic Properties of CoO Nanoparticles, J. Phys. Chem. C. 119 (2015) 9550–9559. doi:10.1021/jp5127909.

[110] X. Zhang, Y. Niu, X. Meng, Y. Li, J. Zhao, Structural evolution and characteristics of the phase transformations between α-Fe2O3, Fe3O4 and γ-Fe2O3 nanoparticles under reducing and oxidizing atmospheres, CrystEngComm. 15 (2013) 8166–8172. doi:10.1039/C3CE41269E.

[111] G.A. P., K.B. A., B.M. C., M.N. S., Investigation of multiplet splitting of Fe 2p XPS spectra and bonding in iron compounds, Surf. Interface Anal. 36 (2004) 1564–1574. doi:10.1002/sia.1984.

[112] Z. Zhou, Y. Zhang, Z. Wang, W. Wei, W. Tang, J. Shi, R. Xiong, Electronic structure studies of the spinel CoFe2O4 by X-ray photoelectron spectroscopy, Appl. Surf. Sci. 254 (2008) 6972–6975. doi:https://doi.org/10.1016/j.apsusc.2008.05.067.

[113] J. Everett, E. Céspedes, L.R. Shelford, C. Exley, J.F. Collingwood, J. Dobson, G. van der Laan, C.A. Jenkins, E. Arenholz, N.D. Telling, Ferrous iron formation following the co-aggregation of ferric iron and the Alzheimer’s disease peptide β-amyloid (1–42), J. R. Soc. Interface. 11 (2014) 20140165. doi:10.1098/rsif.2014.0165.

[114] L. Martín-García, A. Quesada, C. Munuera, J.F. Fernández, M. García-Hernández, M. Foerster, L. Aballe, J. de la Figuera, Atomically Flat Ultrathin Cobalt Ferrite Islands, Adv. Mater. 27 (2015) 5955–5960. doi:10.1002/adma.201502799.

[115] C. Himcinschi, I. Vrejoiu, G. Salvan, M. Fronk, A. Talkenberger, D.R.T. Zahn, D. Rafaja, J.

Kortus, Optical and magneto-optical study of nickel and cobalt ferrite epitaxial thin films and submicron structures, J. Appl. Phys. 113 (2013) 84101. doi:10.1063/1.4792749.

[116] B.S. Holinsworth, D. Mazumdar, H. Sims, Q.-C. Sun, M.K. Yurtisigi, S.K. Sarker, A. Gupta, W.H. Butler, J.L. Musfeldt, Chemical tuning of the optical band gap in spinel ferrites: CoFe2O4 vs NiFe2O4, Appl. Phys. Lett. 103 (2013) 82406. doi:10.1063/1.4818315.

[117] K.-W. Park, A.M. Kolpak, Understanding photocatalytic overall water splitting on CoO nanoparticles: Effects of facets, surface stoichiometry, and the CoO/water interface, J. Catal. 365 (2018) 115–124. doi:https://doi.org/10.1016/j.jcat.2018.06.021.

[118] S. Duangjam, K. Wetchakun, S. Phanichphant, N. Wetchakun, Hydrothermal synthesis of novel CoFe2O4/BiVO4 nanocomposites with enhanced visible-light-driven photocatalytic activities, Mater. Lett. 181 (2016) 86–91. doi:https://doi.org/10.1016/j.matlet.2016.06.024.

[119] J. Low, C. Jiang, B. Cheng, S. Wageh, A.A. Al-Ghamdi, J. Yu, A Review of Direct Z-Scheme Photocatalysts, Small Methods. 1 (2017) 1700080. doi:10.1002/smtd.201700080.

[120] O. Lorret, D. Francová, G. Waldner, N. Stelzer, W-doped titania nanoparticles for UV and visible-light photocatalytic reactions, Appl. Catal. B Environ. 91 (2009) 39–46. doi:https://doi.org/10.1016/j.apcatb.2009.05.005.

[121] D. Maruthamani, D. Divakar, M. Kumaravel, Enhanced photocatalytic activity of TiO2 by reduced graphene oxide in mineralization of Rhodamine B dye, J. Ind. Eng. Chem. 30 (2015) 33–43. doi:https://doi.org/10.1016/j.jiec.2015.04.026.

[122] R. Katoh, A. Furube, K. Yamanaka, T. Morikawa, Charge Separation and Trapping in N-Doped TiO2 Photocatalysts: A Time-Resolved Microwave Conductivity Study, J. Phys. Chem. Lett. 1 (2010) 3261–3265. doi:10.1021/jz1011548.

[123] J. Zhang, C. Pan, P. Fang, J. Wei, R. Xiong, Mo + C Codoped TiO2 Using Thermal Oxidation for Enhancing Photocatalytic Activity, ACS Appl. Mater. Interfaces. 2 (2010) 1173–1176. doi:10.1021/am100011c.

[124] R. Jaiswal, N. Patel, D.C. Kothari, A. Miotello, Improved visible light photocatalytic activity of TiO2 co-doped with Vanadium and Nitrogen, Appl. Catal. B Environ. 126 (2012) 47–54. doi:https://doi.org/10.1016/j.apcatb.2012.06.030.

[125] N. Patel, A. Dashora, R. Jaiswal, R. Fernandes, M. Yadav, D.C. Kothari, B.L. Ahuja, A. Miotello, Experimental and Theoretical Investigations on the Activity and Stability of Substitutional and Interstitial Boron in TiO2 Photocatalyst, J. Phys. Chem. C. 119 (2015) 18581–18590. doi:10.1021/acs.jpcc.5b05290.

[126] S. Sakthivel, M. V Shankar, M. Palanichamy, B. Arabindoo, D.W. Bahnemann, V. Murugesan, Enhancement of photocatalytic activity by metal deposition: characterisation and photonic efficiency of Pt, Au and Pd deposited on TiO2 catalyst, Water Res. 38 (2004) 3001–3008. doi:https://doi.org/10.1016/j.watres.2004.04.046.

[127] Y. Yang, L. Luo, M. Xiao, H. Li, X. Pan, F. Jiang, One-step hydrothermal synthesis of surface fluorinated TiO2/reduced graphene oxide nanocomposites for photocatalytic degradation of estrogens, Mater. Sci. Semicond. Process. 40 (2015) 183–193. doi:https://doi.org/10.1016/j.mssp.2015.06.012.

[128] Y. Shen, T. Xiong, T. Li, K. Yang, Tungsten and nitrogen co-doped TiO2 nano-powders with strong visible light response, Appl. Catal. B Environ. 83 (2008) 177–185. doi:https://doi.org/10.1016/j.apcatb.2008.01.037.

[129] A.M. Márquez, J.J. Plata, Y. Ortega, J. Fdez. Sanz, Structural Defects in W-Doped TiO2 (101) Anatase Surface: Density Functional Study, J. Phys. Chem. C. 115 (2011) 16970–16976. doi:10.1021/jp203223f.

[130] Y. Wang, Y.-Y. Zhang, J. Tang, H. Wu, M. Xu, Z. Peng, X.-G. Gong, G. Zheng, Simultaneous Etching and Doping of TiO2 Nanowire Arrays for Enhanced Photoelectrochemical Performance, ACS Nano. 7 (2013) 9375–9383. doi:10.1021/nn4040876.

[131] R. Pandiyan, N. Delegan, A. Dirany, P. Drogui, M.A. El Khakani, Probing the Electronic Surface Properties and Bandgap Narrowing of in situ N, W, and (W,N) Doped Magnetron-Sputtered TiO2 Films Intended for Electro-Photocatalytic Applications, J. Phys. Chem. C. 120 (2016) 631–638. doi:10.1021/acs.jpcc.5b08057.

[132] T. Putta, M.-C. Lu, J. Anotai, Photocatalytic activity of tungsten-doped TiO2 with hydrothermal treatment under blue light irradiation, J. Environ. Manage. 92 (2011) 2272–2276. doi:https://doi.org/10.1016/j.jenvman.2011.04.016.

[133] I. Cho, O.-K. Kwon, Perturbations in symmetric Lee-Wick bouncing universe, Eur. Phys. J. C. 73 (2013) 1–8. doi:10.1140/epjc/s10052-013-2341-x.

[134] Q. Xiao, L. Gao, One-step hydrothermal synthesis of C, W-codoped mesoporous TiO2 with enhanced visible light photocatalytic activity, J. Alloys Compd. 551 (2013) 286–292. doi:https://doi.org/10.1016/j.jallcom.2012.10.040.

[135] M. Khan, W. Cao, N. Chen, Z. Usman, D.F. Khan, A.M. Toufiq, M.A. Khaskheli, Influence of tungsten doping concentration on the electronic and optical properties of anatase TiO2, Curr. Appl. Phys. 13 (2013) 1376–1382. doi:https://doi.org/10.1016/j.cap.2013.04.023.

[136] B. Tryba, M. Tygielska, M. Grzeskowiak, J. Przepiorski, Improvement of charge separation in TiO2 by its modification with different tungsten compounds, Mater. Res. Bull. 76 (2016) 1–7. doi:https://doi.org/10.1016/j.materresbull.2015.12.001.

[137] E.M. Neville, M.J. Mattle, D. Loughrey, B. Rajesh, M. Rahman, J.M.D. MacElroy, J.A. Sullivan, K.R. Thampi, Carbon-Doped TiO2 and Carbon, Tungsten-Codoped TiO2 through Sol–Gel Processes in the Presence of Melamine Borate: Reflections through Photocatalysis, J. Phys. Chem. C. 116 (2012) 16511–16521. doi:10.1021/jp303645p.

[138] D. Wang, Y. Zou, S. Wen, D. Fan, A passivated codoping approach to tailor the band edges of TiO2 for efficient photocatalytic degradation of organic pollutants, Appl. Phys. Lett. 95 (2009) 12106. doi:10.1063/1.3174917.

[139] X. Zhang, F. Liu, Q.-L. Huang, G. Zhou, Z.-S. Wang, Dye-Sensitized W-Doped TiO2 Solar Cells with a Tunable Conduction Band and Suppressed Charge Recombination, J. Phys. Chem. C. 115 (2011) 12665–12671. doi:10.1021/jp201853c.

[140] Z. Zhang, Z. Wang, S.-W. Cao, C. Xue, Au/Pt Nanoparticle-Decorated TiO2 Nanofibers with Plasmon-Enhanced Photocatalytic Activities for Solar-to-Fuel Conversion, J. Phys. Chem. C. 117 (2013) 25939–25947. doi:10.1021/jp409311x.

[141] Y. Wang, B. Li, C. Zhang, L. Cui, S. Kang, X. Li, L. Zhou, Ordered mesoporous CeO2-TiO2 composites: Highly efficient photocatalysts for the reduction of CO2 with H2O under simulated solar irradiation, Appl. Catal. B Environ. 130–131 (2013) 277–284. doi:https://doi.org/10.1016/j.apcatb.2012.11.019.

[142] H. Sun, S. Wang, Research Advances in the Synthesis of Nanocarbon-Based Photocatalysts and Their Applications for Photocatalytic Conversion of Carbon Dioxide to Hydrocarbon Fuels, Energy & Fuels. 28 (2014) 22–36. doi:10.1021/ef401426x.

[143] Q. Tay, Z. Chen, Effective charge separation towards enhanced photocatalytic activity via compositing reduced graphene oxide with two-phase anatase/brookite TiO2, Int. J. Hydrogen Energy. 41 (2016) 10590–10597. doi:https://doi.org/10.1016/j.ijhydene.2016.04.022.

[144] R. He, W. He, Ultrasonic assisted synthesis of TiO2–reduced graphene oxide nanocomposites with superior photovoltaic and photocatalytic activities, Ceram. Int. 42 (2016) 5766–5771.

doi:https://doi.org/10.1016/j.ceramint.2015.12.114.

[145] V. Georgakilas, J.N. Tiwari, K.C. Kemp, J.A. Perman, A.B. Bourlinos, K.S. Kim, R. Zboril, Noncovalent Functionalization of Graphene and Graphene Oxide for Energy Materials, Biosensing, Catalytic, and Biomedical Applications, Chem. Rev. 116 (2016) 5464–5519. doi:10.1021/acs.chemrev.5b00620.

[146] H.-L. Yu et al, Impact of Addition of FGDB as a Soil Amendment on Physical and Chemical Properties of an Alkali Soil and Crop Yield of Maize in Northern China Coastal Plain, J. Chem. (2015). https://doi.org/10.1155/2015/540604.

[147] P. Wang, J. Wang, T. Ming, X. Wang, H. Yu, J. Yu, Y. Wang, M. Lei, Dye-Sensitization-Induced Visible-Light Reduction of Graphene Oxide for the Enhanced TiO2 Photocatalytic Performance, ACS Appl. Mater. Interfaces. 5 (2013) 2924–2929. doi:10.1021/am4008566.

[148] P. Wang, J. Wang, X. Wang, H. Yu, J. Yu, M. Lei, Y. Wang, One-step synthesis of easy-recycling TiO2-rGO nanocomposite photocatalysts with enhanced photocatalytic activity, Appl. Catal. B Environ. 132–133 (2013) 452–459. doi:https://doi.org/10.1016/j.apcatb.2012.12.009.

[149] P.K. Kalambate, R.A. Dar, S.P. Karna, A.K. Srivastava, High performance supercapacitor based on graphene-silver nanoparticles-polypyrrole nanocomposite coated on glassy carbon electrode, J. Power Sources. 276 (2015) 262–270. doi:https://doi.org/10.1016/j.jpowsour.2014.11.130.

[150] R. Jaiswal, J. Bharambe, N. Patel, A. Dashora, D.C. Kothari, A. Miotello, Copper and Nitrogen co-doped TiO2 photocatalyst with enhanced optical absorption and catalytic activity, Appl. Catal. B Environ. 168–169 (2015) 333–341. doi:10.1016/j.apcatb.2014.12.053.

[151] R. Jaiswal, N. Patel, A. Dashora, R. Fernandes, M. Yadav, R. Edla, R.S. Varma, D.C. Kothari, B.L. Ahuja, A. Miotello, Efficient Co-B-codoped TiO2 photocatalyst for degradation of organic water pollutant under visible light, Appl. Catal. B Environ. 183 (2016) 242–253. doi:10.1016/j.apcatb.2015.10.041.

[152] R. Dholam, N. Patel, M. Adami, A. Miotello, Hydrogen production by photocatalytic water-splitting using Cr- or Fe-doped TiO2 composite thin films photocatalyst, Int. J. Hydrogen Energy. 34 (2009) 5337–5346. doi:https://doi.org/10.1016/j.ijhydene.2009.05.011.

[153] Z. Xiong, Y. Luo, Y. Zhao, J. Zhang, C. Zheng, J.C.S. Wu, Synthesis, characterization and enhanced photocatalytic CO2 reduction activity of graphene supported TiO2 nanocrystals with coexposed {001} and {101} facets, Phys. Chem. Chem. Phys. 18 (2016) 13186–13195. doi:10.1039/C5CP07854G.

[154] T. Lavanya, M. Dutta, K. Satheesh, Graphene wrapped porous tubular rutile TiO2 nanofibers with superior interfacial contact for highly efficient photocatalytic performance for water treatment, Sep. Purif. Technol. 168 (2016) 284–293. doi:https://doi.org/10.1016/j.seppur.2016.05.059.

[155] X.-Y. Zhang, H.-P. Li, X.-L. Cui, Y. Lin, Graphene/TiO2 nanocomposites: synthesis, characterization and application in hydrogen evolution from water photocatalytic splitting, J. Mater. Chem. 20 (2010) 2801–2806. doi:10.1039/B917240H.

[156] M. Shi, J. Shen, H. Ma, Z. Li, X. Lu, N. Li, M. Ye, Preparation of graphene–TiO2 composite by hydrothermal method from peroxotitanium acid and its photocatalytic properties, Colloids Surfaces A Physicochem. Eng. Asp. 405 (2012) 30–37. doi:https://doi.org/10.1016/j.colsurfa.2012.04.031.

[157] M.-S. Seo, I. Jeong, J.-S. Park, J. Lee, I.K. Han, W.I. Lee, H.J. Son, B.-H. Sohn, M.J. Ko, Vertically aligned nanostructured TiO2 photoelectrodes for high efficiency perovskite solar cells via a block copolymer template approach, Nanoscale. 8 (2016) 11472–11479. doi:10.1039/C6NR01010E.

[158] Z. Wang, Q. Dong, Y. Xia, H. Yu, K. Zhang, X. Liu, X. Guo, Y. Zhou, M. Zhang, B. Song, Copolymers based on thiazolothiazole-dithienosilole as hole-transporting materials for high efficient perovskite solar cells, Org. Electron. 33 (2016) 142–149. doi:https://doi.org/10.1016/j.orgel.2016.03.020.

[159] B. Liu, Y. Xue, J. Zhang, B. Han, J. Zhang, X. Suo, L. Mu, H. Shi, Visible-light-driven TiO2/Ag3PO4 heterostructures with enhanced antifungal activity against agricultural pathogenic fungi Fusarium graminearum and mechanism insight, Environ. Sci. Nano. 4 (2017) 255–264. doi:10.1039/C6EN00415F.

[160] J. Nowotny, T. Bak, M.K. Nowotny, L.R. Sheppard, TiO2 Surface Active Sites for Water Splitting, J. Phys. Chem. B. 110 (2006) 18492–18495. doi:10.1021/jp063699p.

[161] O. Akhavan, M. Abdolahad, Y. Abdi, S. Mohajerzadeh, Synthesis of titania/carbon nanotube heterojunction arrays for photoinactivation of E. coli in visible light irradiation, Carbon N. Y. 47 (2009) 3280–3287. doi:https://doi.org/10.1016/j.carbon.2009.07.046.

[162] S. Yang, C. Cao, P. Huang, L. Peng, Y. Sun, F. Wei, W. Song, Sandwich-like porous TiO2/reduced graphene oxide (rGO) for high-performance lithium-ion batteries, J. Mater. Chem. A. 3 (2015) 8701–8705. doi:10.1039/C5TA01744K.

[163] A. Nikfarjam, S. Hosseini, N. Salehifar, Fabrication of a Highly Sensitive Single Aligned TiO2 and Gold Nanoparticle Embedded TiO2 Nano-Fiber Gas Sensor, ACS Appl. Mater. Interfaces. 9 (2017) 15662–15671. doi:10.1021/acsami.6b15554.

[164] Y.-G. Kim, J. Walker, L.A. Samuelson, J. Kumar, Efficient light harvesting polymers for nanocrystalline TiO2 photovoltaic cells, Nano Lett. 3 (2003) 523–525. doi:10.1021/nl0259535.

[165] J. Zhou, Y. Zhang, X.S. Zhao, A.K. Ray, Photodegradation of Benzoic Acid over Metal-Doped TiO2, Ind. Eng. Chem. Res. 45 (2006) 3503–3511. doi:10.1021/ie051098z.

[166] Tian, Liu, DFT Description on Electronic Structure and Optical Absorption Properties of Anionic S-Doped Anatase TiO2, J. Phys. Chem. B. 110 (2006) 17866–17871. doi:10.1021/jp0635462.

[167] D. Qi, M. Xing, J. Zhang, Hydrophobic Carbon-Doped TiO2/MCF-F Composite as a High Performance Photocatalyst, J. Phys. Chem. C. 118 (2014) 7329–7336. doi:10.1021/jp4123979.

[168] M. Yadav, A. Yadav, R. Fernandes, Y. Popat, M. Orlandi, A. Dashora, D.C. Kothari, A. Miotello, B.L. Ahuja, N. Patel, Tungsten-doped TiO2/reduced Graphene Oxide nano-composite photocatalyst for degradation of phenol: A system to reduce surface and bulk electron-hole recombination, J. Environ. Manage. 203 (2017) 364–374. doi:https://doi.org/10.1016/j.jenvman.2017.08.010.

[169] H. Kim, J. Kim, W. Kim, W. Choi, Enhanced Photocatalytic and Photoelectrochemical Activity in the Ternary Hybrid of CdS/TiO2/WO3 through the Cascadal Electron Transfer, J. Phys. Chem. C. 115 (2011) 9797–9805. doi:10.1021/jp1122823.

[170] X. Wang, W. Yang, F. Li, Y. Xue, R. Liu, Y. Hao, In Situ Microwave-Assisted Synthesis of Porous N-TiO2/g-C3N4 Heterojunctions with Enhanced Visible-Light Photocatalytic Properties, Ind. Eng. Chem. Res. 52 (2013) 17140–17150. doi:10.1021/ie402820v.

[171] R. Leary, A. Westwood, Carbonaceous nanomaterials for the enhancement of TiO2 photocatalysis, Carbon N. Y. 49 (2011) 741–772. doi:https://doi.org/10.1016/j.carbon.2010.10.010.

[172] Y. Yao, G. Li, S. Ciston, R.M. Lueptow, K.A. Gray, Photoreactive TiO2/Carbon Nanotube Composites: Synthesis and Reactivity, Environ. Sci. Technol. 42 (2008) 4952–4957. doi:10.1021/es800191n.

[173] M.-Q. Yang, N. Zhang, Y.-J. Xu, Synthesis of Fullerene–, Carbon Nanotube–, and Graphene–TiO2 Nanocomposite Photocatalysts for Selective Oxidation: A Comparative Study, ACS Appl. Mater. Interfaces. 5 (2013) 1156–1164. doi:10.1021/am3029798.

[174] R.K. Upadhyay, N. Soin, S.S. Roy, Role of graphene/metal oxide composites as photocatalysts{,} adsorbents and disinfectants in water treatment: a review, RSC Adv. 4 (2014) 3823–3851. doi:10.1039/C3RA45013A.

[175] W. Iqbal, B. Tian, M. Anpo, J. Zhang, Single-step solvothermal synthesis of mesoporous anatase TiO2-reduced graphene oxide nanocomposites for the abatement of organic pollutants, Res. Chem. Intermed. 43 (2017) 5187–5201. doi:10.1007/s11164-017-3049-6.

[176] Y. Liu, Hydrothermal synthesis of TiO2-RGO composites and their improved photocatalytic activity in visible light, RSC Adv. 4 (2014) 36040–36045. doi:10.1039/c4ra06342b.

[177] H. Yu, P. Xiao, J. Tian, F. Wang, J. Yu, Phenylamine-Functionalized rGO/TiO2 Photocatalysts: Spatially Separated Adsorption Sites and Tunable Photocatalytic Selectivity, ACS Appl. Mater. Interfaces. 8 (2016) 29470–29477. doi:10.1021/acsami.6b09903.

[178] G. Jiang, Z. Lin, C. Chen, L. Zhu, Q. Chang, N. Wang, W. Wei, H. Tang, TiO2 nanoparticles assembled on graphene oxide nanosheets with high photocatalytic activity for removal of pollutants, Carbon N. Y. 49 (2011) 2693–2701. doi:https://doi.org/10.1016/j.carbon.2011.02.059.

[179] J. Yang, Z. Wen, X. Shen, J. Dai, Y. Li, Y. Li, A comparative study on the photocatalytic behavior of graphene-TiO2 nanostructures: Effect of TiO2 dimensionality on interfacial charge transfer, Chem. Eng. J. 334 (2018) 907–921. doi:https://doi.org/10.1016/j.cej.2017.10.088.

[180] Y. Gao, X. Pu, D. Zhang, G. Ding, X. Shao, J. Ma, Combustion synthesis of graphene oxide–TiO2 hybrid materials for photodegradation of methyl orange, Carbon N. Y. 50 (2012) 4093–4101. doi:https://doi.org/10.1016/j.carbon.2012.04.057.

[181] X. Pu, D. Zhang, Y. Gao, X. Shao, G. Ding, S. Li, S. Zhao, One-pot microwave-assisted combustion synthesis of graphene oxide–TiO2 hybrids for photodegradation of methyl orange, J. Alloys Compd. 551 (2013) 382–388. doi:https://doi.org/10.1016/j.jallcom.2012.11.028.

[182] J.S. Lee, K.H. You, C.B. Park, Highly Photoactive, Low Bandgap TiO2 Nanoparticles Wrapped by Graphene, Adv. Mater. 24 (2012) 1084–1088. doi:10.1002/adma.201104110.

[183] G. Williams, B. Seger, P. V Kamat, TiO2-Graphene Nanocomposites. UV-Assisted Photocatalytic Reduction of Graphene Oxide, ACS Nano. 2 (2008) 1487–1491. doi:10.1021/nn800251f.

[184] A. Meidanchi, O. Akhavan, Superparamagnetic zinc ferrite spinel–graphene nanostructures for fast wastewater purification, Carbon N. Y. 69 (2014) 230–238. doi:https://doi.org/10.1016/j.carbon.2013.12.019.

[185] Y. Xin, T. Li, F. Xu, M. Wang, Multidimensional structure and enhancement performance of modified graphene/carbon nanotube assemblies in tribological properties of polyimide nanocomposites, RSC Adv. 7 (2017) 20742–20753. doi:10.1039/C7RA02149F.

[186] T.N. Blanton, D. Majumdar, X-ray diffraction characterization of polymer intercalated graphite oxide, Powder Diffr. 27 (2012) 104–107. doi:DOI: 10.1017/S0885715612000292.

[187] Q. Zhu, X. Wang, J. Jiang, A.-W. Xu, “Healing” Effect of Graphene Oxide in Achieving Robust Dilute Ferromagnetism in Oxygen-Deficient Titanium Dioxide, J. Phys. Chem. C. 121 (2017) 22806–22814. doi:10.1021/acs.jpcc.7b07011.

[188] J. Zhang, H. Yang, G. Shen, P. Cheng, J. Zhang, S. Guo, Reduction of graphene oxide vial-ascorbic acid, Chem. Commun. 46 (2010) 1112–1114. doi:10.1039/b917705a.

[189] H. Al-Kandari, A.M. Abdullah, S. Al-Kandari, A.M. Mohamed, Effect of the graphene oxide reduction method on the photocatalytic and electrocatalytic activities of reduced graphene oxide/TiO2 composite, RSC Adv. 5 (2015) 71988–71998. doi:10.1039/C5RA13065D.

[190] O. Akhavan, Bacteriorhodopsin as a superior substitute for hydrazine in chemical reduction of single-layer graphene oxide sheets, Carbon N. Y. 81 (2015) 158–166. doi:https://doi.org/10.1016/j.carbon.2014.09.044.

[191] S. Umrao, S. Abraham, F. Theil, S. Pandey, V. Ciobota, P.K. Shukla, C.J. Rupp, S. Chakraborty, R. Ahuja, J. Popp, B. Dietzek, A. Srivastava, A possible mechanism for the emergence of an additional band gap due to a Ti–O–C bond in the TiO2–graphene hybrid system for enhanced photodegradation of methylene blue under visible light, RSC Adv. 4 (2014) 59890–59901. doi:10.1039/C4RA10572A.

[192] O. Akhavan, E. Ghaderi, Flash photo stimulation of human neural stem cells on graphene/TiO2 heterojunction for differentiation into neurons, Nanoscale. 5 (2013) 10316–10326. doi:10.1039/C3NR02161K.

[193] O. Akhavan, E. Ghaderi, Photocatalytic Reduction of Graphene Oxide Nanosheets on TiO2 Thin Film for Photoinactivation of Bacteria in Solar Light Irradiation, J. Phys. Chem. C. 113 (2009) 20214–20220. doi:10.1021/jp906325q.

[194] O. Akhavan, E. Ghaderi, Differentiation of human neural stem cells into neural networks on graphene nanogrids, J. Mater. Chem. B. 1 (2013) 6291–6301. doi:10.1039/C3TB21085E.

[195] Y. Zhang, M. Sivakumar, S. Yang, K. Enever, M. Ramezanianpour, Application of solar energy in water treatment processes: A review, Desalination. 428 (2018) 116–145. doi:10.1016/j.desal.2017.11.020.

[196] I. García-Fernández, S. Miralles-Cuevas, I. Oller, S. Malato, P. Fernández-Ibáñez, M.I. Polo-López, Inactivation of E. coli and E. faecalis by solar photo-Fenton with EDDS complex at neutral pH in municipal wastewater effluents, J. Hazard. Mater. (2018) 0–1. doi:10.1016/j.jhazmat.2018.07.037.

[197] M.I. Polo-López, M. Castro-Alférez, I. Oller, P. Fernández-Ibáñez, Assessment of solar photo-Fenton, photocatalysis, and H2O2for removal of phytopathogen fungi spores in synthetic and real effluents of urban wastewater, Chem. Eng. J. 257 (2014) 122–130. doi:10.1016/j.cej.2014.07.016.

[198] H. Haider, W. Ali, S. Haydar, S. Tesfamariam, R. Sadiq, Modeling exposure period for solar disinfection (SODIS) under varying turbidity and cloud cover conditions, Clean Technol. Environ. Policy. 16 (2014) 861–874. doi:10.1007/s10098-013-0677-4.

[199] W. Jin, H. Zhang, S. Liu, H. Zhang, Technological innovation , environmental regulation , and green total factor ef fi ciency of industrial water resources, J. Clean. Prod. 211 (2019) 61–69. doi:10.1016/j.jclepro.2018.11.172.

[200] X. Zhou, B. Zheng, S. Khu, Science of the Total Environment Validation of the hypothesis on carrying capacity limits using the water environment carrying capacity, Sci. Total Environ. 665 (2019) 774–784. doi:10.1016/j.scitotenv.2019.02.146.

[201] A.C. Mecha, M.S. Onyango, A. Ochieng, M.N.B. Momba, Ultraviolet and solar photocatalytic ozonation of municipal wastewater: Catalyst reuse, energy requirements and toxicity assessment, Chemosphere. 186 (2017) 669–676. doi:10.1016/j.chemosphere.2017.08.041.

[202] J. Willet, K. Wetser, J. Vreeburg, H.H.M. Rijnaarts, SC, Water Resour. Ind. (2019) 100110. doi:10.1016/j.wri.2019.100110.

[203] R.R.Z. Tarpani, A. Azapagic, Life cycle costs of advanced treatment techniques for wastewater reuse and resource recovery from sewage sludge, J. Clean. Prod. 204 (2018) 832–847.

doi:10.1016/j.jclepro.2018.08.300.

[204] Y. Zhu, X. Liu, Y. Hu, R. Wang, M. Chen, J. Wu, Y. Wang, S. Kang, Y. Sun, M. Zhu, Behavior, remediation effect and toxicity of nanomaterials in water environments, Environ. Res. (2019). doi:10.1016/j.envres.2019.04.014.

[205] W.H. Glaze, J.-W. Kang, D.H. Chapin, The Chemistry of Water Treatment Processes Involving Ozone, Hydrogen Peroxide and Ultraviolet Radiation, Ozone Sci. Eng. 9 (1987) 335–352. doi:10.1080/01919518708552148.

[206] A.R. Ribeiro, O.C. Nunes, M.F.R. Pereira, A.M.T. Silva, An overview on the advanced oxidation processes applied for the treatment of water pollutants defined in the recently launched Directive 2013/39/EU, Environ. Int. 75 (2015) 33–51. doi:https://doi.org/10.1016/j.envint.2014.10.027.

[207] F.E. Osterloh, Inorganic nanostructures for photoelectrochemical and photocatalytic water splitting, Chem. Soc. Rev. 42 (2013) 2294–2320. doi:10.1039/c2cs35266d.

[208] N. Miranda-García, M.I. Maldonado, J.M. Coronado, S. Malato, Degradation study of 15 emerging contaminants at low concentration by immobilized TiO2in a pilot plant, Catal. Today. 151 (2010) 107–113. doi:10.1016/j.cattod.2010.02.044.

[209] S. Malato, M.I. Maldonado, P. Fernández-Ibáñez, I. Oller, I. Polo, R. Sánchez-Moreno, Decontamination and disinfection of water by solar photocatalysis: The pilot plants of the Plataforma Solar de Almeria, Mater. Sci. Semicond. Process. 42 (2016) 15–23. doi:10.1016/j.mssp.2015.07.017.

[210] B. Wang, Z. Yang, H. An, J. Zhai, Q. Li, H. Cui, Photocatalytic activity of Pt-TiO2films supported on hydroxylated fly ash cenospheres under visible light, Appl. Surf. Sci. 324 (2015) 817–824. doi:10.1016/j.apsusc.2014.11.046.

[211] N. Patel, R. Jaiswal, T. Warang, G. Scarduelli, A. Dashora, B.L. Ahuja, D.C. Kothari, A. Miotello, Efficient photocatalytic degradation of organic water pollutants using V-N-codoped TiO2 thin films, Appl. Catal. B Environ. 150–151 (2014) 74–81. doi:10.1016/j.apcatb.2013.11.033.

[212] R.S. Varma, N. Thorat, R. Fernandes, D.C. Kothari, N. Patel, A. Miotello, Dependence of photocatalysis on charge carrier separation in Ag-doped and decorated TiO2 nanocomposites, Catal. Sci. Technol. 6 (2016) 8428–8440. doi:10.1039/c6cy01605g.

[213] N. Yahya, F. Aziz, N.A. Jamaludin, M. A. Mutalib, A.F. Ismail, W.N. W. Salleh, J. Jaafar, N. Yusof, N. A. Ludin, A review of integrated photocatalyst adsorbents for wastewater treatment, J. Environ. Chem. Eng. (2018) 0–1. doi:10.1016/j.jece.2018.06.051.

[214] H.Y. Jing, T. Wen, C.M. Fan, G.Q. Gao, S.L. Zhong, A.W. Xu, Efficient adsorption/photodegradation of organic pollutants from aqueous systems using Cu2O nanocrystals as a novel integrated photocatalytic adsorbent, J. Mater. Chem. A. 2 (2014) 14563–14570. doi:10.1039/c4ta02459a.

[215] J. Niu, L. Yin, Y. Dai, Y. Bao, J.C. Crittenden, Design of visible light responsive photocatalysts for selective reduction of chlorinated organic compounds in water, Appl. Catal. A Gen. 521 (2016) 90–95. doi:10.1016/j.apcata.2015.11.018.

[216] J. Fenoll, P. Hellín, C.M. Martínez, P. Flores, S. Navarro, Semiconductor oxides-sensitized photodegradation of fenamiphos in leaching water under natural sunlight, Appl. Catal. B Environ. 115–116 (2012) 31–37. doi:10.1016/j.apcatb.2011.12.023.

[217] M. Tanveer, G. Tezcanli Guyer, Solar assisted photo degradation of wastewater by compound parabolic collectors: Review of design and operational parameters, Renew. Sustain. Energy Rev. 24 (2013) 534–543. doi:10.1016/j.rser.2013.03.053.

[218] P. Pichat, Photocatalysis and Water Purification: From Fundamentals to Recent Applications, 2013. doi:10.1002/9783527645404.

[219] S.M. Rodríguez, J.B. Gálvez, M.I.M. Rubio, P.F. Ibáñez, D.A. Padilla, M.C. Pereira, J.F. Mendes, J.C. De Oliveira, Engineering of solar photocatalytic collectors, Sol. Energy. 77 (2004) 513–524. doi:10.1016/j.solener.2004.03.020.

[220] S. Turrini, M. Bettonte, M. Eccher, M. Grigiante, A. Miotello, R.S. Brusa, An innovative small-scale prototype plant integrating a solar dish concentrator with a molten salt storage system, Renew. Energy. 123 (2018) 150–161. doi:10.1016/j.renene.2018.02.053.

[221] C. Kutscher, R. Davenport, R. Farrington, G. Jorgensen, A. Lewandowski, C. Vineyard, Low-cost collectors. System development progress report, Sol. Energy Res. Inst. (1984).

[222] M. Orlandi, N. Filosa, M. Bettonte, M. Fendrich, M. Girardini, T. Battistini, A. Miotello, Treatment of surfactant-rich industrial wastewaters with concentrated sunlight: toward solar wastewater remediation, Int. J. Environ. Sci. Technol. (2018). doi:10.1007/s13762-018-2099-7.

[223] P. Bansal, A. Verma, S. Talwar, Detoxification of real pharmaceutical wastewater by integrating photocatalysis and photo-Fenton in fixed-mode, Chem. Eng. J. 349 (2018) 838–848. doi:10.1016/j.cej.2018.05.140.

[224] N.Z. Muradov, Solar detoxification of nitroglycerine-contaminated water using immobilized titania, Sol. Energy. (1994). doi:10.1016/0038-092X(94)90495-2.

[225] E.M. Rodríguez, G. Fernández, N. Klamerth, M.I. Maldonado, P.M. Álvarez, S. Malato, Efficiency of different solar advanced oxidation processes on the oxidation of bisphenol A in water, Appl. Catal. B Environ. 95 (2010) 228–237. doi:10.1016/j.apcatb.2009.12.027.

[226] O. Sacco, V. Vaiano, L. Rizzo, D. Sannino, Photocatalytic activity of a visible light active structured photocatalyst developed for municipal wastewater treatment, J. Clean. Prod. 175 (2018) 38–49. doi:10.1016/j.jclepro.2017.11.088.

[227] A. Mecha, M. Onyango, A. Ochieng, M. Momba, UV and solar photocatalytic disinfection of municipal wastewater: inactivation, reactivation and regrowth of bacterial pathogens, 2018. doi:10.1007/s13762-018-1950-1.

[228] N. Vela, M. Calín, M.J. Yáñez-Gascón, I. Garrido, G. Pérez-Lucas, J. Fenoll, S. Navarro, Solar reclamation of wastewater effluent polluted with bisphenols, phthalates and parabens by photocatalytic treatment with TiO2/Na2S2O8at pilot plant scale, Chemosphere. 212 (2018) 95–104. doi:10.1016/j.chemosphere.2018.08.069.

[229] T. Sano, N. Negishi, K. Takeuchi, S. Matsuzawa, Degradation of toluene and acetaldehyde with Pt-loaded TiO2 catalyst and parabolic trough concentrator, Sol. Energy. (2004). doi:10.1016/j.solener.2004.03.018.

[230] F.S. Manciu, J.L. Enriquez, W.G. Durrer, Y. Yun, C. V. Ramana, S.K. Gullapalli, Spectroscopic analysis of tungsten oxide thin films, J. Mater. Res. 25 (2010) 2401–2406. doi:10.1557/jmr.2010.0294.

[231] V.I. Shapovalov, A.E. Lapshin, A.G. Gagarin, L.P. Efimenko, Chemical composition and crystal structure of tungsten oxide films, Glas. Phys. Chem. 40 (2014) 553–569. doi:10.1134/S1087659614050150.

[232] L.H. Jin, Y. Bai, C.S. Li, Y. Wang, J.Q. Feng, L. Lei, G.Y. Zhao, P.X. Zhang, Growth of tungsten oxide nanostructures by chemical solution deposition, Appl. Surf. Sci. 440 (2018) 725–729. doi:10.1016/j.apsusc.2018.01.251.

[233] E. Besozzi, D. Dellasega, V. Russo, C. Conti, M. Passoni, M.G. Beghi, Thermomechanical properties of amorphous metallic tungsten-oxygen and tungsten-oxide coatings, Mater. Des. 165

(2019) 107565. doi:10.1016/j.matdes.2018.107565.

[234] T. Tokunaga, T. Kawamoto, K. Tanaka, N. Nakamura, Y. Hayashi, K. Sasaki, K. Kuroda, T. Yamamoto, Growth and structure analysis of tungsten oxide nanorods using environmental TEM, Nanoscale Res. Lett. 7 (2012) 1–7. doi:10.1186/1556-276X-7-85.

[235] H. Na, Y. Eun, M.O. Kim, J. Choi, J. Kim, Low-Temperature Selective Growth of Tungsten Oxide Nanowires by Controlled Nanoscale Stress Induction, Sci. Rep. 5 (2015) 1–8. doi:10.1038/srep18265.

[236] M.I. Nave, K.G. Kornev, Complexity of Products of Tungsten Corrosion : Comparison of the 3D Pourbaix Diagrams with the Experimental Data, Metall. Mater. Trans. A. 48 (2016) 1414–1424. doi:10.1007/s11661-016-3888-6.

[237] J. Zhu, S. Wang, S. Xie, H. Li, Hexagonal single crystal growth of WO3 nanorods along a [110] axis with enhanced adsorption capacity, Chem. Commun. 47 (2011) 4403. doi:10.1039/c1cc00064k.

[238] F. Mitsugi, E. Hiraiwa, T. Ikegami, K. Ebihara, Pulsed laser deposited WO3 thin films for gas sensor, Surf. Coatings Technol. 169–170 (2003) 553–556. doi:10.1016/S0257-8972(03)00208-1.

[239] I.M. Szilágyi, J. Madarász, G. Pokol, P. Király, G. Tárkányi, S. Saukko, J. Mizsei, A.L. Tóth, A. Szabó, K. Varga-Josepovits, Stability and controlled composition of hexagonal WO3, Chem. Mater. 20 (2008) 4116–4125. doi:10.1021/cm800668x.

[240] F. Tavakoli Foroushani, H. Tavanai, M. Ranjbar, H. Bahrami, Fabrication of tungsten oxide nanofibers via electrospinning for gasochromic hydrogen detection, Sensors Actuators, B Chem. 268 (2018) 319–327. doi:10.1016/j.snb.2018.04.120.

[241] X. Xu, M. Arab Pour Yazdi, J.B. Sanchez, A. Billard, F. Berger, N. Martin, Exploiting the dodecane and ozone sensing capabilities of nanostructured tungsten oxide films, Sensors Actuators, B Chem. 266 (2018) 773–783. doi:10.1016/j.snb.2018.03.190.

[242] Y. Yao, M. Yin, J. Yan, S. (Frank) Liu, P-type sub-tungsten-oxide based urchin-like nanostructure for superior room temperature alcohol sensor, Appl. Surf. Sci. 441 (2018) 277–284. doi:10.1016/j.apsusc.2018.02.004.

[243] A. Palla-Papavlu, M. Filipescu, C.W. Schneider, S. Antohe, P.M. Ossi, G. Radnï¿½czi, M. Dinescu, A. Wokaun, T. Lippert, Direct laser deposition of nanostructured tungsten oxide for sensing applications, J. Phys. D. Appl. Phys. 49 (2016). doi:10.1088/0022-3727/49/20/205101.

[244] A. Rougier, F. Portemer, A. Quédé, M. El Marssi, Characterization of pulsed laser deposited WO3 thin films for electrochromic devices, Appl. Surf. Sci. 153 (1999) 1–9. doi:10.1016/S0169-4332(99)00335-9.

[245] Y. Djaoued, S. Balaji, R. Brüning, Electrochromic devices based on porous tungsten oxide thin films, J. Nanomater. 2012 (2012). doi:10.1155/2012/674168.

[246] N. Wang, J. Zhu, X. Zheng, F. Xiong, B. Huang, J. Shi, C. Li, A facile two-step method for fabrication of plate-like WO3 photoanode under mild conditions, Faraday Discuss. 176 (2014) 185–197. doi:10.1039/c4fd00139g.

[247] K. Li, C. Zhang, A. Liu, D. Chu, C. Zhang, P. Yang, Y. Du, J. Huang, Mesoporous tungsten oxide modified by nanolayered manganese-calcium oxide as robust photoanode for solar water splitting, J. Colloid Interface Sci. 516 (2018) 145–152. doi:10.1016/j.jcis.2018.01.053.

[248] A. Mao, J.K. Kim, K. Shin, D.H. Wang, P.J. Yoo, G.Y. Han, J.H. Park, Hematite modified tungsten trioxide nanoparticle photoanode for solar water oxidation, J. Power Sources. 210 (2012) 32–37. doi:10.1016/j.jpowsour.2012.02.112.

[249] G. Vijaya, M.M. Singh, M.S. Krupashankara, M.R. Srinivas, R.S. Kulkarni, Development and Analysis of Tungsten Thin film Coating for Solar Absorption, Mater. Today Proc. 5 (2018) 2555–2563. doi:10.1016/j.matpr.2017.11.039.

[250] X. Ming, A. Guo, G. Wang, X. Wang, Two-dimensional defective tungsten oxide nanosheets as high performance photo-absorbers for efficient solar steam generation, Sol. Energy Mater. Sol. Cells. 185 (2018) 333–341. doi:10.1016/j.solmat.2018.05.049.

[251] Y. Ping, G. Galli, Optimizing the band edges of tungsten trioxide for water oxidation: A first-principles study, J. Phys. Chem. C. 118 (2014) 6019–6028. doi:10.1021/jp410497f.

[252] M.B. Tahir, G. Nabi, M. Rafique, N.R. Khalid, Nanostructured-based WO3photocatalysts: recent development, activity enhancement, perspectives and applications for wastewater treatment, Int. J. Environ. Sci. Technol. 14 (2017) 2519–2542. doi:10.1007/s13762-017-1394-z.

[253] T. Kikuchi, J. Kawashima, S. Natsui, R.O. Suzuki, Fabrication of porous tungsten oxide via anodizing in an ammonium nitrate/ethylene glycol/water mixture for visible light-driven photocatalyst, Appl. Surf. Sci. 422 (2017) 130–137. doi:10.1016/j.apsusc.2017.05.256.

[254] S. Salmaoui, F. Sediri, N. Gharbi, C. Perruchot, S. Aeiyach, I.A. Rutkowska, P.J. Kulesza, M. Jouini, Hexagonal nanorods of tungsten trioxide: Synthesis, structure, electrochemical properties and activity as supporting material in electrocatalysis, Appl. Surf. Sci. 257 (2011) 8223–8229. doi:10.1016/j.apsusc.2011.04.077.

[255] M. Visa, C. Bogatu, A. Duta, Tungsten oxide - fly ash oxide composites in adsorption and photocatalysis, J. Hazard. Mater. 289 (2015) 244–256. doi:10.1016/j.jhazmat.2015.01.053.

[256] I. Aslam, C. Cao, W.S. Khan, G. Engineering, Synthesis of three-dimensional WO3octahedra: Characterization, optical and efficient photocatalytic properties, (2014). doi:10.1039/C4RA05724D.

[257] M. Aslam, I.M.I. Ismail, S. Chandrasekaran, A. Hameed, Morphology controlled bulk synthesis of disc-shaped WO 3 powder and evaluation of its photocatalytic activity for the degradation of phenols, J. Hazard. Mater. 276 (2014) 120–128. doi:10.1016/j.jhazmat.2014.05.022.

[258] F. Barreca, N. Acacia, S. Spadaro, G. Currò, F. Neri, Tungsten trioxide (WO3 - X) nanoparticles prepared by pulsed laser ablation in water, Mater. Chem. Phys. 127 (2011) 197–202. doi:10.1016/j.matchemphys.2011.01.059.

[259] K.J. Lethy, D. Beena, R. Vinod Kumar, V.P. Mahadevan Pillai, V. Ganesan, V. Sathe, D.M. Phase, Nanostructured tungsten oxide thin films by the reactive pulsed laser deposition technique, Appl. Phys. A. 91 (2008) 637–649. doi:10.1007/s00339-008-4492-4.

[260] A. Bailini, F. Di Fonzo, M. Fusi, C.S. Casari, A.L. Bassi, V. Russo, A. Baserga, C.E. Bottani, Pulsed laser deposition of tungsten and tungsten oxide thin films with tailored structure at the nano- and mesoscale, Appl. Surf. Sci. 253 (2007) 8130–8135. doi:10.1016/j.apsusc.2007.02.145.

[261] G. Soto, W. De La Cruz, J.A. Díaz, R. Machorro, F.F. Castillón, M.H. Farías, Characterization of tungsten oxide films produced by reactive pulsed laser deposition, Appl. Surf. Sci. 218 (2003) 281–289. doi:10.1016/S0169-4332(03)00677-9.

[262] S. Shuntaro, T. Suzuki, M. Hirai, H. Suematsu, C. Grigoriu, C. Sima, I. Nicolae, W. Waldhauser, M. Lackner, Synthesis and optimization of tungsten and tungsten oxide films produced by laser ablation, J. Phys. Conf. Ser. 59 (2007) 297–300. doi:10.1088/1742-6596/59/1/062.

[263] P.M. Ossi, Springer Series in Materials Science 274 Advances in the Application of Lasers in Materials Science, n.d.

[264] M. Bettonte, A. Miotello, R.S. Brusa, Solar concentrator, method and equipement for its achievement., 2007.

[265] M. Eccher, S. Turrini, A. Salemi, M. Bettonte, A. Miotello, R.S. Brusa, Construction method and optical characterization of parabolic solar modules for concentration systems, Sol. Energy. 94 (2013) 19–27. doi:10.1016/j.solener.2013.04.028.

[266] S. Yamamoto, A. Inouye, M. Yoshikawa, Structural and gasochromic properties of epitaxial WO3 films prepared by pulsed laser deposition, 2008. doi:10.1016/j.nimb.2007.12.092.

[267] A.L. Smeigh, L. Le Pleux, J. Fortage, Y. Pellegrin, E. Blart, F. Odobel, L. Hammarström, Ultrafast recombination for NiO sensitized with a series of perylene imide sensitizers exhibiting Marcus normal behaviour, Chem. Commun. 48 (2012) 678–680. doi:10.1039/C1CC16144J.

[268] H. Bin Yang, B. Liu, S.Y. Khoo, L.N. Zhu, C.X. Guo, Y.Q. Dong, C.M. Li, One-Step Fabrication of Unique Mesoporous NiO Hollow Sphere Film on FTO for High-Performance P-Type Dye-Sensitized Solar Cells, Adv. Mater. Interfaces. 1 (2014) 1300110. doi:10.1002/admi.201300110.

[269] W. Song, Z. Chen, C.R.K. Glasson, K. Hanson, H. Luo, M.R. Norris, D.L. Ashford, J.J. Concepcion, M.K. Brennaman, T.J. Meyer, Interfacial Dynamics and Solar Fuel Formation in Dye-Sensitized Photoelectrosynthesis Cells, ChemPhysChem. 13 (2012) 2882–2890. doi:10.1002/cphc.201200100.

[270] J. He, H. Lindström, A. Hagfeldt, S.-E. Lindquist, Dye-Sensitized Nanostructured p-Type Nickel Oxide Film as a Photocathode for a Solar Cell, J. Phys. Chem. B. 103 (1999) 8940–8943. doi:10.1021/jp991681r.

[271] C.J. Wood, G.H. Summers, C.A. Clark, N. Kaeffer, M. Braeutigam, L.R. Carbone, L. D'Amario, K. Fan, Y. Farré, S. Narbey, F. Oswald, L.A. Stevens, C.D.J. Parmenter, M.W. Fay, A. La Torre, C.E. Snape, B. Dietzek, D. Dini, L. Hammarström, Y. Pellegrin, F. Odobel, L. Sun, V. Artero, E.A. Gibson, A comprehensive comparison of dye-sensitized NiO photocathodes for solar energy conversion, Phys. Chem. Chem. Phys. 18 (2016) 10727–10738. doi:10.1039/C5CP05326A.

[272] P.H.L. Notten, Rechargeable nickel-metalhydride batteries: a successful new concept BT - Interstitial Intermetallic Alloys, in: F. Grandjean, G.J. Long, K.H.J. Buschow (Eds.), Springer Netherlands, Dordrecht, 1995: pp. 151–195. doi:10.1007/978-94-011-0295-7_7.

[273] C.-G. Granqvist, Out of a niche, Nat. Mater. 5 (2006) 89–90. doi:10.1038/nmat1577.

[274] E. Avendaño, H. Rensmo, A. Azens, A. Sandell, G. de M. Azevedo, H. Siegbahn, G.A. Niklasson, C.G. Granqvist, Coloration Mechanism in Proton-Intercalated Electrochromic Hydrated NiO y and Ni1 − x V x O y Thin Films, J. Electrochem. Soc. . 156 (2009) P132–P138. doi:10.1149/1.3148327 .

[275] J.S.E.M. Svensson, C.G. Granqvist, Electrochromic hydrated nickel oxide coatings for energy efficient windows: Optical properties and coloration mechanism, Appl. Phys. Lett. 49 (1986) 1566–1568. doi:10.1063/1.97281.

[276] I. Bouessay, A. Rougier, P. Poizot, J. Moscovici, A. Michalowicz, J.-M. Tarascon, Electrochromic degradation in nickel oxide thin film: A self-discharge and dissolution phenomenon, Electrochim. Acta. 50 (2005) 3737–3745. doi:https://doi.org/10.1016/j.electacta.2005.01.020.

[277] R.D.L. Smith, M.S. Prévot, R.D. Fagan, Z. Zhang, P.A. Sedach, M.K.J. Siu, S. Trudel, C.P. Berlinguette, Photochemical Route for Accessing Amorphous Metal Oxide Materials for Water Oxidation Catalysis, Science (80-.). 340 (2013) 60 LP-63. doi:10.1126/science.1233638.

[278] L. Trotochaud, J.K. Ranney, K.N. Williams, S.W. Boettcher, Solution-Cast Metal Oxide Thin

Film Electrocatalysts for Oxygen Evolution, J. Am. Chem. Soc. 134 (2012) 17253–17261. doi:10.1021/ja307507a.

[279] S. Klaus, Y. Cai, M.W. Louie, L. Trotochaud, A.T. Bell, Effects of Fe Electrolyte Impurities on Ni(OH)2/NiOOH Structure and Oxygen Evolution Activity, J. Phys. Chem. C. 119 (2015) 7243–7254. doi:10.1021/acs.jpcc.5b00105.

[280] L. Trotochaud, S.L. Young, J.K. Ranney, S.W. Boettcher, Nickel–Iron Oxyhydroxide Oxygen-Evolution Electrocatalysts: The Role of Intentional and Incidental Iron Incorporation, J. Am. Chem. Soc. 136 (2014) 6744–6753. doi:10.1021/ja502379c.

[281] K.M.H. Young, T.W. Hamann, Enhanced photocatalytic water oxidation efficiency with Ni(OH)2 catalysts deposited on α-Fe2O3via ALD, Chem. Commun. 50 (2014) 8727–8730. doi:10.1039/C4CC02598A.

[282] M.G. Walter, E.L. Warren, J.R. McKone, S.W. Boettcher, Q. Mi, E.A. Santori, N.S. Lewis, Solar Water Splitting Cells, Chem. Rev. 110 (2010) 6446–6473. doi:10.1021/cr1002326.

[283] R.D.L. Smith, B. Sporinova, R.D. Fagan, S. Trudel, C.P. Berlinguette, Facile Photochemical Preparation of Amorphous Iridium Oxide Films for Water Oxidation Catalysis, Chem. Mater. 26 (2014) 1654–1659. doi:10.1021/cm4041715.

[284] Q. Liu, F. Cao, F. Wu, H. Lu, L. Li, Ultrathin Amorphous Ni(OH)2 Nanosheets on Ultrathin α-Fe2O3 Films for Improved Photoelectrochemical Water Oxidation, Adv. Mater. Interfaces. 3 (2016) 1600256. doi:10.1002/admi.201600256.

[285] R.D.L. Smith, M.S. Prévot, R.D. Fagan, S. Trudel, C.P. Berlinguette, Water Oxidation Catalysis: Electrocatalytic Response to Metal Stoichiometry in Amorphous Metal Oxide Films Containing Iron, Cobalt, and Nickel, J. Am. Chem. Soc. 135 (2013) 11580–11586. doi:10.1021/ja403102j.

[286] Y. Jia, L. Zhang, G. Gao, H. Chen, B. Wang, J. Zhou, M.T. Soo, M. Hong, X. Yan, G. Qian, J. Zou, A. Du, X. Yao, A Heterostructure Coupling of Exfoliated Ni–Fe Hydroxide Nanosheet and Defective Graphene as a Bifunctional Electrocatalyst for Overall Water Splitting, Adv. Mater. 29 (2017) 1700017. doi:10.1002/adma.201700017.

[287] F. Lin, S.W. Boettcher, Adaptive semiconductor/electrocatalyst junctions in water-splitting photoanodes, Nat. Mater. 13 (2013) 81. https://doi.org/10.1038/nmat3811.

[288] H.Y. Hwang, Y. Iwasa, M. Kawasaki, B. Keimer, N. Nagaosa, Y. Tokura, Emergent phenomena at oxide interfaces, Nat. Mater. 11 (2012) 103. https://doi.org/10.1038/nmat3223.

[289] M.G. KRISHNA, A.K. BHATTACHARYA, QUANTUM CONFINEMENT EFFECTS ON THE OPTICAL PROPERTIES OF ION BEAM SPUTTERED NICKEL OXIDE THIN FILMS, Int. J. Mod. Phys. B. 15 (2001) 191–200. doi:10.1142/S0217979201003740.

[290] L. Trotochaud, T.J. Mills, S.W. Boettcher, An Optocatalytic Model for Semiconductor–Catalyst Water-Splitting Photoelectrodes Based on In Situ Optical Measurements on Operational Catalysts, J. Phys. Chem. Lett. 4 (2013) 931–935. doi:10.1021/jz4002604.

[291] M. Schenato, C.L.A. Ricardo, P. Scardi, R. Edla, A. Miotello, M. Orlandi, R. Morrish, Effect of annealing and nanostructuring on pulsed laser deposited WS2 for HER catalysis, Appl. Catal. A Gen. 510 (2016) 156–160. doi:https://doi.org/10.1016/j.apcata.2015.11.009.

[292] I. Petrov, P.B. Barna, L. Hultman, J.E. Greene, Microstructural evolution during film growth, J. Vac. Sci. Technol. A. 21 (2003) S117–S128. doi:10.1116/1.1601610.

[293] A. Infortuna, A.S. Harvey, L.J. Gauckler, Microstructures of CGO and YSZ Thin Films by Pulsed Laser Deposition, Adv. Funct. Mater. 18 (2008) 127–135. doi:10.1002/adfm.200700136.

[294] M. Orlandi, N. Dalle Carbonare, S. Caramori, C.A. Bignozzi, S. Berardi, A. Mazzi, Z. El Koura, N. Bazzanella, N. Patel, A. Miotello, Porous versus Compact Nanosized Fe(III)-Based Water

Oxidation Catalyst for Photoanodes Functionalization, ACS Appl. Mater. Interfaces. 8 (2016) 20003–20011. doi:10.1021/acsami.6b05135.

[295] A. Mazzi, A. Miotello, Simulation of phase explosion in the nanosecond laser ablation of aluminum, J. Colloid Interface Sci. 489 (2017) 126–130. doi:https://doi.org/10.1016/j.jcis.2016.08.016.

[296] R. Kelly, A. Miotello, Contribution of vaporization and boiling to thermal-spike sputtering by ions or laser pulses, Phys. Rev. E. 60 (1999) 2616–2625. doi:10.1103/PhysRevE.60.2616.

[297] A. Ojeda-G-P, C.W. Schneider, T. Lippert, A. Wokaun, Pressure and temperature dependence of the laser-induced plasma plume dynamics, J. Appl. Phys. 120 (2016) 225301. doi:10.1063/1.4971251.

[298] A. Mazzi, F. Gorrini, A. Miotello, Liquid nanodroplet formation through phase explosion mechanism in laser-irradiated metal targets, Phys. Rev. E. 92 (2015) 31301. doi:10.1103/PhysRevE.92.031301.

[299] R.E. Dietz, G.I. Parisot, A.E. Meixner, Infrared Absorption and Raman Scattering by Two-Magnon Processes in NiO, Phys. Rev. B. 4 (1971) 2302–2310. doi:10.1103/PhysRevB.4.2302.

[300] N. Mironova-Ulmane, A. Kuzmin, I. Steins, J. Grabis, I. Sildos, M. Pärs, Raman scattering in nanosized nickel oxide NiO, J. Phys. Conf. Ser. 93 (2007) 12039. doi:10.1088/1742-6596/93/1/012039.

[301] C. Johnston, P.R. Graves, In situ Raman Spectroscopy Study of the Nickel Oxyhydroxide Electrode (NOE) System, Appl. Spectrosc. 44 (1990) 105–115. doi:10.1366/0003702904085769.

[302] NIST X-ray Photoelectron Spectroscopy Database, n.d. https://srdata.nist.gov/xps/.

[303] G.A. Niklasson, C.G. Granqvist, Electrochromics for smart windows: thin films of tungsten oxide and nickel oxide, and devices based on these, J. Mater. Chem. 17 (2007) 127–156. doi:10.1039/B612174H.

[304] M.K. Carpenter, D.A. Corrigan, Photoelectrochemistry of Nickel Hydroxide Thin Films, J. Electrochem. Soc. . 136 (1989) 1022–1026. doi:10.1149/1.2096777 .

[305] R.J. Powell, W.E. Spicer, Optical Properties of NiO and CoO, Phys. Rev. B. 2 (1970) 2182–2193. doi:10.1103/PhysRevB.2.2182.

[306] H. Bode, K. Dehmelt, J. Witte, Zur kenntnis der nickelhydroxidelektrode—I.Über das nickel (II)-hydroxidhydrat, Electrochim. Acta. 11 (1966) 1079-IN1. doi:https://doi.org/10.1016/0013-4686(66)80045-2.

[307] C.C.L. McCrory, S. Jung, J.C. Peters, T.F. Jaramillo, Benchmarking Heterogeneous Electrocatalysts for the Oxygen Evolution Reaction, J. Am. Chem. Soc. 135 (2013) 16977–16987. doi:10.1021/ja407115p.

[308] Y. Matsumoto, E. Sato, Electrocatalytic properties of transition metal oxides for oxygen evolution reaction, Mater. Chem. Phys. 14 (1986) 397–426. doi:https://doi.org/10.1016/0254-0584(86)90045-3.

[309] S. Trasatti, Electrocatalysis by oxides — Attempt at a unifying approach, J. Electroanal. Chem. Interfacial Electrochem. 111 (1980) 125–131. doi:https://doi.org/10.1016/S0022-0728(80)80084-2.

[310] F. Jiao, H. Frei, Nanostructured Cobalt Oxide Clusters in Mesoporous Silica as Efficient Oxygen-Evolving Catalysts, Angew. Chemie Int. Ed. 48 (2009) 1841–1844. doi:10.1002/anie.200805534.

[311] G. Rahman, O.-S. Joo, Electrodeposited nanostructured α-Fe2O3 thin films for solar water splitting: Influence of Pt doping on photoelectrochemical performance, Mater. Chem. Phys. 140 (2013) 316–322. doi:https://doi.org/10.1016/j.matchemphys.2013.03.042.

[312] M. Orlandi, S. Caramori, F. Ronconi, C.A. Bignozzi, Z. El Koura, N. Bazzanella, L. Meda, A. Miotello, Pulsed-Laser Deposition of Nanostructured Iron Oxide Catalysts for Efficient Water Oxidation, ACS Appl. Mater. Interfaces. 6 (2014) 6186–6190. doi:10.1021/am501021e.

[313] Z. Zhang, C. Gao, Y. Li, W. Han, W. Fu, Y. He, E. Xie, Enhanced charge separation and transfer through Fe2O3/ITO nanowire arrays wrapped with reduced graphene oxide for water-splitting, Nano Energy. 30 (2016) 892–899. doi:https://doi.org/10.1016/j.nanoen.2016.08.059.

[314] H. Tüysüz, Y.J. Hwang, S.B. Khan, A.M. Asiri, P. Yang, Mesoporous Co3O4 as an electrocatalyst for water oxidation, Nano Res. 6 (2013) 47–54. doi:10.1007/s12274-012-0280-8.

[315] S. Gupta, A. Yadav, S. Bhartiya, M.K. Singh, A. Miotello, A. Sarkar, N. Patel, Co oxide nanostructures for electrocatalytic water-oxidation: effects of dimensionality and related properties, Nanoscale. 10 (2018) 8806–8819. doi:10.1039/C8NR00348C.

[316] F. Jiao, H. Frei, Nanostructured cobalt and manganese oxide clusters as efficient water oxidation catalysts, Energy Environ. Sci. 3 (2010) 1018–1027. doi:10.1039/C002074E.

[317] H. Sen Soo, A. Agiral, A. Bachmeier, H. Frei, Visible Light-Induced Hole Injection into Rectifying Molecular Wires Anchored on Co3O4 and SiO2 Nanoparticles, J. Am. Chem. Soc. 134 (2012) 17104–17116. doi:10.1021/ja306162g.

[318] M. Zhang, M. de Respinis, H. Frei, Time-resolved observations of water oxidation intermediates on a cobalt oxide nanoparticle catalyst, Nat. Chem. 6 (2014) 362. https://doi.org/10.1038/nchem.1874.

[319] A. Kargar, S. Yavuz, T.K. Kim, C.-H. Liu, C. Kuru, C.S. Rustomji, S. Jin, P.R. Bandaru, Solution-Processed CoFe2O4 Nanoparticles on 3D Carbon Fiber Papers for Durable Oxygen Evolution Reaction, ACS Appl. Mater. Interfaces. 7 (2015) 17851–17856. doi:10.1021/acsami.5b04270.

[320] X.-F. Lu, L.-F. Gu, J.-W. Wang, J.-X. Wu, P.-Q. Liao, G.-R. Li, Bimetal-Organic Framework Derived CoFe2O4/C Porous Hybrid Nanorod Arrays as High-Performance Electrocatalysts for Oxygen Evolution Reaction, Adv. Mater. 29 (2017) 1604437. doi:10.1002/adma.201604437.

[321] W. Yan, X. Cao, J. Tian, C. Jin, K. Ke, R. Yang, Nitrogen/sulfur dual-doped 3D reduced graphene oxide networks-supported CoFe2O4 with enhanced electrocatalytic activities for oxygen reduction and evolution reactions, Carbon N. Y. 99 (2016) 195–202. doi:https://doi.org/10.1016/j.carbon.2015.12.011.

[322] Q. Guo, W. Shi, F. Liu, M. Arita, Y. Ikoma, K. Saito, T. Tanaka, M. Nishio, Effects of oxygen gas pressure on properties of iron oxide films grown by pulsed laser deposition, J. Alloys Compd. 552 (2013) 1–5. doi:https://doi.org/10.1016/j.jallcom.2012.10.088.

[323] S. Murcia-López, C. Fàbrega, D. Monllor-Satoca, M.D. Hernández-Alonso, G. Penelas-Pérez, A. Morata, J.R. Morante, T. Andreu, Tailoring Multilayered BiVO4 Photoanodes by Pulsed Laser Deposition for Water Splitting, ACS Appl. Mater. Interfaces. 8 (2016) 4076–4085. doi:10.1021/acsami.5b11698.

[324] C. Fàbrega, S. Murcia-López, D. Monllor-Satoca, J.D. Prades, M.D. Hernández-Alonso, G. Penelas, J.R. Morante, T. Andreu, Efficient WO3 photoanodes fabricated by pulsed laser deposition for photoelectrochemical water splitting with high faradaic efficiency, Appl. Catal. B Environ. 189 (2016) 133–140. doi:https://doi.org/10.1016/j.apcatb.2016.02.047.

[325] J.D. Blakemore, H.B. Gray, J.R. Winkler, A.M. Müller, Co3O4 Nanoparticle Water-Oxidation

Catalysts Made by Pulsed-Laser Ablation in Liquids, ACS Catal. 3 (2013) 2497–2500. doi:10.1021/cs400639b.

[326] Y. Popat, M. Orlandi, N. Patel, R. Edla, N. Bazzanella, S. Gupta, M. Yadav, S. Pillai, M.K. Patel, A. Miotello, Pulsed laser deposition of CoFe2O4/CoO hierarchical-type nanostructured heterojuction forming a Z-scheme for efficient spatial separation of photoinduced electron-hole pairs and highly active surface area, Appl. Surf. Sci. 489 (2019) 584–594. doi:https://doi.org/10.1016/j.apsusc.2019.05.314.

[327] A. Mazzi, M. Orlandi, N. Patel, A. Miotello, Laser-Inducing Extreme Thermodynamic Conditions in Condensed Matter to Produce Nanomaterials for Catalysis and the Photocatalysis BT - Advances in the Application of Lasers in Materials Science, in: P.M. Ossi (Ed.), Springer International Publishing, Cham, 2018: pp. 89–106. doi:10.1007/978-3-319-96845-2_4.

[328] V. V Atuchin, D.A. Vinnik, T.A. Gavrilova, S.A. Gudkova, L.I. Isaenko, X. Jiang, L.D. Pokrovsky, I.P. Prosvirin, L.S. Mashkovtseva, Z. Lin, Flux Crystal Growth and the Electronic Structure of BaFe12O19 Hexaferrite, J. Phys. Chem. C. 120 (2016) 5114–5123. doi:10.1021/acs.jpcc.5b12243.

[329] T.J. Chuang, C.R. Brundle, D.W. Rice, Interpretation of the x-ray photoemission spectra of cobalt oxides and cobalt oxide surfaces, Surf. Sci. 59 (1976) 413–429. doi:https://doi.org/10.1016/0039-6028(76)90026-1.

[330] G. Mattogno, C. Ferragina, M.A. Massucci, P. Patrono, A. La Ginestra, X-ray photoelectron spectroscopic evidence of interlayer complex formation between Co(II) and N-heterocycles in α-Zr(hpo4)2 · H2O, J. Electron Spectros. Relat. Phenomena. 46 (1988) 285–295. doi:https://doi.org/10.1016/0368-2048(88)85026-6.

[331] N.S. McIntyre, M.G. Cook, X-ray photoelectron studies on some oxides and hydroxides of cobalt, nickel, and copper, Anal. Chem. 47 (1975) 2208–2213. doi:10.1021/ac60363a034.

[332] A.R. Burke, C.R. Brown, W.C. Bowling, J.E. Glaub, D. Kapsch, C.M. Love, R.B. Whitaker, W.E. Moddeman, Ignition mechanism of the titanium–boron pyrotechnic mixture, Surf. Interface Anal. 11 (1988) 353–358. doi:10.1002/sia.740110614.

[333] E.Z. Kurmaev, V. V Fedorenko, V.R. Galakhov, S. Bartkowski, S. Uhlenbrock, M. Neumann, P.R. Slater, C. Greaves, Y. Miyazaki, Analysis of oxyanion (BO33−, CO32−, SO42−, PO43−, SeO44-) substitution in Y123 compounds studied by X-ray photoelectron spectroscopy, J. Supercond. 9 (1996) 97–100. doi:10.1007/BF00728433.

[334] H. Chen, S. Ouyang, M. Zhao, Y. Li, J. Ye, Synergistic Activity of Co and Fe in Amorphous Cox–Fe–B Catalyst for Efficient Oxygen Evolution Reaction, ACS Appl. Mater. Interfaces. 9 (2017) 40333–40343. doi:10.1021/acsami.7b13939.

List of Publications

I. Y. Popat, M. Orlandi, N. Patel, R. Edla, N. Bazzanella, S. Gupta, M. Yadav, S. Pillai, M.K. Patel and A. Miotello, Applied Surface Science 489 (2019), 584-594. https://doi.org/10.1016/j.apsusc.2019.05.314

II. Alberto Mazzi, Michele Orlandi, Nicola Bazzanella, Yaksh J. Popat, Luca Minati, Giorgio Speranzaa and Antonio Miotello, Materials Science in Semiconductor Processing 97 (2019), 29-34. https://doi.org/10.1016/j.mssp.2019.02.036

III. A. Yadav, M. Yadav, S. Gupta, Y. Popat, A. Gangan, B. Chakraborty, L.M. Ramaniah, R. Fernandes, A. Miotello, M.R. Press and N. Patel, Carbon 143 (2019), 51-62. https://doi.org/10.1016/j.carbon.2018.10.090

IV. Manisha Yadav, Asha Yadav, Rohan Fernandes, Yaksh Popat, Michele Orlandi, Alpa Dashora, D.C. Kothari, Antonio Miotello, B.L. Ahuja and Nainesh Patel, Journal of Environmental Management 203 (2017), 364-374. https://doi.org/10.1016/j.jenvman.2017.08.010

Acknowledgements

It gives me immense pleasure to thank everyone who has been a part of my life personally and professionally during the past 3 years of my PhD life. Coming to a new country for higher studies was never an easy decision to make and I am so grateful that I made the right choice of coming to University of Trento for my PhD.

Firstly, I would like to thank my PhD supervisor Prof. Antonio Miotello who always considers me as his friend first and student later. It is because of him that I have had a wonderful experience here in Italy and did not face any issue. Thank you sir for giving me the opportunity to work in your research group and demonstrate my potential. I am very grateful for the support I received during my doctorate studies be it my personal life issues, taking leaves to go to India or research related problems. The freedom of working freely on new ideas with full support from the group is something I really loved in this group. Secondly, I would like to thank Dr. Nainesh Patel who has been associated with me for the past 5 years. It is because of him that I got the opportunity of interacting with Prof Antonio Miotello which eventually landed me with the PhD degree. He has been a constant support for me throughout my master's and PhD and his advices and life lessons have benefited me tremendously. Apart from being my overseas collaborator, he has been a mentor I always dreamt of, a friend I could trust with my insecurities and most importantly a very good human being who understands people. I have no words to express the admiration I have for these two people both professionally and personally and I cannot thank them enough ever.

I would also like to thank everyone in IdEA laboratory at University of Trento who have been a part of my PhD life. To start with, I would like to thank Dr. Michele Orlandi who has been my go-to person whenever I needed advices or assistance. He has been always available for me and I will miss knocking his door for assistance after my PhD. With his guidance, I developed myself to work more independently and improved myself as a researcher. I thank him for his daily support on a personal level which I believe was very important to make me feel comfortable at work. I would also like to thank Dr. Alberto Mazzi who finished his doctorate during my first year of PhD. I learnt a lot of things from his short presence and collaboration and I am grateful for his support. I thank the technicians Claudio Cestari, Nicola Bazzanella, Marco Bettonte and Massimo Cazzanelli for their help throughout. I would thank Claudio Cestari specially for being available with his technical assistance almost instantly when needed. He has also been my office partner and I thank him for all his daily association and support which extended also outside the research work. Nicola Bazznella has been a similar help to me throughout the three years with his SEM measurements and research advices. Lastly, I would like to thank my colleagues Luca Basso, Murilo Fendrich and Asma El Golli for being with me throughout this journey and making work joyful and productive.

I am also grateful to Dr. Rohan Fernandes for his help and support from the past 4 years of our association. I enjoyed working with him and exchanging research ideas. I take this opportunity to thank Dr. Suraj Gupta and Dr. Raju Edla who have been assisting and helping me understand my field of interest and have a scientific approach. I am grateful for their support and collaborations. I would also like to express my gratitude to my senior colleagues back in University of Mumbai, Dr. Asha Yadav and Manisha Yadav. They have played a vital role in building my scientific career and were the first people to teach me the basics of the field. I am indebted to both of them for helping me in my research work and also giving me valuable life advices and PhD motivation. I would also like to thank all my friends with whom I have spent countless memories in the past few years, back in India and also in Italy. They were my support system outside the University and I am extremely grateful for such amazing friends.

Lastly and most importantly, I would express my gratitude towards my family. It is because of their patience, constant love and support towards understanding my dreams and ambitions that I am able to complete my PhD studies. I am forever indebted for their support and I owe my degree to them. They have believed in me when the times were difficult and I can never repay the sacrifices they have made for my bright future.

I thank all those who were directly or indirectly associated with me during these years and helped me to successfully complete my doctorate.